Author/s:
Czuba-Wojnilowicz, Ewa Irena

Title:
Material-based gene therapy approaches for HIV and neurodegenerative diseases

Date:
2020

Persistent Link:
https://hdl.handle.net/11343/240578

Material-based gene therapy approaches for HIV and neurodegenerative diseases

Ewa Czuba-Wojnilowicz

ORCID ID: 0000-0001-9723-8178

Submitted in total fulfilment of the requirements of the degree of Doctor of Philosophy

March 2020

Department of Chemical Engineering

School of Chemical and Biomedical Engineering

The University of Melbourne

Abstract

Gene therapy is of interest in medicine as it allows potential treatment of inherited and acquired diseases that cannot be treated or prevented using conventional methods. The introduction of new genetic material into the cells aims to improve cellular functions by either replacing a malfunctioning gene with a functional transgene or silencing the expression of specific genes implicated in various human diseases. The delivery of plasmid DNA provides an opportunity to replace defective or missing genes by utilizing cellular gene expression apparatus to produce encoded proteins. RNA therapeutics act *via* the RNA interference pathway to target intermediate gene expression product for degradation and prevent its translation to protein. Free nucleic acids typically experience rapid blood clearance and a short circulation lifetime and are unable to cross biological membranes due to electrostatic repulsion between DNA/RNA phosphate groups and phospholipids in the cell membrane. Therefore, there is a need to formulate gene carriers for improved pharmacokinetics of DNA/RNA therapeutics and efficient delivery to the site of action. The main objective of this research project was to develop material-based systems for gene delivery and apply it to HIV therapy and Friedreich's ataxia (FRDA). Polyarginine-containing capsules were prepared *via* layer-by-layer assembly and enabled efficient complexation of anti-HIV siRNA. The functional effect *via* transcriptional gene silencing of the viral genome was demonstrated in virus-infected primary cells. To investigate how cellular changes associated with cell activation and viral infection influence the particle-cell interactions, particles association with activated primary cells and pseudovirus-infected T cells was investigated. In the second part of the thesis, the optimization of DNA binding by polyarginine-containing LbL core-shell particles and the delivery of frataxin-encoding plasmid DNA to address the FRDA-associated frataxin depletion was demonstrated using patient-derived iPSC neurons. The role of particle size, charge and density in the interaction of particles with iPSC 3D neuronal organoids was also demonstrated. This thesis presents the preparation and characterization of LbL-assembled particles as a versatile system with easily tailorable properties and its application in gene therapy for viral and neurodegenerative diseases. The presented research also aims to gain a fundamental understanding of bio-nano interactions in various biological systems.

Declaration

This is to certify that:

(i) The thesis comprises only my original work towards the PhD except where indicated in the preface,

(ii) Due acknowledgement has been made in the text to all other material used,

(iii) The thesis is less than 100,000 words in length, exclusive bibliographies, tables, appendices, and footnotes.

Ewa Czuba-Wojnilowicz

Preface

In Chapter 3, Dr Gyeongwon Yun and Qizhi Zhong performed AFM measurements. Mr Zhixing Lin performed SEM imaging of particles and Dr Jianhua Li performed TEM imaging of capsules. Miss Vera Klemm and Dr Chantelle Ahlenstiel performed studies with infected cell cultures, imaging and analyses of reverse transcriptase assays.

In Chapter 4, Dr Yi Ju provided MS@PEG particles and PEG capsules. Miss Agata Glab provided BG-EDA particles and performed AFM measurement.

In Chapter 5, Dr Gyeongwon Yun performed AFM analysis. Mr Zhixing Lin performed SEM imaging of particles. Dr Serena Viventi performed differentiation of stem cells and qPCR analyses.

In Chapter 6, Miss Sara Miellet provided neurospheres. Miss Agata Glab provided BG-EDA particles.

Publications

Following publications were produced during this PhD candidature:

1. E. Czuba-Wojnilowicz, S. Viventi, S. E. Howden, C. Cortez-Jugo, M. Dottori and F. Caruso, *Particle-mediated Delivery of Frataxin Plasmid to a Human Sensory Neuronal Model of Friedreich's Ataxia*. Submitted.

2. J. Chen, J. Li, J. Zhou, Z. Lin, F. Cavalieri, E. Czuba-Wojnilowicz, Y. Hu, A. Glab, Y. Ju, J. J. Richardson and F. Caruso, *Metal–Phenolic Coatings as a Platform to Trigger Endosomal Escape of Nanoparticles*, ACS Nano, **2019**, 13, 11653-11664.

3. E. Czuba-Wojnilowicz, V. Klemm, C. Cortez-Jugo, S. G. Turville, F. Caruso, A. D. Kelleher, C. L. Ahlenstiel, *Layer-by-Layer Particles Deliver Epigenetic Silencing siRNA to HIV-1 Latent Reservoir Cell Types*. Manuscript in preparation.

4. E. Czuba-Wojnilowicz, S. Miellet, A. Glab, S. Viventi, F. Cavalieri, C. Cortez-Jugo, M. Dottori, F. Caruso, *Distribution of particles in stem cell-derived 3D neuronal cell models: effect of particle size, charge and density*. Manuscript in preparation.

Acknowledgements

This thesis summarizes my research work over the last 3.5 years. While I did my best to find myself in this place, I know well enough that it would not be possible without the work and support of other people.

I would like to thank Professor Frank Caruso for giving me an opportunity to pursue my PhD degree in NIMS group. He created a research group filled with amazing scientists with diverse backgrounds and encourages them to work towards multidisciplinary projects by providing great facilities and collaboration opportunities. For me, it was particularly important to be involved in collaborative research projects with scientists from the University of New South Wales and the University of Wollongong, as it significantly enriched my PhD experience and progressed my project towards biological applications. I am also grateful to my co-supervisor Dr Christina Cortez-Jugo, who was generous in offering her time, energy and support to make sure that I stay on track. What I am perhaps the most grateful about to Frank and Christina is that they remained calm and patient, especially during difficult times. While they made sure I knew that their help was available, they also allowed me to work in my own style, pace and direction so that I could be prepared to be an independent researcher.

I would like to thank my colleagues at the Chemical Engineering department and all NIMS group members, visitors and administration team. You have created a great atmosphere, stimulating for intellectual and personal development, and I enjoyed your companionship and help during everyday activities.

I would like to thank my advisory committee chair, Dr Daniel Heath, for reviewing my research progress during our annual meetings.

I would like to acknowledge the Materials Characterisation and Fabrication Platform, Melbourne Cytometry Platform and Melbourne Histology platform and thank Paul Brannon, Dr Andrew Mitchel, Dr Alexis Gonzalez and Laura Leone for their assistance in performing experiments.

My expression of gratitude goes also to our collaborators: Professor Anthony Kelleher, Dr Chantelle Ahlenstiel and Vera Klemm who hosted me in their group at the Kirby Institute, UNSW; and Professor Mirella Dottori, Dr Serena Viventi and Sara Miellet from the University of Wollongong who offered their expertise in stem cell technologies.

Table of contents

List of Figures

List of Schemes

List of Tables

Chapter 1

Literature Review

1.1. Gene therapy

Gene therapy is based on the concept of controlling human diseases by regulating the expression of the implicated genes by introducing new genetic material in the form of nucleic acids.[1] Many diseases have genetic bases,[2,3] and more is known about gene profiles either predisposing to the development of certain types of diseases[4] or to cause disruptions in the gene expression process, leading to impaired cellular functions. Therefore, gene therapy aims to introduce new products into the cell or correct/downregulate mutated genes.[5] Generally, deoxyribonucleic acids (DNA) provide an opportunity to replace defective or missing genes.[6] Ribonucleic acids (RNA) have emerged as therapeutic agents that can be employed in a natural gene silencing process termed RNA interference (RNAi) to silence the translation of proteins encoded by incorrect genes.[7] With recent advances, reverse genetic technologies including Zinc-finger nucleases (ZNF),[8] transcription activator-like effector nucleases (TALEN) and CRISPR/Cas9 offer further opportunities for direct genome editing.[9,10] The following section will discuss the mechanism of the most common gene therapy strategies.

1.1.1. Gene expression of DNA therapeutics

The main group of DNA-based therapeutics involves plasmid DNA (pDNA), which are high molecular weight double-stranded transgenes.[11] DNA-encoded genes can be expressed upon intracellular delivery using the gene expression apparatus of the transfected cell. Efficient nuclear translocation through nuclear pores and appropriate plasmid design are the main limiting steps of the therapeutic efficiency of DNA transfection.[12] In the nucleus, the transcription of the genes encoded by delivered DNA occurs *via* the natural gene expression process. In the first step, RNA polymerase enzyme is used to transcribe the DNA to an RNA. Upon binding to the promoter region of double-stranded DNA, RNA polymerase unwinds DNA strands to generate a single-stranded template, which is used to synthesize a complementary RNA sequence.[12] Upon transcription termination, RNA is released from RNA polymerase to form pre-mRNA. Further modification of pre-mRNA ends (polyadenylations, capping) and splicing (excision of non-coding introns) enable the formation of correct transcript mRNA,[13] that can be directed to the cytoplasm and employed in the second step of gene expression, i.e., translation or protein production.

In the process of translation, mRNAs are decoded in ribosomes to produce amino acid chains.[14] This process starts with an initiation step, where transfer RNA (tRNA) containing anticodon sequence binds to specific fragments of mRNA. The binding process is enabled by a reorganization of ribosome subunits, that come close together. In the elongation step, mRNA codons are read one by one to translate encoded amino acids. The binding of amino acids to form a polypeptide chain is catalyzed by ribosomes.[15] Upon translation termination, the newly-synthesized polypeptide is transferred into the endoplasmic reticulum (ER) for storage or released from the ribosome and may require further posttranslational modifications, including conformational changes.[16] Functional protein is next exported to the site of action, either inside the cell or to the extracellular space.[14,17]

Gene expression in a highly controlled process and its activity can be modulated by cells depending on the current demand, extracellular factors or metabolic activity.[18,19,20] In gene therapy, a better understanding of the underlying mechanism allows identifying genetic changes associated with various diseases to minimize and/or prevent their effect and improve cellular functions by pharmacological intervention. Therefore, gene therapy aims to introduce exogenous genetic material and enforce its synthesis inside the cell.

1.1.2. Gene silencing by siRNA therapeutics

The first observation of RNA silencing *via* sequence-specific RNA degradation was reported in plants,[21] and shortly after was described in eukaryotes.[22,23,24] The process of RNA interference (RNAi) regulates the gene expression *via* small non-coding RNAs (sncRNAs) that target mRNA to suppress its translation into protein and thus enabling post-transcriptional gene silencing (PTGS).[25] The process was first identified in Caenorhabditis elegans, where modulation of gene expression by double-stranded RNA (dsRNA) binding to mRNA was observed.[26] Later, gene silencing in mammalian cells was reported using short synthetic short RNA (21 nucleotides),[27] which today are called small-interfering RNAs (siRNAs). PTGS involves three major classes of sncRNA, specifically siRNA (exogenous and endogenous), microRNAs (miRNAs) and piwi-associated RNAs (piRNAs).[28]

The RNA sequence involved in PTGS can originate either from the cleavage of long dsRNA or synthetic siRNA delivered to the cells using transfection methods. The loading of siRNA onto Argonaute-2 (Ago-2) enables the recruitment of heat shock protein 90 (HSP90) to form the pre-RNA-induced silencing complex (pre-RISC).[29,30] In the next step, the passenger strand

of RNA is cleaved and removed by component 3 promoter of RISC complex (C3PO) to activate the RNA-induced gene silencing complex (RISC) containing only one RNA guide strand.[31] In the activated form, RISC can scan and recognize mRNA sequence complementary to the RISC-loaded single-stranded RNA (ssRNA), leading to mRNA cleavage and degradation (**Figure 1.1**).[32]

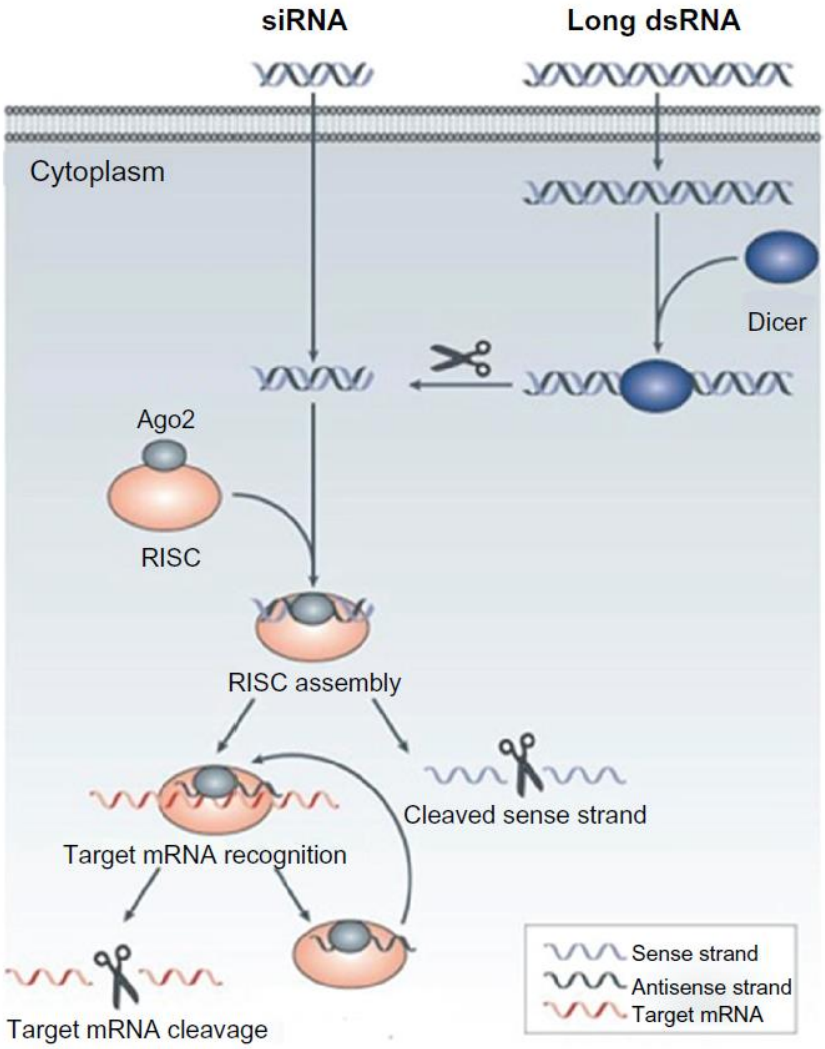

Figure 1.1. RNA interference (RNAi) mechanism. Adapted from reference 33.

1.1.3. Genome editing technologies

In addition to silencing *via* RNAi, other genome editing technologies have emerged in the past decade. Zinc-finger nucleases (ZFNs) are synthetic proteins used for genome editing.[34] They comprise two units with separate activities, namely the DNA-binding domain and DNA-

cleavage domain.[35] The targeting of ZFNs to the specific gene is achieved by the engineering of the DNA-binding domain to recognize the specific locus in the genome. Following target recognition, nucleases of DNA-cleavage domain induce DNA break.[35] Using ZFNs in gene therapy allows creating a customized genome editing tool. Importantly, the ZFN-induced DNA mutation triggers natural DNA repair processes, through homologous recombination and non-homologous end joining.[36] As a result, the use of ZFN technology allows the cell genome to be modified without permanently damaging them.[37,38] However, a safe application of ZFNs requires precisely engineered zinc finger domains to avoid off-target cleavage, which could generate multiple mutations and lead to cell death.[39] Additionally, exogenous proteins such as ZNFs may induce activation of an immune response.

Transcription activation-like effector nucleases (TALENs) also rely on DNA cleavage mechanism and comprise two units allowing for DNA recognition and breakage.[40] However, the DNA-binding unit is based on Transcription-activator-like effector (TALE) protein, originated from Xanthomonas bacteria.[41] It contains a 33-34 amino acid sequence, with a variable region between 12^{th} and 13^{th} position called repeat variable diresidues (RVD). The RVD of TALENs enables the recognition of target nucleotides sequence.[42] Engineering DNA-binding domains of TALENs typically include targeting to exons sequence close to the 5' end. Like ZFNs, TALENs induce double-strand break in the specific genome site,[43] followed by endogenous DNA repair processes. Importantly, the enzyme of DNA-cleavage unit requires dimerization to become active, therefore there is a need to use two TALENs construct for one target sequence to induce a double-strand break.[44,45] As a result, the off-target spontaneous mutation caused by non-specific DNA cleavage by TALENs are not often observed.[46]

Clustered regularly-interspaced short palindromic repeats (CRISPR) are fragments of prokaryotic DNA and CRISPR-associated protein 9 (Cas9) is an enzyme able to recognize and cleave CRISPR-complementary sequence.[47] CRISPR/Cas9 is a natural defense mechanism in bacteria and archaea in response to infection.[48] The sequence specificity is enabled by CRISPR RNA (sgRNA), which targets Cas9 to a chromosomal target site. The RNA-DNA binding is enhanced by recognition of the protospacer adjacent motif (PAM) on the non-target strand.[49] Gene therapy has adapted the CRISPR/Cas9 mechanism to develop novel genome splicing and editing technology. The sequence recognition in CRISP/Cas9 is achieved by the precise engineering of single guide RNA (sgRNA).[50] Upon sequence recognition, Cas9 is directed to a target sequence and induces DNA cleavage, followed by DNA repair similar to ZFNs or TALENs. As most of the genome editing tools, CRISPR/Cas9 requires high specificity to avoid

off-target genome modification and evidence suggests that the efficiency of DNA cleavage may be related to the accessibility of chromatin (i.e., open confirmation),[51,52], therefore, limiting CRISPR/Cas9 applicability in transcriptionally silence genes.

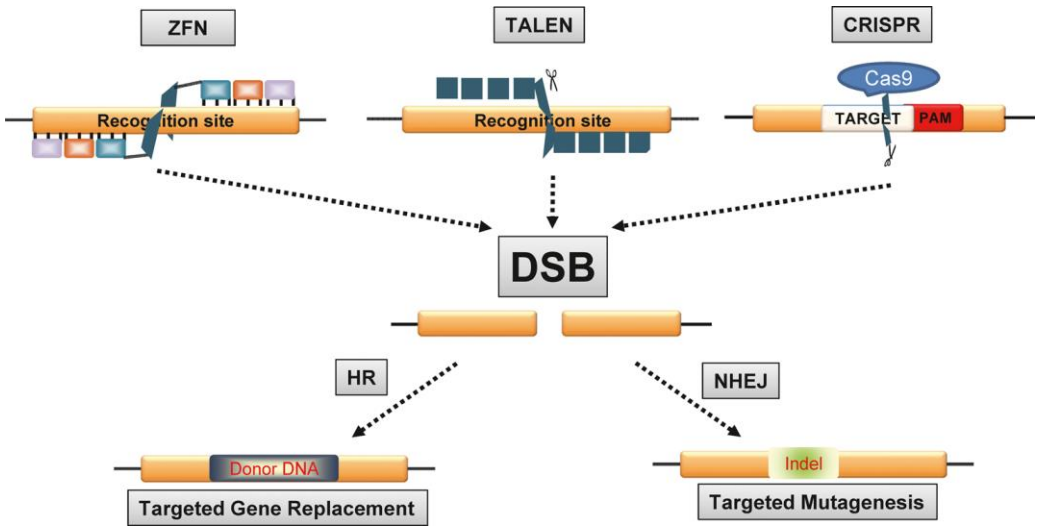

Figure 1.2. Nuclease-based genome editing technologies. Mechanism of DNA cleavage (double-strand break, DSB) and repair *via* nonhomologous end joining (NHEJ) and homologous recombination (HR). Adapted from reference 53.

1.1.4. Challenges in gene delivery

Advances in gene therapy technologies has allowed the use of nucleic acids to control the expression of genes implicated in various diseases. However, physicochemical properties of DNA/siRNA, including hydrophilicity and negative charge, significantly affects their ability to cross biological membranes comprising negatively charged phospholipids.[54] Nucleic acids are also susceptible to degradation by nucleases and in their free form are characterized by short circulation lifetime and suffer from rapid blood clearance.[55,56] While these challenges have been partly addressed by physical delivery methods, e.g. electroporation,[57] they are often not applicable for *in vivo* delivery. Therefore, the successful delivery of nucleic acids requires formulation of gene carriers, that will provide protection from degradation and deliver the cargo across cellular membranes.

Early formulations of RNA and DNA therapeutics involved the study of systems based on viral vectors such as lentivirus vectors (LV), adenovirus-associated vectors (AAV) and retrovirus vectors (RV). [58,59,60,61,62] Viral vectors are prepared from the virus, with the original genetic material being replaced by the therapeutic cargo (nucleic acid). Viral-based vectors vary in stability, efficacy and loading capacity.[59] Although promising, this strategy is not without challenges. Recombination of the viral genome can lead to the generation of the infectious forms of virus, potentially when components responsible for viral propagation are not completely removed.[58,59]Additionally, viral-based formulations may cause stimulation of an immune response, inflammatory reactions and allergies. Research into addressing efficacy and safety concerns of viral-base gene delivery vectors is underway. The next section will discuss examples of non-viral gene delivery systems.

1.2. Non-viral nucleic acid delivery systems

Non-viral nucleic acid delivery methods have been drawing much attention over potentially immunogenic viral-based systems. They carry a promise of minimized off-target immune response activation, lower toxicity, low cost of production, versatility with cargo loading and simplified targeting strategies.[65]

1.2.1. Cationic polymers and lipids

Cationic polymers and lipids constitute a significant group of non-viral carriers for gene delivery. Synthetic polymers such as dimethylamino ethyl methacrylate (DMAEMA),[66] poly-L-lysine (PLL),[67,68] polyethyleneimine (PEI)[69,70] and lipofectamine[71] are examples of positively charged polyelectrolytes used in studies on gene knockdown.[72] The formation of complexes with negatively charged nucleic acids is based on self-assembly driven by electrostatic interactions, to form polyplexes (polymer-nucleic acids complex) and lipoplexes (lipid-nucleic acid complex). [73] However, both formulations provide limited control over complex size.[74] Cationic lipid formulations for gene delivery are formed from the positively charged tail of the phospholipid, which binds nucleic acid, with the hydrophilic head interacting with a water phase. This structure enables effective fusion with cell membranes and release of

cargo into the cytosol. One of the first reported nucleic acid-lipid formulations was DNA complexed by DOTMA-based liposomes used to transfect mammalian cells.[75] It has been demonstrated that the stability and cytotoxicity of cationic lipid-based formulations may be affected by the complexation ratio with DNA.[76,77] Cytotoxic effect was assigned to the strong interaction of cationic groups of lipids with negatively-charged phospholipid bilayer surrounding cells, that may potentially lead to membrane damage and/or rupture.[78,79] In an attempt to address it, the addition of polyethylene glycol (PEG) conjugates was proposed to neutralize the cytotoxicity of the particles, however, it may also reduce cell association.[80,81] Nevertheless, successful gene silencing was demonstrated in cancer therapy using DSPE/DOTAP/DOPE lipoplexes.[82]

Polymer-based cationic systems are among the most popular formulations used to condense nucleic acids and form polyplexes. Polycations are positively charged macrocyclic structures with well-defined 3D topology and shape.[83] Cyclodextrins (CDs) are the products of synthetic starch degradation, chain splitting and intermolecular rearrangements resulting in cyclic glucose oligomers. CDs are highly soluble in aqueous solutions due to a high number of hydroxyl groups and they possess a hydrophobic cavity suitable for the formation of inclusion complexes with small hydrophobic drugs. [84] Many formulations based on cyclodextrin include modifications of the CD backbone to make the material applicable for gene delivery.[85] Examples of such materials involve the attachment of cationic polymers to introduce a nucleic acid binding motif. The positive charge of polymers is used to interact with siRNA and neutralize the overall charge of the system so that the risk of potential cytotoxicity is reduced.[86] The co-delivery of anti-EGFR siRNA and anticancer drug in glioblastoma cells were demonstrated using cyclodextrin modified with polyamines.[87] Another example of polyplexes in gene delivery formulation containing salicylamide linked with PEI to load DNA and RNA,[88] and conjugates of PEI with stearic acid were efficient in forming mRNA-containing polyplexes.[89]

Dendrimers are hyperbranched structures with a defined morphology. The size and branching direction is determined by the core, molecular weight and flexibility are defined by the number of repeating units, and external functional groups determine the type of cargo that can be loaded into the dendrimer. Examples of dendrimer-based siRNA formulations include the use of polyamidoamine (PAMAM) to induce gene silencing *in vivo*.[90]

Among inorganic based nanoparticles (NP), one of the pioneering formulation for siRNA delivery and gene knockdown was achieved with small gold nanoparticles (~15 nm) coated with thiolated polyethylene glycol – polyacrylmethacrylate (PEG-PAMA) polymers to enhance cellular uptake.[91] Silica nanoparticles have also been investigated for gene delivery with mesoporous silica nanoparticles providing a large surface area and additional space for the infiltration of RNA and DNA within template pores. Particles can be further engineered in various ways, to provide protection from nucleases, enhanced cellular uptake, and have an external stimuli-driven release mechanism.[92]

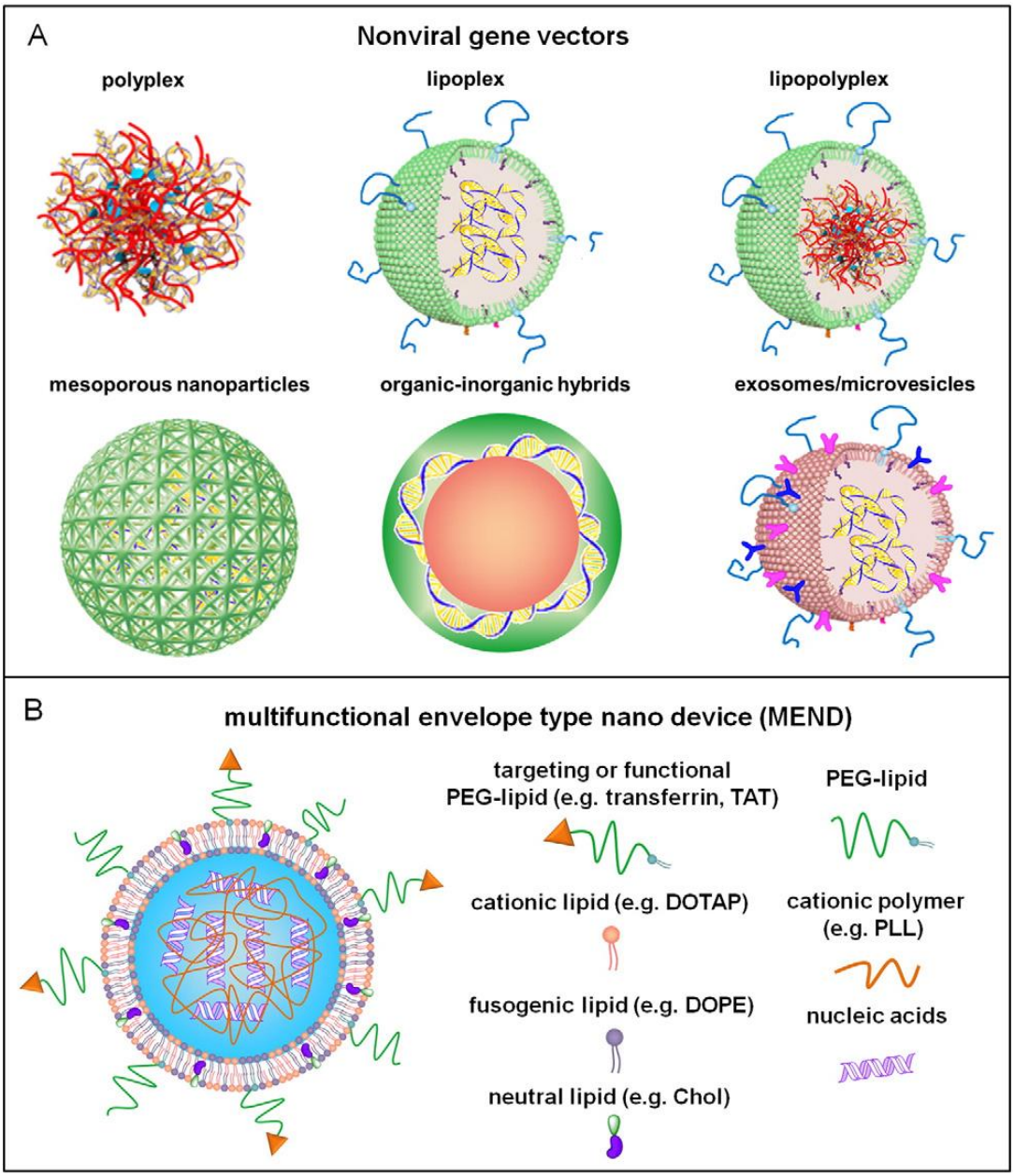

Figure 1.3. Types of gene delivery systems. Adapted from reference 100.

A significant group of biopolymers studied for nucleic acid delivery comprises amine-rich cell-penetrating peptides (CPP) and nuclear localization signals (NLS), however, they are usually used in conjugation with other molecules due to their small molecular weight.[93,94] Examples of such formulation include the system based on poly-l-lysine (PLL) used to form polyplexes when modified with hydrophobic polymer[95,96] or the use of protamine to form polyplexes with DNA.[97] Bioconjugates of PEI and arginine were also used to complex DNA and exhibit a high cellular uptake in kidney fibroblast cells.[98] In another study, a library of cationic peptides with varying lysine/arginine ratios was investigated to form polyplexes with DNA. Two arginine-rich formulations were identified as best candidates to protect DNA from degradation by DNase and to target HepG2 cells.[99]

1.2.2. Layer-by-layer particles

Layer-by-Layer (LbL) is a method of multilayer thin film deposition on an interacting surface or template.[101] LbL assembly on colloidal templates, to produce core-shell particles or capsules, provides a great opportunity to tune the physicochemical properties of the resulting carriers, including size, shape, surface/stealth properties, as well as material (polyelectrolyte) composition and the method of nucleic acid loading. Most commonly, siRNA or DNA can be pre- or post- loaded onto the particle surface or deposited within the polyelectrolyte multilayer.[102] This flexibility makes LbL assembly one of the most widely used systems for fundamental studies on drug and gene delivery, biomedical diagnosis and tissue engineering.[103,104]

LbL assembly has been studied for DNA delivery in the encapsulated form or deposited on the particle surface.[105] An LbL system for siRNA encapsulation composed of a multilayer film of thiolated poly(methacrylic acid) (PMA_{SH}) adsorbed on a mesoporous silica template infiltrated with PLL polycation was reported.[106] The knockdown (30%) of the BIRC5 gene in PC3 cells was demonstrated. A redox-responsive siRNA delivery system made of poly(ethylene glycol)-poly(L-lysine) (NPEG-PLL) capsules was used to induce survivin knockdown (~60% 120h post-transfection) as demonstrated in prostate cancer cells.[107] Multilayered particles with a PLGA core and DNA/PEI shell were also demonstrated to efficiently transfect macrophages as a proposed system for vaccine development.[108] A system

in which polymerized oligonucleotides (ODN) served as a template for LbL assembly of DNA/PLL thin film layers was also demonstrated.[109] In another study, LbL particles containing poly-Larginine and dextran were used to deliver siRNA to reduce the level of secreted SPARC proteins associated with tissue scarring and fibrosis.[110] Surface-mediate gene silencing utilizing LbL technology was demonstrated by the assembly of siRNA and poly-L-lysine films as a support for cell growth to demonstrate a dose-dependent gene silencing.[111]

The wide choice of materials available for particle preparation provides an advantage to engineer novel gene delivery carriers with unique properties and tailored for specific applications. Conjugation of targeting ligands, such as antibodies, can facilitate the specific binding on nanomaterials with cells of interest. The addition of PEG on the surface of the particles can improve blood circulation by shielding them from immune system recognition. Finally, the addition of fusogenic peptides (PLL) and lysosomotropic agents may contribute to effective particle entry to the cytosol and provide a mechanism for endosomal escape.[112,113]

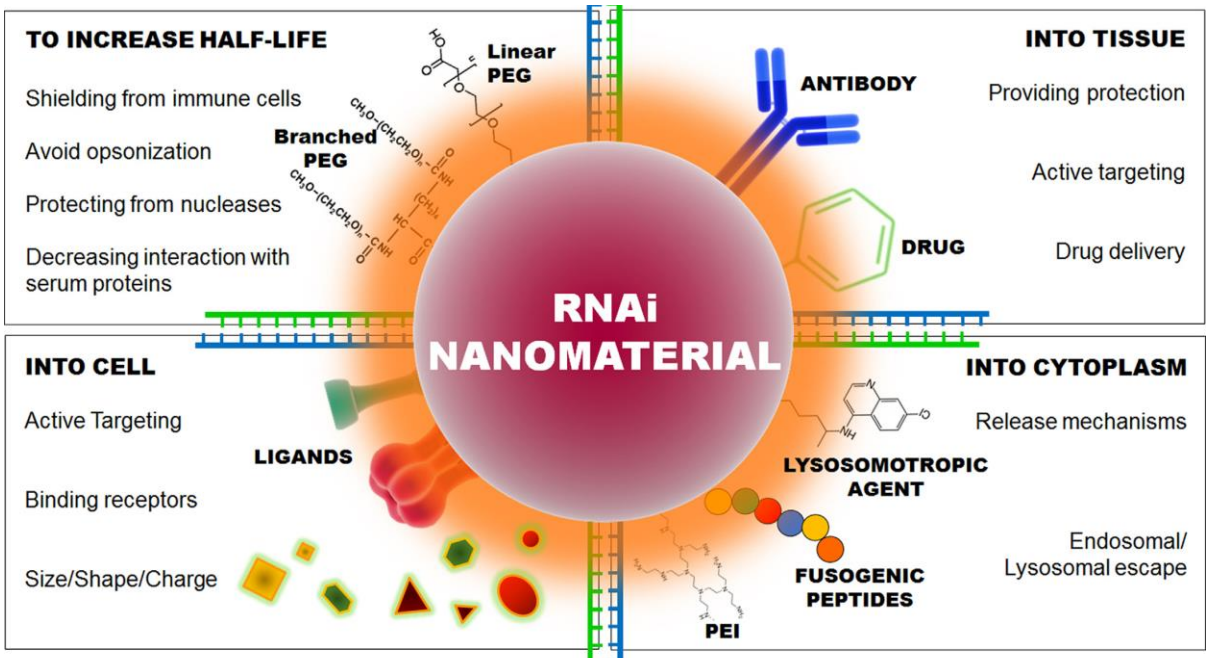

Figure 1.4. Engineering a particle for siRNA delivery. Adapted from reference 114.

1.3. Human Immunodeficiency Virus (HIV)

1.3.1. Immune system

The immune system is composed of organs, cells and proteins able to generate an immune response to provide a defence mechanism against infection. The majority of immune cells circulate in the body, but can also reside in different locations in the body, including thymus, bone marrow and lymph nodes.[115] The immune response can be divided into innate and adaptive immune response.[116] The innate response provides a quick defence mechanism against encountered pathogens, typically by monocytes, macrophages, neutrophils, natural killer cells and dendritic cells together with a set of complement proteins. Adaptive immunity is often called acquired immunity, as it is build up over the years upon encountering different pathogens to initiate a highly specific immune response *via* T cells and B cells for the reoccurring infection.

Neutrophils comprise the majority of white blood cells and the increase in their count is often an indication of the ongoing infection. Neutrophils can migrate to the site of infection and are involved primarily in the ingestion of bacteria by fusion with cells membrane.[117]

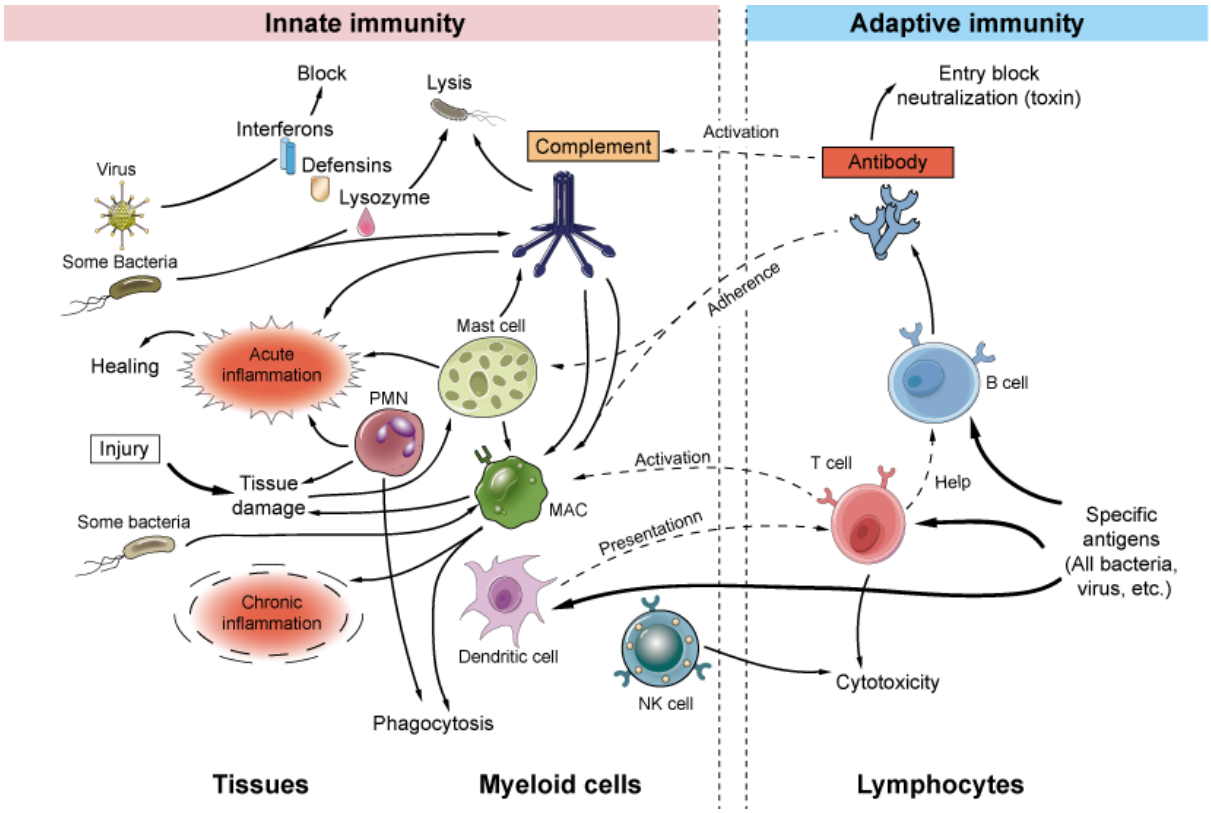

Figure 1.5. Mechanism of innate and adaptive immunity. Adapted from reference 123.

Monocytes are phagocytic cells able to ingest foreign material in the bloodstream. They can differentiate into macrophages in tissues,[118] and like macrophages they can mediate the innate immune response by direct ingestion of foreign material or marking it for degradation. Natural killer cells are involved in the response against viral infection. Dendritic cells can recognize and bind antigen, which is then displayed on their surface as an epitope to be recognized by cells involved in the adaptive immune system.[119] B cells are primarily involved in the production of antibodies.[120] T cells can be divided into different groups, depending on their function.[116] Helper T cells are involved in the maturation and activation of other lymphocytes when they encounter antigen-presenting cells, leading to cytokines secretion to initiate signalling pathways involved in the immune response. They can mature into memory and effector T cells that can be activated again when the same antigen will be presented. Cytotoxic T cells have been implicated in the recognition and clearance of tumour and virus-infected cells.[121,122] Regulatory T cells are involved in the suppression of the T cell-mediated immune response.

The immune system consists of interacting cells, tissues and proteins that provide a defence mechanism against infection. However, the immune response is sometimes insufficient to clear the infection. Moreover, some diseases attacking immune cells can significantly affect their function and induce cell death, leading to impairment of natural immune functions.

1.3.2. HIV infection

HIV remains a global pandemic with millions of people affected around the world. Current treatment involves a life-long therapy of antiretroviral drugs (ART). Although it can suppress the viral load in the plasma to undetectable levels, it is associated with side effects, including cardiovascular diseases and liver injury, as well as the risk of virus rebound upon ART cessation.[124] Symptoms of HIV infection can differ between people and progressive impairment of immune function can lead to the development of Acquired Immunodeficiency Syndrome (AIDS). HIV affects the immune system, however, the infection generates a very limited immune response, therefore the preventative approach to fight HIV is currently very limited.[125]

HIV is a retrovirus, which carries its genetic material in the form of RNA. It attacks specific types of immune cells expressing the CD4 receptor, which are used for viral entry together with CCR5 and/or CXCR4 co-receptors.[126]

A

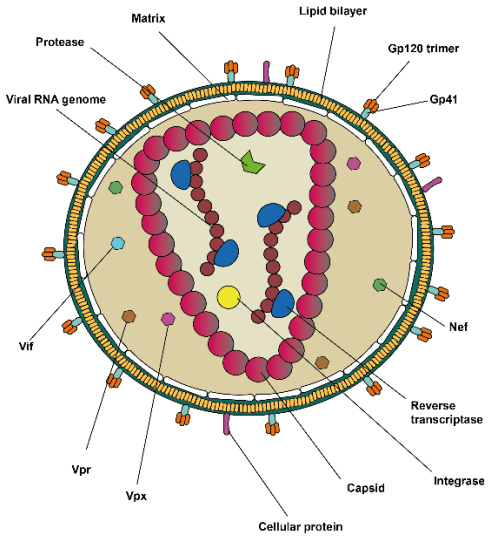

B

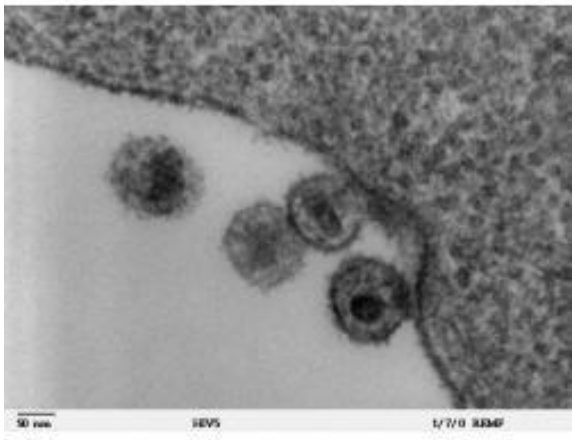

Figure 1.6. Schematic representation (A) and electron microscopy image (B) of HIV. Adapted from references 127 and 128.

After membrane fusion, the virus releases RNA into the cytosol of the host cell and uses reverse transcriptase to convert its genetic material into DNA.[129] Another enzyme encoded by HIV, integrase, promotes translocation of proviral DNA into the nucleus of the host cell, where it is integrated into the genome of the infected immune cell. At this stage, the virus can use the host's molecular machinery to produce proteins necessary for new HIV virions formation. Viral particles escape from the cell by budding from the plasma membrane and infect the next cells, which in turn leads to the loss of CD4+ T cells.[130] When the white blood count (WBT) falls below a critical level, the cell-mediated immune response is lost and the organism is no longer able to fight opportunistic infections.

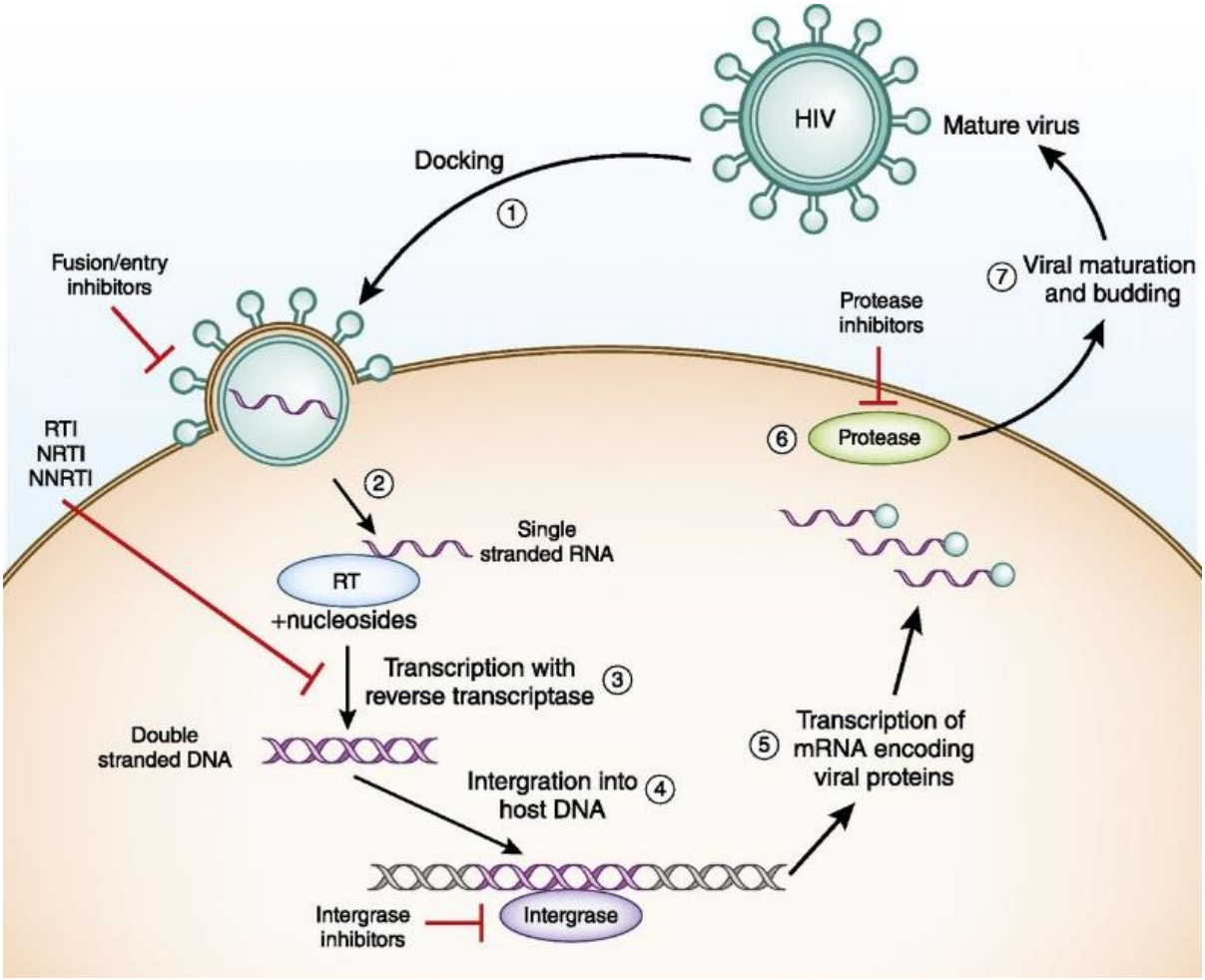

Figure 1.7. Mechanism of HIV infection. Adapted from reference 131.

HIV is transmitted through close contact with body fluids and infection is most often diagnosed with a blood assay targeting virus-specific antibodies. The major reservoir of HIV infection is present in CD4+ T cells, macrophages, dendritic cells and monocytes.[132] ART controls active infection, however, it does not affect the latent HIV reservoir in long-lived memory cells and lymph nodes, nervous system or genital tract. The presence of latent viral reservoirs at cellular and anatomical sites is a major obstacle to eradicating the virus.[133]

1.3.3. HIV latency

The latent HIV reservoir affects mainly resting CD4+ T-cells (i.e., long-lived memory T cells), but can also reside in the brain, tissues and lymph nodes. Although the size of the

reservoir may be dependent on how soon after infection ART was initiated, it is an acceptable estimation that only one in a million of resting cells carries a transcriptionally silent viral DNA.[134] The mechanism of HIV latency is not fully understood, however, several mechanisms have been identified for their contribution into silencing HIV gene expression and replication, including i) transcriptional interference at the site of HIV integration, ii) epigenetic regulation and chromatin remodelling around the HIV long terminal repeat (LTR) fragment, and iii) insufficient amount of transcription factors (TF), expressed at lower levels in resting cells.[135,136,137,138] As a result, the presence of a stably integrated proviral DNA enables viral persistence and contributes to the production of new virions following ART cessation or memory T-cells activation upon exposure to an antigen. Therefore, one of the main therapeutic strategies focused on finding an HIV cure is to reduce or deactivate HIV latent reservoirs.

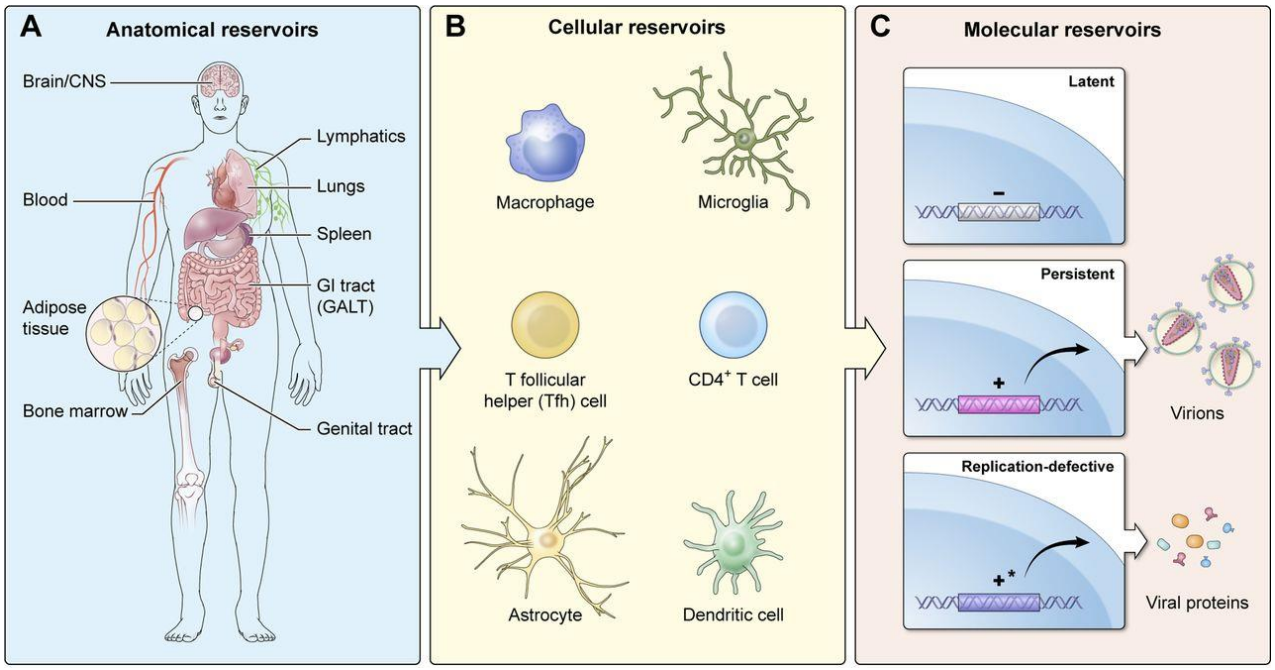

Figure 1.8. HIV latent reservoirs. Adapted from reference 132.

1.3.4. HIV therapy: Shock and kill strategy

One of the first recommended steps is to implement combination ART (cART) at a very early stage of infection, as evidence suggests that such intervention may reduce the efficiency of establishing latent infection.[139] Another way is the 'shock and kill therapy' which involves

the effective activation of the quiescent virus using latency-reversing agents (LRAs), to induce the state of active infection.[140] In this approach, newly-produced virions are then targeted by anti-viral drugs. Despite promising results for "kill" agents such as histone deacetylase inhibitors (HDACi), histone methyltransferases inhibitors, disulfiram and protein kinase C agonist, LRAs vary in efficiency to purge the virus and clinical studies have shown that LRAs fail to significantly reduce the size of the latent reservoir.[141,142,143] Targeting one mechanism associated with latency seems to be insufficient to achieve prolonged effect *in vivo*, and the use of LRAs could be associated with adverse effects in the host genome and impaired immune mechanisms, such as the cytotoxic T cell (CTL) response, aimed to kill HIV infected cells.[144] Moreover, the treatment of SIV-infected macaques with toll-like-receptor (TLR) agonist, aimed at activation of immune signalling in T cells, prevented viral rebound upon ART cessation only when combined with another therapeutic, e.g. modified vaccinia virus Ankara (MVA) vaccination or broadly neutralizing antibody.[145,146] These results indicate the need to target multiple latency mechanisms, potentially combined with immune-boosting treatment, to achieve a therapeutic effect.

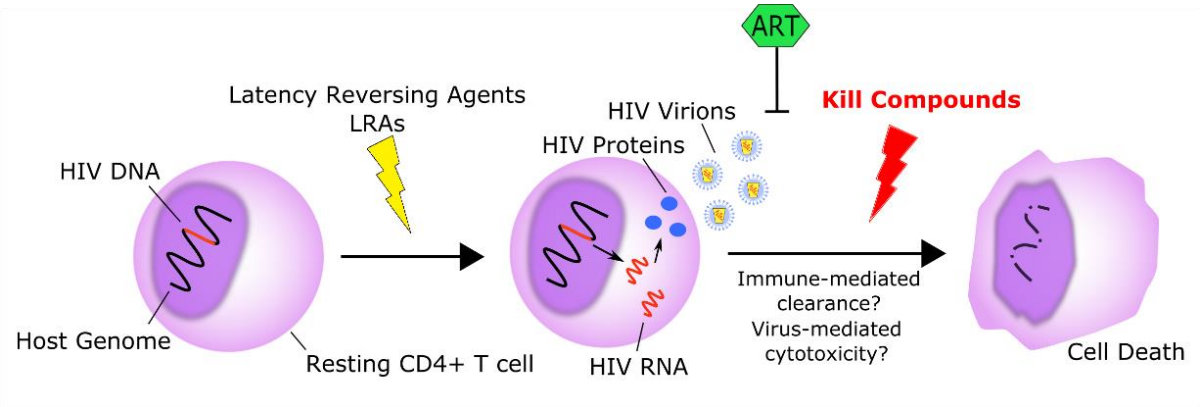

Figure 1.9. Mechanism of LTR-mediated 'shock and kill' therapy. Adapted from reference 147.

1.3.5. Gene therapy

The success of cell replacement therapy for the Berlin Patient, who received a hematopoietic stem cell transplant from a donor with a non-functional CCR5 receptor and is now considered cured of HIV, inspired research targeting the mechanism of virus entry into cells.[148] Engineered ZFN was the first gene-editing technology in HIV therapy used to modulate CCR5 expression

in cell lines and primary cells, and later to excise CCR5 gene in CD4 T cells and CD34+ HSCs.[149,150,151] Although many studies are underway to utilize ZFN to tackle HIV latency, the success of such treatment greatly relies on the efficiency of receptor expression knockdown to make cells unsusceptible to CCR5-tropic HIV. It should be acknowledged that even if successful, it does not provide protection against virus strains using the CXCR4 receptor. On the other hand, the downregulation of CXCR4 would not target the HIV reservoir in cell populations not expressing CXCR4. It demonstrates that targeting host genes in HIV therapy has limited use and is often associated with side-effects on the already weakened immune system of the affected people. Alternatively, the integrated proviral DNA has become a target in gene therapy to either excise or permanently silence its transcription. The use of Cre recombinases (Tre) has been demonstrated to recognize and excise HIV long terminal repeat (LTR) in infected cell lines,[152] and was later shown to prevent HIV replication in a humanized mice model.[153] CRISPR/Cas9 has been applied to excise HIV fragment in mice and rat models of HIV infection.[154] These studies demonstrated the feasibility of the approach to disrupt HIV DNA, and its success partly relies on a highly effective delivery of genome editing technologies to all infected cells.

1.3.6. Transcriptional gene silencing

The use of the RNAi pathway to target viral RNA or mRNA has also been investigated in HIV therapy. Blocking the translation of proteins involved in viral replication could provide a valuable tool to stop the assembly of new virions. However, the virus can still scape at the level of reverse transcription or transcription.[155,156] Therefore, another approach focused on direct control of integrated viral DNA, became an interesting strategy to inhibit viral transcription in the nucleus through transcriptional gene silencing (TGS).

TGS is a mechanism of gene regulation that has been studied in plant models and yeast. In mammals, siRNA fragments are loaded by Argonaute-1 (Ago-1) to form an RNA-induced initiator of transcriptional gene silencing complex (RITS).[157] RITS-loaded siRNA is directed to the nucleus presumably driven by sequence complementarity to the genomic DNA, where it induces heterochromatin formation *via* recruitment of histone methyltransferases and chromodomain binding protein, thus inhibiting gene transcription.[158] The TGS pathway in humans is not yet fully understood, and the main controversy lies in the mechanism enabling sequence recognition and nuclear translocation of siRNA. It has been proposed that TGS is

directed mainly by Ago-1, as opposed to Ago-2 (with catalytic activity) in PTGS. TGS has potential in HIV therapy, as it could provide a mechanism for a prolonged, stable and inheritable control over integrated viral genome by delivering HIV-targeting siRNA/shRNA. An siRNA sequence called PromA that is complementary to a fragment of the HIV promoter has been identified by Suzuki et al.[159] and it has been proposed that the observed HIV silencing effect by PromA occurs *via* TGS. Such discovery gives grounds for further studies into controlling the HIV reservoir by permanently locking virus transcription in a "lock and block" approach. Importantly, it provides an opportunity to target latent infection as contrary to PTGS that targets viral mRNA to block translation, TGS can be utilized in resting cells to control gene transcription to minimize the opportunity for mutant virus to escape.

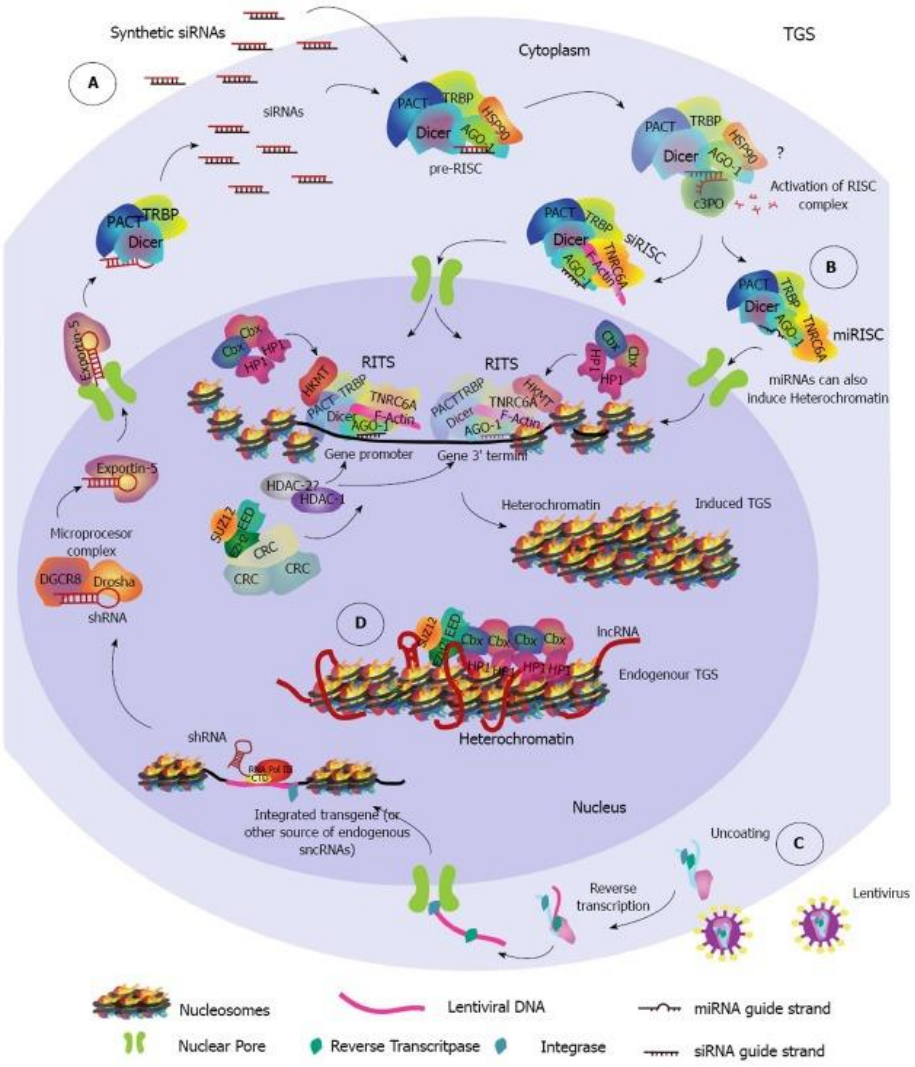

Figure 1.10 Transcriptional gene silencing-proposed mechanism. Adapted from reference 158.

1.3.7. Nanoparticles in gene therapy for HIV

Delivery of gene-based therapeutics remains a challenge, particularly in developing an effective treatment strategy. Among the HIV-related RNA therapeutics in clinical trials, the dominant delivery method is based on *ex vivo* culture of CD34+ HSC or CD4+ T cells and transduction with a viral vector before infusing back into the bloodstream.[160] The weakness of using viral-based carriers lies in their limited ability to enter resting T cells. In addition, the efficiency of transduction levels can be affected by ART treatment, as many of the lentivirus-based vectors comprise partly of the HIV genome.[161] The development of alternative delivery methods that overcome the above obstacles is needed.

Nanoparticle-mediated RNAi response is dependent on many factors, including circulation time, targeting, cell internalization and release of the cargo in the cytosol. Cytotoxicity and potential off-target effects should be evaluated. To exploit the RNAi pathway, the delivered molecule should reach the target cell in an unchanged, functional form. Therefore, permanent chemical modifications such as conjugation of the siRNA to a carrier are not preferable. As siRNA is a natural electrolyte (negatively charged above pH 3) electrostatic interaction can be used to load the molecule within positively charged nanoparticles. This type of interaction allows the siRNA to be transported into the cell in a form of a complex with the carrier which protects the cargo from degradation until the moment of release into the cytosol, where it be translocated to the molecular machinery of RNAi.

Among the nanoparticle-based siRNA delivery systems, carbosilane dendrimers that bind negatively charged RNA *via* electrostatic interactions were used for the transfection of HIV-infected PBMCs for GAPDH downregulation.[162] Dendrimers are branched polymers and after modification with positively charged functional groups, the dendrimer was used as an RNA binding agent. The system was characterized in terms of RNA binding and protection and results of *in vitro* experiments using immune PBMC cells infected with HIV demonstrated the inhibition of virus replication. Second generation dendrimers were used to target viral Nef to primary CD4 T cells to inhibit HIV replication.[163] Viral and cellular transcripts were downregulated using siRNA delivered *via* PAMAM dendrimers *in vitro* in human T cells and PBMCs, and *in vivo* to viremic humanized mice, where treatment significantly reduce viral load.[164]

Liposome and lipoplex delivery systems are also based on electrostatic interactions between negatively charged siRNA and positively charged lipids. Although lipid formulations have

been extensively studied as carriers for siRNA, there are a limited number of reports for their application in anti-HIV therapy. A lipid-based system called Neutraplex (Nx) was demonstrated as a small lipid vesicle with tunable surface properties.[165] Integrin-targeting and stabilized liposomes were used to deliver anti-CCR5 siRNA in mice to provide leukocytes protection again HIV reactivation and prevented CD4 T cell loss.[166]

Cell-penetrating peptides (CPPs) have also been investigated as potential siRNA carriers in HIV therapy. Their high positive charge enables siRNA binding and transport across cell membranes. A system based on nona-d-arginine peptide fused with the CD7-specific single-chain antibody has been described.[167] The conjugation of the antibody was aimed at increasing association with human T- cells, and the siRNA was targeted to downregulate CCR5.

An example of a polymer-based delivery system, composed of PEI and polyethylene glycol (PEG), was also reported.[168] PEI served as a binding site for siRNA and contributed to the release mechanism in the endosomes, while polyethylene glycol (PEG) increased the stability of the polyplex. In this work, the authors presented a delivery strategy into "hard-to-transfect" T-cells. The system provided inhibition of viral replication, however, it required re-application every three days in HIV-infected T-cells.

These are several examples of anti-HIV siRNA delivery approaches; however, it should be noted that there are not many published reports on the delivery of anti-HIV siRNA using nanoparticles. In addition, all of these studies involved the PTGS pathway of siRNA-induced gene knockdown. Nanoparticle-mediated delivery of siRNA targeting a TGS pathway or epigenetic gene silencing remains to be demonstrated.

A

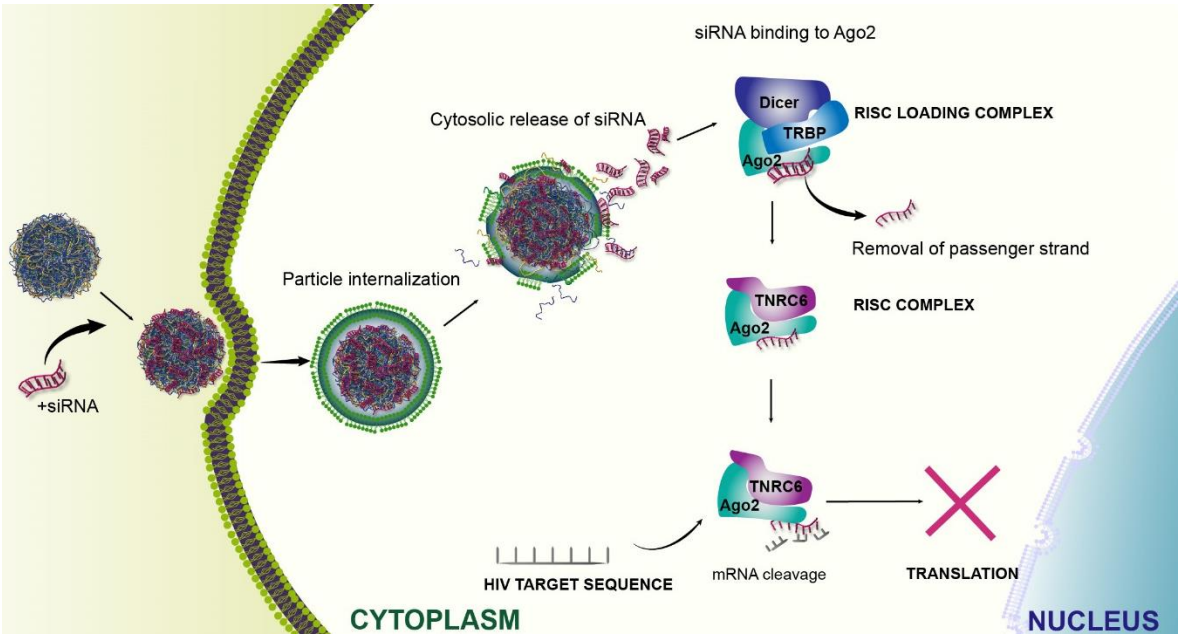

B

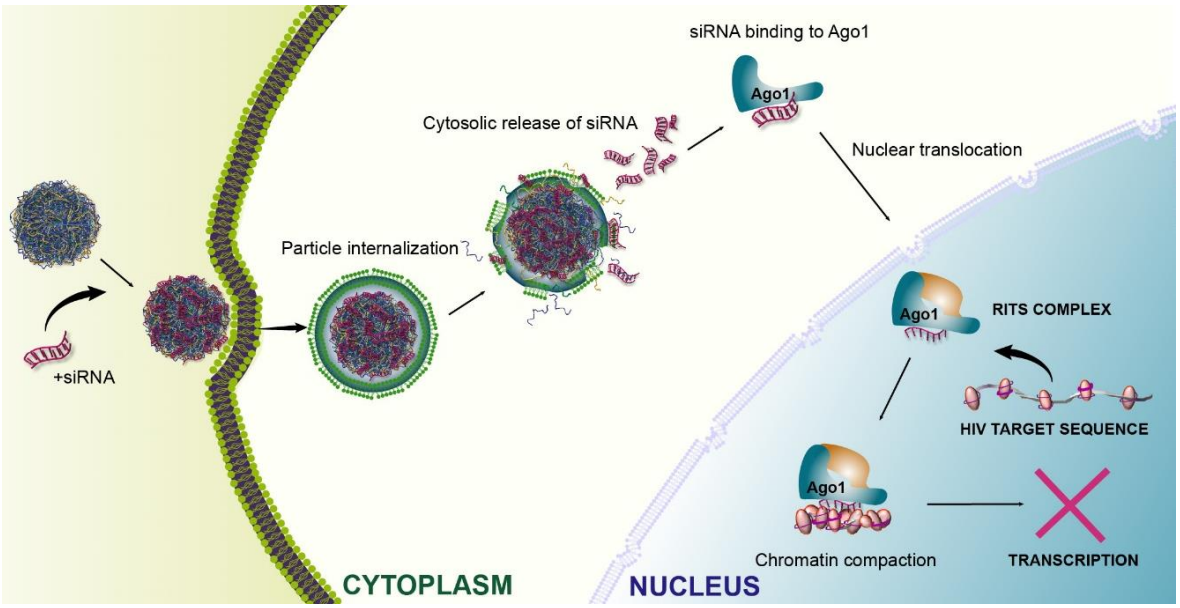

Figure 1.11 Particle-mediated HIV gene silencing via PTGS (A) and TGS (B).

1.4. Friedreich's Ataxia

1.4.1. Human nervous system

The human nervous system comprises of nerves and neurons able to transmit signals throughout the body. The central nervous system (CNS) includes the spinal cord and brain, while the peripheral nervous system (PNS) includes ganglion and nerves.[169] Cells of the nervous system can be divided into actively communicating neurons and supportive glial cells, forming a complex system with different neuronal subtypes.[170] The structure of neurons and presences of neuronal processes (neurites) play an important part in the signal transduction process. While axons connect neurons with their targets, dendrites enable neurons to receive signals from other neurons.[169] Among components of the CNS, brain cells are mainly involved in the perception and processing of somatic and autonomic stimuli, including voluntary motor function by sending the signal to the muscle or regulation and maintenance of body functions. It allows us to receive and interpret information from the outside. The spinal cord is a communication tract that allows the brain to receive information about stimuli. The importance of the CNS manifests in the evolutionary adjustment to contain its components within hard tissues of the skull and spinal cord in vertebrae. In a simplified classification, PNS act as a link between CNS and the rest of the body. In the PNS fibers consisting of axon clusters are called nerves and are primarily responsible for transmitting an electric signal to communicate with other tissues. [171] The signal from the brain can be sent to different body parts *via* efferent nerves. Reversely, the signal can be passed from tissues and organs back to the brain *via* afferent nerves. PNS can be divided into somatic (implicated in the control of voluntary body movements) and autonomic (regulating the function of internal organs) nervous systems.

Neurodegeneration is a progressive and irreversible process in which neurons lose their function and are no longer able to support the functioning of the nervous system.[172] The most common neurodegenerative diseases are Alzheimer's disease and Parkinson's disease.[173] Although significant advances have been made to understand the cause of neurodegenerative disorders, there is currently no effective cure or treatment that would significantly slow disease progression. Some of the neurodegenerative disorders can be caused by an underlying genetic mutation manifesting in progressive damage of the nervous system.[174]

1.4.2. Friedreich's ataxia

Friedreich's ataxia (FRDA) is one of the most common hereditary ataxias.[175] It affects the peripheral and central nervous systems and the heart[176,177] and is characterized by progressive limb ataxia, loss of lower limb reflexes,[178] and progressive visual changes.[179] Non-neurological symptoms involve cardiomyopathy and diabetes.[177,180] It is an autosomal recessive disease involving neurodegeneration of large sensory neurons of dorsal root ganglia (DRG) and spinocerebellar tract.[181] The underlying genetic cause of FRDA is a mutation in the first intron of gene encoding mitochondrial protein frataxin (FXN) involved in cellular iron metabolism and regulation of iron-sulfur clusters containing enzymes.[180,182] The triplet guanine-adenine-adenine repeat expansion (GAA) mutation leads to an insufficient level of FXN in all tissues.

The GAA expansion results in a progressive loss of frataxin mRNA in affected cells. Several factors have been identified to affect FXN transcription, including disrupted transcriptional elongation, chromatin remodeling and DNA methylation.[175] Low levels of FXN lead to abnormalities in mitochondrial respiration, dysfunction of ATP synthesis and accumulation of reactive oxygen species and iron, leading to toxicity and cell death within the nervous system and cardiac tissue.[182]

The onset of FRDA usually occurs in puberty, with a life expectancy between 40 and 50 years.[183] The mechanism of the disease is not yet fully understood and there is no effective cure that would significantly slow down the neurodegeneration. Therefore, currently available therapies are aimed mainly at providing relief in symptoms to improve patient's quality of life and partly at the improvement of mitochondrial function. More recently, with the development of cell and gene replacement technologies, novel therapeutic approaches are emerging to restore frataxin level to stabilize disease progression.

1.4.3. FRDA treatment: pharmacological compounds

One of the proposed solutions for effective FRDA therapy is to increase the FXN level by pharmacological compounds. Although the mutation causing the disease mainly affects the amount of FXN produced, the protein remains functionally correct. Hence long-term and stable increase in FXN level will potentially provide therapeutic effects of improved mitochondrial function and significant inhibition of disease progression. The use of antioxidant coenzyme Q,[184] iron chelators[185] and antioxidant resveratrol[186] to increase mitochondrial frataxin level

has been proposed. Initial studies demonstrated that treatment with erythropoietin (EPO) increase FXN levels in various tested cells *in vitro* and lymphocytes from FRDA patients.[187] However, further clinical trials found modest or none increase in FXN levels and no changes in haemoglobin, suggesting a poor functional outcome and raised concerns about side-effects.[188,189] Initially promising studies looking at interferon-gamma as a means to increase FXN levels *in vitro* and FRDA mice model further failed to replicate a long-lasting increase in FXN levels in clinical trials.[190] Different therapeutic approach for FRDA is aimed at epigenetic changes, such as histone deacetylations, associated with the presence of GAA expansion. Administration of HDAC inhibitors RG2833, disabling enzymes involved in histones deacetylations, resulted in increased levels of frataxin in heart and neural tissue and improved locomotion in an FRDA mice model.[191,192] Further clinical studies found an increase in FXN mRNA in patient-derived PBMCs and work to identify safer derivatives targeting an FXN gene are in development. There is a considerable effort toward the development of new treatment for FRDA and several agents showed promising results in animal and cellular models, however, the results from clinical trials were inconclusive.

1.4.4. Cell therapies

Gene and cell replacement therapies are proposed as an alternative treatment and have been initiated for several diseases. In FRDA, a pilot study using the granulocyte-colony stimulating factor (G-CSF) to modulate the production of stem cells in the brain to demonstrate improved nerve cell repair in FRDA was initiated,[193] encouraged by a successful outcome in patient-derived fibroblasts expressing FXN upon exposure to mesenchymal stem cells -derived soluble factors.[194] Bone marrow transplantation to FRDA mice model has been shown to improve motor coordination and increase frataxin levels up to 6 months post-transplanation.[195] Cell replacement therapy using hematopoietic stem and progenitor cells reversed neurodegeneration of large sensory neurons in DRG of wild-type mice and improved function of mitochondria within brain and heart tissue.[196] Increased cell survival was observed in patient-derived cultured stem cell-conditioned medium in the presence of adipose from healthy donors associated with the presence of trophic factors in the medium, providing the neuroprotection to FRDA cell models.[197] A similar concept using bone marrow mesenchymal cells from the FRDA mouse model was demonstrated later, where DRG cells cultured in conditioned medium show

increased survival and restored frataxin levels and demonstrated the use of autologous stem cell transplantation in FRDA therapy.[198]

1.4.5. Gene therapy

Gene therapy in FRDA aims at excising and/or replacing the malfunctioning FXN gene to introduce new DNA into the cell and increase levels of frataxin. Therapeutic genetic manipulation can also be aimed at translation to stimulate the production of frataxin from cytosolic FXN mRNA. Lentiviral (LV) and adeno-associated viral (AAV) vectors were used to deliver FXN cDNA to induce frataxin expression as demonstrated in FRDA patient-derived fibroblasts to show expression of FXN in FRDA patient-derived fibroblast.[199]

The intravenous injection of the AAV-based system expressing FXN to FRDA-associated cardiomyopathy mouse model resulted in improved cardiac function.[200] More recently, a rapid and complete reversal of sensory neuropathy was demonstrated following treatment with FXN-expressing AAV to a newly established mouse model characterized by FXN deletion in proprioceptive neurons.[201]

Another class of viral vectors derived from herpes simplex virus type 1 (HSV-1) was used to introduce FXN gene to FRDA fibroblasts, resulting in increased FXN expression and improved cell resistance to oxidative stress.[202] Therapeutic strategy aimed at a sustained expression of FXN was then demonstrated using infectious viral delivery vector in mice following injection to the cerebellum.[203] The delivery of FXN-expressing HSV1 vector to an FRDA mice model restored motor coordination.[204] More recently, a modified HSV-1 vector carrying FXN cDNA was reported to induce sustained expression of FXN mRNA and protein as demonstrated in cultured fetal rat DRG neurons up to 1 month.[205]

An attempt to excise the mutated fragment of FXN gene was demonstrated using zinc-finger nucleases (ZFNs) to remove the GAA expansion in FRDA patient-derived cells.[206] This strategy resulted in increased FXN mRNA and protein expression. Moreover, the therapeutic effect and improved phenotype was sustained in reprogrammed cells differentiated to neurons, hence supporting the potential of cell replacement therapies in FRDA. A similar approach was presented to address FRDA-associated cardiomyopathy, where following GAA excision, significantly higher expression of frataxin was observed in ZFN-edited cells presenting transcriptomic profiles similar to healthy cardiomyocytes.[207] More recently, electroporation

was used to deliver CRISPR system comprising Cas9-expressing plasmid and sgRNAs to excise GAA expansion, however, the functional effect and increase in FXN expression is yet to be demonstrated.[208]

The delivery of exogenous FXN to improve mitochondrial functions was demonstrated in patient-derived cells and *in vivo* FRDA mouse model. Transactivator of transcription (TAT) protein was fused with human FXN protein and provided an improved cell resistance to oxidative stress *in vitro*, and improved cardiac function *in vivo*.[209] Protein fusion construct using TAT and TALE protein was used to transfect patient-derived fibroblast *via* nucleofection and a twofold increase of FXN mRNA was demonstrated, followed by FXN levels increase in a mouse model, demonstrating the potential of promoter-targeting proteins to increase proteins expression and reduce FRDA symptoms.[210]

The attempt to modulate FXN expression was also demonstrated by transfection by electroporation to deliver oligonucleotides and duplex RNAs to stem cell-derived neuronal progenitor cells. The nucleic acid-targeting GAA expansion restored FXN RNA and protein levels.[211] The activation of FXN expression was also evaluated by natural and synthetic oligonucleotides SINEUPs, targeting FXN mRNA to upregulate mRNA translation into a functional protein and improve mitochondrial functions in FRDA-derived cells.[212]

Among nanomaterial-based methods, there is one reported example of lipid nanoparticles containing FXN mRNA, that were administered intravenously in adult mice.[213] Particle uptake was demonstrated in hepatocytes and analysis showed 50% of delivered mFXN being processed to mature protein. Following intrathecal administration, human recombinant FXN was detected in the DRG.

1.5. Scope of the thesis

Gene therapy is of interest to researchers and the general public as it allows potential treatment of inherited and acquired diseases which are not curable with conventional methods. RNA based therapy has emerged as a promising approach for gene silencing, while the delivery of plasmid DNA provides an opportunity to replace defective or missing genes. The main objective of this research project was to develop material-based systems for gene delivery. The PhD thesis will focus on applying polyarginine-containing templated particles in HIV and Friedreich's ataxia, which involve delivery to hard-to-transfect cells including T cells and neurons. While a plethora of particle systems have been investigated for nucleic acid delivery, in this thesis, particles were prepared by the layer-by-layer technique due to the need to use a versatile particle system with easily modifiable properties (including size, shape and composition) that enable tailoring the carrier for a given application and allow loading of different types of nucleic acids (i.e., plasmid DNA, siRNA). This thesis also aims to gain a fundamental understanding of bio-nano interactions in various biological systems, including virus-infected cell lines, primary cells and stem cell-derived 3D neuronal organoids.

Chapter 1 includes the literature review and identifies knowledge gaps used as a motivation to pursue the research described in subsequent chapters. **Chapter 2** describes the methodology and instrumentation used in this thesis.

Chapter 3: Multilayered particles for siRNA delivery to induce epigenetic silencing of HIV.

In this chapter, the use of polyarginine-terminated particles to deliver siRNA in HIV therapy is described. The preparation of core-shell particles and capsules *via* layer-by-layer assembly, film characterization and optimization of siRNA loading is presented. The cytotoxicity, cell internalization and gene silencing properties of siRNA-loaded particles were investigated in non-infected cell lines. The proposed system was applied to deliver anti-HIV siRNA to induce transcriptional gene silencing of the viral genome in infected cell lines and primary cells as assessed by reverse transcriptase assay. The functionalization of the particle surface using an HIV-derived envelope for enhanced cellular uptake is also presented.

Chapter 4: Effect of cell properties on bio-nano interactions: particle-cell interactions in activated and virus-infected cells. In this chapter, the effect of cell activation and viral infection on cell-particles interactions was investigated. The association and internalization of polyarginine-containing LbL core-shell particles, polyethylene glycol mesoporous/hydrogel particles and amine-functionalised bovine glycogen were tested in isolated human immune cells, virus-infected cell lines and an HIV latency model. The cell-particles interactions were assessed using flow cytometry, imaging flow cytometry and confocal microscopy.

Chapter 5: Particle-mediated delivery of frataxin plasmid DNA to a human sensory neuronal model of Friedreich's Ataxia. In this chapter, engineered polyarginine-terminated particles were used to deliver plasmid DNA in Friedreich's ataxia (FRDA) therapy. Particle preparation, characterization and optimization of plasmid DNA loading is presented. The uptake and cell association of particles with various sizes were investigated *via* confocal microscopy and flow cytometry. Particles were used to deliver frataxin-encoding plasmid patient-derived FRDA iPSCs and the functional effect was demonstrated by qPCR analysis.

Chapter 6: Distribution of particles in stem cell-derived 3D neuronal cell models: effect of particle size, charge and density. In this chapter, the effect of physicochemical properties of nanoparticles on association and distribution in iPSC-derived neurospheres was investigated. Preparation of layer-by-layer particles with different sizes, densities and composition is described. The particles-cell interactions were studied by flow cytometry and confocal microscopy to assess particles penetration into neurospheres. A soft, self-assembled system based on bovine glycogen was also studied and used to deliver EGFP-expressing plasmid DNA to neurospheres.

The thesis ends with conclusions and perspective presented in **Chapter 7.**

1.6. References

1. M. Mustafa, A. F. Salih, E. M. IIIzam, B. Almohtafar, S. Hamed, M. K. Nang and A. M. Sharifa, *IOSR-JDMS*, 2017, **16**, 89-95.
2. F. J. Accurso, *Am. J. Respir. Crit. Care Med.*, 2006, **173**, 944-947.
3. G. P. Bates, *Nat. Rev.*, 2005, **6**, 766-773.
4. T. Donenberg, J. Lunn, D. Curling, T. Turnquest, E. Krill-Jackson, R. Royer, S. A. Narod and J. Hurley, *Breast Cancer Res. Treat*., 2011, **125**, 591-596.
5. D. Wang and G. Gao, *Discov. Med.*, 2014, **18**, 151-161.
6. S. D. Patil, D. G. Rhodes, D. J. Burgess, *AAPS J.*, 2005, **7**, 9.
7. Nat. Med., 2019, **25**, 1321.
8. D. Carroll, Genetics, 2011, 188, 773-782.
9. *Nat. Methods*, 2012, **9**, 1.
10. A. Hendel, R. O. Bak, J. T. Clark, A. B. Kennedy, D. E. Ryan, S. Roy, I. Steinfeld, B. D. Lunstad, R. J. Kaiser, A. B. Wilkens, R. Bacchetta, A. Tsalenko, D. Dellinger, L. Bruhn and M. H. Porteus, *Nat. Biotechnol.*, 2015, **33**, 985-989.
11. F. Sousa, L. Passarinha and J. A. Queiroz, *Biotechnol. Genet. Eng.*, 2009, **26**, 83-116.
12. H. Bai, G. M. S. Lester, L. C. Petishnok and D. A. Dean, *Biosci. Rep.*, 2017, **37**, BSR20160616.
13. H. Lodish, A. Berk, S. L. Zipursky, P. Matsudaira, D. Baltimore and J. Darnell, in *Molecular Cell Biology*, W. H. Freeman, New York, 4, 2000, Section 11.2, Processing of Eukaryotic mRNA.
14. G. M. Cooper, in *The Cell: A Molecular Approach*, Sunderland (MA): Sinauer Associates, 2, 2000, Translation of mRNA.
15. D. A. Hiller, V. Singh, M. Zhong and S. A. Strobel, *Nature*, 2011, **476**, 236-239.
16. E. S. Groban, A. Narayanan and M. P. Jacobson, *PLoS. Comput. Biol.*, 2006, **2**, e32.
17. M. M. Kincaid and A. A. Cooper, *Mol. Biol. Cell*, 2007, **18**, 455-463.
18. A. Remenyi, H. R. Scholer and M. Wilmanns, Nat. Struct. Mol. Biol., 2004, **11**, 812-815.
19. N. J. McKenna and B. W. O'Malley, *Cell*, 2002, **108**, 465-474.
20. D. Beckett, *PNAS*, 2009, **106**, 22035-22036.
21. A. Fire, S. Xu, M. K. Montgomery, S. A. Kostas, S. E. Driver and C. C. Melo, *Nature*, 1998, **391**, 806-811.

22. S. M. Hommond, E. Bernstein, D. Bech and G. J. Hannon, *Nature*, 2000, **404**, 293-296.
23. N. Abraham, D. F. Stojdl, P. I. Duncan, N. Me´thot, T. Ishii, M. Dube´, B. C. Vanderhyden, H. L. Atkins, D. A. Gray, M. W. McBurney, A. E. Koromilas, E. G. Brown, N. Sonenberg and J. C. Bell, *J. Biol. Chem.*, 1999, **274**, 5953-5962.
24. B. L. Bass, *Cell*, 2000, **101**, 235-238.
25. N. Agrawal, P. V. Dasaradhi, A. Mohmmed, P. Malhotra, R. K. Bhatnagar and S. K. Mukherjee, *Microbiol. Mol. Biol. Rev.*, 2003, **67**, 657-685.
26. A. Fire, D. Albertson, S. White-Harrison and D. G. Moerman, *Development*, 1991, **113**, 503-514.
27. S. M. Elbashir, J. Harboth, W. Lendeckel, A. Yalcin, K. Weber and T. Tuschl, *Nature*, 201, **411**, 494-498.
28. C. Y. Chu and T. M. Rana, *J. Cell Physiol.*, 2007, **213**, 412-419.
29. G. Meister, M. Landthaler, A. Patkaniowska, Y. Dorsett, G. Teng and T. Tuschl, *Mol. Cell*, 2004, **15**, 185-197.
30. J. M. Pare, N. Tahbaz, J. Lopez-Orozco, P. LaPointe, P. Lasko and T. C. Hobman, *Mol. Biol. Cell*, 2009, **20**, 3273-3284.
31. X. Ye, N. Huang, Y. Liu, Z. Paroo, C. Huerta, P. Li, S. Chen, Q. Liu and H. Zhang, *Nat. Struct. Mol. Biol.*, 2011, **18**, 650-657.
32. J. Martinez, A. Patkaniowska, H. Urlaub, R. Luhrmann and T. Tuschl, *Cell*, 2002, **110**, 563-574.
33. S. Chen, X. Ge, Y. Chen, N. Lv, Z. Liu and W. Yuan, *Drug Des. Devel. Ther.*, 2013, **7**, 117-125.
34. C. A. Gersbach, T. Gaj and C. F. Barbas, 3rd, *Acc. Chem. Res.*, 2014, **47**, 2309-2318.
35. F. D. Urnov, E. J. Rebar, M. C. Holmes, H. S. Zhang and P. D. Gregory, *Nat. Rev. Genet.*, 2010, **11**, 636-646.
36. M. R. Lieber, *Annu. Rev. Biochem.*, 2010, **79**, 181-211.
37. X. Meng, M. B. Noyes, L. J. Zhu, N. D. Lawson and S. A. Wolfe, *Nat. Biotechnol.*, 2008, **26**, 695-701.
38. Y. Doyon, J. M. McCammon, J. C. Miller, F. Faraji, C. Ngo, G. E. Katibah, R. Amora, T. D. Hocking, L. Zhang, E. J. Rebar, P. D. Gregory, F. D. Urnov and S. L. Amacher, *Nat. Biotechnol.*, 2008, **26**, 702-708.
39. V. Pattanayak, C. L. Ramirez, J. K. Joung and D. R. Liu, *Nat. Methods*, 2011, **8**, 765-770.

40. N. Sun and H. Zhao, *Biotechnol. Bioeng.*, 2013, **110**, 1811-1821.
41. J. Boch, H. Scholze, S. Schornack, A. Landgraf, S. Hahn, S. Kay, T. Lahaye, A. Nickstadt and U. Bonas, *Science*, 2009, **326**, 1509-1512.
42. T. Sakuma, H. Ochiai, T. Kaneko, T. Mashimo, D. Tokumasu, Y. Sakane, K. Suzuki, T. Miyamoto, N. Sakamoto, S. Matsuura and T. Yamamoto, *Sci. Rep.*, 2013, **3**, 3379.
43. M. Christian, T. Cermak, E. L. Doyle, C. Schmidt, F. Zhang, A. Hummel, A. J. Bogdanove and D. F. Voytas, *Genetics*, 2010, **186**, 757-761.
44. W. Yan, C. Smith and L. Cheng, *Sci. Rep.*, 2013, **3**, 2376.
45. D. Matsumoto, H. Tamamura and W. Nomura, *Biochemistry*, 2020, **59**, 197-204.
46. A. Veres, B. S. Gosis, Q. Ding, R. Collins, A. Ragavendran, H. Brand, S. Erdin, C. A. Cowan, M. E. Talkowski and K. Musunuru, *Cell Stem Cell*, 2014, **15**, 27-30.
47. R. Barrangou, C. Fremaux, H. Deveau, M. Richards, P. Boyaval, S. Moineau, D. A. Romero and P. Horvath, *Science*, 2007, **315**, 1709-1712.
48. L. A. Marraffini and E. J. Sontheimer, *Science*, 2008, **322**, 1834-1845.
49. E. Semenova, M. M. Jore, K. A. Datsenko, A. Semenova, E. R. Westra, B. Wanner, J. van der Oost, S. J. Brouns and K. Severinov, *Proc. Natl. Acad. Sci. USA*, 2011, **108**, 10098-10103.
50. Y. Dang, G. Jia, J. Choi, H. Ma, E. Anaya, C. Ye, P. Shankar and H. Wu, *Genome Biol.*, 2015, **16**, 280.
51. J. M. Janssen, X. Chen, J. Liu and M. Goncalves, *Mol. Ther. Nucleic Acids*, 2019, **16**, 141-154.
52. G. Liu, K. Yin, Q. Zhang, C. Gao and J. L. Qiu, *Genome Biol.*, 2019, **20**, 145.
53. K. Khalili, R. Kaminski, J. Gordon, L. Cosentino and W. Hu, *J. Neurovirol.*, 2015, **21**, 310-321.
54. K. Garber, *Nat. Biotechnol.*, 2017, **35**, 198-202.
55. R. S. Geary, D. Norris, R. Yu and C. F. Bennett, *Adv. Drug Deliv. Rev.*, 2015, **87**, 46-51.
56. F. Liu, L. M. Shollenberger, C. C. Conwell, X. Yuan and L. Huang, *J. Gene. Med.*, 2007, **9**, 613-619.
57. J. Shi, Y. Ma, J. Zhu, Y. Chen, Y. Sun, Y. Yao, Z. Yang and J. Xie, *Molecules*, 2018, 23, 3044.
58. A. R. de Fougerolles, *Hum. Gene Ther.*, 2008, **19**, 125-132.
59. M. Pan, J. Ni, H. He, S. Gao and X. Duan, *BMB Rep.*, 2015, **48**, 147-152.
60. K. V. Morris and J. J. Rossi, *Gene Ther.*, 2006, **13**, 553-558.

61. R. S. Tomar, H. Matta and P. M. Chaudhary, *Oncogene*, 2003, **22**, 5712-5715.
62. G. L. Storvold, E. Gjernes, H. A. Askautrud, A. L. Borresen-Dale, C, M. Perou and E. Frengen, *Mol. Biotechnol.*, 2007, **35**, 275-280.
63. N. Somia and I. M. Verma, *Genetics*, 2000, **1**, 91-99.
64. C. E. Thomas, A. Ehrhardt and M. A. Kay, *Nat. Rev. Genet.*, 2003, **4**, 346-358.
65. M. Ramamoorth and A. Narvekar, *J. Clin. Diagn. Res.*, 2015, **9**, GE01-06.
66. A. J. Convertine, C. Diab, M. Prieve, A. Paschal, A. S. Hoffman, P. H. Johnson and P. S. Stayton, *Biomacromolecules*, 2010, **11**, 2904-2911.
67. Y. Inoue, R. Kurihara, A. Tsuchida, M. Hasegawa, T. Nagashima, T. Mori, T. Niidome, Y. Katayama and O. Okitsu, *J. Control. Release*, 2008, **126**, 59-66.
68. H. Mandal, S. S. Katiyar, R. Swami, V. Kushwah, P. B. Katare, A. Kumar Meka, S. K. Banerjee, A. Popat and S. Jain, *Int. J. Pharm.*, 2018, **542**, 142-152.
69. S. Nimesh and R. Chandra, *Eur. J. Pharm. Biopharm.*, 2009, **73**, 43-49.
70. U. Lungwitz, M. Breunig, T. Blunk and A. Gopferich, *Eur. J. Pharm. Biopharm.*, 2005, **60**, 247-266.
71. B. Dalby, S. Cates, A. Harris, E. C. Ohki, M. L. Tilkins, P. J. Price and V. C. Ciccarone, *Methods*, 2004, **33**, 95-103.
72. Y. Zhou, C. Zhang and W. Liang, *J. Control. Release*, 2014, **193**, 270-281.
73. B. Ballarin-Gonzalez and K. A. Howard, *Adv. Drug Deliv. Rev.*, 2012, **64**, 1717-1729.
74. S. Dincer, M. Turk and E. Piskin, *Gene Ther.*, 2005, **12**, S139-145.
75. P.L. Feigner and G.M. Ringold, *Nature*, 1989, **337**, 387-388.
76. R. Marty, C. N. N'Soukpoe-Kossi, D. Charbonneau, C. M. Weinert, L. Kreplak and H. A. Tajmir-Riahi, *Nucleic Acids Res.*, 2009, **37**, 849-857.
77. F. Sakurai, T. Nishioka, H. Saito, T. Baba, A. Okuda, O. Matsumoto, T. Taga, F. Yamashita,Y. Takakura and M. Hashida, *Gene Ther.*, 2001, **8**, 677-686.
78. H. Lee and R. G. Larson, *J. Phys. Chem. B*, 2008, **112**, 12279-12285.
79. A. Mecke, D. Lee, A. Ramamoorthy, B. G. Orr and Mark M. Banaszak Hall, *Langmuir*, 2005, **21**, 8588-8590.
80. A. Kolate, D. Baradia, S. Patil, I. Vhora, G. Kore and A. Misra, *J. Control. Release*, 2014, **192**, 67-81.
81. S. Essex, G. Navarro, P. Sabhachandani, A. Chordia, M. Trivedi, S. Movassaghian and V. P. Torchilin, *Gene Ther.*, 2015, **22**, 257-266.
82. M. Nourbakhsh, M. R. Jaafari, H. Lage, K. Abnous, F. Mosaffa, A. Badiee and J. Behravan, Iran *J. Basic. Med. Sci.*, 2015, **18**, 385-392.

83. E. Junquera and E. Aicart, *Adv. Colloid Interface Sci.*, 2016, **233**, 161-175.
84. M. E. Davis and M. E. Brewster, *Nat. Rev. Drug Discov.*, 2004, **3**, 1023-1035.
85. H. Gonzalez, S. J. Hwang and M. E. Davis, *Bioconjugate Chem.*, 1999, **10**, 1068-1074.
86. S. H. Pun, N. C. Bellocq, A. Liu, G. Jensen, T. Machemer, E. Quijano, T. Schluep, S. Wen, H. Engler, J. Heidel and M. E. Davis, *Bioconjugate Chem.*, 2004, **15**, 831-840.
87. C. Kim, B. P. Shah, P. Subramaniam and K. B. Lee, *Mol. Pharm.*, 2011, **8**, 1955-1961.
88. M. Chiper, N. Tounsi, R. Kole, A. Kichler and G. Zuber, *J. Control. Release*, 2017, **246**, 60-70.
89. M. Zhao, M. Li, Z. Zhang, T. Gong and X. Sun, *Drug Deliv.*, 2016, **23**, 2596-2607.
90. J. Finlay, C. M. Roberts, G. Lowe, J. Loeza, J. J. Rossi and C. A. Glackin, *Biomed. Res. Int.*, 2015, **2015**, 382745.
91. J. Lee, J. J. Green, K. T. Love, J. Sunshine, R. Langer and D. G. Anderson, *Nano Lett.*, 2009, **9**, 2402-2406.
92. J. Conde, A. Ambrosone, Y. Hernandez, F. Tian, M. McCully, C. C. Berry, P. V. Baptista, C. Tortiglione and J. M. de la Fuente, *Nano Today*, 2015, **10**, 421-450.
93. S. Deshayes, S. Gerbal-Chaloin, M. C. Morris, G. Aldrian-Herrada, P. Charnet, G. Divita and F. Heitz, *Biochim. Biophys. Acta*, 2004, **1667**, 141-147.
94. L. Crombez, M. C. Morris, S. Dufort, G. Aldrian-Herrada, Q. Nguyen, G. Mc Master, J. L. Coll, F. Heitz and G. Divita, *Nucleic Acids Res.*, 2009, **37**, 4559-4569.
95. Q. Chen, R. Qi, X. Chen, X. Yang, S. Wu, H. Xiao and W. Dong, *Mol. Ther.*, 2017, **25**, 92-101.
96. S. T. Crowley, J. A. Poliskey, N. J. Baumhover and K. G. Rice, *Gene Ther.*, 2015, **22**, 993-999.
97. J. Dileo, R. Banerjee, M. Whitmore, J. V. Nayak, L. D. Falo and L. Huang, *Mol. Ther.*, 2003, **7**, 640-648.
98. S. R. Doyle and C. K. Chan, *Genet. Vaccines Ther.*, 2007, **5**, 11.
99. S. M. van Rossenberg, A. C. van Keulen, J. W. Drijfhout, S. Vasto, H. K. Koerten, F. Spies, J. M. van 't Noordende, T. J. van Berkel and E. A. Biessen, *Gene Ther.*, 2004, **11**, 457-464.
100. Z. Zhou, X. Liu, D. Zhu, Y. Wang, Z. Zhang, X. Zhou, N. Qiu, X. Chen and Y. Shen, *Adv. Drug Deliv. Rev.*, 2017, **115**, 115-154.

101. K. Ariga, Y. M. Lvov, K. Kawakami, Q. Ji and J. P. Hill, *Adv. Drug Deliv. Rev.*, 2011, **63**, 762-771.
102. Y. Yan, G. K. Such, A. P. R. Johnston, H. Lomas and F. Caruso, *ACS Nano*, 2011, **5**, 4252–4257.
103. M. Saraswathy and S. Gong, *Mater. Today*, 2014, **17**, 298-306.
104. X. Q. Liu and C. Picart, *Adv. Mater.*, 2016, **28**, 1295-1301.
105. C. M. Jewell and D. M. Lynn, *Adv. Drug Deliv. Rev.*, 2008, **60**, 979-999.
106. A. L. Becker, N. I. Orlotti, M. Folini, F. Cavalieri, A. N. Zelikin, A. P. R. Johnston, N. Zaffaroni and Frank Caruso, *ACS Nano*, 2011, **5**, 1335–1344.
107. F. Cavalieri, G. L. Beretta, J. Cui, J. A. Braunger, Y. Yan, J. J. Richardson, S. Tinelli, M. Folini, N. Zaffaroni and F. Caruso, *Biomacromolecules*, 2015, **16**, 2168-2178.
108. S. Kakade, D. S. Manickam, H. Handa, G. Mao and D. Oupicky, *Int. J. Pharm.*, 2009, **365**, 44-52.
109. Y. H. Roh, J. B. Lee, K. E. Shopsowitz, E. C. Dreaden, S. W. Morton, Z. Poon, J. Hong, I. Yamin, D. K. Bonner and P. T. Hammond, *ACS Nano*, 2014, **8**, 9767–9780.
110. Y. F. Tan, R. C. Mundargi, M. H. Chen, J. Lessig, B. Neu, S. S. Venkatraman and T. T. Wong, *Small*, 2014, **10**, 1790-1798.
111. C. A. Hong, H. Y. Son and Y. S. Nam, *Sci. Rep.*, 2018, **8**, 7738.
112. S. Oliveira, I. van Rooy, O. Kranenburg, G. Storm and R. M. Schiffelers, *Int. J. Pharm.*, 2007, **331**, 211-214.
113. Y. J. Kwon, *Acc. Chem. Res.*, 2012, **45**, 1077-1088.
114. J. Conde, C. E. Arnold, F. Tian and N. Artzi, *Mater. Today*, 2016, **19**, 29-43.
115. E. Zhao, H. Xu, L. Wang, I. Kryczek, K. Wu, Y. Hu, G. Wang and W. Zou, *Cell. Mol. Immunol.*, 2012, **9**, 11-19.
116. D.A. Hume, *Curr. Opin. Immunol.*, 2006, **18**, 49-53.
117. S. de Oliveira, E. E. Rosowski and A. Huttenlocher, *Nat. Rev. Immunol.*, 2016, **16**, 378-391.
118. P. Italiani and D. Boraschi, *Front. Immunol.*, 2014, **5**, 514.
119. K. Inaba and M. Inaba, *Int. J. Hematol.*, 2005, **81**, 181-187.
120. W. Hoffman, F. G. Lakkis and G. Chalasani, *Clin. J. Am. Soc. Nephrol.*, 2016, **11**, 137-154.
121. D. Ostroumov, N. Fekete-Drimusz, M. Saborowski, F. Kuhnel and N. Woller, Cell. Mol. Life Sci., 2018, **75**, 689-713.

122. D. Moskophidis and D, Kioussis, *J. Exp. Med.*, 1998, **188**, 223-232.
123. CD Creative Diagnostics, https://www.creative-diagnostics.com/innate-and-adaptive-immunity.htm (accessed February 2020).
124. T. W. Chun, J. S. Justement, D. Murray, C. W. Hallahan, J. Maenza, A. C. Collier, P. M. Sheth, R. Kaul, M. Ostrowski, S. Moir, C. Kovacs and A. S. Fauci, *AIDS*, 2010, **24**, 2803-2808.
125. S. Rerks-Ngarm, P. Pitisuttithum, S. Nitayaphan, J. Kaewkungwal, J. Chiu, R. Paris, N. Premsri, C. Namwat, M. de Souza, E. Adams, M. Benenson, S. Gurunathan, J. Tartaglia, J. G. McNeil, D. P. Francis, D. Stablein, D. L. Birx, S. Chunsuttiwat, C. Khamboonruang, P. Thongcharoen, M. L. Robb, N. L. Michael, P Kunasol and J. H. Kim, *N. Engl. J. Med.*, 2009, **361**, 2209-2220.
126. T. Dragic, V. Litwint, G. P. Allawayt, S. R. Martin, Y. Huang, K. A. Nagashimat, C. Cayanan, P. J. Maddont, R. A. Koup, J. P. Moore and W. A. Paxton, *Nature*, 1996, **382**, 667-673.
127. Wikimedia Commons, https://commons.wikimedia.org/wiki/File:HIV_virion.png (accessed February 2020).
128. National Informal Stem Education Network, https://www.nisenet.org/catalog/scientific-image-hiv-infected-cells (accessed February 2020).
129. W. S. Hu and S. H. Hughes, *Cold Spring Harb. Perspect. Med.*, 2012, **2**, a006882.
130. A. A. Okoye and L. J. Picker, *Immunol. Rev.*, 2013, **254**, 54-64.
131. M. G. Atta, S. Se Seigneux and G. M. Lucas, Clin. J. Am. Soc. Nephrol., 2019, **14**, 435-444.
132. L. J. Henderson, L. B. Reoma, J. A. Kovacs and A. Nath, *J. Virol.*, 2020, **94**, e00375-19.
133. T. W. Chun and A. S. Fauci, *Proc. Natl. Acad. Sci. USA*, 1999, **96**, 10958–10961.
134. D. D. Richman, *Nature*, 2017, **543**, 499-500.
135. D. C. Cary, K. Fujinaga and B. M. Peterlin, *J. Clin. Invest.*, 2016, **126**, 448-454.
136. S. Saleh, H. K. Lu, V. Evans, D. Harisson, J. Zhou, A. Jaworowski, G. Sallmann, K. Y. Cheong, T. M. Mota, S. Tennakoon, T. A. Angelovich, J. Anderson, A. Harman, A. Cunningham, L. Gray, M. Churchill, J. Mak, H. Drummer, D. N. Vatakis, S. R. Lewin and P. U. Cameron, *Retrovirology*, 2016, **13**, 49.
137. A. W. Turnera and D. M. Margolis, *YJBM*, 2017, **90**, 229-243.

138. C. Li, H. B. Wang, W. D. Kuang, X. X. Ren, S. T. Song, H. Z. Zhu, Q. Li, L. R. Xu, H. J. Guo, L. Wu and J. H. Wang, *J. Virol.*, 2017, **91**, e01830-16.
139. J. Ananworanich, K. Dube and N. Chomont, *Curr. Opin. HIV AIDS*, 2015, **10**, 18-28.
140. I. Sadowski and F. B. Hashemi, *Cell. Mol. Life Sci.*, 2019, **76**, 3583-3600.
141. N. M. Archin, A. L. Liberty, A. D. Kashuba, S. K. Choudhary, J. D. Kuruc, A. M. Crooks, D. C. Parker, E. M. Anderson, M. F. Kearney, M. C. Strain, D. D. Richman, M. G. Hudgens, R. J. Bosch, J. M. Coffin, J. J. Eron, D. J. Hazuda and D. M. Margolis, *Nature*, 2012, **487**, 482-485.
142. N. Beliakova-Bethell, J. X. Zhang, A. Singhania, V. Lee, V. H. Terry, D. D. Richman, C. A. Spina and C. H. Woelk, *AIDS*, 2013, **27**, 29-37.
143. Y. C. Ho, L. Shan, N. N. Hosmane, J. Wang, S. B. Laskey, D. I. Rosenbloom, J. Lai, J. N. Blankson, J. D. Siliciano and R. F. Siliciano, *Cell*, 2013, **155**, 540-551.
144. R. B. Jones, R. O'Connor, S. Mueller, M. Foley, G. L. Szeto, D. Karel, M. Lichterfeld, C. Kovacs, M. A. Ostrowski, A. Trocha, D. J. Irvine and B. D. Walker, *PLoS Pathog.*, 2014, **10**, e1004287.
145. E. N. Borducchi, C. Cabral, K. E. Stephenson, J. Liu, P. Abbink, D. Ng'ang'a, J. P. Nkolola, A. L. Brinkman, L. Peter, B. C. Lee, J. Jimenez, D. Jetton, J. Mondesir, S. Mojta, A. Chandrashekar, K. Molloy, G. Alter, J. M. Gerold, A. L. Hill, M. G. Lewis, M. G. Pau, H. Schuitemaker, J. Hesselgesser, R. Geleziunas, J. H. Kim, M. L. Robb, N. L. Michael and D. H. Barouch, *Nature*, 2016, **540**, 284-287.
146. E. N. Borducchi, J. Liu, J. P. Nkolola, A. M. Cadena, W. H. Yu, S. Fischinger, T. Broge, P. Abbink, N. B. Mercado, A. Chandrashekar, D. Jetton, L. Peter, K. McMahan, E. T. Moseley, E. Bekerman, J. Hesselgesser, W. Li, M. G. Lewis, G. Alter, R. Geleziunas and D. H. Barouch, *Nature*, 2018, **563**, 360-364.
147. Y. Kim, J. L. Anderson and S. R. Lewin, *Cell Host Microbe*, 2018, **23**, 14-26.
148. B. P. Burke, M. P. Boyd, H. Impey, L. R. Breton, J. S. Bartlett, G. P. Symonds and G. Hutter, *Viruses*, 2013, **6**, 54-68.
149. R. Badia, E. Riveira-Munoz, B. Clotet, J. A. Este and E. Ballana, *J. Antimicrob. Chemother.*, 2014, **69**, 1755-1759.
150. N. Holt, J. Wang, K. Kim, G. Friedman, X. Wang, V. Taupin, G. M. Crooks, D. B. Kohn, P. D. Gregory, M. C. Holmes and P. M. Cannon, *Nat. Biotechnol.*, 2010, **28**, 839-847.

151. P. Tebas, D. Stein, W. W. Tang, I. Frank, S. Q. Wang, G. Lee, S. K. Spratt, R. T. Surosky, M. A. Giedlin, G. Nichol, M. C. Holmes, P. D. Gregory, D. G. Ando, M. Kalos, R. G. Collman, G. Binder-Scholl, G. Plesa, W. T. Hwang, B. L. Levine and C. H. June, *N. Engl. J. Med.*, 2014, **370**, 901-910.
152. I. Sarkar, I. Hauber, J. Hauber and F.Buchholz, *Science*, 2007, **316**, 1912-1915.
153. I. Hauber, H. Hofmann-Sieber, J. Chemnitz, D. Dubrau, J. Chusainow, R. Stucka, P. Hartjen, A. Schambach, P. Ziegler, K. Hackmann, E. Schrock, U. Schumacher, C. Lindner, A. Grundhoff, C. Baum, M. G. Manz, F. Buchholz and J. Hauber, *PLoS Pathog.*, 2013, **9**, e1003587.
154. R. Kaminski, R. Bella, C. Yin, J. Otte, P. Ferrante, H. E. Gendelman, H. Li, R. Booze, J. Gordon, W. Hu and K. Khalili, *Gene Ther.*, 2016, **23**, 690-695.
155. M. E. Abram, A. L. Ferris, K. Das, O. Quinones, W. Shao, S. Tuske, W. G. Alvord, E. Arnold and S. H. Hughes, *J. Virol.*, 2014, **88**, 7589-7601.
156. J. M. Cuevas, R. Geller, R. Garijo, J. Lopez-Aldeguer and R. Sanjuan, *PLoS Biol.*, 2015, **13**, e1002251.
157. S. I. Grewal and S. C. Elgin, *Nature*, 2007, **447**, 399-406.
158. C. Mendez, C. L. Ahlenstiel and A. D. Kelleher, *World J. Virol.*, 2015, **4**, 219-244.
159. C. Ahlenstiel, C. Mendez, S. T. Lim, K. Marks, S. Turville, D. A. Cooper, A. D. Kelleher and K. Suzuki, *Mol. Ther. Nucleic Acids*, 2015, **4**, e261.
160. V. Klemm, J. Mitchell, C. Cortez-Jugo, F. Cavalieri, G. Symonds, F. Caruso, A. D. Kelleher and C. Ahlenstiel, *Genes*, 2016, **7**, 199.
161. V. N. Kim, K. Mitrophanous, S. M. Kingsman and A. J. Kingsman, *J. Virol.*, 1998, **72**, 811-816.
162. N. Weber, P. Ortega, M. I. Clemente, D. Shcharbin, M. Bryszewska, F. J. de la Mata, R. Gomez and M. A. Munoz-Fernandez, *J. Control. Release*, 2008, **132**, 55-64.
163. A. J. Perise-Barrios, J. L. Jimenez, A. Dominguez-Soto, F. J. de la Mata, A. L. Corbi, R. Gomez and M. A. Munoz-Fernandez, *J. Control. Release*, 2014, **184**, 51-57.
164. J. Zhou, C. P. Neff, X. Liu, J. Zhang, H. Li, D. D. Smith, P. Swiderski, T. Aboellail, Y. Huang, Q. Du, Z. Liang, L. Peng, R. Akkina and J. J. Rossi, *Mol. Ther.*, **2011**, 19, 2228-2238.

165. C. Lavigne, K. Slater, N. Gajanayaka, C. Duguay, E. Arnau Peyrotte, G. Fortier, M. Simard, A. J. Kell, M. L. Barnes and A. R. Thierry, *Expert Opin. Biol. Ther.*, 2013, **13**, 973-985.
166. S. S. Kim, D. Peer, P. Kumar, S. Subramanya, H. Wu, D. Asthana, K. Habiro, Y. G. Yang, N. Manjunath, M. Shimaoka and P. Shankar, *Mol. Ther.*, 2010, **18**, 370-376.
167. P. Kumar, H. S. Ban, S. S. Kim, H. Wu, T. Pearson, D. L. Greiner, A. Laouar, J. Yao, V. Haridas, K. Habiro, Y. G. Yang, J. H. Jeong, K. Y. Lee, Y. H. Kim, S. W. Kim, M. Peipp, G. H. Fey, N. Manjunath, L. D. Shultz, S. K. Lee and P. Shankar, *Cell*, 2008, **134**, 577-586.
168. N. D. Weber, O. M. Merkel, T. Kissel and M. A. Munoz-Fernandez, *J. Control. Release*, 2012, **157**, 55-63.
169. P. E. Ludwig and M. Varacallo, Neuroanatomy, Central Nervous System (CNS), StatPearls, Treasure Island, FL, 2019.
170. C. S. von Bartheld, J. Bahney and S. Herculano-Houzel, *J. Comp. Neurol.*, 2016, **524**, 3865-3895.
171. S. G. Waxman, J. D. Kocsis, and P. K. Stys, The Axon: Structure, Function and Pathophysiology. Oxford University Press, New York, 1995.
172. K. A. Jellinger, *J. Cell. Mol. Med.*, 2010, **14**, 457-487.
173. A. Xie, J. Gao and D. Meng, *Biomed. Res. Int.*, 2014, **2014**, 648740.
174. L. Pihlstrom, S. Wiethoff and H. Houlden, *Handb. Clin. Neurol.*, 2017, **145**, 309-323.
175. S. Jayadev and T. D. Bird, *Genet. Med.*, 2013, **15**, 673-683.
176. A. Durr, M. Cossee, Y. Agid, V. Campuzano, C. Mignard, C. Penet, J. M., A. Brice, M. Koening, *N. Engl. J. Med.*, 1996, **335**, 1169-1175.
177. J. A. Morral, A. N. Davis, J. Qian, B. B. Gelman and A. H. Koeppen, *Acta Neuropathol.*, 2010, **120**, 97-108.
178. M. B. Delatycki, R. Williamson and S. M. Forrest, *Med. Genet.*, 2000, **37**, 1-8
179. R. W. Green, *Arch. Ophthalmol.*, 2007, **125**, 273-274.
180. A. Filla, G. de Michele, F. Cavalcanti, L. Pianese, A. Monticelli, G. Campanella and S. Cocozza, A*m. J. Hum. Genet.*, 1996, **59**, 554-560.
181. A. H. Koeppen, J. A. Morral, A. N. Davis, J. Qian, S. V. Petrocine, M. D. Knutson, W. M. Gibson, M. J. Cusack and D. Li, *Acta Neuropathol.*, 2009, **118**, 763-776.
182. M. Li-Hsuan Huang, E. M. Becker, M. Whitnall, Y. Suryo Rahmanto, P. Ponka and D. R. Richardson, *PNAS*, 2009, **106**, 16381-16386.

183. K. Burk, *Cerebellum Ataxias*, 2017, **4**, 4.
184. M. H. Parkinson, J. B. Schulz and P. Giunti, *J. Neurochem.*, 2013, **126** (Suppl. 1), 125-141.
185. D.R. Richardson, C. Mouralian, P. Ponka and E. Becker, *Biochim. Biophys. Acta.*, 2001, **1536**, 133-140.
186. E. M. Yiu, G. Tai, R. E. Peverill, K. J. Lee, K. D. Croft, T. A. Mori, B. Scheiber-Mojdehkar, B. Sturm, M. Praschberger, A. P. Vogel, G. Rance, S. E. Stephenson, J. P. Sarsero, C. Stockley, C. Y. Lee, A. Churchyard, M. V. Evans-Galea, M. M. Ryan, P. J. Lockhart, L. A. Corben and M. B. Delatycki, *J. Neurol.*, 2015, **262**, 1344-1353.
187. C. Mariotti, W. Nachbauer, M. Panzeri, W. Poewe, F. Taroni and S. Boesch, *J. Neurochem.*, 2013, **126** Suppl 1, 80-87.
188. E. Cubo, M. Gonzalez, I. del Puerto, J. G. de Yebenes, O. F. Arconada, J. M. Gabriel y Galan and G. European Huntington's Disease Initiative Study, *Mov. Disord.*, 2012, **27**, 439-442.
189. F. Sacca, G. Puorro, A. Marsili, A. Antenora, C. Pane, C. Casali, C. Marcotulli, G. Defazio, D. Liuzzi, C. Tatillo, D. M. Cambriglia, G. Schiano di Cola, L. Giuliani, V. Guardasole, A. Salzano, A. Ruvolo, A. De Rosa, A. Cittadini, G. De Michele and A. Filla, *Mov. Disord.*, 2016, **31**, 734-741.
190. L. Seyer, N. Greeley, D. Foerster, C. Strawser, S. Gelbard, Y. Dong, K. Schadt, M. G. Cotticelli, A. Brocht, J. Farmer, R. B. Wilson and D. R. Lynch, *Acta Neurol. Scand.*, 2015, **132**, 7-15.
191. E. Soragni, W. Miao, M. Iudicello, D. Jacoby, S. De Mercanti, M. Clerico, F. Longo, A. Piga, S. Ku, E. Campau, J. Du, P. Penalver, M. Rai, J. C. Madara, K. Nazor, M. O'Connor, A. Maximov, J. F. Loring, M. Pandolfo, L. Durelli, J. M. Gottesfeld and J. R. Rusche, *Ann. Neurol.*, 2014, **76**, 489-508.
192. M. Rai, E. Soragni, C. J. Chou, G. Barnes, S. Jones, J. R. Rusche, J. M. Gottesfeld and M. Pandolfo, *PLoS One*, 2010, **5**, e8825.
193. K. C. Kemp, N. Cerminara, K. Hares, J. Redondo, A. J. Cook, H. R. Haynes, B. R. Burton, M. Pook, R. Apps, N. J. Scolding and A. Wilkins, *Ann. Neurol.*, 2017, **81**, 212-226.
194. K. Kemp, R. Dey, A. Cook, N. Scolding and A. Wilkins, *Cerebellum*, 2017, **16**, 840-851.
195. K. C. Kemp, K. Hares, J. Redondo, A. J. Cook, H. R. Haynes, B. R. Burton, M. A. Pook, C. M. Rice, N. J. Scolding and A. Wilkins, *Ann. Neurol.*, 2018, **83**, 779-793.

196. C. J. Rocca, S. M. Goodman, J. N. Dulin, J. H. Haquang, I. Gertsman, J. Blondelle, J. L. M. Smith, C. J. Heyser and S. Cherqui, *Sci. Transl. Med.*, 2017, **9**, doi:10.1126/scitranslmed.aaj2347.
197. J. Jones, A. Estirado, C. Redondo, C. Bueno and S. Martinez, *Stem Cells Dev.*, 2012, **21**, 2817-2826.
198. J. Jones, A. Estirado, C. Redondo and S. Martinez, *PLoS One*, 2013, **8**, e62807.
199. J. Fleming, A. Spinoulas, M. Zheng, S. C. Cunningham, S. L. Ginn, R. C. McQuilty, P. B. Rowe and I. E. Alexander, *Hum. Gene Ther.*, **16**, 947-956.
200. M. Perdomini, B. Belbellaa, L. Monassier, L. Reutenauer, N. Messaddeq, N. Cartier, R. G. Crystal, P. Aubourg and H. Puccio, *Nat. Med.*, 2014, **20**, 542-547.
201. F. Piguet, C. de Montigny, N. Vaucamps, L. Reutenauer, A. Eisenmann and H. Puccio, *Mol. Ther.*, 2018, **26**, 1940-1952.
202. S. Gomez-Sebastian, A. Gimenez-Cassina, J. Diaz-Nido, F. Lim and R. Wade-Martins, *Mol. Ther.*, 2007, **15**, 248-254.
203. A. Gimenez-Cassina, R. Wade-Martins, S. Gomez-Sebastian, J. C. Corona, F. Lim and J. Diaz-Nido, *Gene Ther.*, 2011, **18**, 1015-1019.
204. F. Lim, G. M. Palomo, C. Mauritz, A. Gimenez-Cassina, B. Illana, F. Wandosell and J. Diaz-Nido, *Mol. Ther.*, 15, 1072-1078.
205. M. Ventosa, Z. Wu and F. Lim, *J. Gene Med.*, 2017, **19**, 376-386.
206. Y. Li, U. Polak, A. D. Bhalla, N. Rozwadowska, J. S. Butler, D. R. Lynch, S. Y. R. Dent and M. Napierala, *Mol. Ther.*, 2015, **23**, 1055-1065.
207. J. Li, N. Rozwadowska, A. Clark, D. Fil, J. S. Napierala and M. Napierala, *Stem Cell Res.*, 2019, **40**, 101529.
208. D. L. Ouellet, K. Cherif, J. Rousseau and J. P. Tremblay, *Gene Ther.*, 2017, **24**, 265-274.
209. P. M. Vyas, W. J. Tomamichel, P. M. Pride, C. M. Babbey, Q. Wang, J. Mercier, E. M. Martin and R. M. Payne, *Hum. Mol. Genet.*, 2012, **21**, 1230-1247.
210. P. Chapdelaine, Z. Coulombe, A. Chikh, C. Gerard and J. P. Tremblay, *Mol. Ther. Nucleic Acids*, 2013, **2**, e119.
211. X. Shen, S. Beasley, J. N. Putman, Y. Li, T. P. Prakash, F. Rigo, M. Napierala and D. R. Corey, *RNA*, 2019, **9**, 1118-1129.
212. C. Bon, R. Luffarelli, R. Russo, S. Fortuni, B. Pierattini, C. Santulli, C. Fimiani, F. Persichetti, D. Cotella, A. Mallamaci, C. Santoro, P. Carninci, S. Espinoza, R. Testi,

S. Zucchelli, I. Condo and S. Gustincich, *Nucleic Acids Res*., 2019, **47**, 10728-10743.

213. J. F. Nabhan, K. M. Wood, V. P. Rao, J. Morin, S. Bhamidipaty, T. P. LaBranche, R. L. Gooch, F. Bozal, C. E. Bulawa and B. C. Guild, *Sci. Rep.*, 2016, **6**, 20019.

Chapter 2

Instrumentation and Techniques

2.1. Dynamic Light Scattering and Zeta Potential Measurements

Particles suspended in liquid media are susceptible to spontaneous movements, called Brownian motion, which is fundamental in dynamic light scattering (DLS) measurements.[1] DLS is a commonly used technique for determination of particle size, and capillary microehelctropheresis is used for determination of surface potential.[2]

In the DLS technique, suspension of particles is illuminated by a source of light of certain intensity.[3] As a result of the particle movement, the light becomes scattered in all directions causing localized changes in the refractive index of the media and formation of speckle pattern consisting of bright and dark areas. Because particles are constantly in motion, this speckle pattern fluctuates over different light intensities in microsecond timescale. Fluctuations occur more rapidly when smaller particles are illuminated since in liquid media small particles move faster than the larger one.[4] The relationship between the rate of particle movement (diffusion coefficient) and its size is defined by the Stokes-Einstein equation:[3-5]

$$D = \frac{k_B T}{6\pi\eta R_h}$$

where D is diffusion coefficient, k_B is Boltzmann constant, T is temperature, η is a viscosity of liquid and R_h is a hydrodynamic radius of the particle.

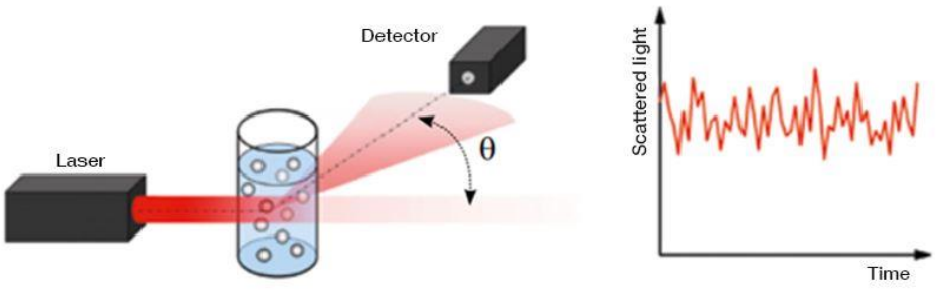

Figure 2.1. Schematic illustration of a dynamic light scattering instrumentation setup. Adapted from reference 6.

Hence Stokes-Einstein equation correlates only the diffusion rate of a particle with its size and not with the fluctuation of light, DLS uses autocorrelation functions where decay rate (Γ) of scattered light is approximated to the particle diffusion coefficient,[3] which is expressed as:

$$\Gamma = \tau^{-1} = q^2 D$$

where τ is a correlation time and q is a scattering vector magnitude, defined as:

$$q = \frac{4\pi n}{\lambda_0} sin\left(\frac{\theta}{2}\right)$$

Where n is a refractive index of the solvent, λ_0 is a wavelength of incident light and θ is a scattering angle of light.

For surface potential measurememnts, particles are subjected to movement due to application of electric field. When the objects are in motion, they scatter and reflect irradiated light, which can be estimated to their velocity. This phenomenon is known as a Doppler effect, and can be used to determine charge on the surface of particle.[4] Surface potential of the particle suspended in the liquid is defined by the presence of ionisable groups and chemical species associated with the particle surface. The ionisation of chemical groups is accompanied by adsorption of counterions that consequently lead to the formation of electrical double-layer, referred to as the Stern layer. The stern layer may be further associated with loosely attached ions forming diffuse layer, which can be easily disturbed upon particle movement. Therefore, an interface between Stern layer and diffuse layer defines the surface potential of the particle, also known as zeta potential (ζ-potential), which can be indicative of the net particle charge.[7]

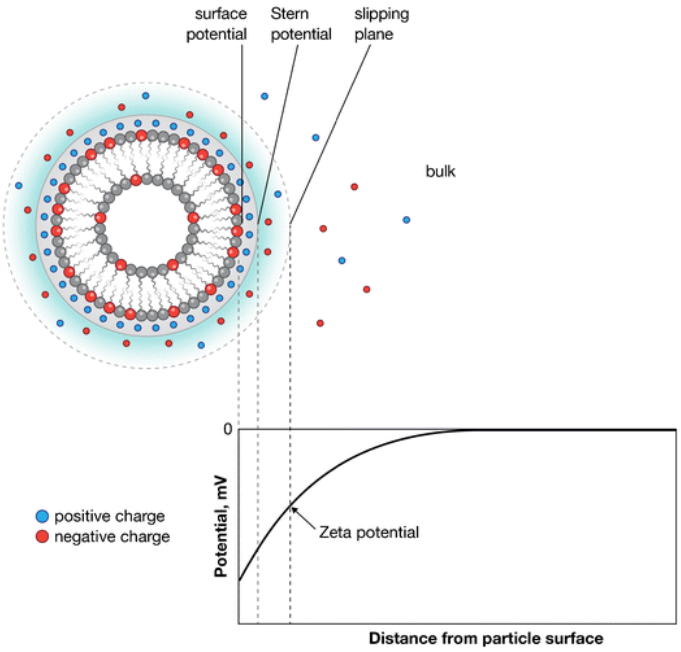

Figure 2.2. Schematic illustration of the formation of electrical double layer and diagram showing a change in potential as a function of distance from charged particle surface. Adapted from reference 8.

Zeta potential measurement takes place in a capillary micro electrophoretic chamber equipped in two electrodes. Upon application of electric current, charged particles can be attracted to the electrodes of opposite charges, setting them in motion. As earlier discussed, particle movement can be detected by fluctuations in light scattering, using the DLS setup. Here, the wavelength of the incident light is altered proportionally to the velocity of the moving particle. The velocity of the particle is then proportional to the electrophoretic mobility and ζ-potential,[9,4] which is correlated by Smoluchowski equation:

$$\mu = \frac{V}{E} = \frac{\varepsilon_R \varepsilon_0 \zeta}{\eta}$$

where μ is electrophoretic mobility, V is particle velocity, E is a strength of electric field, ε_R is relative permittivity of the solution, ε_0 is permittivity of vacuum, ζ is zeta potential and η is viscosity of the medium.

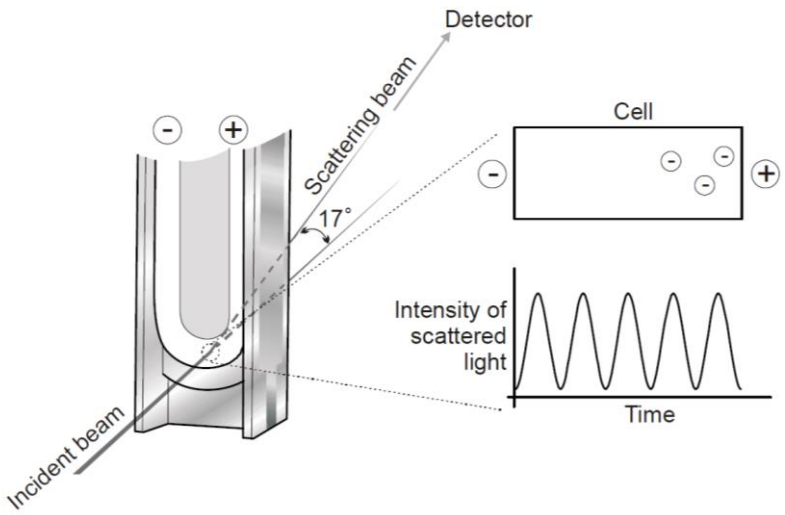

Figure 2.3. Illustration showing simplified zeta potential measurement using light scattering method. Adapted from reference 4.

Standard DLS instrumentation consists of the following compartments: i. source of light (e.g. monochromatic light, laser); ii. measurement cell; iii. detector; iv. attenuator, which regulates an amount of the light reaching the detector; v. correlator, which translates a fluctuated light into a digital signal; and vi. computer used for the analysis of the signal and derivatisation of the data.

In this thesis, the size and charge of particles were determined in chapters 3, 4, 5, 6 using Malvern Zetasizer Nano ZS instrument.

2.2. Gel Electrophoresis

Charged macromolecules, such as nucleic acids and proteins, can be separated on a porous, anticonvective gel for analysis of their properties and functions.[10] This process is called gel electrophoresis and the separation takes place when an electric field is applied, forcing macromolecules to move across the gel according to their charge, size and conformation. All these parameters affect the movement through the gel, resulting in a retardation of macromolecule within the gel pores. For instance, less charged molecules at given buffer conditions will be moving at a slower rate through the gel, compared to molecules with greater charge. Similarly, larger macromolecules will retain within the gel due to unease of penetration of the pores, while smaller fragments will migrate faster having more space to move within the

gel.[11,10] Typical materials used in gel electrophoresis are agarose and polyacrylamide and the choice depends on the resolution power and application. Agarose is a seaweed polysaccharide and forms large-sized pores gels in aqueous media, ideal for large DNA molecules such as plasmid DNA, while polyacrylamide gel is formed by chemical crosslinking of acrylamide and results in small pore size being ideal for separation of proteins and small nucleic acids, including siRNA.

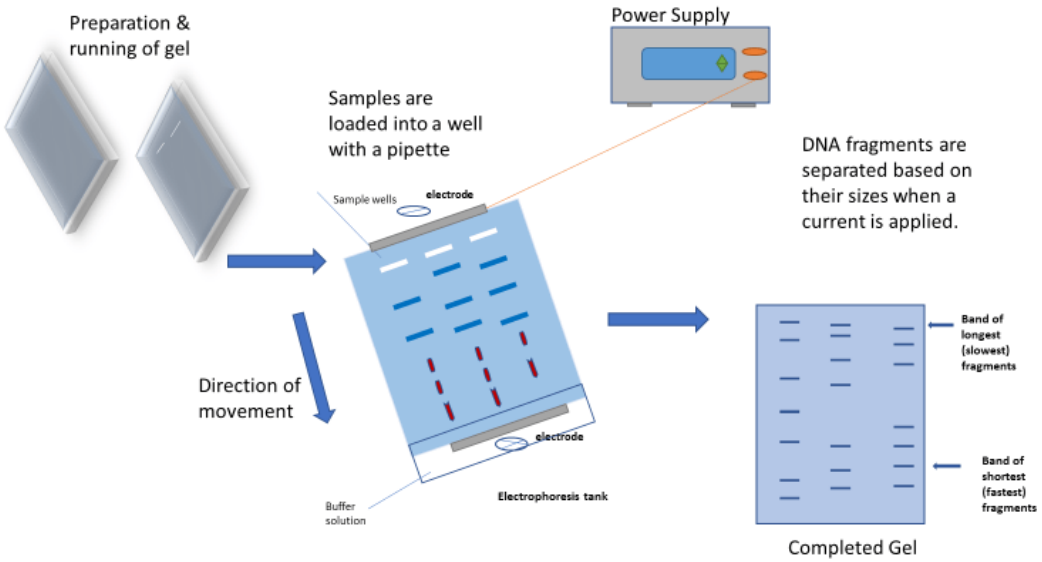

Figure 2.4. Illustration showing principles of gel electrophoresis and instrument setup. Adapted from reference 12.

Nucleic acids, i.e. plasmid DNA (pDNA) and siRNA, are highly negative molecules due to the presence of phosphate groups in a backbone, giving the highly negative charge and uniform charge-to-mass ratio per unit length. Therefore, the movement of pDNA or siRNA in the gel is inversely proportional to their size. While shorter fragments of pDNA may be moving at a faster rate, it can also be due to DNA conformation. DNA can be present in several forms, such as linear, circular or open circle, depending on the origin and genetic manipulations (e.g. unfinished plasmid ligation, linear plasmid of bacteriophage λ). Thus, all these forms of the same size will migrate differently, resulting in a varying pattern on the gel.[10]

The gel electrophoresis setup consists of a gel holder/cassette, an electrophoretic chamber filled with electrolyte buffer that maintains the pH and conducts an electric current, and power supply. After electrophoresis, the resulting DNA/RNA bands are visualized using fluorescent stains, such as ethidium bromide or safer alternatives such as SyBr Safe and SyBr Gold, which intercalate into the minor groove of the nucleic acid strand. The fluorescent signal is then detected using an imaging system composed of the UV irradiation source and high-sensitivity digital camera to image the gel.[13]

In this thesis, polyacrylamide gel electrophoresis was used to assess the loading capabilities of siRNA in chapter 3 and agarose gel electrophoresis was used to assess the loading of pDNA in chapter 5 into poly-L-arginine terminated LbL particles and pDNA complexation by BG-EDA in Chapter 6. In these assays, retardation or the absence of nucleic acids was taken as evidence of successful binding on the particle surface. Gels were stained with SyBr Gold and images of the gel were taken with a BioRad ChemiDoc XRS+.

2.3. Quartz Crystal Microbalance with Dissipation Monitoring

Quartz crystal microbalance with dissipation monitoring (QCM-D) is a powerful technique measuring mass changes occurring on the surface resulting from thin film formation, interactions and reactions. At the heart of QCM-D apparatus is a quartz crystal located between a pair of electrodes. After applying voltage, the quartz crystal starts to oscillate with a resonance frequency dependent on crystal's thickness. Hence, deposition of a thin film layer on the crystal causes a change in its thickness and consequently in its mass, resulting a decrease in the resonance frequency of the oscillating crystal. For thin and rigid films, the change in resonance frequency corresponds to the deposited mass, therefore, QCM-D acts as a super-sensitive balance for nanoscale materials.[14] A value of deposited mass can be obtained using Sauerbrey equation:[15]

$$\Delta f = -\frac{2f_0^2}{A\sqrt{\rho_q \mu_g}}\Delta m$$

where, Δf is the change in frequency measured in hertz (Hz), f_0 is the fundamental resonance frequency of the quartz crystal, A in cm^2 is the piezoelectrically active crystal area, ρ_q is the

density of the quartz crystal equal 2.648 g cm^{-3}, μ_q is the shear modulus of the quartz crystal equal 2.947×10^{11} g cm^{-1} s^{-2}, and Δm is the mass change in grams.

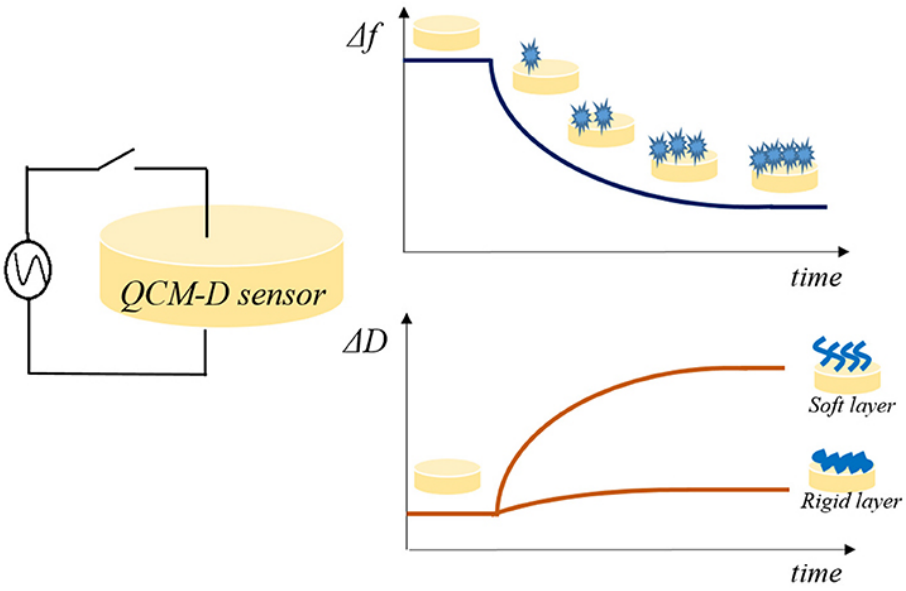

Figure 2.5. Schematic illustration of quartz crystal microbalance with dissipation monitoring. The quartz crystal is located between two electrodes creating an electric field. Deposition of polymer results in change of the resonance frequency and energy dissipation in response to absorption of the mass and rigidity of the coating, respectively. Adapted from reference 16.

In QCM-D, an additional parameter that can be provided during the measurement is energy dissipation. In many cases, the formed film is not rigid and Sauerbrey equation is invalid, which may underestimate an actual film mass. Dissipation (D) is a parameter defining soft and viscoelastic materials and occurs as an energy dissipating from the system when a driving voltage is turned off. Therefore, dissipation provides information about the rigidity of the sample and arrangements of the molecules at the surface under given conditions, which may change with different buffer or solvent system, after drying process and under vacuum.[14] Dissipation is defined by the following equation:[17]

$$D = \frac{E_{lost}}{2\pi E_{store}}$$

where, E_{lost} is energy loss per oscillation period, and E_{store} is total energy stored in the system.

In this thesis, QCM-D was used to determine to follow the layer-by-layer assembly and to estimate the mass of deposited pDNA and siRNA on the LbL thin film surface. The measurements were performed using a Q-sense E4 instrument.

2.4. Laser Scanning Confocal Microscopy

Laser scanning confocal microscopy (LSCM) is a high-resolution fluorescence microscopy technique, that has emerged as an essential tool for analysis of cellular structures and biological specimens.[18] Like other fluorescence microscopy techniques, LSCM uses a phenomenon of fluorescence to visualize the analysed sample. Fluorescence is a type of radiation, in which a fluorescent signal occurs *via* excitation/emission processes resulting from irradiation of the fluorophore at specific wavelength (excitation), which causes a transition of valance electron from ground to excited state due to absorbed amount of energy, followed by re-emission of light with the lower energy than absorbed (emission) upon returning of electron from excited to the ground state. The difference between excitation/emission wavelengths is called Stokes shift and is a consequence of intramolecular energy loss through vibrational relaxation at sublevels of excited state.[19]

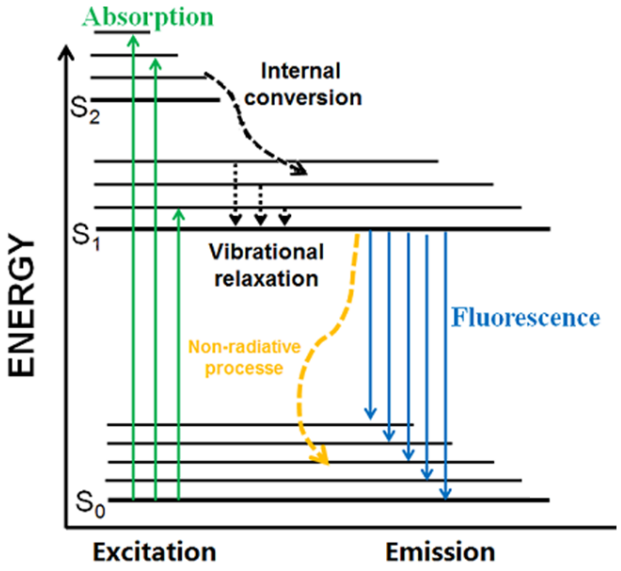

Figure 2.6. Jablonski diagram illustrating the phenomenon of fluorescence. Adapted from reference 20.

To visualise the fluorescent signal, fluorescence microscopes are equipped with: the irradiation source, typically mercury lamp or lasers; set of excitation filters, which allows a narrow band wavelength to reach the sample; dichroic mirrors responsible to direct an excitation light to the specimen; emission filters, which filters out any scattered light or bleed-through signal to reduce the background noise; and photodetector or optical lenses to produce an image. Therefore, to capture an image, excitation light is filtered with a specific bandpass of the filter and position to the sample by dichroic mirrors. Consequently, after absorption of the light, emitted fluorescence returns *via* the same path and hit the photodetector, which conveys the signal into an image.[18,21]

Nevertheless, standard fluorescence microscopy techniques offer low resolution due to the refraction limit of light. When excitation light reaches the sample, it bends at the edges of an object resulting in a blur of the signal. Therefore, the resolution of the microscope is defined as a minimum distance in x-y direction between two objects that can be identified without overlapping and is expressed by Abbe's equation:[22]

$$\Delta xy \approx \frac{0.61\lambda}{NA}$$

where Δxy is a lateral resolution of the microscope, λ is a wavelength of the emitted light, and NA is the numerical aperture of an objective, which is proportional to refractive index on the medium (n) and semiaperture angle of the objective lens (α), according to the equation:

$$NA = n\,sin\alpha$$

Moreover, axial resolution (z-direction) is two to three times larger than the lateral resolution.

LSCM offers several advantages over standard fluorescence microscopy and improves the resolution of the technique, e.g. the presence of pinhole, which limits collected amount of light by excluding out of focus blur from the focal plane of the image. Thus, pinhole allows for collection only the light from the focused plane of the sample, while reducing the amount of the light detected from the spatial plane of the sample. When changing the focus of the

objective, the new focal plane becomes confocal with the pinhole, which allows for the acquisition of image z-stack from different focal planes and final reconstruction of 3D image. In addition, LSCM image is taken basing on the point illumination of the sample with a laser beam, which moves along the sample at the focused plane creating a final image pixel by pixel. That results in improved signal to noise ratio and enhanced around 1.4 times lateral resolution of this technique.[18]

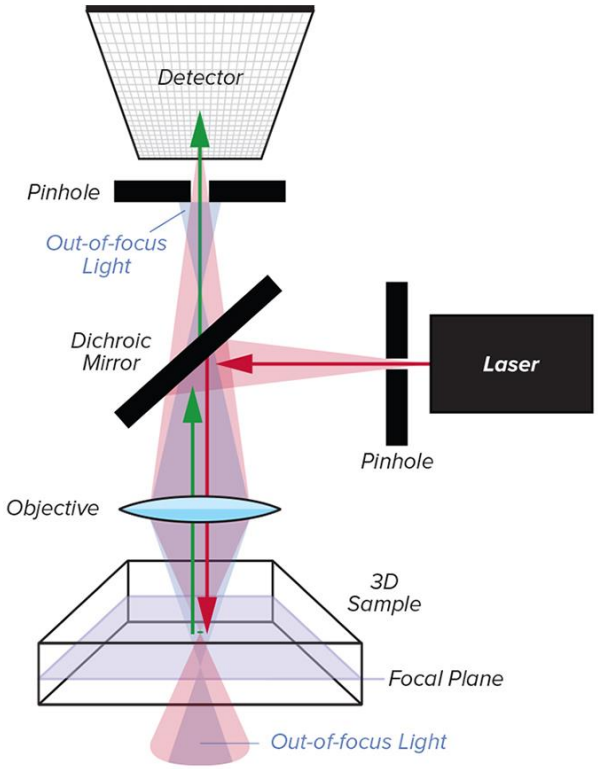

Figure 2.7. Simplified schematic of a laser scanning confocal microscope. Adapted from reference 23.

In this thesis, fluorescence microscopy, especially LSCM, was extensively used in chapters 3, 4, 5, 6. LSCM images were taken with a Nikon A1R.

2.5. Transmission Electron Microscopy

Transmission electron microscopy (TEM) is a type of optical microscope, in which the beam of light is replaced by a narrow beam of electrons. Therefore, TEM is subjected to the same

principles of light diffraction as other optical microscopy techniques,[24] including fluorescence microscopy, however, the electron beam is focused into a thin, narrow beam using condenser lenses which exclude high angle electrons, improving optical resolution several orders of magnitude. Electron beam is produced by an electron gun, which consists of a filament (cathode), typically made of a hairpin-shaped tungsten wire.[25] A high voltage is driven through the filament to achieve a release of electrons. A point at which good thermal emission of electrons is reached is called saturation point. Highly negative electrons are then attracted by an anode located below the electron gun. Anode is electrically at ground, which produces constant positive potential allowing for the collection of electrons with the same velocity. The velocity of electrons is given by an accelerating voltage of 100 keV, 200 keV and 300 keV, which corresponds to their wavelengths of λ 3.70 pm, 2.51 pm and 1.96 pm, respectively. To maintain a constant velocity of the electrons, TEM operates under vacuum environment to prevent air molecules obstructing the electron beam.[24-26]

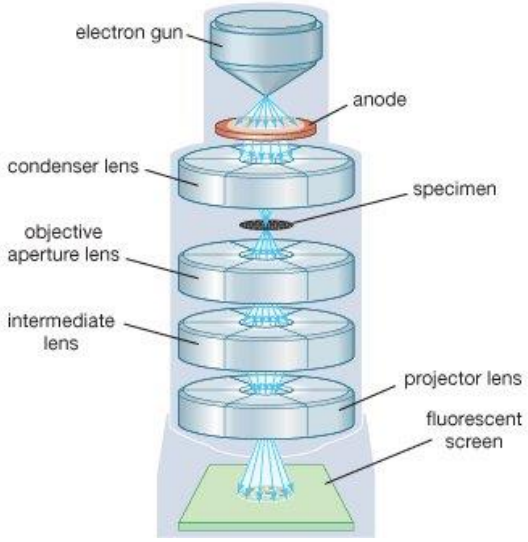

Figure 2.8. Schematic illustration of a transmission electron microscope. Adapted from reference 25.

TEM utilizes a fluorescent phosphor screen to visualize the sample. Once electron beam hits the sample, a transmitted light is focused by objective lenses into an image on a phosphor screen and charged coupled device (CCD) camera. The amount of transmitted light depends on the sample thickness and electron transparency of the specimen. Usually, darker areas of the image correspond to the sample features where a small portion of electrons was transmitted while lighter regions of the image show areas of the sample which transmitted more electrons.[26]

In this thesis, TEM was used to image LbL capsules in chapter 3.

2.6. Scanning Electron Microscopy

Similar to TEM, scanning electron microscopy (SEM) is a type of optical microscopy that uses an electron beam to image the sample. However, SEM image is created based on the information on re-emitted radiation and scattered electrons, rather than sample transmission. In addition, SEM sample requires coating with an electrically conductive material, such as gold or carbon tape, to prevent charge build-up.[27]

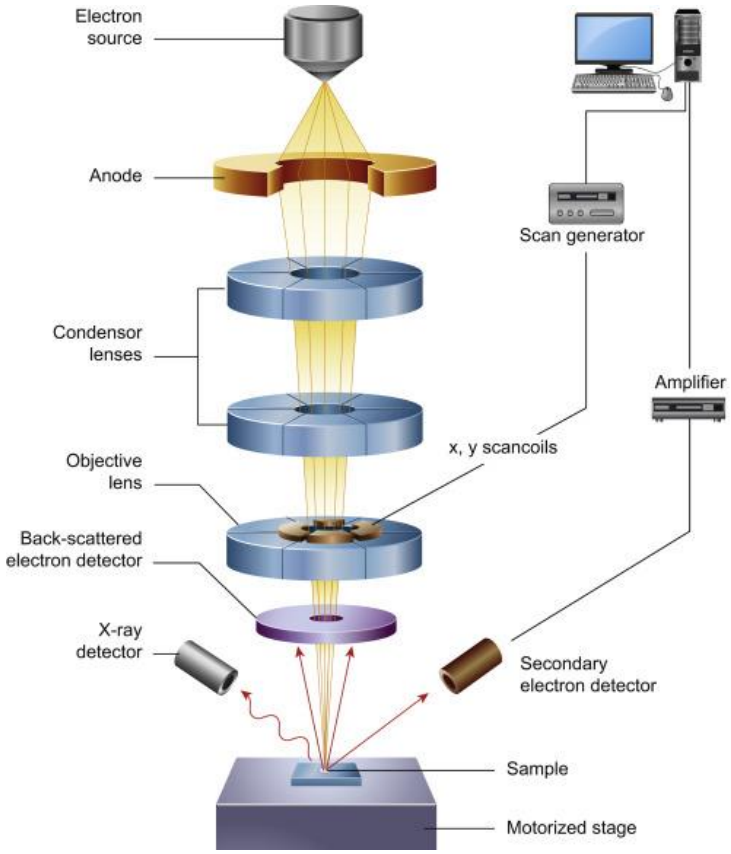

Figure 2.9. Schematic showing core elements of a scanning electron microscope. Adapted from reference 28.

In SEM setup, the electron beam is emitted under vacuum from an electron gun at the top of the column and passes through the condenser lenses to create a focused beam of electrons, which consequently hit the sample. Once the beam strikes the sample with high energy, it initiates the series of events, leading to the production of secondary electrons, backscattered electrons and X-ray radiation, coming from different regions of the sample. Backscattered

electrons are a type of primary electrons reflected due to elastic interactions between the beam and the sample and originate from the deeper sample regions. Secondary electrons are a result of electron emission from atoms at the surface of the sample. Therefore, both types of emitted electrons carry out different information, allowing for 3D analysis of topography and morphology of the sample. X-ray radiation originates from electron-matter interactions and is a kind of sample fingerprint that can provide information about the elemental composition of the sample. All these signals are collected by at least one detector system, i.e. secondary electron detector, to produce a digital image of analysed sample.[27,28]

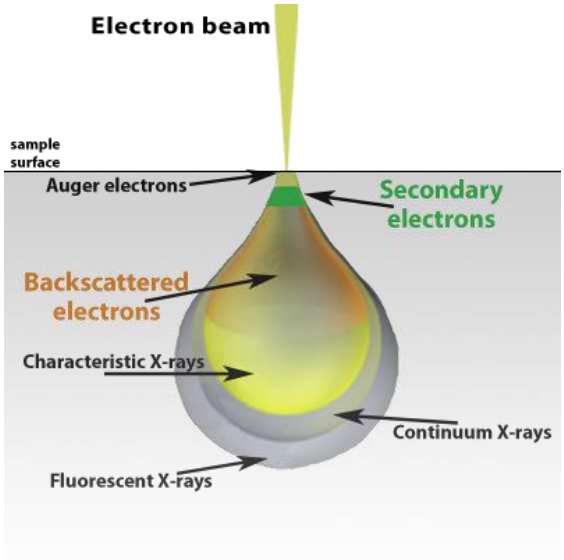

Figure 2.10. Schematic showing types of radiations emitted upon electron beam interactions. Adapted from reference 29.

In this thesis, SEM was used to image LbL particles in chapter 3 and 5.

2.7. Atomic Force Microscopy

Atomic force microscopy (AFM) is a technique that provides a detailed analysis of local properties of materials deposited on the substrate (e.g. mica, gold). Therefore, AFM allows for measurements of film roughness, stiffness, height of deposited polymer layer or size of the particles.[30] AFM measurement is done by a highly sensitive microtip, which runs along with

the sample, constantly interacting with the surface *via* attractive and repulsive forces, including electrostatic, van der Waals and mechanical contact. The microtip is attached to the cantilever, which reflects off a beam of laser into a photodiode array. The change in the topography of the surface results in the elastic deflection of the cantilever and simultaneous change in the position of the laser beam on a photodiode detector. Detector transmits the signal further giving a topological image of analysed sample.[30,31]

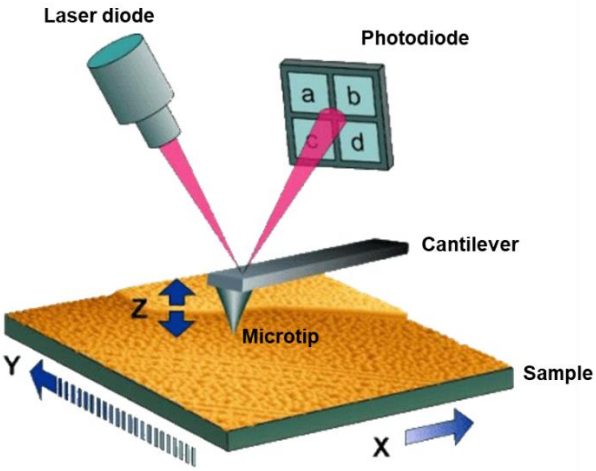

Figure 2.11. Schematic illustrating operation of an atomic force microscope. Adapted from reference 32.

AFM can operate in one of several modes: i) contact mode, in which microtip remains in contact with the surface all the time and change the position due to repulsive topology enforced by repulsive forces; ii) non-contact mode, in which microtip does not touch the surface, oscillating within its resonance frequency; iii) tapping or intermittent contact mode, where microtip operates in proximity of its resonance frequency and coming into interactions with the surface temporarily.

In this thesis, AFM was used in chapter 3 and 5 to demonstrate the change in surface roughness after deposition of pDNA and siRNA on the LbL film deposited on a planar substrate. It was also used to image LbL capsules in chapter 3 and BG-EDA particles in chapter 6.

2.8. Flow Cytometry

Flow cytometry is a high-throughput laser-based technique that provides information on the unique characteristics of cells and particles in a heterogeneous population.[33] It allows for analysis of physical properties, such as granularity, size and immunophenotyping, by scanning each cell or particle one by one in a stream of fluid.[33,34] During measurement, the sample is illuminated with the beam of light. When the beam hits the particle or cell, the light is scattered in all direction, which intensities are measured from two angles. A detector located up to 20° from the direction of the beam of light collects light refracted by the cell and continues along the original path of light, which is called forward scattered light (FSC). Another set of detectors, situated at 90° from the direction of a beam of light, collect the light that is refracted in a direction other than the direction of the beam of light and is called side scattered light (SSC). FSC and SSC are then graphically plotted, proving unique for every cell/particle information on physical features. Typically, FSC provides information on the particle/cell size, while SSC is indicative of shape and granularity. Additional information about cell phenotyping, endogenous and surface proteins, and interactions can be obtained by utilizing specific fluorescent antibodies. The cell or particle is excited with a laser beam of a specific wavelength and the fluorescent signal can be filtered out by the set of filters of a specific bandwidth, detected, amplified and plotted as series of 'events'.

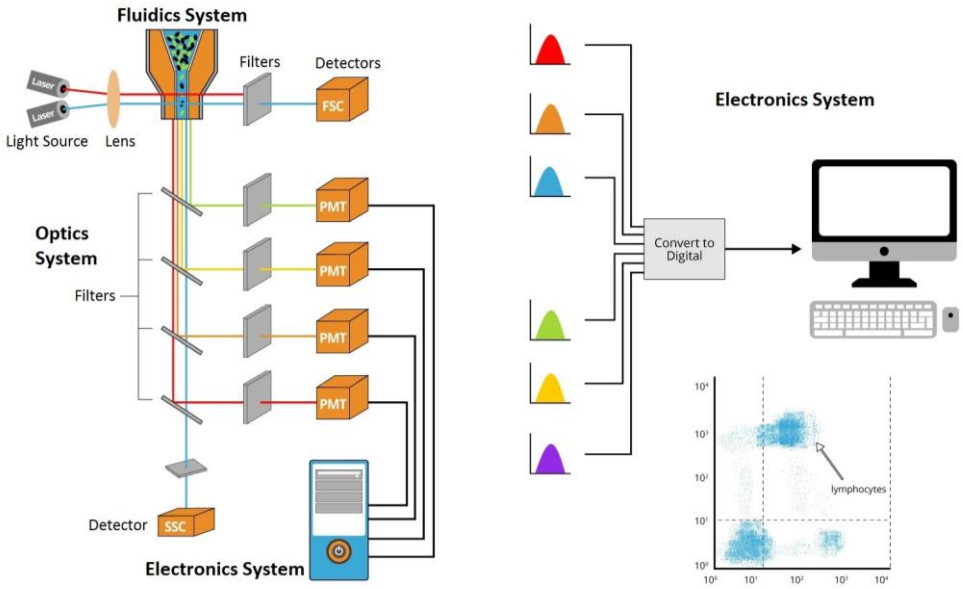

Figure 2.12. Schematic illustration of key components of a flow cytometer. Adapted from reference 35.

During measurement, the sample is aspirated by a microfluidic system, which injects the sample into the central core of the instrument. In the process called hydrodynamic focusing, randomly distributed cells or particles are aligned with the sheath fluid, which moves faster within the microfluidic system. Sheath fluid drags out the particles from the slowly flowing sample in the central core and accelerate its flow, consequently forming single-particle or single-cell flow stream.

In this thesis, flow cytometry was used in chapter 3,4,5 and 6 to analyse the cellular association of fabricated particle systems with cell lines and PBMCs. It was also used to monitor the concentration of core-shell particles and capsules is suspension. Flow cytometry measurements were done using a BD Accuri C6 and an Apogee A-50.

2.9. Imaging Flow Cytometry

Imaging flow cytometry (IFC) is a hybrid technology that combines the features of standard flow cytometry with fluorescence microscopy allowing for high-throughput analysis of a single cell in a fluid stream. This provides high-throughput information based on fluorescence intensities even in case of very faint stainings and cellular morphologies, being advantageous over other high-throughput techniques, including sequencing platforms, microarrays and western blotting or ELISA used for analysis and quantification of various cell biology aspects.[36]

A pioneer and a winner in IFC instrumentation is Amnis Corp with their ImageStream series. ImageStream can produce up to 12 images simultaneously with 60x objective magnification using a combination of transmitted light, scattered light and fluorescence.[38] It is equipped with CCD camera, which operates in time delay integration (TDI) mode. TDI electronically track cells by integrating pixels from every row from top to the bottom of the TDI sensor. This results in a series of images that are synchronized with the velocity of the cell using control apparatus of the TDI line readout rate. Although integration times are longer than those in standard flow cytometry, TDI technology prevents form image streaking, resulting in 12 bits resolution digital image.[37,39] Collected light is split into separate images of the same object using stacks of spectral filters. All collected information allows for extracting high-content information of

cellular processes and morphologies, including intracellular trafficking, co-localization, morphological changes or nuclear translocation.[39]

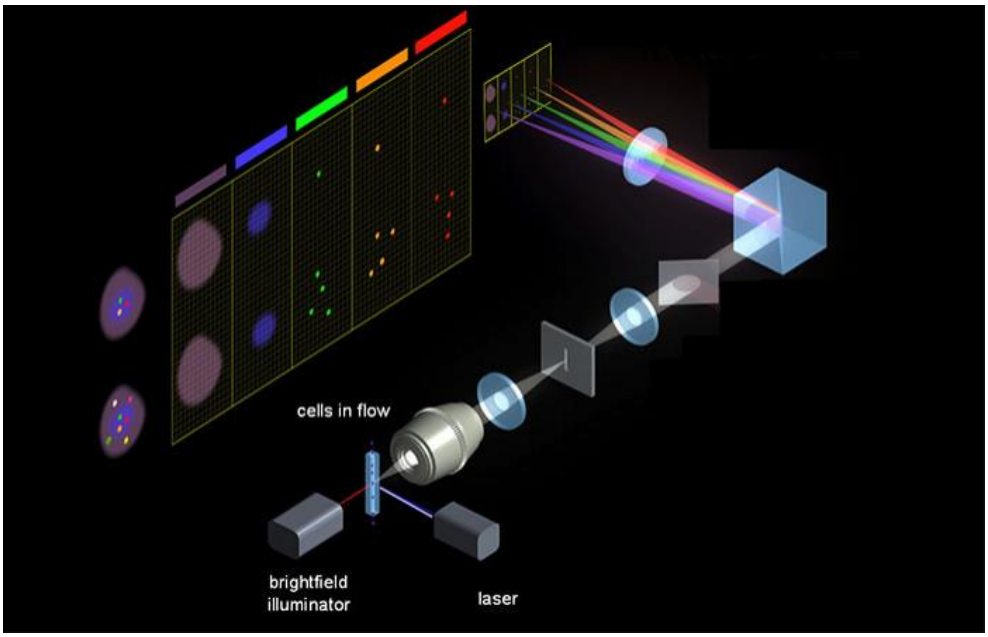

Figure 2.13. Schematic diagram of an Amnis ImageStreatem imaging flow cytometer. Adapted from reference 37.

In this thesis, AMNIS ImageStreamX MarkII imaging flow cytometer was used to study internalization of particles by activated- and non-activated PBMCs in chapter 4.

2.10. References

1. P. Bartlett and W. van Megen, in *Granular Matter*, ed. A. Mehta, Springer, New York, N. Y., 1994, Physics of Hard-Sphere Colloidal Suspensions, 195-257.
2. S. Bhattacharjee, *J. Control. Release*, 2016, **235**, 337.
3. R. Pecora, *J. Nanopart. Res.*, 2000, **2**, 123.
4. Zetasizer Nano User Manual: MANO485 Issue 1.1. Malvern Instruments: 2013
5. B. J. Berne and R. Pecora, *Dynamic Light Scattering: With Applications to Chemistry, Biology, and Physics*, Dover Publications, Mineola, N. Y., 2000.
6. Anton Paar, https://wiki.anton-paar.com/au-en/the-principles-of-dynamic-light-scattering/ (accessed February 2020).
7. R. J. Hunter, R. H. Ottewill and R. L. Rowell, *Zeta Potential in Colloid Science: Principles and Applications*, Academic Press, London, 1981.
8. M. C. Smith, R. M. Crist, J. D. Clogston and S. E. McNeil, *Anal. Biochem.*, 2017, **409**, 5779.
9. M. Kaszuba, J. Corbett, F. M. Watson and A. Jones, *Philos. Trans. A Math. Phys. Eng. Sci.*, 2010, **368**, 4439.
10. I. I. Amarakoon, S. L. Hamilton, S. A. Mitchell, P. F. Tennant and M. E. Roye, in *Pharmacognosy*, ed. S. Badal and R. Delgoda, Academic Press, 2017, Chapter 28 – Biotechnology, 549-563.
11. N. C. Stellwagen and E. Stellwagen, *J. Chromatogr. A*, 2009, **1216**, 1917.
12. Expedon on abcam company, https://www.expedeon.com/resources/applications/introduction-to-dna-and-protein-gel-electrophoresis/ (accessed February 2020)
13. P. Y. Lee, J. Costumbrado, C. Y. Hsu and Y. H. Kim, *J. Vis. Exp.*, 2012, **62**, 3923.
14. Biolin Scientific Holding AB. 2014, Q-Sense, https://www.biolinscientific.com/q-sense/ (accessed February 2020).
15. G. Sauerbrey, *Z. Phys.*, 1959, **155**, 206.
16. C. Tonda-Turo, I. Carmagnola and G. Ciardelli, *Front. Bioeng. Biotechnol.*, 2018, **6**, 158.
17. M. C. Dixon, *J. Biomol. Tech.*, 2008, **9**,151.
18. L. Schermelleh, R. Heintzmann and H. Leonhardt, *J. Cell Biol.*, 2010, **190**, 165.
19. J. R. Lakowicz, *Principles of Fluorescence Spectroscopy*, Springer, 2006.

20. Institut de Biologie Structurale, https://www.ibs.fr/research/research-groups/dynamics-and-kinetics-of-molecular-processes-group-m-weik/pixel/photophysics-of-fluorescent/?lang=fr (accessed February 2020).
21. J. W. Lichtman, and J. A Conchello, *Nat. Methods*, 2005, **2**, 910.
22. S. W. Hell, M. Dyba and S. Jakobs, *Curr. Opin. Neurobiol.*, 2004, **14**, 599.
23. Laser 2000, https://www.laser2000.co.uk/applications/confocal-microscopy (accessed February 2020).
24. D. B. Murphy, *Fundamentals of Light Microscopy and Electronic Imaging*. John Wiley & Sons, New York, NY, 2001
25. Encyclopedia Britannica, https://www.britannica.com/technology/transmission-electron-microscope (accessed February 2020)
26. D. B. Williams, and C. B. Carter, *Transmission Electron Microscopy: A Textbook for Materials Science*, Springer, US, 2009.
27. R. F. Egerton, *Physical Principles of Electron Microscopy: An Introduction to TEM, SEM, and AEM*. Springer, US, 2006.
28. B. J. Inkson, in *Materials Characterization Using Nondestructive Evaluation (NDE) Methods*, Ed. G. Hubschen, I. Alpter, R. Tschuncky and H. G. Herman, Woodhead Publishing, 2016, Scanning electron microscopy (SEM) and transmission electron microscopy (TEM) for materials characterization, 17-43.
29. NanoScience Instruments https://www.nanoscience.com/techniques/scanning-electron-microscopy/ (accessed February 2020).
30. J. Grobelny, F. W. DelRio, N. Pradeep, D. I. Kim, V. A. Hackley, and R. F. Cook, in Characterization of Nanoparticles Intended for Drug Delivery, Humana Press, 2011, Size Measurement of Nanoparticles Using Atomic Force Microscopy, 71-82.
31. G. Binnig, C. F. Quate, and C. Gerber, *Phys. Rev. Lett.*, 1986, **56**, 930.
32. Nanoprobe group, Yale University https://www.eng.yale.edu/nanomechanics/research_methods.html (accessed February 2020).
33. Antibodies online, https://www.antibodies-online.com/resources/17/1247/what-is-flow-cytometry-facs-analysis/ (accessed February 2020).
34. T. A. Fleisher and J. B. Oliveira, In *Clinical Immunology*., Elsevier, 2018, Flow Cytometry, 1239-1251.
35. Boster antibody and ELISA experts, https://www.bosterbio.com/protocol-and-troubleshooting/flow-cytometry-principle (accessed February 2020).

36. N. S. Bartenova, E. Fasler-Kan and I. A. Vorobjev, *J. Histochem. Cytochem.*, 2012, **60**, 723.
37. Luminex, https://www.luminexcorp.com/imaging-flow-cytometry/ (accessed February 2020).
38. G. Holzner, B. Mateescu, D. van Leeuwen, G. Cereghetti, R. Dechant, A. DeMello and S. Stavrakis, *bioRxiv*, 2019, preprint, DOI: https://doi.org/10.1101/695361.
39. BiteSizeBio, https://bitesizebio.com/20123/seeing-is-believing-an-introduction-to-imaging-flow-cytometry/ (accessed February 2020).

Chapter 3

Multilayered particles for siRNA delivery to induce epigenetic silencing of HIV

3.1. Abstract

Small interfering RNA (siRNA) therapeutics have great potential to alter gene expression in a pathway called RNA interference (RNAi), that provides a mechanism of gene silencing by the degradation of messenger RNA in the cytosol through post-transcriptional gene silencing (PTGS). Recent evidence suggests that siRNAs may act also in the nucleus, by inducing heterochromatin formation at a target gene, thus suppressing gene transcription *via* transcriptional gene silencing (TGS). Implementation of therapeutic strategies utilizing RNAi provides promising treatment opportunities for diseases that are not curable by currently available methods. Human immunodeficiency virus (HIV) infection affects millions of people around the world but is mostly manageable by anti-retroviral therapy (ART). However, the ability of HIV to establish the latent infection in long-lived immune cells, that can produce new virions upon ART cessation, is the main obstacle to virus eradication.

In the present chapter, the use of polyarginine-terminated multilayered particles and capsules to deliver siRNA is described. The gene silencing effect of particle-delivered luciferase-targeting siRNA *via* PTGS was first demonstrated in HEK239T, resulting in 50 and 40 % luciferase downregulation upon siRNA delivery *via* core-shell particles and capsules, respectively. The gene silencing *via* TGS was demonstrated in HIV-infected cells. LbL capsules were used to deliver HIV-targeting siRNA, that induced a significant viral suppression 16 post-treatment as demonstrated by a reverse transcriptase assay in infected primary CD4 T cells and macrophages. Particle engineering approach to introduce viral-like functionality by coating LbL particles with an HIV-derived envelope was also demonstrated. Enhanced particle binding and uptake in CD4 CCR5-expressing TZM-bl cells were demonstrated by confocal microscopy. This work highlights the application of RNA therapeutics beyond the conventional PTGS process. It demonstrates particle-mediated siRNA delivery for transcriptional gene silencing in HIV infection cell models, paving the way for future studies on therapeutic approaches for gene therapy aimed at epigenetic control of gene expression.

3.2. Introduction

HIV remains a global pandemic with millions of people affected around the world.[1] HIV infects CD4+ T cells, macrophages, dendritic cells and monocytes with the major reservoir of HIV infection residing in lymphoid tissue.[2] Nowadays infection can be controlled by antiretroviral therapy (ART), sustaining plasma viral load to an almost undetectable level.[3] However, it is associated with a burden of life-long treatment and risk of virus-rebound after ART cessation, due to the presence of a latent HIV reservoir in long-lived memory cells.[4] The ability of HIV to establish the latent infection remains the major challenge to virus eradication or an HIV cure.[5] Although transcriptionally silent, latent infection contributes to a highly stable proviral DNA reservoir, which can produce replicating HIV after ART cessation or memory T-cells activation upon exposure to an antigen.[6,7]

Small interfering RNAs (siRNA) enable treatment of diseases by regulation of a natural gene expression process by targeting messenger RNA (mRNA) for degradation, thus inhibiting the protein translation *via* post-transcriptional gene silencing (PTGS).[8] In HIV treatment, it could provide a tool to control the latent reservoir by either protecting cells against new HIV infection[9] or preventing viral reactivation by downregulation of host and viral genes.[10] However, the limitation of the PTGS pathways is the opportunity for virus mutants to escape at the level of viral genes transcription and reverse transcription.[11] Therefore, another approach targeting host-integrated viral DNA to inhibit transcription in the nucleus through transcriptional gene silencing (TGS) has gained more attention in recent years.[12] In this process, exogenous siRNA is translocated from the cytosol to the nucleus *via* RNA-Induced Initiation of Transcriptional Silencing (RITS) complex, where it binds to target DNA and induce chromatin compaction to stop gene transcription.[13,14] Controlling HIV replication through TGS limits the opportunity of virus mutations, as it acts directly on the gene promoter and not on multiple copies of mRNA in the cytosol. Suzuki et al. identified a siRNA sequence complementary to a fragment of viral genome in the 5' long terminal repeat (LTR) region of the promoter and demonstrated prolonged silencing effect *in vitro* and *in vivo*.[15,16] This highly specific siRNA potently suppressed viral replication, paving way for further studies of controlling the HIV latent reservoir by permanently locking latent cells in the quiescent state.

Early formulation of siRNA therapeutics involved the study of systems based on viral vectors.[17,18] Although promising, this strategy is not without challenges, including low delivery efficiency, high toxicity and non-specific activation of immune system and allergies.[19,20,21] In

HIV therapy the efficiency of transduction levels can be affected by an ongoing ART treatment,[22] as many of the lentivirus-based vectors comprise part of the HIV genome. Therefore, non-viral delivery systems have been drawing much attention as an alternative carrier material for gene therapy for HIV. Loading of nucleic acids cargo in particles can increase their stability in biological fluid and can potentially minimize off-target immune response activation, have lower toxicity and provide versatility with cargo loading (e.g., combination therapy, to target viral and host genes by decreasing virus transcription and host cells susceptibility to HIV, respectively).[23,24] Delivery systems based on lipids (e.g., micelles, liposomes),[25,26] polymers (e.g., polyethyleneimine, cyclodextrin)[27,28] and inorganic particles (e.g., silica, gold, quantum dots)[29,30,31] have been used to mediate post-transcriptional gene silencing effect of delivered siRNA in several applications. However, nanoparticle-mediated delivery of siRNA targeting a TGS pathway or epigenetic gene silencing remains to be demonstrated.

This chapter describes the use of poly-L-arginine (PLArg)-terminated multilayered particles and capsules for the delivery of siRNA to induce epigenetic silencing in HIV cell models. Core-shell particles and capsules were prepared *via* layer-by-layer (LbL) assembly of PLArg and poly-4-styrene sulfonate (PSS) on silica template. LbL assembly provides versatility in terms of substrate and material type, and particle surface can be easily modified by the attachment of targeting ligands, enabling targeting to specific cell populations, e.g. CD4/CCR5-expressing T cell for application in HIV therapy. Characterization of the particles and capsules (upon silica core dissolution) and optimization of siRNA loading is demonstrated. The efficacy of siRNA delivery was first demonstrated with luciferase gene downregulation *via* PTGS in non-infected cells. The engineered particles were then applied to deliver siRNA targeting HIV 5' LTR promoter region to the nucleus of infected cell lines, primary CD4 T cells and macrophages. The epigenetic silencing effect of delivered siRNA *via* TGS was assessed using a reverse transcriptase (RT) assay, indicating virus suppression in infected cultures 16 days post-treatment. Targeting strategy using dualtropic viral envelope on particle surface for enhanced binding and cellular uptake *via* CD4 and CCR5 receptors was also demonstrated. This work demonstrates particle-mediated delivery of siRNA for TGS for the first time and could inspire further research into non-viral particle platforms for siRNA delivery to achieve epigenetic silencing of HIV.

3.3. Experimental section

3.3.1. Materials

Silica particles (0.837 ± 0.003 μm, 5% w/v aqueous solution) were purchased from microParticles GmbH (Berlin, Germany). Poly(ethylenimine) (PEI) low molecular weight 50 wt% solution in water, poly-L-arginine hydrochloride, molecular weight >70000; poly(sodium 4-styrenesulfonate) (PSS) molecular weight ~70000, albumin from bovine serum (BSA), Dulbecco's phosphate buffered saline (DPBS), without calcium chloride or magnesium chloride, agarose, glucose, Hoechst 33342, Luciferase silencer G2 duplex, HEK239T cell line were purchased from Sigma-Aldrich (St. Louis, MI, USA). Sodium chloride (NaCl) was purchased from Chem-Supply (Gillman, Australia). Alexa Fluor N-hydroxysuccinimide (NHS) dyes (AF_{488}), Alamar blue cell viability reagent, wheat germ agglutinin (WGA), Alexa Fluor 488 conjugate (WGA-AF_{488}), Hoechst 33342 (10 mg mL−1 solution in water), lipofectamine, Dialysis tubing (molecular weight cutoff (MWCO) 3.5 kDa), Nunc Lab-Tek II Chamber microscopy slides, RiboGreen Quantification assay were purchased from Thermo Fisher Scientific (Scoresby, Australia). RNA electrophoresis sample loading dye was purchased from Bio-Rad (Gladesville, Australia). DMEM (with 4.5 g L−1 glucose and L-glutamine), RPMI-1640 medium and trypsin (10X) were purchased from Lonza (Basel, Switzerland). Fetal bovine serum was purchased from Bovogen Biologicals (Keilor East, Australia). Paraformaldehyde 4% aqueous solution (EM grade, 4% PFA) was purchased from Electron Microscopy Sciences. AllStar negative control AF647-siRNA was purchased from Qiagen. HeLa (ATCC CRM-CCL-2), HuT 78 (ATCC TIB-161) and RAW 264.7 (ATCC TIB-71) cell lines were purchased from ATCC. Steady Glo luciferase kit was purchased from Promega. HeLa T4 and TZM-bl cells were obtained from NIH AIDS reagents program. All the reagents for experiments using infected cells were obtained by Professor Anthony Kelleher's group from Kirby Institute, UNSW. Virus-like-particle 'spln_env7' were a gift from Professor Stuart Turville and Dr Chantelle Ahlenstiel, UNSW.

3.3.2. Film formation on a planar surface

Quartz crystal microbalance. Quartz crystal microbalance with dissipation monitoring (QCM-D) was used to follow the layer-by-layer (LbL) formation of film consisting of

polyethylenimine (PEI), poly (sodium 4-styrene sulfonate) (PSS) and poly-L-arginine (PLArg) on a planar surface and to study siRNA binding onto PLArg-terminated film. The gold crystal QCM-D surface was cleaned using Piranha solution for 2 minutes (one part of 30% H_2O_2 in three parts of H_2SO_4), washed extensively with Milli-Q water and dried with nitrogen. *Caution: Piranha solution is highly corrosive. Extreme care should be taken when handling Piranha solution and only small quantities should be prepared.* PEI solution (2 mg/mL) was prepared in Milli-Q water with 1 M NaCl. PSS solution (1 mg/mL) was prepared in 50 mM sodium acetate buffer pH 5.2 with 0.5 M NaCl. PLArg solution (1 mg/mL) was prepared in 50 mM sodium acetate buffer pH 5.2, and the same buffer was used in subsequent washing steps. PEI was used as a first layer, followed by deposition of four PSS/PLArg bilayers. Adsorption of each layer was carried out for 15 minutes, followed by a 5 minutes wash with either MilliQ-water after PEI deposition or 50 mM sodium acetate buffer after subsequent layers. The assembled PEI-$(PSS/PLArg)_4$ film was used to study binding of siRNA. siRNA (provide details) was prepared=(0.5mg/mL) in sodium acetate buffer. Nucleic acid was deposited for 20 minutes, followed by three washing cycles with 50 mM sodium acetate buffer pH 5.2. The mass of adsorbed siRNA was calculated using Saurebrey's $\Delta m = -C \cdot \Delta f/n$, where C equals 17.7 ng/ ($cm^{-2} \cdot Hz$), assuming thin and rigid mass deposition on the surface.[32]

Atomic force microscopy. Atomic force microscopy (AFM) was used to measure the thickness of the films before and after siRNA adsorption. Silicon wafers were first cleaned by placing in absolute ethanol for two hours, followed by drying under a nitrogen stream. Next, two types of films, i.e. PEI-$(PSS/PLArg)_2$ and PEI-$(PSS/PLArg)_2$-siRNA, were prepared by LbL assembly on the silicon wafers using the conditions as described above for QCM-D. AFM experiments were carried out with a JPK NanoWizard II BioAFM. Typical scans were performed in tapping mode with MikroMasch silicon cantilevers (NSC/CSC). The roughness of the air-dried films was analyzed using JPK SPM image processing software (version V.3.3.32).

3.3.3. Multilayered particle preparation

LbL assembly on silica particles. The LbL method was used to fabricate multilayered film on 837 nm spherical silica template. Silica particles (40 µl, 0.05 wt %) were washed three times by resuspension/centrifugation cycle (200 µl of Milli-Q water, 500 *g* for 1.5 minutes) and resuspended in 200 µl of Milli-Q water before priming the LbL buildup by adsorption of PEI

(200 µl) for 15 minutes. Particles were washed twice by centrifugation (500 *g* for 1.5 minutes) with Milli-Q water (200 µl) then twice more with 50 mM sodium acetate buffer pH 5.2 (200 µl), which was used in all subsequent washing steps. For subsequent layer deposition, 500 µl of either PSS or PLArg solution was added to 200 µl particles suspension and incubated for 15 minutes. After deposition of nine layers, particles with a shell structure PEI-$(PSS/PLArg)_4$ were resuspended in 100 µl of buffer, counted by flow cytometry and stored at 4°C until further use.

ζ-potential measurement. Microelectrophoresis was performed to monitor the formation of the multilayered film by measuring the change in ζ-potential after each deposition step. 2 µl of the sample (~ $8x10^6$ particles; taken after each layer deposition) was dispersed in 798 µl of water. All measurements were performed at 25°C in folded capillary cells (DTS1070, Malvern Instruments) using a Zetasizer Nano-ZS instrument (Malvern Instruments).

Silica core removal and capsule formation. Capsules were prepared by dissolving the silica core with HF. PLArg-terminated core-shell particles (~ $6x10^8$ particles) were re-dispersed in 40 µl of 50 mM sodium acetate buffer pH 5.2, followed by addition of 300 µl of buffered hydrofluoric acid (2 M HF, 8 M NH_4F pH 4) and 5 minutes incubation at room temperature. *[Caution! HF is highly toxic. Extreme care should be taken when handling HF solution].* The capsules were pelleted by centrifugation at 4500g, 10min. The supernatant was removed and capsules were then washed by centrifugation with ultrapure water (once) and sodium acetate buffer three times to ensure that the HF was fully removed.

Preparation of AlexaFluor 647-labelled particles and capsules. To prepare fluorescently labelled particles, the PLArg used as a seventh layer of the film was modified with an Alexa Fluor dye. PLArg solution (2 mg/mL) was prepared in 50 mM sodium acetate buffer pH 5.2 and mixed with 1.75 µL of AF_{488}-NHS or 3.5 µL of AF_{647}-NHS (the equivalent of 2.8 x 10^{-3} mmol) and incubated for at least 2 hours, with mixing, at room temperature. Free dye was removed by extensive dialysis (MWCO 3.5 kDa) against Milli-Q water for two days. The final product was freeze-dried and dissolved in 50 mM sodium acetate buffer, pH 5.2 and used in LbL assembly, as described for non-labelled PLArg.

3.3.4. Particle imaging

Confocal microscopy. Particles (core-shell and capsules) were imaged with a Nikon A1R microscope using 60x 1.4NA oil immersion or 40 x 1.2 NA water objectives. Particle

suspensions were prepared in 400 µL of 1xDPBS, 50 mM sodium acetate buffer or RPMI medium supplement with 10% FBS, typically at a concentration of 1.5 $x10^4$ particles/ µL and transferred to 8-well chamber slide before imaging.

Scanning Electron Microscopy. Changes in the surface morphology of the silica templates before and after LbL assembly were analysed by scanning electron microscopy (SEM). Silicon wafer (substrate) was cleaned in a bath (100 ml 80% H_2SO_4, 35 ml H_2O_2 and 20 ml Milli-Q water) for 15 minutes at room temperature and dried with a nitrogen stream. Particles (~ $2x10^6$ particles) were deposited on a clean silicon wafer and were washed three times with Milli-Q water within 24 hours, allowing the sample to air-dry between washing steps. Images were acquired using an FEI Quanta 200 field emission SEM with 10kV operation voltage.

Atomic Force Microscopy. The thickness of the capsules was analysed by AFM. Capsules (~ $1x10^7$ capsules) were deposited on a clean glass microscope slide, air-dried for 24 hours at room temperature and analysed with a JPK NanoWizard II BioAFM instrument as described above (film formation on a planar surface).

3.3.5. Quantification of siRNA-particle complexation

Gel electrophoresis. Complexation of siRNA was studied by polyacrylamide gel electrophoresis. Samples with a varying number of particles (from $1x10^3$ to $1x10^6$) were prepared in 15 µL of 50 mM sodium acetate buffer and mixed with 15 µL of siRNA solution containing 3 pmol of siRNA. Samples were incubated for 20 minutes at room temperature, followed by addition of 5 µL of nucleic acid loading dye. Then, 30 µL of each sample was loaded onto a10% tris-borate-EDTA (TBE) polyacrylamide gel and electrophoresis was carried out for 1 hour at 150 V. Gel was stained with SyBr Gold reagent and imaged using a ChemiDoc XRS-Imaging System.

Quantification RiboGreen RNA Assay. Complexation of siRNA by particles was studied with a Quant-iT RiboGreen RNA Assay Kit. All the reagents were prepared as outlined by the manufacturer's protocol. Particles suspension and siRNA solution were prepared in 15.7 mM DPBS immediately before use. Samples with particles number varying from $1x10^6$ to $2x10^7$ (20 µL final volume) were equilibrated for 5 minutes at room temperature, followed by addition of 20 µL of siRNA solution (3 pmol of siRNA per individual particle-containing sample). Particles-siRNA complexes were incubated for 20 minutes at room temperature, with vortex

mixing every 5 minutes. Next, samples were pelleted at 600 *g* for 5 minutes, and 10 µL of supernatant was transferred to a 96-well microplate and mixed with 90 µL of 1xTE buffer from the kit. Sample containing only buffer, particles only control ($1x10^6$) and positive control containing only siRNA (3 pmol) were also prepared. All samples were incubated with 100 µL of RiboGreen reagent for 2 minutes at room temperature, protected from light. Measurement of fluorescence (490 excitation and 520 nm emission) was performed with an Infinite M200 microplate reader.

ζ-potential measurement. Influence of siRNA binding on particles ζ-potential was studied by microelectrophoresis. Particles-siRNA and capsules-siRNA complexes were prepared in DPBS at the optimal particle-to-siRNA ratio ($2x10^6$ particles per 1 pmol of siRNA). After 20 minutes incubation at room temperature, 40 µL of complexes was transferred to 760 µL of Milli-Q water and mixed by vortexing (10 s) before zeta potential measurement.

3.3.6. Imaging of particle-siRNA complexes

Using the same particle-to-siRNA ratio as determined by gel electrophoresis and RiboGreen assay, complexes of core-shell particles and capsules with AF647-labelled siRNA were prepared and imaged using a Nikon A1R confocal microscope with a 60x 1.4NA oil immersion objective.

3.3.7. Particle/siRNA stability

Particles-siRNA and capsules-siRNA complexes were prepared in DPBS at the optimal particle-to-siRNA ratio ($2x10^6$ particles per 1 pmol of AF_{647}-siRNA). After 20 minutes incubation at room temperature, 40 µL of complexes were transferred to 360 µL of either DPBS or RPMI containing 10% FBS. Particles suspension was transferred to an 8-well chamber slide and incubated at 37°C, 5% CO_2 in a humidified atmosphere. Particles were imaged using a Nikon A1R confocal microscope at Day 1, 2 and 3 using the same camera and laser settings for consistency.

3.3.8. Cell viability, association and internalization in non-infected cells

Cell culture. Hela (ATCC CRM-CCL-2) and RAW 264.7 (ATCC TIB-71) cell lines were cultured in DMEM with GlutaMAX, supplemented with 10 % foetal bovine serum. HuT 78 cell line (ATCC TIB-161) were cultured in RPMI 1640 medium supplemented with 10% foetal bovine serum. Cells were cultured at 37ºC, 5% CO_2 in a humidified atmosphere unless indicated otherwise.

Cytotoxicity. Cell viability was assessed by the Alamar Blue assay. Cells were seeded at $1x10^5$ cells per well in a 96-well microplate (flat-bottom for HeLa and RAW 264.7 cells, round-bottom for HuT78 cells) and left overnight in cell culture conditions. Particle and particles-siRNA complexes were prepared in 1xDPBS at three different particle-to-cell ratios: 50, 200 and 1000 corresponding to $5x10^5$, $2x10^6$ and $1x10^7$ total particles per well, respectively. Particles-siRNA complexes were prepared in 15.7 mM DPBS by adding 15 ul of particles suspension containing a varying number of particles (as for non-siRNA samples), to 15 ul of siRNA solution (keeping the ratio at $2x10^6$ particles per 1 pmol of siRNA). Samples were mixed and incubated for 20 min at room temperature as described above. Cell culture media was removed from plated cells and replaced with 120 µL of fresh medium and 30 µL of particles or particle-siRNA suspension was added to each well for a 24 h incubation under cell culture conditions. After incubation, the medium in wells with adherent HeLa and RAW 264.7 cells was removed and replaced with 150 µL of fresh DMEM and 15 µL of Alamar Blue viability reagent was added. HuT78 suspension cells were transferred to 1.5 mL microtube and centrifuged (300 g for 7 minutes). The supernatant was discarded and the cell pellet was re-dispersed in 150 µL of medium mixed with 15 µL of Alamar Blue reagent and cell suspension transferred to a 96-well plate. Cells were incubated at 37°C, 5% CO_2 in a humidified atmosphere for a further 4 h (HeLa and RAW264.7) or 24 h (HuT78). The fluorescence of the cell supernatant was measured on Tecan Infinite M200 microplate reader using 560 nm and 590 nm as excitation and emission wavelengths, respectively.

Confocal microscopy. Internalization of particles and capsules complexed with AF_{647}-labelled siRNA was assessed by confocal microscopy. Cells (HeLa, RAW 264.7 and HuT-78) were seeded in 8-well chamber slides at $6x10^4$ cells per well in 400 µL medium and left overnight in cell culture conditions. Complexation of siRNA by particles and capsules was done in 15.7 mM DPBS as described above by incubation of siRNA with particles for 20 minutes at room temperature ($1.2x10^7$ particles per 6 pmol of siRNA, 30 µL final volume).

Before addition to cells, the media was aspirated and replaced with 370 µL of fresh medium, followed by addition of particles suspension and incubation for 24 h at cell culture conditions. Before analysis, cells were washed 3 times with 200 µL of DPBS (HuT 78 were washed by centrifugation/resuspension cycle) to remove excess unbound complexes and fixed with 4% paraformaldehyde for 10 minutes at room temperature. Nuclei were stained with Hoechst (1 µg/mL) and cell membranes were stained with WGA_{488} (5 µg/mL) for 5 minutes at room temperature, followed by two more washes with DPBS. Images were acquired with a Nikon A1R confocal microscope with a 60x1.4NA oil immersion objective and analysed using Fiji software.

3.3.9. Luciferase gene knockdown in non-infected HEK239T.

HEK293TLuc cells expressing the luciferase gene were cultured in DMEM supplemented with 10% FBS. Cells were seeded at 5.0 x 10^3 cells per well in 100 µL of DMEM medium on a 96-well white plate and incubated overnight at 37ºC, 5% CO_2 in a humidified atmosphere. The next day, the medium was replaced by 70 µL of fresh DMEM medium and 30 µL sodium acetate buffer containing particles complexed with siRNA (6x10^6 particles per 3 pmol of siLuc, #AM4629) was added to cells for 6 h or 24 h incubation. After incubation, the medium was replaced with 150 µL of fresh medium. Gene knockdown was evaluated 48 h post-transfection using a Steady-Glo Luciferase kit (Promega). Luminescence was measured on an Infinite M200 microplate reader (Tecan, Switzerland). Background control samples were prepared as Steady Glo reagent only (BG). Luciferase downregulation was expressed as % of untreated cells (CTR):

$$\%=\left(\frac{Sample\ luminescence-BG}{CTR\ luminescence-BG}\right)*100$$

3.3.10. Cell culture-infected cells

Infected cells were cultured by Miss Vera Klemm and Dr Chantelle Ahlenstiel in a PC3 facility at Kirby Institute, UNSW.

Cell lines. HEK239T, HeLa T4 and TZM-bl cells were cultured in DMEM supplemented with 10% FBS, 100 U mL penicillin and 100 μg/mL streptomycin. HeLa T4cells were grown in the presence of G418 antibiotic (200 μg/mL) to maintain culture of CD4-expressing cells.

Isolation of primary cells. Peripheral blood mononuclear cells (PBMCs) were isolated from fresh blood of healthy donors using Ficoll density gradient. Antibody-associated magnetic beads were used to isolate selected cell population. Monocytes were purified using anti-CD14 MicroBeads and cultured in RPMI medium supplement with 10% hAB and 2 mM GlutaMax for 7 days before particle addition. CD4 T cell isolation kit (Miltenyi Biotech, Gladbach, Germany) was used to select CD4 T cells by negative selection, according to the manufacturer's protocol. Resting CD4 T cells were cultured in RPMI medium supplemented with 2% hAB and 2 mM Glutamax without additional treatment. Activated cells were treated for 48 h with T Cell Activation/Expansion kit following the manufacturer's protocol. Before particle additional, cells were seeded at a concentration of $1x10^6$ cells mL^{-1}.

Cells infection with pseudovirus. Cells were infected at MOI=1 at the time of seeding. HIV-1_{SF162} virus was used to infect HeLa T4+ and HuT78 cells. HIV-$1_{NL4.3}$ was used to infect activated CD4 T (spinoculation, 2000 *g* for 2 h at 37°C) and HIV-$1_{pBalI\text{-}NL4.3}$ was used to infect macrophages (spinoculation, 200 *g* for 1 h at 37°C).

For imaging, cells were infected with VSV-G envelope pseudotyped HIV-$1_{NL4.3\text{-}\Delta env}$ expressing mOrange. HeLa T4+, HuT-78 and macrophages were infected for 4 days ad activated CD4 T cells for 3 days prior to particle addition. Resting CD4 T cells were infected with HIV-$1_{NL4.3\text{-}IRESGFP}$ (gift from Stuart G. Turville) for 5 days prior to particle addition. HIV-1 virus, lentivirus and plasmid used to generate the model of HIV infection was obtained from the NIH AIDS Reagent Program and produced at the Kirby Institute, UNSW.

3.3.11. Particles addition to infected cells for epigenetic silencing

Polyarginine-terminated capsules were used to deliver siRNA targeting the HIV promoter (PromA) and induce HIV epigenetic silencing. Scramble siRNA, particles with no siRNA, DPBS buffer and infected cells (mock) controls were also prepared.

HeLa T4+. Cells were seeded at $2.0x10^4$ cells per well in a 96-well plate. For the RT assay, 10 pmol of siRNA was complexed with $2x10^7$ capsules, corresponding to particle-to-cell ratio

1000. For imaging, cells were seeded at $4.0x10^3$ cells per well in a 384-well plate and 2 pmol of AF_{647}-siRNA was complexed by $4.0x10^6$ particles (particle-to-cell ratio 1000).

Activated CD4 T cells. Cells were seeded at $1x10^5$ cells per well in a 96-well plate. For the RT assay, 10 pmol of siRNA was complexed by $2x10^7$ capsules (particle-to-cell ratio 200). For imaging, cells were seeded at $5.0x10^4$ cells per well in a 384-well plate and 2 pmol of AF_{647}-siRNA was complexed by $4.0x10^6$ particles (particle-to-cell ratio 80).

Resting CD4 T cells. Cells were seeded at $5.0x10^4$ per well in 384 well plate. No RT assay could be performed in resting cells. For imaging, 2 pmol of AF647-siRNA was complexed by 4.0x106 capsules (particle-to-cell ratio 80).

Macrophages. Cells were seeded at $1.0x10^5$ cells per well in 96 well plate for RT assay and imaging. Non-fluorescent siRNA was used for RT assay and AF_{647}-siRNA used for imaging (10 pmol of siRNA complexed by $2.0x10^7$ capsules, particle-to-cell ratio 200).

3.3.12. Reverse transcriptase assay

The RT assays were performed by Vera Klemm and Dr Chantelle Ahlenstiel. Supernatant from infected cell cultures was collected 16 (primary cells) or 20 (HeLa T4) days after particle-siRNA addition. The assay was performed by Vera Klemm and Dr Chantelle Ahlenstiel using the previously described protocol.[33]

3.3.13. Imaging of infected cells

Following 48 h incubation with particles, nuclei were stained with NucBlue Live Cell Stain and fixed with 4% PFA for 12 min at room temperature and stored at 4°C until analysis. Imaging was performed on a DeltaVision Elite Image Restoration Microscope in a PC3 facility using the 60x oil immersion lens with 1.58 NA. Deconvolution of images was performed using the SoftWoRx software. Arbitrary line intensity profile was used to determine the overlap of siRNA and nucleus fluorescent signal, therefore identifying nuclear events (siRNA present in the nucleus). 3D Volume viewer was further used to generate 3D projection of the nucleus to exclude siRNA present in nuclear pockets. Analysis of acquired images was performed by Vera Klemm and Dr Chantelle Ahlenstiel at the Kirby Institute, UNSW.

3.3.14. Preparation of VLP-coated capsules

Preparation of VLP-coated capsules. A titer of virus-like-particles targeting CD4 and CCR5 receptors was a gift from Dr Chantelle Ahlenstiel and A. Prof. Stuart Turville. Capsules were incubated with VLP at a virus-to-particle ratio 1 in sodium acetate buffer pH 5.2 for 30 min at room temperature. A small portion of VLP-coated capsules was used to measure changes in particle ζ-potential before and after VLP-adsorption using a Zetasizer Nano-ZS instrument (Malvern Instruments). All measurements were performed at 25°C in folded capillary cells.

Transmission Electron Microscopy. The morphology of the VLP-coated capsules was observed by transmission electron microscopy (TEM) by using an FEI Tecnai TF20 instrument with an operating voltage of 200 kV. The sample suspensions were allowed to air-dry on formvar-carbon coated copper grids before imaging.

3.3.15. VLP-coated LbL capsules: *in vitro* experiments in HeLa and TZM-bl cell lines

Cell culture. Binding and uptake of VLP-coated particles was tested using CD4+ and CCR5 + TZM-bl cells and CD4- CCR5- HeLa cells were used as a negative control. Cells were seeded at $6.0x10^4$ cells per well in 400 µL of DMEM medium supplemented with 10% FBS on 8-well chamber slide.

Binding on ice. Particles were incubated with VLPs for 30 min in 50 mM sodium acetate buffer pH 5.2 prior to addition to cells (particle-to-cell ratio 100) for 1 h incubation at 4°C. Next, cells were washed 3 times with cold DPBS and fixed with 4% PFA for 5 min at RT. Nuclei were stained with Hoechst (1:10000 solution in DPBS) for 5 min, followed by 2 washes with 400 µL of DPBS. Cells were imaged using a Nikon A1R confocal microscope with a 40x water objective.

Internalization in 37°C. Particles were incubated with VLPs for 30 min in 50 mM sodium acetate buffer pH 5.2 prior to addition to cells at a particle-to-cell ratio of 100 for 24 h incubation at 37°C, 5% CO_2 in a humidified atmosphere. Next, cells were washed 4 times with 400 µL of DPBS and fixed for 5 min at RT with 4% PFA. Following two more washes, the cell membrane was stained with AF_{488}-wheat germ agglutinin (5 µg/mL, 5 min at room temperature) and nuclei were stained with Hoechst (1:10000 in DPBS, 5 min at room

temperature). Cells were imaged using a Nikon A1R confocal microscope with a 40x water objective.

3.4. Results and discussion

3.4.1. Multilayer assembly on planar and spherical substrates

The complexation of siRNA by nanoparticles usually relies on electrostatic interaction between cationic material and negatively charged phosphate groups in siRNA.[34] Complexation of siRNA *via* nanoparticle has a number of advantages, including protection from degradation by enzymes present in the blood serum and enhanced penetration through biological membranes.[35,36] Particle design typically introduces a mechanism of endosomal escape to enable the cytosolic release of delivered siRNA to bind to messenger RNA (mRNA), thus blocking its translation *via* PTGS. For TGS, after cytosolic release, the siRNA needs to be translocated to the cell nucleus, where it can bind to its target genomic sequence and block transcription of the desired gene.

In this study, multilayered particles were used for the complexation of siRNA. Preparation of multilayered films on a colloidal template, such as silica, *via* LbL method provides an opportunity to finely control particles size and shape, and the choice of coating materials allows tuning particles surface chemistry.[37] LbL films are typically formed by deposition of interacting polyelectrolytes. Here, multilayered particles were prepared by subsequent adsorption of interacting PSS and PLArg on ~850 nm silica particles. PLArg is a cationic polypeptide that can complex negatively charged siRNA by electrostatic interactions (**Scheme 3.1**).[38] The use of arginine-rich materials in drug delivery formulation has been associated with an enhanced intracellular translocation of various cargoes.[39,40] The mechanism was assigned to cell-penetrating properties of arginine, similar to arginine-rich HIV-derived transactivator of transcription (Tat) - first identified cell-penetrating peptide (CPP).[41] CPPs (synthetic or from natural sources) have been since used to conjugate various therapeutic molecules, including small molecules, antibodies and proteins, and in gene therapy to bind and translocate negatively charged nucleic acids into the cell.[42,43]

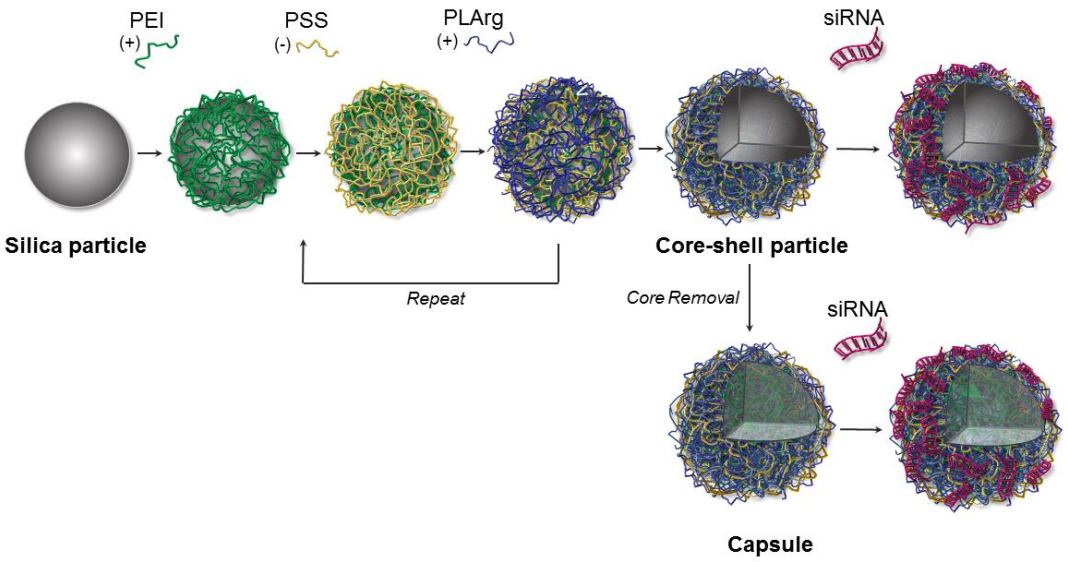

Scheme 3.1. LbL assembly on silica particles. LbL core-shell particles were prepared by the deposition of anionic PSS and cationic PLArg on PEI-coated silica template. Hollow capsules were formed by dissolution of the silica core. siRNA was adsorbed on the particle surface (PLArg-terminated) *via* electrostatic interactions.

The aim of this study was to use LbL particles to deliver PromA siRNA to the nucleus of infected cells and induce silencing of HIV- 1 *via* TGS. Given that the target 5` LTR promoter region is in the nucleus, delivery of PromA by PLArg-containing particles could potentially result in an enhanced nuclear translocation of the delivered sequence, as described for arginine-rich nuclear localization signals (NLS) involved in the transport of proteins to the cell nucleus.[44]

Formation of the multilayered film consisting of eight alternating layers of PSS and PLArg deposited on PEI-coated crystal was first studied by QCM-D. QCM-D allows real-time analysis of LbL growth and estimation of mass adsorbed after each polyelectrolyte deposition based on changes in resonance frequency of an oscillating piezoelectric crystal. QCM-D data (**Figure 3.1A**) show changes in resonance frequency after the addition of each layer, suggesting that the multilayered film is formed and stabilized by electrostatic interaction between anionic PSS and cationic PLArg. The same film was used in the next step to confirm the binding of siRNA. The observed change in resonance frequency confirmed the deposition of siRNA on PLArg-terminated film and was converted to the amount of adsorbed mass using the Sauerbrey's equation (255 ng siRNA per 1 cm^2).[32] Changes in film morphology before and after siRNA

adsorption was then studied by AFM. The observed increase in surface roughness from 0.6 nm for PEI-$(PSS/PLArg)_2$ to 1 nm for PEI-$(PSS/PLArg)_2$-siRNA confirm siRNA deposition (**Figure 3.1B and C**).

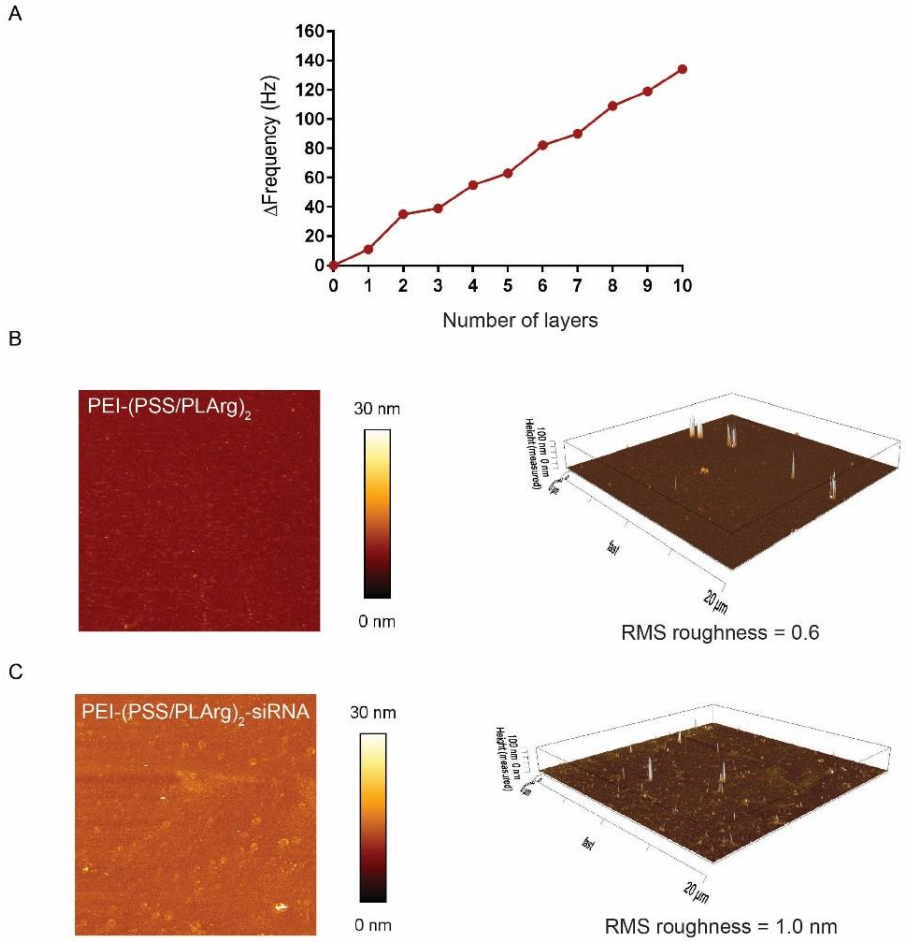

Figure 3.1. Characterization of LbL film on a planar surface. LbL film assembly was monitored by QCM-D. The odd layer numbers correspond to PLArg (except Layer 1, which is PEI), and the even layer number corresponds to PSS (except Layer 10, which is siRNA). AFM analyses of film roughness before (B) and after (C) siRNA adsorption.

The film structure described above was then used to prepare core-shell particles *via* LbL assembly on silica templates. Silica particles (837 nm in diameter) were first coated with PEI and used to deposit four PSS/PLArg bilayers. The assembly process was followed by ζ-potential measurements. Microelectrophoresis data (**Figure 3.2A**) showed a reversal of charge

after deposition of each layer, which is indicative of multilayered film formation on colloidal support. Particle formation and morphology were followed using various imaging techniques. Adsorption of fluorescently labelled PLArg as a seventh layer of the film allowed imaging particles by confocal microscopy (**Figure 3.2B)** and SEM analysis indicated increased roughness of silica template surface after PEI-(PSS/PLArg)$_4$ film deposition (**Figure 3.2C and D**). SEM was also used to assess the thickness of the shell by comparing particle size after LbL assembly with the size of the silica template. Data obtained by measurement of particles (n=50) using Fiji software show an increase in particles size from 846 ± 32 nm for silica template to 905 ± 32 nm after LbL assembly. This indicates the formation of ~41 nm thick film on particles surface after deposition of nine polyelectrolyte layers or 4.5 nm per layer.

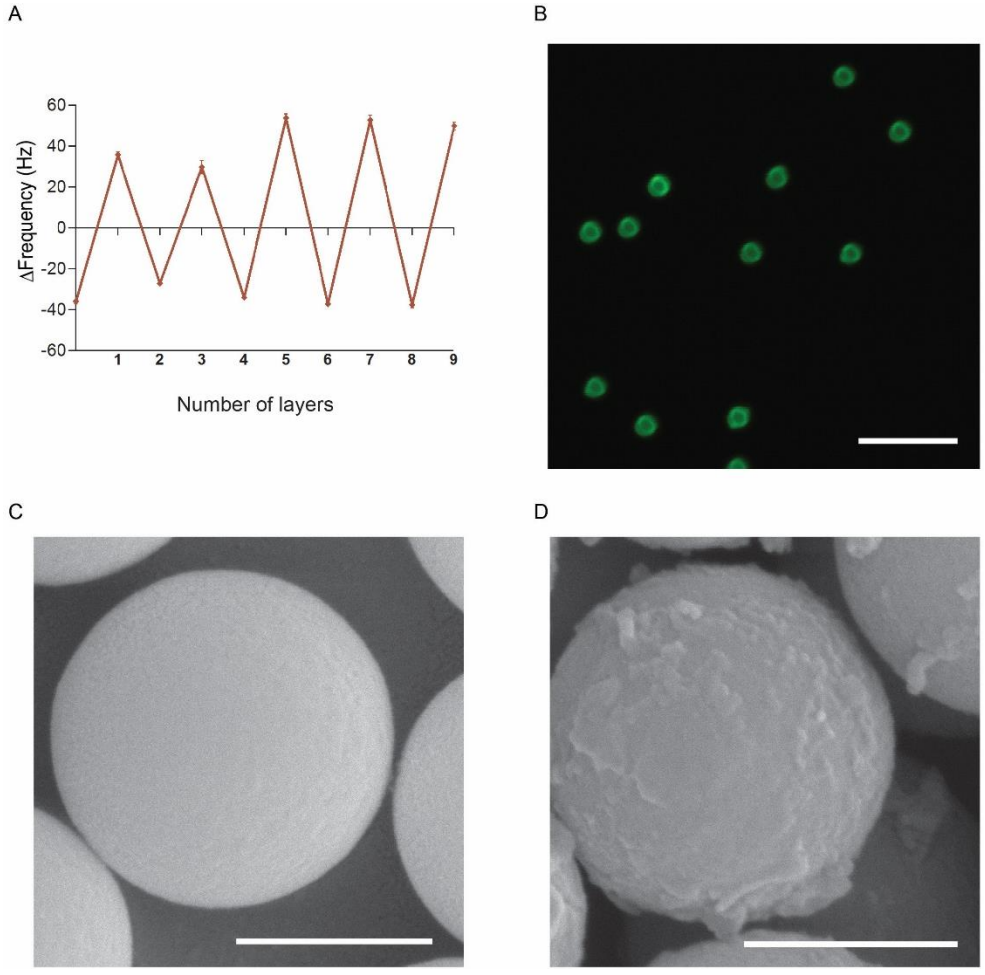

Figure 3.2. Preparation of LbL particles. (A) ζ-potentials measurement showing the LbL film deposition on silica particles (Layer 0). (B) Confocal microscopy image of fluorescently labelled particles (AF_{488}-PLArg used as 7th layer). SEM image of silica core (C) and LbL particles (D). *Scale bars are 5 µm (B) and 500 nm (C and D).*

An alternative particle system (hollow capsules) with a similar size and composition, but distinct mechanical properties, was also prepared. Dissolution of silica cores after LbL assembly resulted in the formation of hollow capsules that can potentially carry a therapeutic cargo not only on the surface but also within the capsule cavity.[45] Removal of core material eliminates potential concerns associated with silica degradation, and PLArg-containing microcapsules have been previously reported to deliver and release the loaded cargo upon degradation of the carrier by intracellular proteases.[46]

Capsules composed of PEI-(PSS/PLArg)$_4$ were formed by removing the silica template with HF buffered with an ammonium salt. The presence of hollow capsules after core removal was first confirmed by AFM (**Figure 3.3A**). Images of capsules in the air-dried state showed collapsed and monodispersed structures with a 45 nm wall thickness and agrees with the shell thickness obtained for core-shell particles. DIC microscopy of capsules in a hydrated state show uniform capsules of ~900 nm in size (**Figure 3.3B**), and the use of AF$_{647}$-PLArg during assembly process allowed =visualization of capsules *via* confocal microscopy (**Figure 3.3C**).

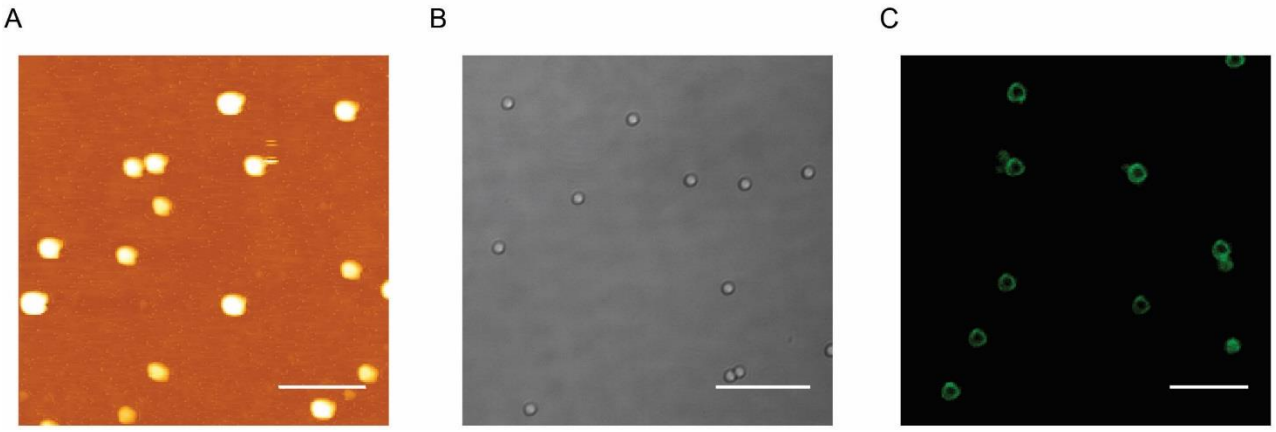

Figure 3.3. Preparation of LbL capsules. (A) AFM image of hollow capsules in a dried state. (B) DIC microscopy of capsules in a hydrated state. (C) Confocal microscopy images of fluorescently-labelled capsules (AF$_{488}$-PLArg used as 7th layer). *Scale bars are 2 µm (A), 10 µm (B) and 5 µm (C).*

3.4.2. siRNA/particle complex formation

Complexation of siRNA by LbL particles was tested by gel electrophoresis to evaluate the amount of particle that binds siRNA at concentration relevant for *in vitro* experiments. Free siRNA can migrate through the gel and band intensity after visualisation is an indication of the amount of unbounded molecules present in the solution. It was estimated that 1 pmol siRNA is complexed by 2.0 x 10^6 particles (**Figure 3.4A**). The ability of PLArg-terminated particles to complex siRNA was further assessed by Quant-iT RiboGreen RNA Assay kit. Complexation of siRNA at varying particle-to-siRNA ratios was carried out for 20 minutes and a small portion of supernatant was then analysed for the content of free siRNA. Recorded fluorescence intensity was used to determine optimal binding condition, following equation:

$$\%\ adsorbed\ siRNA = 100 - \frac{S - BG}{C - BG} x\ 100$$

where S is fluorescence of the samples, BG is fluorescence of the background (no siRNA or particles) and C is fluorescence of the naked siRNA control (no particles).

It was estimated that 2x10^6 particles is required to fully complex 1 pmol of siRNA (**Figure 3.4B**), which corresponds to an estimated coverage of 266 ng siRNA per cm^2 of a spherical surface and agrees with the data obtained for the planar surface. The influence of siRNA adsorption of particle surface charge was studied by DLS. Adsorption of siRNA causes a shift in particle ζ-potential, from positive 50 ± 4 mV for bare particles to 6 ±4 mV upon siRNA binding, as presented in **Figure 3.4C**. Similarly, the initial ζ-potential of capsules (49 ± 5 mV) decreases to (-4 ± 6 mV) upon incubation with siRNA at a ratio of 2x10^6 capsules per 1 pmol of siRNA (**Figure 3.4C**). Confocal microscopy was used to image particles-siRNA complexes formed between PLArg-terminated core-shell particles/capsule and AF_{647}-labelled siRNA (**Figure 3,4D and E**). The presence of fluorescently labelled particles further confirms the presence of siRNA on the particle surface.

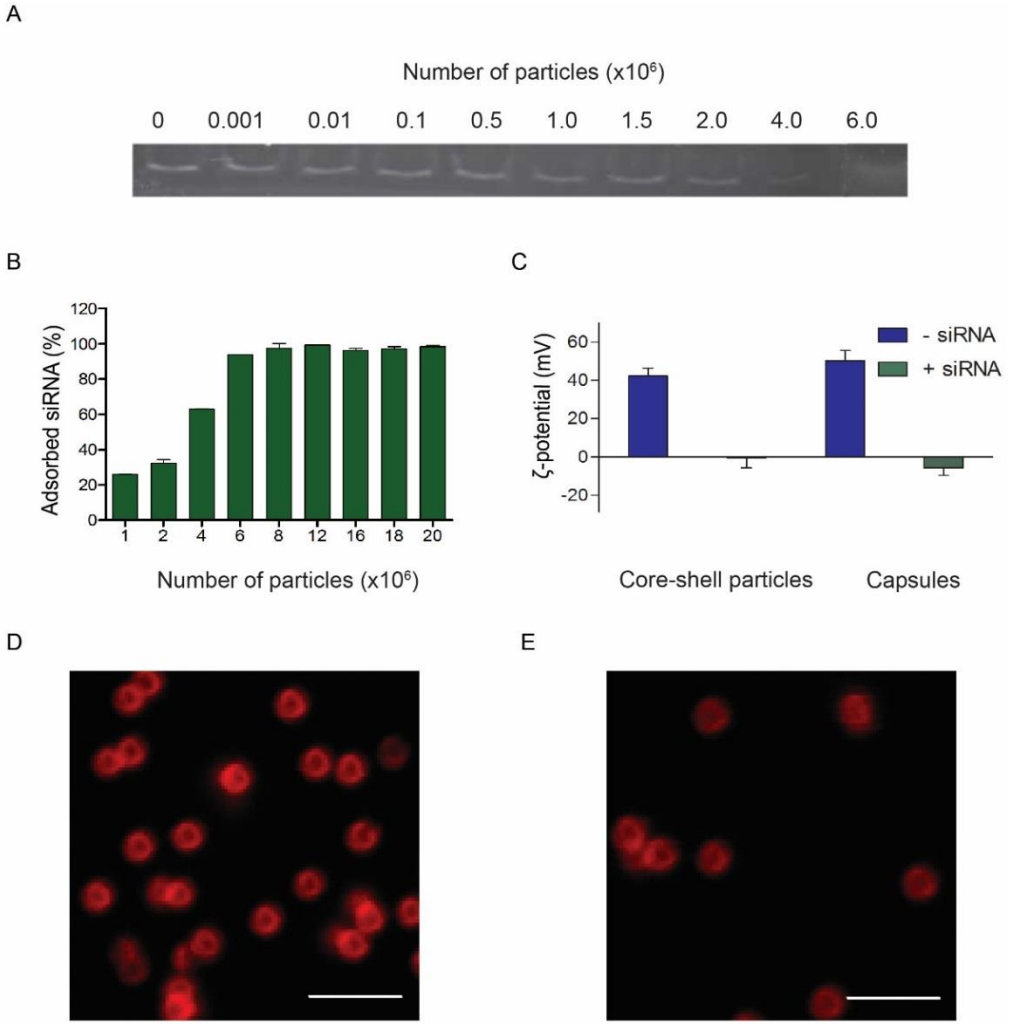

Figure 3.4. siRNA complexation by LbL particles. (A) Agarose gel electrophoresis analysis of siRNA complexation by particles: Lane 1, siRNA; Lanes 2–10, particle/siRNA complexes at different ratios. Quantification of siRNA binding by Ribo Green assay (B) and particle/capsule ζ-potential changes before and after siRNA adsorption (C). Confocal microscopy images of core-shell particles (D) and capsules (E) complexed with AF_{647}-siRNA. *Scale bars are 2 μm.*

3.4.3. Particle/siRNA complex stability

The stability of particles-siRNA complexes was tested in two types of physiological buffers: (1) in DPBS (pH 7), which is the buffer used for siRNA complexation, and (2) cell culture medium, i.e., RPMI supplemented with 10 % FBS to test whether serum proteins destabilize particle-siRNA complexes. Using AF_{647}-siRNA, complexes were formed at the optimal

particle:siRNA ratio and incubated under cell culture conditions (37°C, 5% CO_2 in a humidified atmosphere) for 3 days. Images taken at day 1, 2 and 3 (**Figure 3.5**) by confocal microscopy indicates that the complexes remain intact after the absorption of siRNA, which is not displaced by serum proteins at the tested concentration.

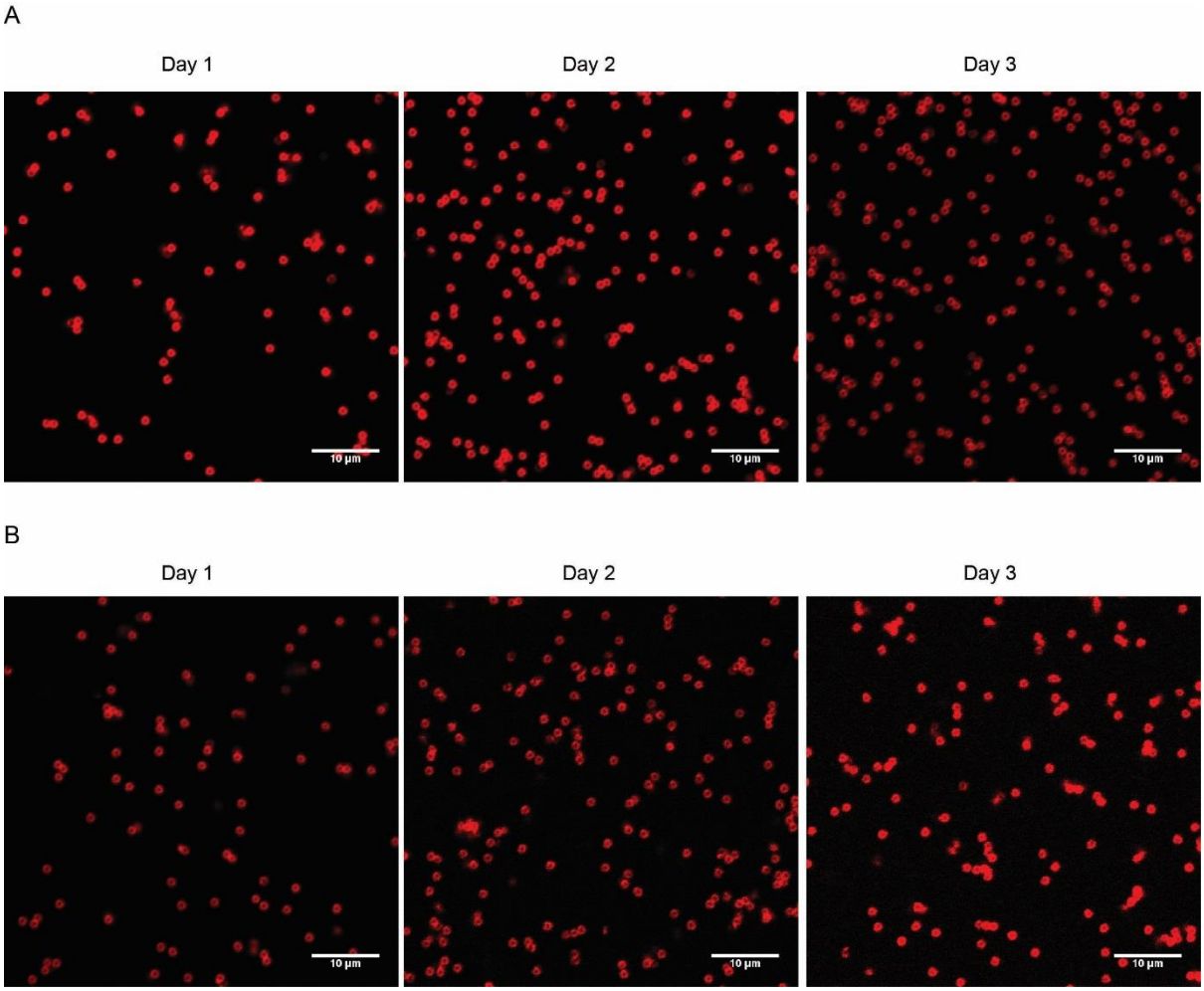

Figure 3.5. Particle-siRNA complex stability. Particles complexed with AF_{647}-siRNA in DPBS (A) and RPMI supplemented with 10 % FBS (B) after incubation for 1, 2 or 3 days at 37°C, 5% CO_2 in a humidified atmosphere.

3.4.4. Cytotoxicity and internalization

Cytotoxicity of core-shell particles and capsules was tested in non-infected HeLa, HuT 78 and RAW 264.7 cell lines by Alamar Blue viability assay. Both bare particles and particles-

siRNA complexes were incubated with cells at particles-to-cell ratio 50, 200 and 1000, to reflect conditions used in later experiments in infected culture. In all tested conditions, no significant difference in cell viability in treated and untreated samples controls was observed (**Figure 3.6**). The capacity of proposed carriers to deliver siRNA inside the cells was further tested by confocal microscopy. Results showed an efficient cellular uptake after 24 hours incubation, as confirmed by the presence of labelled structures inside the cells (**Figure 3.7**).

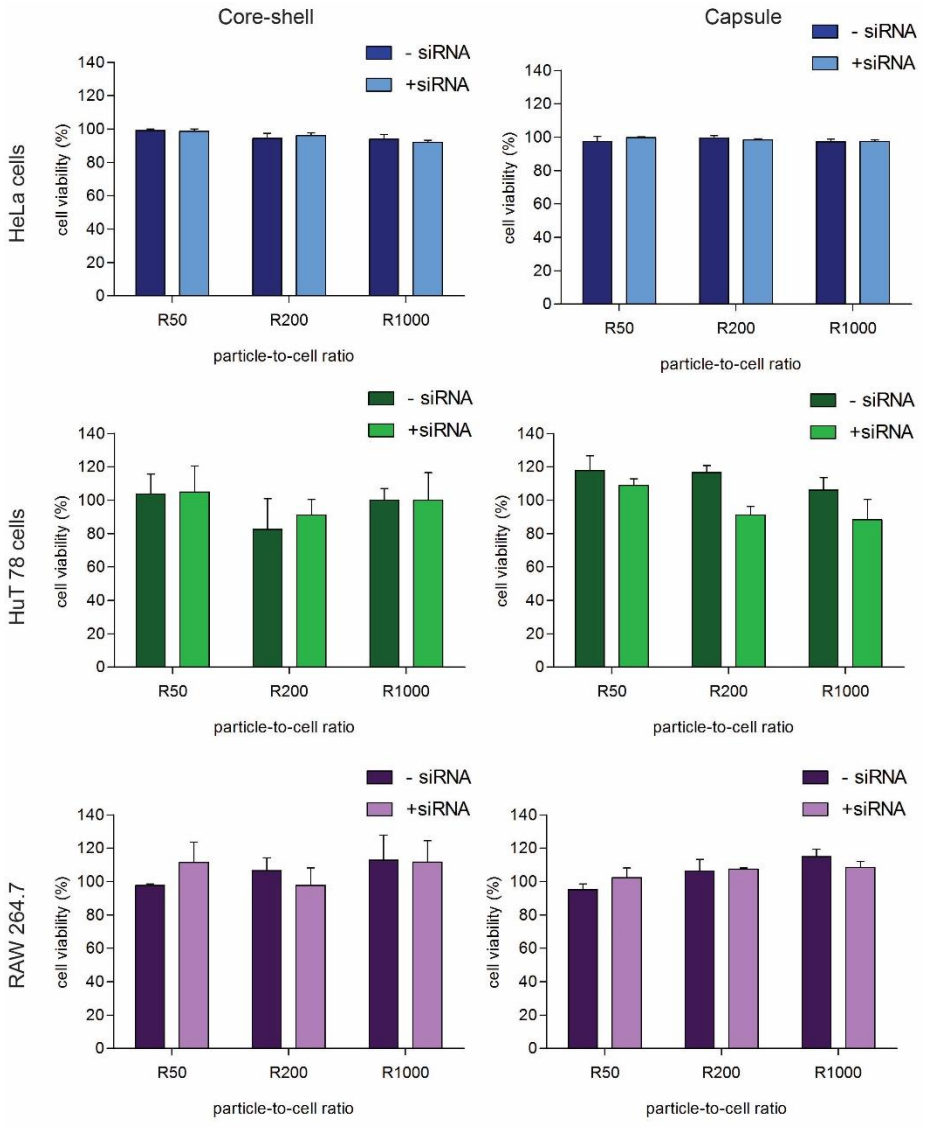

Figure 3.6. Particles cytotoxicity in non-infected cells. Cell viability following 24 h incubation with LbL core-shell particles and capsules with or without siRNA at varying particle-to-cell ratio. Viability in samples was expressed as % of untreated cell control. Data are shown as average mean with standard deviation (n = 3).

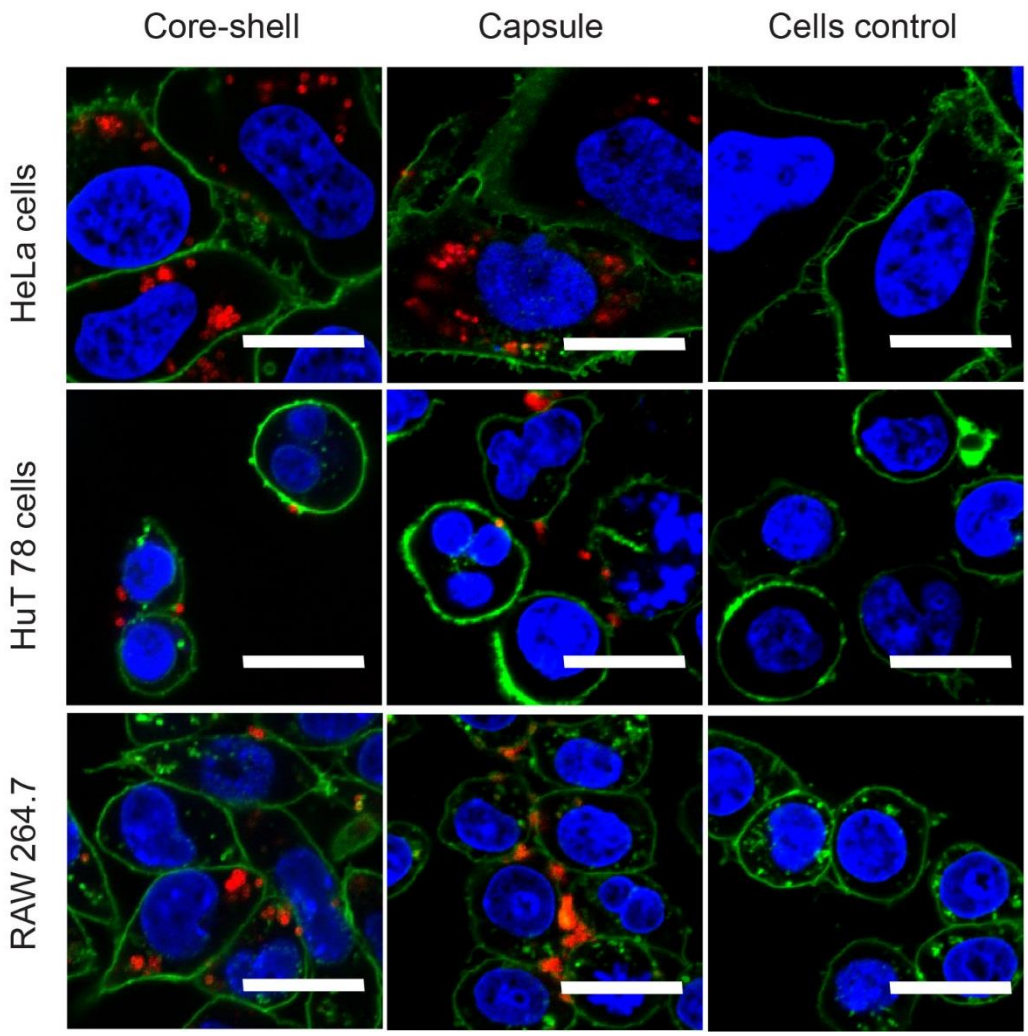

Figure 3.7. Particles internalization and siRNA delivery in non-infected cells. AF_{647}-siRNA (red) was complexed by PLArg-terminated core-shell particles (left) or capsules (middle) and incubated with Hela, HuT 78 or RAW264.7 cells for 24 hours. Images were acquired by confocal microscopy. Nuclei were stained with Hoechst (blue) and cell membranes were stained with Wheat Germ Agglutinin (green). *Scale bars are* 20 μm.

3.4.5. Luciferase gene knockdown

To test the ability of the particles to deliver siRNA, particle-mediated gene silencing *via* PTGS was first evaluated in luciferase-expressing HEK293T cells using siRNA against luciferase. The read-out (luminescence) was carried out on a plate reader, where decreased luminescence can be recorded as a result of the successful delivery of firefly luciferase silencer

siRNA. The luciferase downregulation results presented in **Figure 3.8** were obtained 48 h post-transfection, for two different incubation times with particles or capsules (6 and 24 h, respectively), and in comparison, with the standard transfection agent Lipofectamine. The difference in luciferase downregulation efficiency for core-shell particles and capsules can be explained presumably by a longer time needed for the latter to be internalised. Nevertheless, as measured 48 post-transfection siRNA delivered by core-shell particles induced 50% gene knockdown (**Figure 3.8A**) when particles were incubated with cells for 6 h, and the capsule-delivered siRNA induced 40% gene downregulation (**Figure 3.8B**) when capsules were incubated with cells for 24 h.

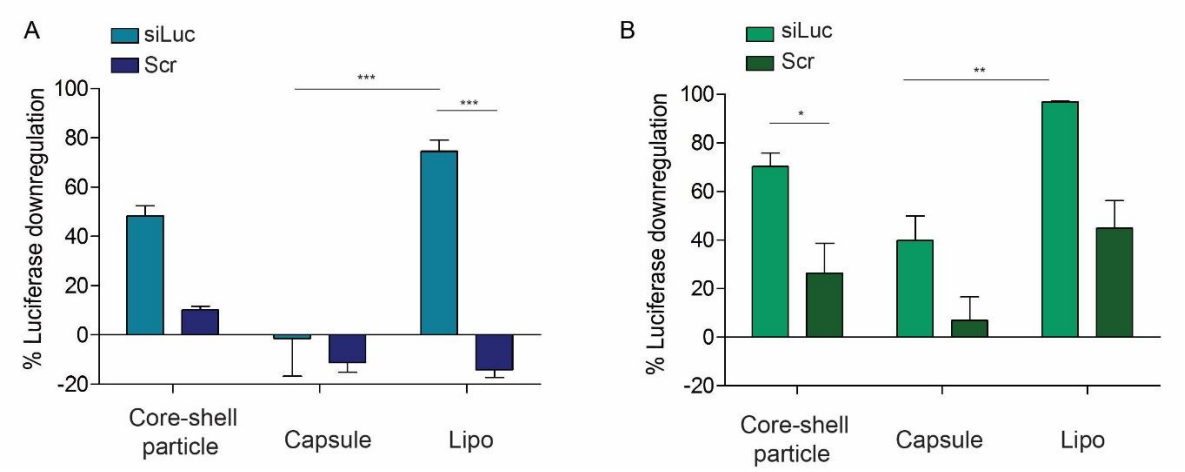

Figure 3.8. Luciferase gene downregulation in HEK239T-Luc cells. Luciferase gene downregulation measured 48 h post-transfection with siLuc-LbL particles and capsules. Core-shell particles and capsules were incubated with cells for 6 h (A) or 24 h (B), followed by medium change and further incubation in cell culture condition. Samples were collected for analysis 48 h after particles/capsules addition. Downregulation of luciferase in samples was expressed as % of luciferase expression in untreated cell control. Lipo: cells treated with siRNA/Lipofectamine. Data are shown as the average mean ± standard error of the mean (n = 3). Statistical analyses were performed using one way-ANOVA with Tukey's multiple comparison test. ***$p < 0.001$

It should be noted that extended incubation time resulted in a greater luciferase knockdown following treatment with Scr siRNA, for core-shell particles and Lipofectamine. Nevertheless, these results demonstrate knockdown of genes *via* the PTGS pathway using PLArg-containing

LbL particles. Importantly, they serve as an indication that the siRNA is being released inside the cells, which warrants their use in epigenetic silencing *via* the TGS pathway.

3.4.6. Epigenetic silencing in HIV cell models

The following studies, using PLArg-terminated capsules to deliver PromA siRNA in HIV-infected cells, were carried out in collaboration with researchers from the Kirby Institute, UNSW. The aim of the delivery of epigenetic silencing-inducing siRNA to cell models of HIV infection is to induce and maintain a latency-like state, and therefore decrease viral activity in infected cells. The siRNA sequence used in this study (PromA) targets NF-κB motifs in the 5' LTR region of the integrated viral genome. To establish a model of infection, VSV-G pseudotyped HIV expressing mOrange (pseudovirus) was used. The pseudovirus-infected cells were used to assess nuclear localization and viral suppression in HeLa T4, primary CD4 T cells and primary macrophages.

The first cell model used was HeLa T4, i.e. HeLa cells modified to express the CD4 receptor, which is present in most cells susceptible to HIV infection and is used by the virus in the first step of cellular entry. Therefore, HeLa T4 is a relatively accessible and easy model in preliminary studies of PromA delivery, as it warrants a high level of infection and as presented in the previous section, non-infected HeLa cells efficiently internalize capsule-siRNA complexes.

Imaging analysis of the cells by deconvolution microscopy following incubation with particle-siRNA complexes allowed the detection of the fluorescence of AF_{647}-siRNA in the nucleus of infected (mOrange-positive) cells (**Figure 3.9A**). Among the analyzed cells, no PromA was found in the nuclei of uninfected cells, and no scramble control (Scr) was found in nuclei of infected/uninfected cells, which is consistent with previous studies that studied the target specificity of promA siRNA.

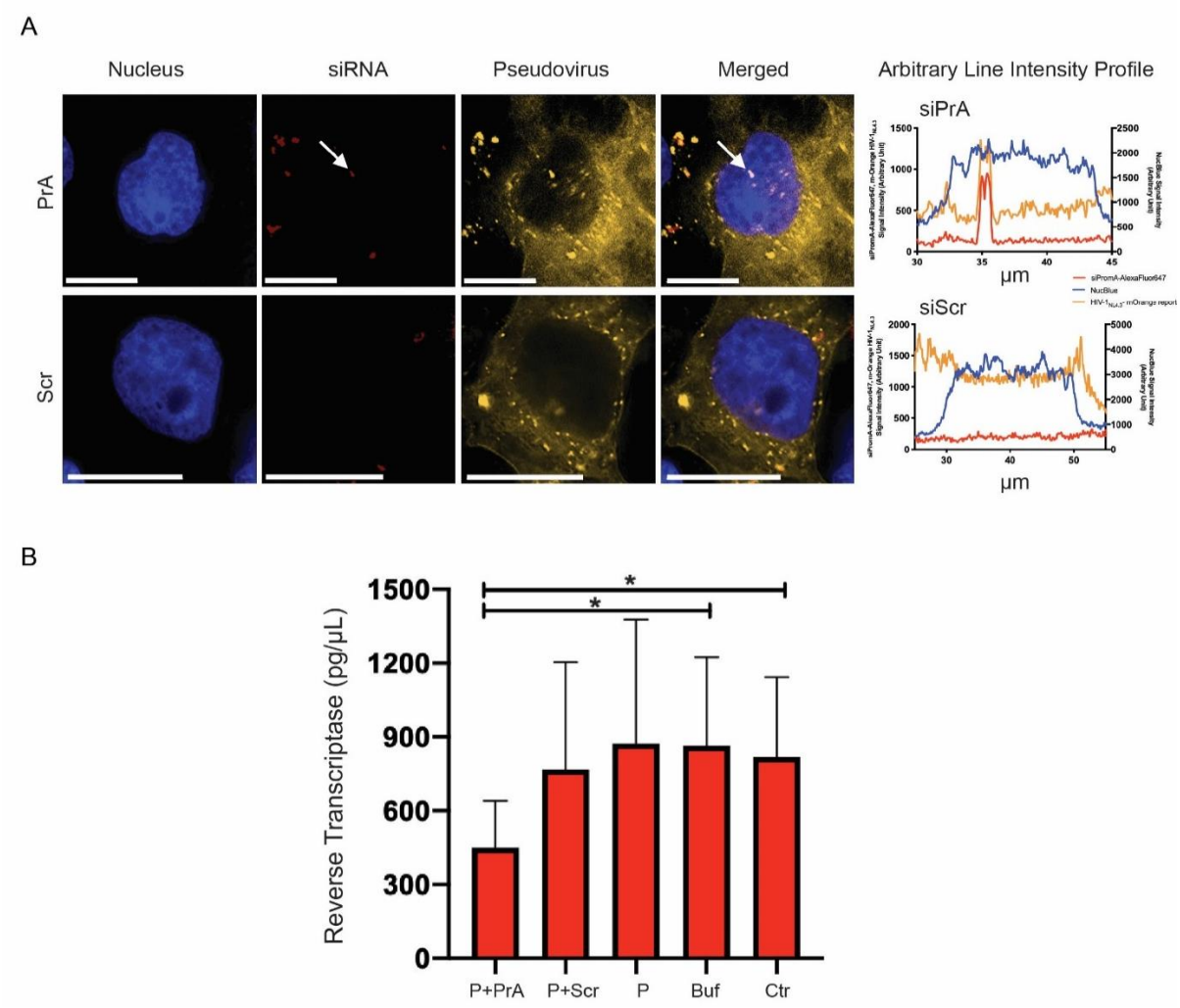

Figure 3.9. Nuclear delivery of PromA and epigenetic silencing in infected HeLa T4 cells. Cells were infected with VSV-G envelope pseudotyped, m-Orange expressing HIV-$1_{NL4.3-\Delta env}$ (A) or HIV-1_{SF162} for RT-Assay (B). AF_{647}-PromA was complexed with LbL capsules and used to transfect cells. Images were acquired following 2 days incubation with particles. Imaging panel shows nuclear (PromA) or cytosolic (Scr) location of delivered siRNA. (B). Viral suppression 20 days post-transfection with siRNA/capsules complexes was measured by RT assay. *Scale bars are 25 µm.* Data are shown as the average mean ± standard error of the mean (n = 4). Statistical analyses were performed using unpaired t-test with Welch's correction. *p < 0.03

As PromA has been identified as a sequence specific to the HIV 5' LTR promoter region, such observation can be explained by the absence of target sequence in the nucleus of the non-infected cell, i.e., lack of integrated HIV genome to which PromA would bind. However, recent results suggest that epigenetic silencing of HIV is an active process occurring *via* RITS complex (including genome-targeting PromA and Ago 1), specific to and triggered only in infected cells, hence explaining the presence of PromA only in the nucleus of infected cells. To confirm the functional effect of the delivered siRNA sequence, an assay measuring the activity of reverse transcriptase (RT) enzyme, indicative of the progression of infection, was carried out. The level of RT in the cells treated by the capsules-PromA was compared with the level of the enzyme in the mock control, i.e. infected cells. Particle-mediated PromA delivery resulted in a ~2-fold decrease in viral infection level (**Figure 9B**). In addition, various controls including non-specific siRNA sequence (Scr), cells treated with capsules only and cells treated with DPBS buffer also showed levels of infection comparable to the mock control. These results indicate that LbL capsules facilitate the intracellular delivery of PromA, which is released into the cytosol and translocated into the nucleus presumably by the disassembly of multilayered film inside the cells. Importantly, HIV silencing was observed only in infected cells to which siRNA sequence specific to HIV 5' LTR was delivered, suggesting that the mechanism involved is specific to HIV infection. Particle-mediated PromA delivery significantly slowed down the progression of infection up to 16 days post-treatment.

Virus suppression was then examined in primary CD4 T cells. Primary cells as a drug delivery model are much more challenging, as they have been experimentally shown to be less responsive to transfection methods utilized in other cell types.[47] It can be hypothesized that this is due to a different structure and composition of receptors on the cell membrane, high nucleus-to-cytoplasm ratio, and reduced activity of certain endocytosis pathways.[48] Nevertheless, this is the type of cells most at risk of being infected with HIV *in vivo* and therefore the use of capsules to deliver PromA in such cell model would allow for a more advanced assessment of its therapeutic effect. Here, infected primary T cells were incubated with capsules complexed with PromA for 48 h. Microscopic analysis showed the nuclear localization of capsule-delivered PromA in nuclei of infected cells (**Figure 3.10A**).

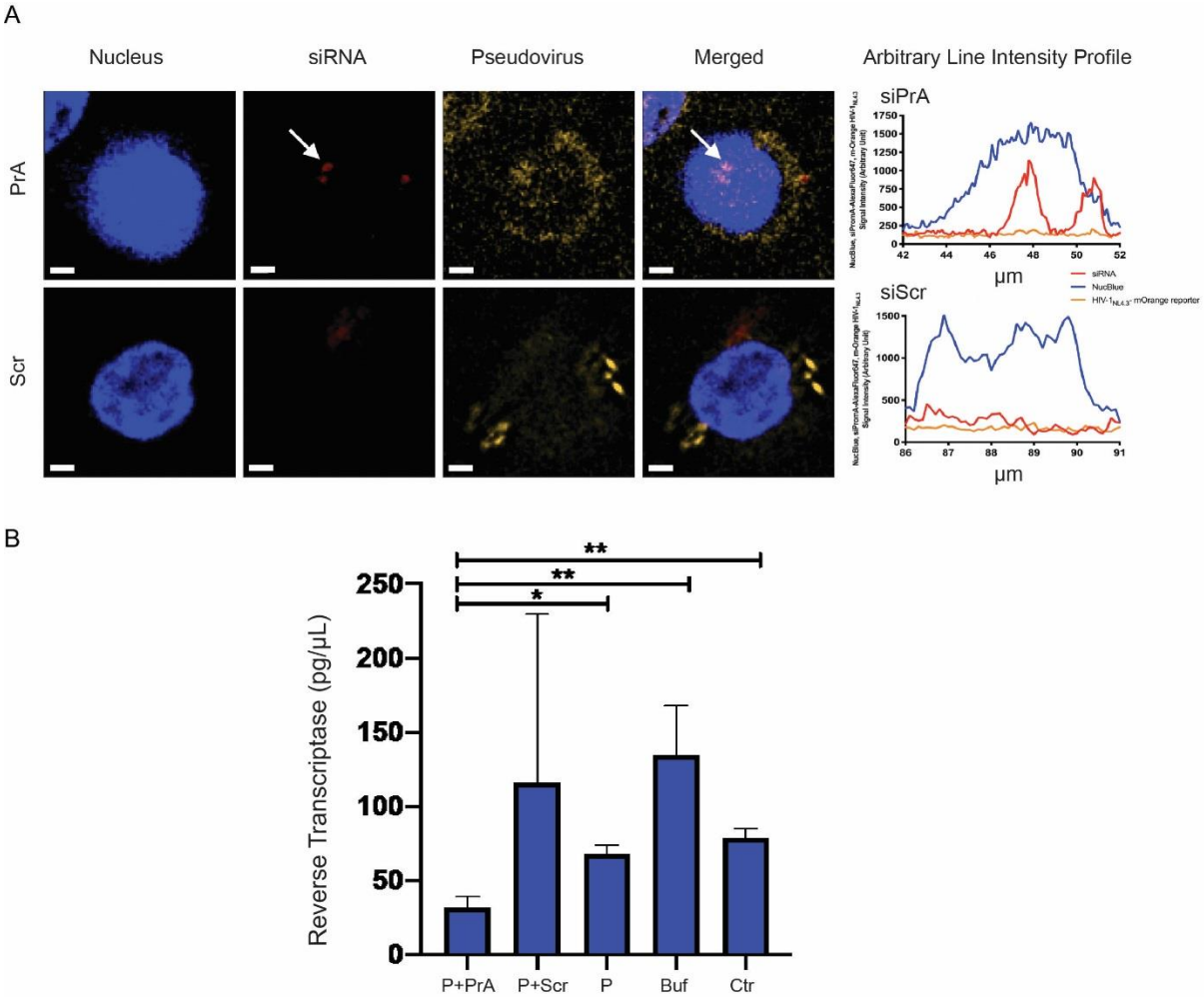

Figure 3.10. Nuclear delivery of PromA and epigenetic silencing in infected activated primary CD4 T cells. Cells were infected with VSV-G envelope pseudotyped, m-Orange expressing HIV-$1_{NL4.3\text{-}\Delta env}$ (A) or HIV-$1_{NL4.3}$ for RT-Assay (B). AF_{647}-PromA was complexed with LbL capsules and used to transfect cells. Images were acquired following 2 days incubation with particles. Imaging panel shows nuclear (PromA) or cytosolic (Scr) location of delivered siRNA. (B). Viral suppression 16 days post-transfection with siRNA/capsules complexes was measured by RT assay. *Scale bars are 1 µm.* Data are shown as the average mean ± standard error of the mean (n = 4). Statistical analyses were performed using unpaired t-test with Welch's correction. **p < 0.003

However, no 'nuclear events' for Scr sequence or uninfected cells were found. Viral suppression was assessed by RT assay. It should be noted that the level of infection in CD4 T cells mock control was ~10 times lower than in the HeLa cells, due to a less efficient pseudovirus-infection in primary cells. Nevertheless, PromA delivery resulted in ~2-fold

decrease of viral load, as indicated by a reduced level of viral enzyme in the cell culture supernatant following 16 days incubation with PromA/capsule complexes (**Figure 3.10B**).

The ultimate goal of the HIV therapy *via* epigenetic silencing is to deliver siRNA to the nucleus of primary resting CD4 T cells, which harbour latent infection, i.e., carry an integrated HIV fragment, but does not produce active virions. Although such cells occur in a very low abundance, they enable viral reactivation and rebound after cessation of ART. It is the most challenging cell model used in this study, as in addition to transfection difficulties mentioned for activated CD4 T cells, resting cells are also non-dividing and therefore expected to show reduced metabolic activity and particle uptake. It is not possible to perform a functional assay in resting cells as there is no active transcription, however, the microscopic analysis allowed the identification of PromA in the nuclei of cells infected with GFP-expressing virus, as shown in **Figure 3.11**.

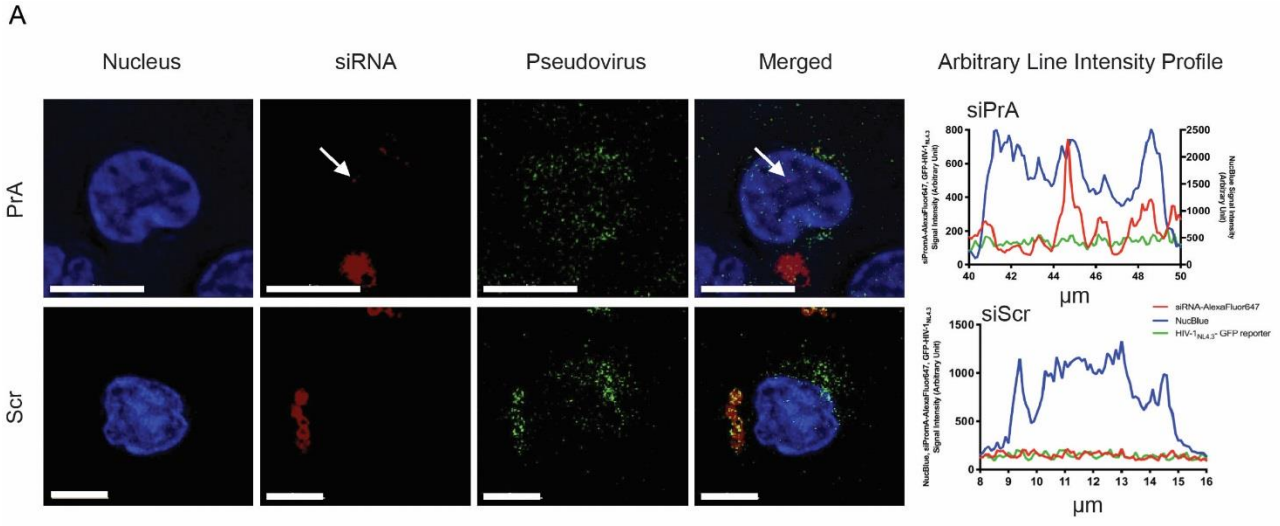

Figure 3.11. Nuclear delivery of PromA in infected primary resting CD4 T cells. Cells were infected with HIV-$1_{NL4.3\text{-}IRESGFP}$. AF_{647}-PromA was complexed with LbL capsules and used to transfect cells. Images were acquired following 2 days incubation with particles. AF_{647}-Scr complexed with LbL capsules were used as controls. The imaging panel shows nuclear (PromA) or cytosolic (Scr) location of delivered siRNA. *Scale bars are 1 μm.*

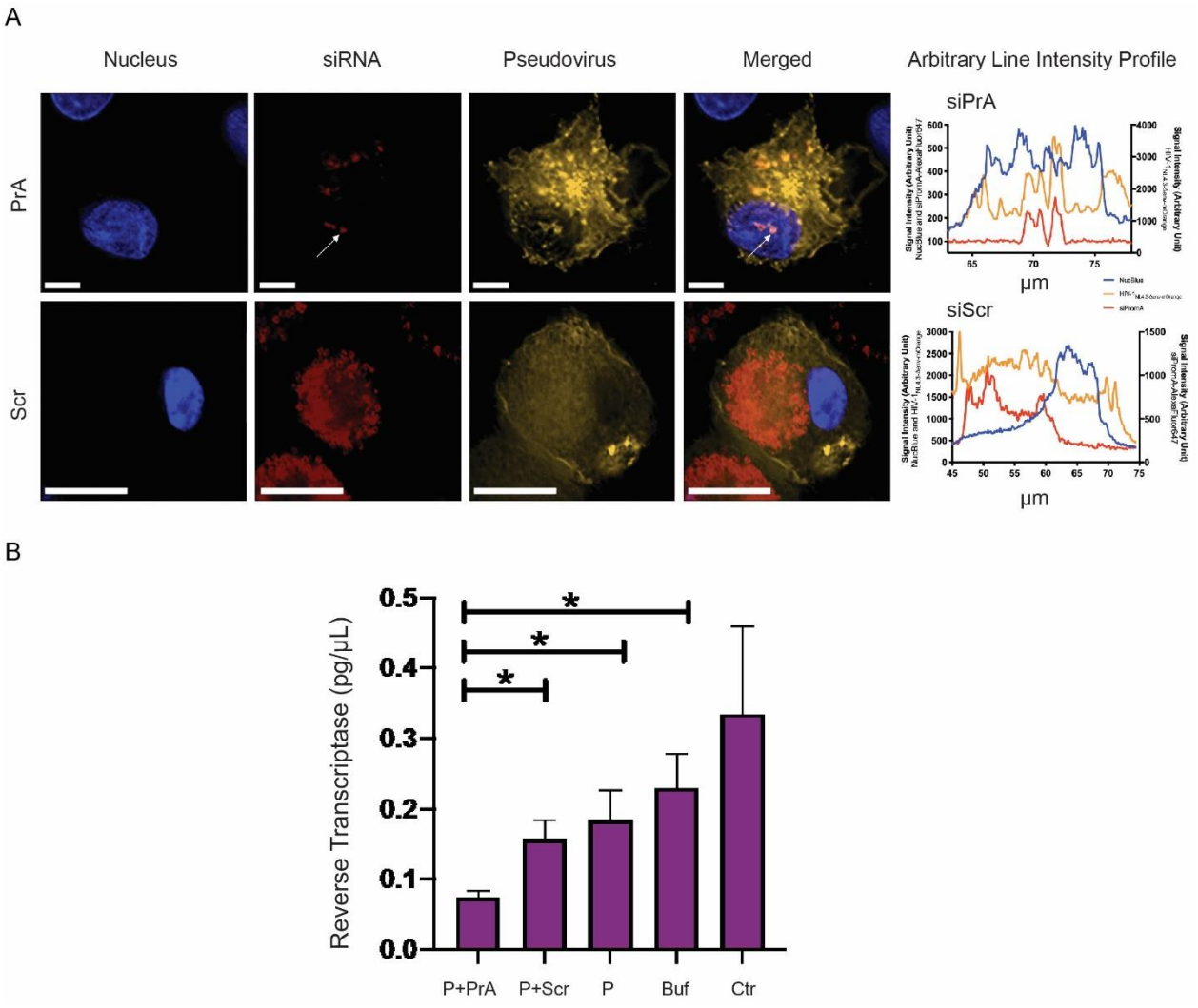

Figure 3.12. Nuclear delivery of PromA and epigenetic silencing in HIV-infected activated primary macrophages. Cells were infected with VSV-G envelope pseudotyped, m-Orange expressing HIV-$1_{NL4.3\text{-}\Delta env}$ (A) or HIV-$1_{BalI\text{-}NL4}$ for RT-Assay (B). AF_{647}-PromA was complexed with LbL capsules and used to transfect cells. Images were acquired following 2 days incubation with particles. Imaging panel shows nuclear (PromA) or cytosolic (Scr) location of delivered siRNA. (B). Viral suppression 16 days post-transfection with siRNA/capsules complexes was measured by RT assay. *Scale bars are 5 µm (A) and 15 µm (B).* Data are shown as the average mean ± standard error of the mean (n = 4). Statistical analyses were performed using unpaired t-test with Welch's correction. *$p < 0.036$

The other HIV infection cell model used was the primary monocytes-derived macrophages. Although the population of infected macrophages *in vivo* is low compared to CD4 T cells, they play a significant role in the progression of the infection. Macrophages can survive long after

infection (especially long-lived macrophages) and pass the virus to lymphocytes in lymph nodes.[49] Macrophages are also the main HIV target in the central nervous system. As with HeLa and activated CD4 T cells, the PromA delivery *via* LbL capsules was analyzed in two ways, using i) imaging techniques to assess nuclear delivery of PromA and ii) functional assay to assess virus suppression. PromA was found in the nuclei of infected cells, while Scr control was present in the cytosolic compartment of cells (**Figure 3.12 A**). Contrary to primary T cells, high capsules internalization was expected in macrophages as it is the cell population involved in particles clearance *in vivo*. The functional assay confirmed a reduced infection level following treatment with PromA/capsules complexes. These results indicate that the proposed polyarginine-containing particle offers versatility to deliver epigenetic silencing-inducing siRNA to various cell types.

3.4.7. Particles engineering using virus-like particles

Engineering of particles often includes the coating of ligands/antibodies on particles to obtain enhanced binding to target cells based on the expression of specific proteins on the cell surface.[50] To address HIV infection in CD4 T cells, a targeting strategy needs to overcome challenges associated with an inefficient internalization of the CD4 receptor as the main marker of cell susceptible to infection. While studies are underway to identify novel targeting receptors, the present section will describe particle engineering by introducing a virus functionality on the particle surface. Virus-like particles (VLPs) are protein cages derived from the virus that retain much of the original virus characteristic, including the mechanism of virus-cell interactions, but without the genetic material responsible for the infection.[51] VLPs are emerging as a new class of transfection vectors, however, herein they have been used to modify particles to enhance cellular uptake *via* receptors used by HIV, namely CD4 and CCR5/CXCR4 receptors. A similar design was presented by Fischlechner et al., where rubella-like particles were used to fuse with phosphatidylserine-terminated LbL particles, resulting in enhanced cell binding, induction of endocytosis and fusion into the late endosome membrane.[52]

Poly-arginine terminated capsules were coated with VLPs originated from dualtropic HIV strain (using CD4 and CCR5 receptor to enter the cell). The incubation of capsules with VLP and siRNA resulted in a decrease of particles surface charge to -9 ±1 mV (compared to 49 ± 5 mV for uncoated capsules), and the morphology of capsules and VLP-coated capsules was studied *via* confocal microscopy and TEM (**Figure 3.13**). The observed increase in capsule

thickness following incubation with VLP suggests a formation of VLP coating on capsule surface.

Importantly, *in vitro* experiments showed enhanced binding of VLP-coated siRNA/LbL capsules to CD4/CCR5-expressing TZM-bl cells (at 4ºC and 37ºC) compared with CD4/CCR5-negative Hela cells (**Figure 3.14**). These preliminary results show great potential in the use of viral coatings, including HIV-like coating, to fabricate particles with desirable surface properties to overcome barriers to T cell entry and facilitate drug delivery to resting T cells.

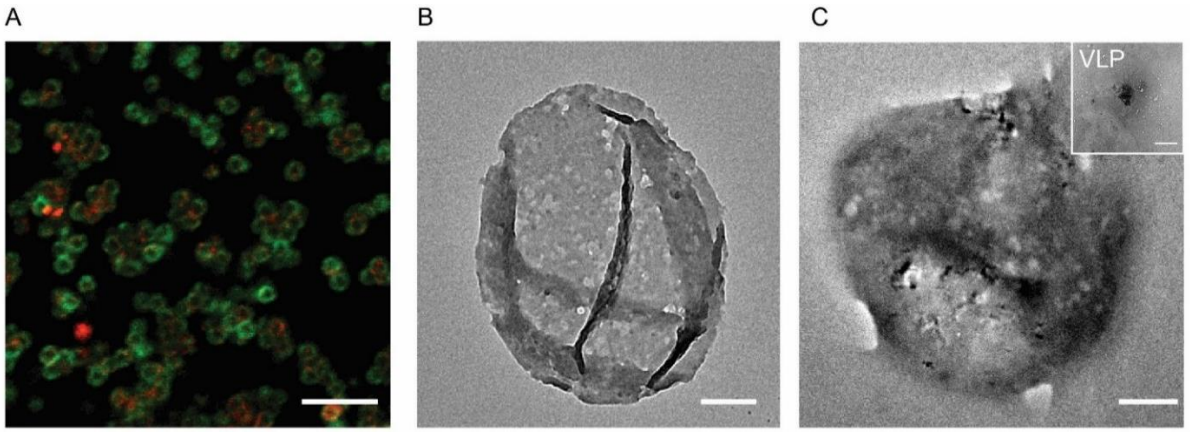

Figure 3.13. Preparation of VLP-coated capsules. (A) Confocal microscopy images of AF_{488}-LbL capsules complexed with mOrange-VLP. TEM images of capsules (B) and VLP-coated capsules (C). *Scale bars are 5 μm (A) and 200 nm (B and C).*

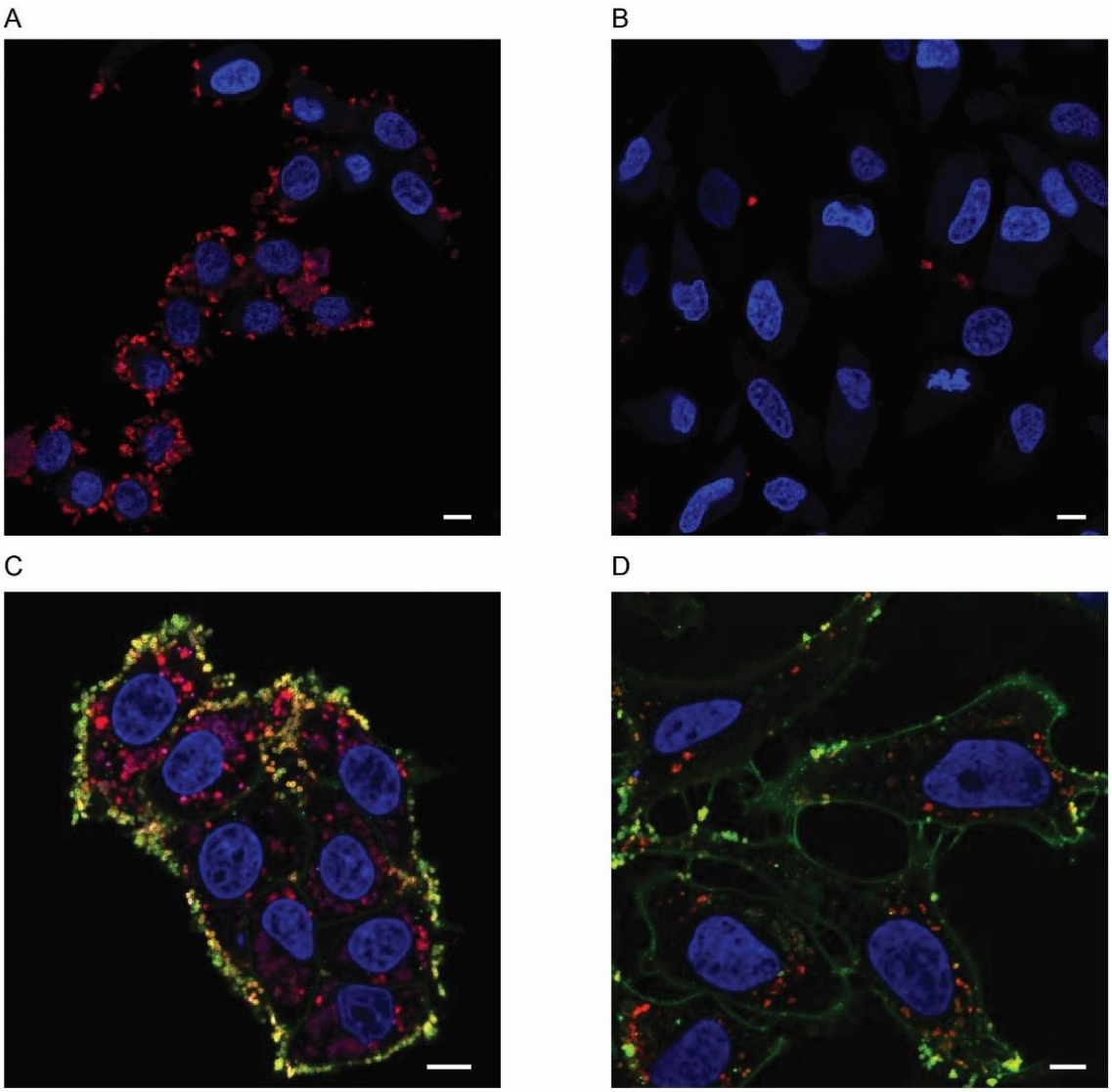

Figure 3.14. Particles targeted to CD4 and CCR5 receptors using VLPs. Confocal microscopy images showing VLP-coated siRNA/particles complexes binding to TZM-bl (A) and HeLa (B) cells following 1 h incubation on ice. Particles internalization in TZM-bl (C) and HeLa (D) cells following 24 h incubation with VLP-coated siRNA/particles complexes at 37ºC. siRNA was labelled with AF_{647} (red), cell membranes were stained with wheat germ agglutinin (green), VLPs were labelled with mOrange (purple) and nuclei were stained with Hoechst (blue). *Scale bars are 10 μm.*

3.5. Conclusions

In summary, this chapter demonstrates the use of polyarginine-containing LbL particles to deliver siRNA and induce luciferase gene silencing *via* PTGS as demonstrated in HEK239-Luc cells. The formulated siRNA/particles system was applied to deliver epigenetic silencing siRNA targeting the HIV 5' LTR promoter region to the nucleus of infected cell lines and primary cells. Treatment resulted in significant viral activity suppression in primary CD4 T cells and monocyte-derived macrophages up to 16 days post-transfection. It also demonstrated the delivery of HIV-targeting siRNA to primary resting CD4 T cells, which is a model of latently-infected cells which remains a major obstacle to eradicating viral infection *in vivo*. Particle engineering *via* VLP-coating introduced a virus-like functionality on the particle surface for enhanced binding and uptake by TZM-bl cells. This demonstrates a targeting strategy utilizing co-receptors used by HIV, therefore providing a tool to overcome entry restrictions in resting cells.

3.6. References

1. R. W. Eisinger and A. S. Faucci, *Emerg. Infect. Dis.*, 2018, **24**, 413-416.
2. J. K. Wong and S. A. Yukl, *Curr. Opin. HIV AIDS*, 2016, **11**, 362-370.
3. C. Pasquier, M. Walschaerts, S. Raymond, N. Moinard, K. Saune, M. Daudin, J. Izopet and L. Bujan, *Basic Clin. Androl.*, 2017, **27**, 17.
4. T. W. Chun, J. S. Justement, D. Murray, C. W. Hallahan, J. Maenza, A. C. Collier, P. M. Sheth, R. Kaul, M. Ostrowski, S. Moir, C. Kovacs and A. S. Fauci, *AIDS*, 2010, **24**, 2803-2808.
5. J. T. Kimata, A. P. Rice and J. Wang, *Curr. Opin. Immunol.*, 2016, **42**, 65-70.
6. E. Hamlyn, F. M. Ewings, K. Porter, D. A. Cooper, G. Tambussi, M. Schechter, C. Pedersen, J. F. Okulicz, M. McClure, A. Babiker, J. Weber, S. Fidler, S. Insight and S. Investigators, *PLoS One*, 2012, **7**, e43754.
7. N. A. Kumar, K. Cheong, D. R. Powell, C. da Fonseca Pereira, J. Anderson, V. A. Evans, S. R. Lewin and P. U. Cameron, *Retrovirology*, 2015, **12**, 76.
8. K. V. Morris, *Biotechniques*, 2006, Suppl, 7-13.
9. M. L. Bobbin, J. C. Burnett and J. J. Rossi, *Genome Med.*, 2015, **7**, 50.
10. R. J. Scarborough and A. Gatignol, *Viruses*, 2017, **10**, E8.
11. M. E. Abram, A. L. Ferris, K. Das, O. Quinones, W. Shao, S. Tuske, W. G. Alvord, E. Arnold and S. H. Hughes, *J. Virol.*, 2014, **88**, 7589-7601.
12. A. Kwarteng, S. T. Ahuno and G. Kwakye-Nuako, *AIDS Res. Ther.*, 2017, **14**, 32.
13. K. Suzuki, S. Hattori, K. Marks, C. Ahlenstiel, Y. Maeda, T. Ishida, M. Millington, M. Boyd, G. Symonds, D. A. Cooper, S. Okada and A. D. Kelleher, *Mol. Ther. Nucleic Acids*, 2013, **2**, e137.
14. C. Mendez, C. L. Ahlenstiel and A. D. Kelleher, *World J. Virol.*, 2015, **4**, 219-244.
15. C. Ahlenstiel, C. Mendez, S. T. Lim, K. Marks, S. Turville, D. A. Cooper, A. D. Kelleher and K. Suzuki, *Mol. Ther. Nucleic Acids*, 2015, **4**, e261.
16. C. Mendez, S. Ledger, K. Petoumenos, C. Ahlenstiel and A. D. Kelleher, *Retrovirology*, 2018, **15**, 67.
17. K. Lundstrom, *Diseases*, 2018, **6**, E42.
18. R. S. Tomar, H. Matta and P. M. Chaudhary, *Oncogene*, 2003, **22**, 5712-5715.
19. R. Goswami, G. Subramanian, L. Silayeva, I. Newkirk, D. Doctor, K. Chawla, S. Chattopadhyay, D. Chandra, N. Chilukuri and V. Betapudi, *Front. Oncol.*, 2019, **9**, 297.

20. C. E. Thomas, A. Ehrhardt and M. A. Kay, *Nat. Rev. Genet.*, 2003, **4**, 346-358.
21. R. Alemany, C. Balague and D. T. Curiel, *Nat. Biotechnol.*, 2000, **18**, 723-727.
22. M. E. Olszko and G. D. Trobridge, *Viruses*, 2013, **5**, 2585-2600.
23. B. Berkhout, H. C. J Ertl and M. S. Weinberg, *Gene Therapy for HIV and Chronic Infections*, Springer, New York, NY, 2015.
24. D. Stone, H. P. Kiem and K. R. Jerome, *Curr. Opin. HIV AIDS*, 2013, **8**, 217-223.
25. Z. Cao, H. Xiao, L. Li, M. Liu, G. Lin, P. Zhai, K. T. Yong, X. Wang and G. Xu, *Front. Pharmacol.*, 2019, **10**, 1194.
26. Y. Sato, H. Matsui, R. Sato and H. Harashima, *J. Control. Release*, 2018, **284**, 179-187.
27. O. M. Merkel, A. Beyerle, D. Librizzi, A. Pfestroff, T. M. Behr, B. Sproat, P. J. Barth and T. Kissel, *Mol. Pharm.*, 2009, **6**, 1246-1260.
28. A. Kulkarni, K. DeFrees, S. H. Hyun and D. H. Thompson, *J. Am. Chem. Soc.*, 2012, **134**, 7596-7599.
29. S. K. Lee, M. S. Han, S. Asokan and C. H. Tung, *Small*, 2011, **7**, 364-370.
30. M. Zhang, R. Xu, X. Xia, Y. Yang, J. Gu, G. Qin, X. Liu, M. Ferrari and H. Shen, *Biomaterials*, 2014, **35**, 423-431.
31. G. Lin, T. Chen, J. Zou, Y. Wang, X. Wang, J. Li, Q. Huang, Z. Fu, Y. Zhao, M. C. Lin, G. Xu and K. T. Yong, *Front. Pharmacol.*, 2017, **8**, 182.
32. G. Sauerbrey, Z. Phys., 1959, **155**, 206.
33. K. Suzuki, B. P. Craddock, T. Kano and R. T. Steigbigel, *J. Virol. Methods*, 1993, **41**, 21-28.
34. A. C. Grayson, A. M. Doody and D. Putnam, *Pharm. Res.*, 2006, **23**, 1868-1876.
35. A. Babu, R. Muralidharan, N. Amreddy, M. Mehta, A. Munshi and R. Ramesh, *IEEE Trans. Nanobioscience.*, 2016, **15**, 849-863.
36. M. S. Draz, B. A. Fang, P. Zhang, Z. Hu, S. Gu, K. C. Weng, J. W. Gray and F. F. Chen, *Theranostics*, 2014, **4**, 872-892.
37. Y. Yan, M. Bjornmalm and F. Caruso, *Chem. Mater.*, 2014, **26**, 452-460.
38. E. P. Holowka, V. Z. Sun, D. T. Kamei and T. J. Deming, *Nat. Mater.*, 2007, **6**, 52-57.
39. Y. H. Wang, Y. W. Hou and H. J. Lee, *J. Biochem. Biophys. Methods*, 2007, **70**, 579-586.
40. I. Nakase, K. Noguchi, A. Aoki, T. Takatani-Nakase, I. Fujii and S. Futaki, *Sci. Rep.*, 2017, **7**, 1991.
41. A. D. Frankel and C. O. Pabo, *Cell*, 1988, **55**, 1189-1193.

42. J. Temsamani and P. Vidal, *Drug Discov. Today*, 2004, **9**, 1012-1019.
43. J. B. Rothbard, E. Kreider, C. L. VanDeusen, L. Wright, B. L. Wylie and P. A. Wender, *J. Med. Chem.*, 2002, **45**, 3612-3618.
44. A. D. Ragin, R. A. Morgan and J. Chmielewski, *Chem. Biol.*, 2002, **8**, 943-948.
45. C. Schuler and F. Caruso, *Biomacromolecules*, 2001, **2**, 921-926.
46. P. Rivera-Gil, S. De Koker, B. G. De Geest and W. J. Parak, *Nano Lett.*, 2009, **9**, 4398-4402.
47. J. L. Hartley, *Protein Expression in Mammalian Cells*, Humana Press, New York, NY, 2012.
48. L. Bracq, M. Xie, S. Benichou and J. Bouchet, *Front. Immunol.*, 2018, **9**, 260.
49. M. Arruebo, M. Valladares and Á. González-Fernández, *J. Nanomater.*, 2009, **2009**, 1-24.
50. M. J. Rohovie, M. Nagasawa and J. R. Swartz, *Bioeng. Transl. Med.*, 2017, **2**, 43-57.
51. M. Fischlechner, L. Toellner, P. Messner, R. Grabherr and E. Donath, *Angew. Chem. Int. Ed. Engl.*, 2006, **45**, 784-789.

Chapter 4

Effect of cell properties on bio-nano interactions: particle-cell interactions in activated and virus-infected cells

4.1. Abstract

Engineering more effective drug delivery systems require a comprehensive understanding of particle-cell interactions, which greatly relies on the physicochemical properties of the carrier. Treatment of cells with nanomaterials are likely to induce a physiological response, which depends on the cell and material type. Significant advances have been made to understand how cellular function changes upon interactions with various particle types. Contrary, in the present chapter the effect of cell properties, i.e., cell activation and viral infection, on cell-particle interactions was investigated. Studies were carried out using primary cells, pseudovirus-infected T cells and HIV latency cell line model. Four types of particles with distinct physicochemical properties were used (polyarginine-containing LbL silica particles, polyethylene glycol mesoporous/hydrogel particles and amine-functionalised bovine glycogen). Among the tested formulations, PEG particles with a mesoporous template showed increased association with the investigated activation/infection cell models and internalization of particles was observed in pseudovirus-infected cells. The work described in this chapter highlights that the state of the cell can strongly influence particle internalization and that understanding cell properties can guide in the design of nanomedicines, particularly when targeting immune cells.

4.2. Introduction

Nanomedicine offers the possibility of delivering various drugs to cells, enabling an efficient drug loading by engineered nanoparticles, protection from degradation, increased stability and transport across cellular membranes for improved therapeutic outcomes.[1,2,3] Particle cellular uptake occurs mainly *via* an energy-dependent pathway, including macropinocytosis, clathrin-dependent and caveolae-dependent endocytosis.[4] Studies indicate that efficient uptake greatly depends on particle physicochemical properties, such as size, surface chemistry and composition.[5,6] Particle-cell interaction can be also affected by sedimentation rate *in vitro*, particularly for heavier nanoformulations.[7] More recent reports have focused on bio-nano interactions of newly engineered particles with components of the extracellular matrix (ECM) in 3D cell models.[8,9] In addition, various cellular responses upon exposure of immune cells to nanomaterials have been reported.[10,11] These results suggest that treatment of cells with nanomaterials often results in a complex physiological response, which depends on both material and cell type.

Engineering new and effective drug delivery systems require a comprehensive understanding of particle-cell interactions and should not be limited to studying only the effect of particles on cellular function. Instead, the physiological state of the cell and its implication on cell-particle interactions should also be considered. For example, it has been reported that estimation of particle cellular uptake could not be fully accurate without considering a 'particle dilution' factor due to cell division,[12] and particle accumulation in cells varies depending on the phase of the cell cycle.[13] Similarly, a question arises how the same cell subtypes in different physiological state interact with nanomaterials.

Activation of immune cells is not solely a result of contact with nanoparticles but is a naturally occurring physiological state of cells enabling proper functioning of the immune system.[14] Cell activation is associated with various changes, including altered expression of surface receptors, cytokines secretion and DNA changes.[15,16] Researchers studying immune responses often use chemical agents (phorbol 12-myristate 13-acetate (PMA)), antibodies or cell co-culture in attempts to mimic activation to elucidate the complex cellular response exhibited by different cell populations.[17,18,19] During activation *in vitro*, the induced changes will differ depending on the stimulant and cell used, but it generally involves activation of specific signalling pathways and changes in protein expression, e.g. expression of surface markers typical for a given group of cells. In the drug delivery field,

similar to the discovery of cell cycle-dependent particle uptake, such alterations in cellular metabolism may have significant implications in bio-nano interactions and can guide nanoparticle engineering. One of the cell subtypes involved in the adaptive immune system is CD4 positive (CD4+) T cells.[20] It is also a major cell population susceptible to HIV infection[21] and as such, introducing CD4-targeting moieties on particle surface could seemingly be a valid approach to achieve enhanced association with HIV-infected cells. However, in recent years it has been reported that upon cell activation the expression of CD4 receptor is downregulated, hence questioning its suitability to be used for cell targeting.[22]

An accurate understanding of cell physiological state and its implication on particles uptake is especially important in the case of cell models studying human immunodeficiency virus (HIV) infection. In the *in vitro* model used in Chapter 3, human peripheral blood mononuclear cells (PBMCs) are activated by specific antibodies, followed by infection with pseudovirus to introduce an intracellular target to evaluate the efficacy of delivered short interfering RNA (siRNA). It can be expected that the physiology of activated, pseudovirus-infected cell will differ from a resting cell, i.e., untreated cells isolated from blood. HIV entry and infection progression *in vivo* are largely dependent on viral control over actin cytoskeleton of the host.[23] Cell cytoskeleton is involved in various cellular process, including the maintenance of the cell architecture,[24] and is crucial for maintaining healthy cellular functions. It is also an important component involved in particle-cell interaction, as actin reorganization controls cell-cortex remodelling occurring in all energy-dependent pathways involved in particles internalization.[25] Therefore, it can be hypothesized that alteration in the cytoskeleton, due to the ongoing infection, can affect nanoparticle-cell interactions.

To this end, this chapter attempts to answer how activation and the presence of a pseudovirus infection affect cell interaction with nanoparticles. Focused on general activation, rather than the induction of specific pathways during activation, we used PMA/Ionomycin to non-specifically activate human PBMCs. PMA is a protein kinase C activator, inducing cell proliferation and activation of inflammatory pathways.[26] Ionomycin is an ionophore used to stimulate cytokines production.[27] In addition, we tested two T cell lines, i.e. pseudovirus-infected HuT 78 cells as a cell model of infection and JLat cells carrying a fragment of HIV promoter, as a cell model of HIV latency to assess the uptake of particles in reactivated cells. Four types of particles were tested: i) multilayered polyarginine-containing silica particles, used in Chapter 3 to deliver siRNA to HIV infection models; ii) templated mesoporous PEG particles (MS@PEG) and their template-free counterpart PEG hydrogel capsules, that have

shown distinct cell association pattern when tested previously in whole human blood *ex vivo*;[28,29] iii) glycogen nanoparticles, which has been previously used in drug delivery to complex nucleic acids.[30] The selection of these particle systems was dictated by their inherent physicochemical properties that allow for comparison of particle internalization based on size, charge and stiffness, in activated and non-activated cells. Multilayered silica particles provide great versatility in terms of the size range, surface functionalization and rigid spherical structure. MS@PEG particles and PEG hydrogel capsules represent a particle class with low-fouling and stealth properties and allow for comparison between 'hard' and 'soft' systems of similar properties. Glycogen particles are nanometre-sized spherical macromolecules representing 'soft' materials. While the physicochemical properties differ between the different particles types, understanding how these various delivery systems interact with activated and non-activated cells is important for their potential application in HIV therapy and T cell targeting.

4.3. Experimental section

4.3.1. Materials

Silica particles (0.837nm, 387 nm and 235 nm, 5% w/v aqueous solution) and polystyrene particles (Fluorospheres FITC-labelled, 1000 nm, 450 nm, and 288 nm, 5% w/v aqueous solution) were purchased from microParticles GmbH (Berlin, Germany). Poly(ethylenimine) (PEI) low molecular weight 50 wt% solution in water, poly-L-arginine hydrochloride, molecular weight >70000; poly(sodium 4-styrenesulfonate) (PSS) molecular weight ~70000, albumin from bovine serum (BSA), Dulbecco's phosphate buffered saline (DPBS), without calcium chloride or magnesium chloride, agarose, glucose, Hoechst 33342, Ficoll PM400 were purchased from Sigma-Aldrich (St. Louis, MI, USA). Sodium chloride (NaCl) was purchased from Chem-Supply (Gillman, Australia). Alexa Fluor N-hydroxysuccinimide (NHS) dyes (AF647), wheat germ agglutinin (WGA), Alexa Fluor 555 conjugate (WGA-AF555), Hoechst 33342 (10 mg mL−1 solution in water), Nunc Lab-Tek II Chamber microscopy slides were purchased from Thermo Fisher Scientific (Scoresby, Australia). RPMI-1640 medium was purchased from Lonza (Basel, Switzerland). Fetal bovine serum was purchased from Bovogen Biologicals (Keilor East, Australia). Paraformaldehyde 4% aqueous solution (EM grade, 4% PFA) was purchased from Electron Microscopy Sciences. PE anti-human CD19 (#302208),

FITC anti-human CD45 (#304038), Brilliant Violet 510 anti-human CD3 (#344828), Brilliant Violet 785 anti-human CD14 (#301840), Brilliant Violet 785 anti-human CD69 (#310931) were purchased from Biolegend and used at 1:100 dilution. JLat A2 cell line with GFP reporter was obtained from NIH AIDS reagents program. All the reagents for experiments using pseudovirus-infected cells were obtained by Professor Anthony Kelleher's group from Kirby Institute, UNSW.

4.3.2. Particle preparation

LbL Si particles were prepared by layer-by-layer assembly of polystyrene-4-sulfonate and poly-L-arginine on PEI-coated silica template (837 nm). A detailed protocol is described in Chapter X (page x). MS@ PEG and PEG capsules were prepared by Dr Yi Ju (The University of Melbourne) using a previously published protocol.[28] Briefly, 8-arm-PEG-NH_2 with a hexaglycerol core structure was used to infiltrate the pores of 400 nm mesoporous silica (MS) template *via* electrostatic interactions, followed by crosslinking with 8-arm-PEG-succinimidyl carboxyl methyl ester (8-arm-PEG-NHS). PEG capsules, were prepared by subsequent dissolution of the MS template in 2 M HF/8 M NH_4F solution (pH ~5). Bovine liver-derived glycogen nanoparticles functionalized with amines (BG-EDA) were prepared by Agata Glab (The University of Melbourne) using a previously published protocol.[30] Briefly, BG-EDA were obtained *via* periodate oxidation of bovine liver glycogen, followed by reductive amination with ethylenediamine.

4.3.3. Particle interaction with activated peripheral blood mononuclear cells (PBMCs)

Cell culture. PBMCs from healthy donors were isolated from blood by density gradient centrifugation using Ficoll-Paque Plus according to the manufacturer's protocol. Isolated cells were frozen in RPMI medium containing 10 % FBS and 5% DMSO and kept in -80^{o}C until further use. This research was approved by the University of Melbourne Human Research Ethics Committee (#1750753).

Isolated PBMCs were thawed and seeded in 24-well plate at density $1.0x10^6$ per well in 600 µL of RPMI medium containing 10% FBS and left overnight in 37ºC, 5% CO_2 and humidified atmosphere to recover after thawing. Next, cells were transferred to 1.5 mL tubes and spun at 200 *g* for 5 min to pellet. The supernatant was then removed, cells were resuspended in fresh medium, counted and diluted in RPMI supplemented with 10% FBS to a final concentration of $1.0x10^6$ cells/mL. To activate cells, cells were seeded in 96-well plate at $1.x10^5$ cells per well in 200 µL of medium with 16nM PMA and 0.5 µM ionomycin. Cells were incubated for 24 h in 37ºC, 5% CO_2 and humidified atmosphere. For non-activated cells, PMA and ionomycin were not added to cells. After counting, cells were seeded at $1.0x10^5$ cells per well in 200 µL of medium and incubated in 37ºC, 5% CO_2 and humidified atmosphere for 24 h.

The following day, cells were transferred to a 96-well round bottom plate and washed by centrifugation at 200 *g* for 8 min. The supernatant was removed and cells were suspended in 200 µL of cell culture medium prior to particles addition.

Particle addition. LbL Si, MS@PEG and PEG capsules (AF_{647}-labelled) were counted using Apogee A-50 Flow Cytometer and added to activated or non-activated cells at a particle-to-cell ratio of 100. Particles were prepared in 20 µL of DPBS immediately before addition. BG-EDA solution was prepared in 0.1x DPBS and added to cells at a final concentration of 10 µg mL^{-1}. Cells were incubated with particles for 4 or 24 h.

Immunostaining. After incubation time with particles was completed, 100 µL of DPBS with 1% BSA was added to wells. Cells were centrifuged at 500 *g* for 10 min and the supernatant was discarded. Two more washes with 200 µL 1% BSA-DPBS was carried out. Cells were resuspended in 100 µL of 1% BSA-DPBS and left on ice for 15 min. A cocktail of antibodies (anti-CD3, anti-CD19, anti-CD14 and anti-CD45) was prepared in DPBS at 1:50 antibody solution. Then, 100 µL of antibody solution was added to cells and incubated for 45 min at 4ºC. Additionally, an activation control was prepared by incubation with anti-CD69 only. Cells were washed 3 times with 200 µL of FACS buffer (DPBS containing 2mM EDTA and 2% FBS) and fixed with 4% PFA for 15 min at 4ºC. Cells were again centrifuged (1000 *g* for 10 min), the supernatant was removed, and cell pellet resuspended in 150 µL of FACS buffer for analysis. Cells were analysed using a DS CytoFLEX LX (Beckman Coulter Life Sciences). Data were analyzed using the CytExpert software (Beckman Coulter Life Sciences).

4.3.4. Particle interaction with pseudovirus-infected HuT 78 cells.

Cell culture. Cell culture and infection were performed by Vera Klemm in a PC3 facility at the Kirby Institute, University of New South Wales. HuT 78 cells were seeded at $6.0x10^4$ cells per well in 100 μL of RPMI medium supplemented with 10% FBS. For infected cells, mOrange-expressing HIV pseudovirus was added at a multiplicity of infection (MOI) 1 (virus-to-cell ratio 1) and MOI 0.2 (virus-to-cell ratio 0.2) to generate high and low infection, respectively. Cells were incubated with the pseudovirus for 72 h in 37ºC, 5% CO_2 and humidified atmosphere. The level of infection of Hut 78 cells was measured by the fluorescence intensity of the reporter protein mOrange as expressed by the pseudovirus. For non-infected cells, HuT78 were seeded at the same time and density, however, no pseudovirus was added.

Particle addition. LbL Si, MS@PEG and PEG capsules (AF_{647}-labelled) were added to pseudovirus-infected and non-infected cells at particle-to-cell ratio of 100. Particles were prepared in 20 μL of DPBS immediately before addition. BG-EDA solution was prepared in 0.1x DPBS and added to cells at a final concentration of 10 μg mL^{-1}. Cells were incubated with particles for 1, 4 or 24 h at 37ºC, 5% CO_2 and humidified atmosphere. After incubation, cells were transferred to 1.5 mL tubes. Next, 1.2 mL of DPBS was added to tubes and cells were centrifuged at 500 *g* for 10 min. The supernatant was removed, and cells were fixed with 4% PFA for 15 min at room temperature, followed by addition of 1 mL of DPBS and centrifugation at 350 *g* for 15 min. Cells were resuspended in 150 μL of DPBS and stored at 4ºC until further analysis.

Flow cytometry and confocal microscopy. Cell association was measured by BD Accuri C6 flow cytometer. Particle-cell association was assessed by the fluorescence intensity of cells after incubation with AF_{647}-labelled particles. Flow cytometry data were analysed using FlowJo v.10.

For confocal microscopy, nuclei were stained with Hoechst (1:10000 solution in DPBS, 5 min incubation at room temperature). Cells were suspended in 400 μL of DPBS and transferred to 8-well chamber slides and imaged on a Nikon A1R confocal microscope using 40x water objective.

4.3.5. Particle interaction with reactivated HIV latent cells

Cell culture. JLat 9.2 A2 cells were seeded at $1.0x10^5$ cells per well in a 96- well plate in 200 μL of RPMI medium supplemented with 10% FBS. Reactivated cells were treated with 16

nM PMA and 0.5 μM ionomycin for 24 h, as described for PBMCs. Non-reactivated (latent) cells were not treated with PMA/ionomycin. Before particle addition, cells were centrifuged at 500 g for 7 min. The supernatant was removed and 200 μL of fresh RPMI medium containing 10 % FBS was added.

Particles addition. LbL Si, MS@PEG and PEG capsules (AF_{647}-labelled) were added to cells at a particle-to-cell ratio of 100. Particles were prepared in 20 μL of DPBS immediately before addition. BG-EDA solution was prepared in 0.1x DPBS and added to cells at a final concentration of 10 μg mL^{-1}. Reactivated and latent JLat cells were incubated with particles for 4 h at 37ºC, 5% CO2 in a humidified atmosphere.

Imaging flow analysis. After incubation, cells were centrifuged at 500 *g* for 7 min and washed with 200 μL of 1% BSA in DPBS, followed by centrifugation. This process was repeated twice more. After the last centrifugation, the supernatant was removed, and cells were fixed with 4% PFA for 10 min at room temperature. After fixation, 200 μL of 1% BSA-DPBS was added to wells and cells were centrifuged at 1000 *g* for 10 min. Next, the supernatant was removed and 100 μL of DPBS was added to cells. Cell membrane staining was carried out by incubation with AF_{594}-wheat germ agglutinin (5 μg mL^{-1}) for 5 min at room temperature. After staining, cells were washed twice (200 μL DPBS, centrifugation for 10 min at 1000 *g*) and resuspended in 100 μL of DPBS for analysis. Samples were analysed using an ImageStreamX® MK II (ISX) imaging flow cytometer. Data analysis was performed using the Image Stream Software.

4.4. Results and discussion

Four types of particles were prepared to probe their interactions with immune cells in their inactive and actives state. LbL Si particles terminated with poly-L-arginine were prepared as described in chapter 3 *via* layer-by-layer assembly of PSS and PLArg on PEI-coated 887 nm silica templates. MS@PEG particles were fabricated by the use of 8-arm-PEG-NH_2 with a hexaglycerol core structure to infiltrate the pores of 400 nm mesoporous silica (MS) template *via* electrostatic interactions, followed by crosslinking with 8-arm-PEG-succinimidyl carboxyl methyl ester (8-arm-PEG-NHS), resulting in core-shell particles of charge around -20 mV. Its template-free counterpart, namely PEG capsules, were prepared by subsequent dissolution of

the MS template in 2 M HF/8 M NH_4F solution (pH ~5), resulting in neutrally charged particles. It has been previously shown that template-free formulations of PEG particles have prolonged blood circulation and largely improved stealth properties, displaying minimal interactions with monocytes and granulocytes in whole blood assays, in comparison with MS@PEG particles that exhibited significant association with both cell types in the same experiment, or HeLa and THP-1 cell lines.[29] PEG capsules have been successfully employed for extracellular tumour targeting *in vitro* using conjugated antibodies and receptors ligands.[31] Amine-functionalized glycogen particles (BG-EDA) were prepared *via* periodate oxidation of bovine liver glycogen, followed by reductive amination with ethylenediamine, as previously reported. The resulting particles were around 27 nm in diameter and positively charged (~ 35 mV), and have been previously used to deliver siRNA to prostate cancer PC3 cell line in 2D and 3D cell culture models. Glycogen itself is a hyper-branched glucose polymer that serves as a glucose reservoir for many organs, including heart, liver, brain and skeletal muscles, and helps to maintain glucose homeostasis across the body.[32] All four particle systems used in this study are presented in **Figure 4.1**.

4.4.1. Primary cells activated with PMA/Ionomycin

Peripheral blood mononuclear cells (PBMC) consists of a mixture of lymphocytes and monocytes that can be obtained from human blood or buffy coats (white blood cells separated from human blood).[33] In drug development, PBMCs are used as a cell model to study materials biocompatibility and cellular uptake and to assess the expression of activation markers and cytokine secretion by immune cells.[34,35] The use of fluorescently labelled antibodies allows identifying individual cell subsets *via* flow cytometry.[36] In the present work, populations of lymphocytes and monocytes were identified by the difference in scattering, and the use of antibodies specific to CD3 and CD19 enabled the identification of T cell and B cell populations, respectively (**Figure 4.2A**).

T cells and B cells are involved in adaptive immune response triggered upon exposure to an antigen, acting *via* cell-mediated (T cells) or humoral (B cells) immunity.[37] The third population of lymphocytes, i.e., natural killer (NK) cells, was identified as population negative for CD3 and CD19 markers but positive for CD45. NK cells are part of the innate immune system, providing a quick response to encountered pathogens.[38] Monocytes include two major cell subsets, i.e., macrophages and dendritic cells.[39] However, it should be noted that such

classification is simplified and does not account for the complex marker expression patterns identified in recent years in cells of myeloid lineage. For this analysis, anti-CD14 was used to identify cells expressing CD14 (CD14+) that is typically present on the surface of monocytes and most tissue-resident macrophages involved in the innate immune system to detect bacterial infection.[40]

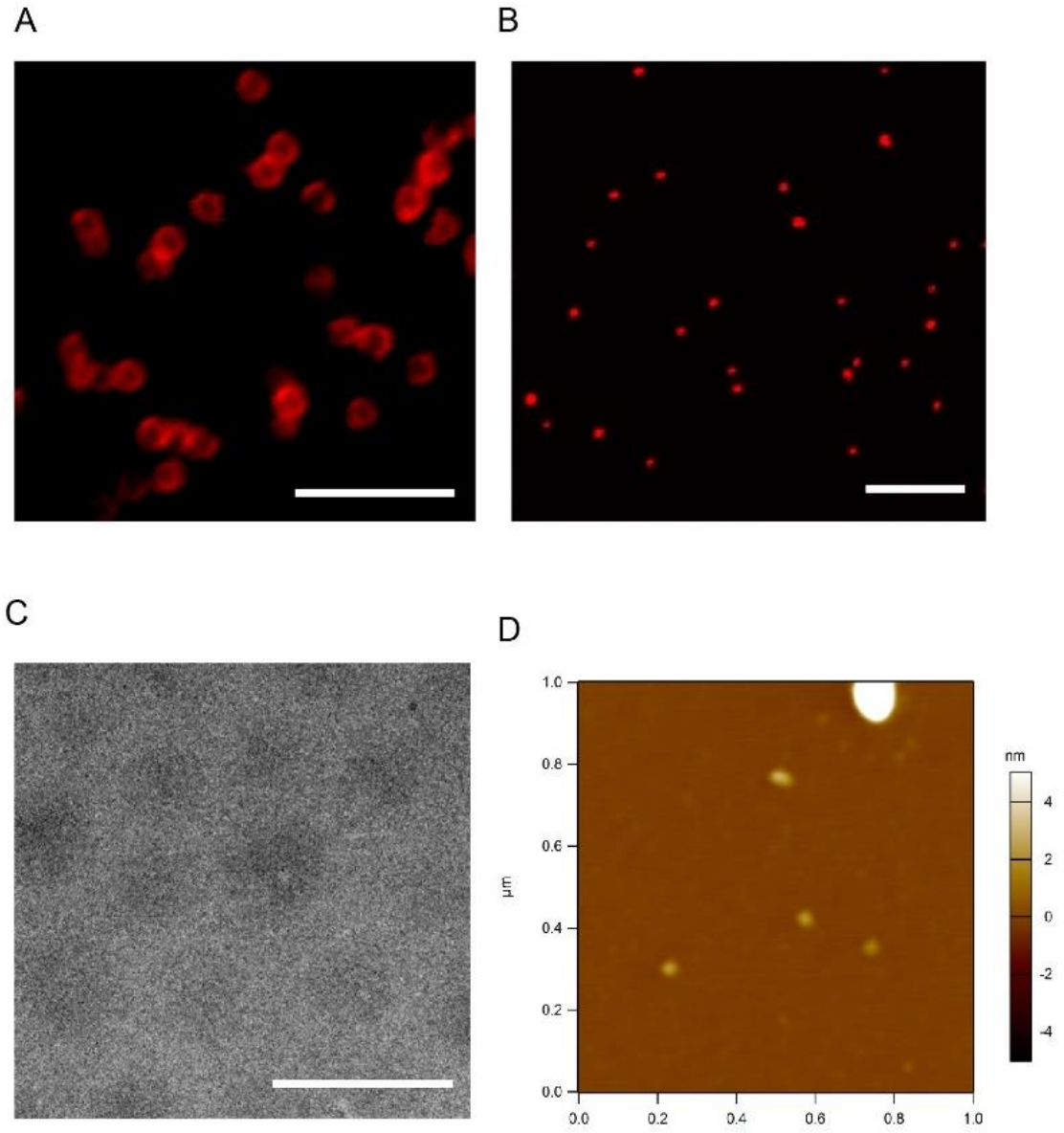

Figure 4.1. Particles preparation. Confocal microscopy image of AF_{647}-labelled LbL Si particles (A) and MS@PEG (B). TEM image of PEG capsules (C). AFM image of BG-EDA (D). *Scale bars are 5 µm (A and B) and 1 µm (C).*

Particles association (AF_{647}-labelled LbL Si, MS@PEG, PEG capsules and BG-EDA) with activated (PMA/Ionomycin treated) and non-activated (untreated) cells was assessed after 4 and 24 h incubation *via* flow cytometry. The population of particle-associated cells in four different subpopulations, i.e. CD14+ Monocytes, T cells, B cells and NK cells, was assessed by gating for each cell population based on the cell surface markers and determining the percentage of cells positive for AF_{647} fluorescence (from AF_{647}-particles) (**Figure 4.2B**). Contribution of each tested cell subtypes to PBMC population for each treatment condition was also confirmed (**Figure 4.2C**) and agrees with data reported in the literature, except for a low abundance of monocytes in activated cells population.[41] To confirm cell activation upon PMA/Ionomycin treatment, we assessed the expression level of CD69 as an early activation marker of T cells and NK cells (**Figure 4.2D**).[42] The increased expression of CD69 marker was observed following PBMCs activation.

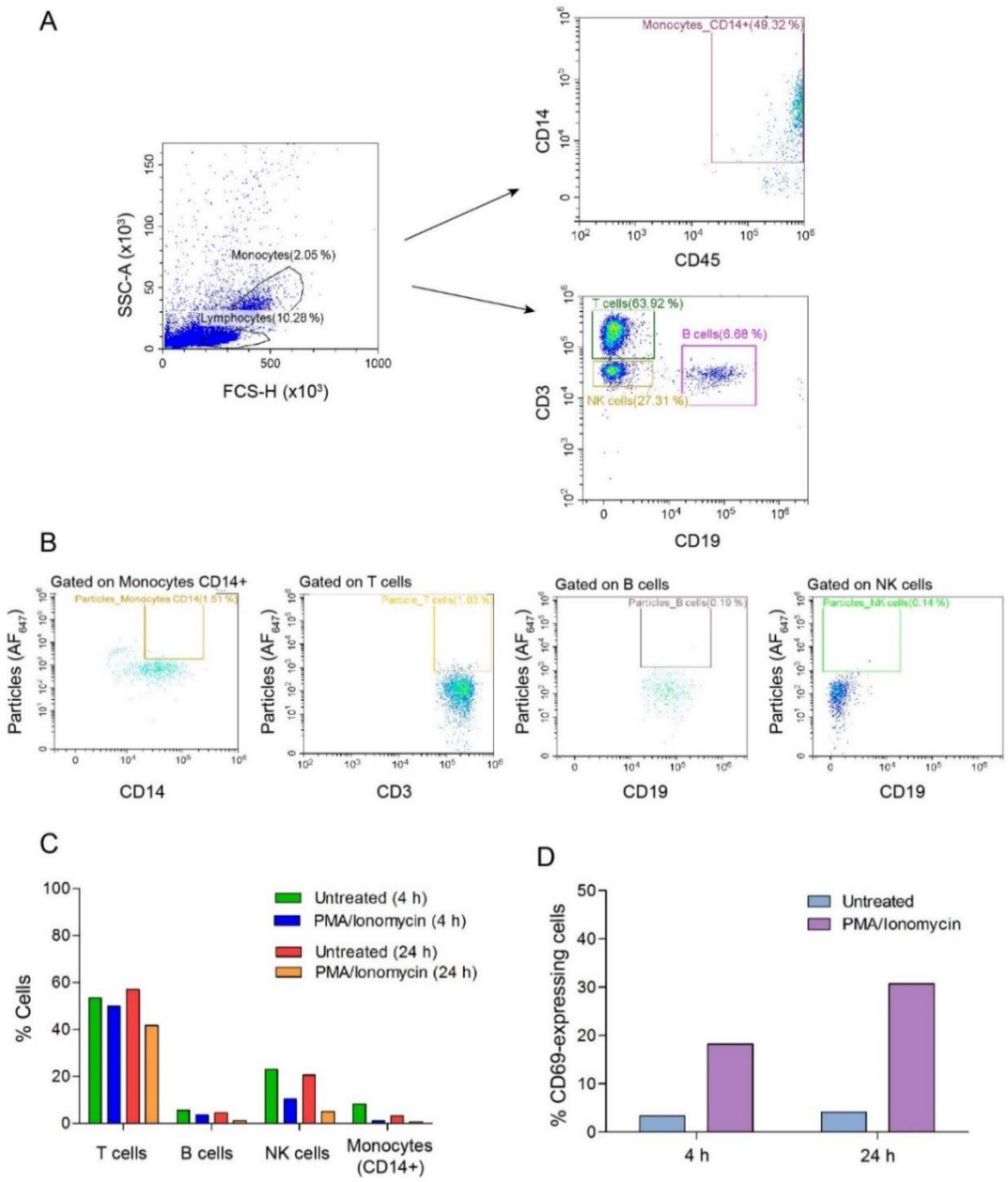

Figure 4.2. Identification of different cell populations in PBMCs and assessment of cell activation via flow cytometry. Gating strategy to identify individual cell subtypes in PBMC (A). Identification of particle-associated cell subtypes (B). Quantification of T cell, B cells, NK cells and Monocytes population in PBMC (C). Expression of an early activation marker CD69 (D).

Different association patterns with lymphocytes populations were observed among tested particles. LbL Si particles showed relatively low association (~12-25%) with T cells after 4 and 24 h incubation, regardless of the cell activation state (**Figure 4.3A**). From all investigated cell subtypes, the dominant population associated with LbL Si is inactivated B cells, showing over 70% association after 4 h and ~ 40% at 24 h post-treatment. Interestingly, activation of B

cells significantly reduced the association with particles to 30% and 10% after 4 and 24 h incubation, respectively (**Figure 4.3B**). Association of LbL Si with NK cells was low, reaching ~12% regardless of cell activation or incubation time (**Figure 4.3C**).

The presence of PEG on the particle surface has been shown to improve stealth properties of the carrier and reduce cell association to evade recognition by immune cells. The PEG-containing particles used in this study are MS@PEG (i.e., particles with mesoporous core, which have shown increase association with monocytes and granulocytes when tested in whole blood in previous studies) and PEG capsules (i.e., hydrogel capsules without the mesoporous core, which have shown a minimal association with monocytes and granulocytes). MS@PEG particles used in this study showed ~ 20 % association for activated T cells (**Figure 4.3A**) and ~3% for activated NK cells (**Figure 4.3C**) following 4 h incubation. Further incubation for 24 h led to an increased particle association to 45% for T cells and 25% for NK cells. In contrast, 24 h treatment of non-activated cells with MS@PEG resulted in only 10 and 2 % of associated T cells and NK cells, respectively. PEG capsules have been previously used to demonstrate superior stealth properties, resulting in prolonged blood circulation *in vivo*. Our results confirmed expectations of a generally low association (1-3%) with immune cells *in vitro*, excluding a slight increase in association with activated NK cells to ~ 10% following 24 h particle treatment.

Amine-functionalized glycogen nanoparticles (BG-EDA) are ~30 nm in diameter with a net positive charge. BG-EDA showed >90% association with all lymphocyte subsets after 4 hours of incubation, regardless of cell activation. Following 24 h incubation, a distinct difference between association with activated and non-activated cells was observed. Specifically, association with activated B cell and NK cells has decreased to ~ 60 and ~20%, respectively. As primary cells are generally non-dividing *in vitro*, such decrease could not be explained by progressing cell division, therefore other activation-related changes, including cell differentiation or cell death after 24 h *in vitro* culture could provide an explanation and should be further confirmed.

Macrophages are primarily responsible for the clearance of foreign nanomaterials *in vivo*, therefore the CD14+ monocytes subpopulation was expected to exhibit high particle association. In fact, this is the cell subpopulation where the most distinct difference in particles association between activated and non-activated cells was observed (**Figure 4.3D**). For all tested carriers and incubation times (except for LbL Si, 24 h) a significant decrease in cell

association with activated monocytes was observed. A possible explanation could be that upon *in vitro* activation of a mixed cell population, such as isolated PBMC, certain cells become more engaged in the interaction with nanoparticles, reducing the contribution from cells normally involved in particles uptake (e.g., macrophages). However, this is not supported by the results, as a decrease in particle association with monocytes should be balanced by a proportional increase among lymphocytes. A possible explanation is that following activation and 24 h *in vitro* culture, monocytes adhere to the plate and the used method of cell harvesting did not suffice to recover whole monocyte population. It should be noted that in this work, the analysis of cell subtypes was simplified, hence potentially other cells participating in interactions with particles could be unaccounted for, especially considering the overall low number of monocytes detected 24 h post-activation (**Figure 4.2C**).

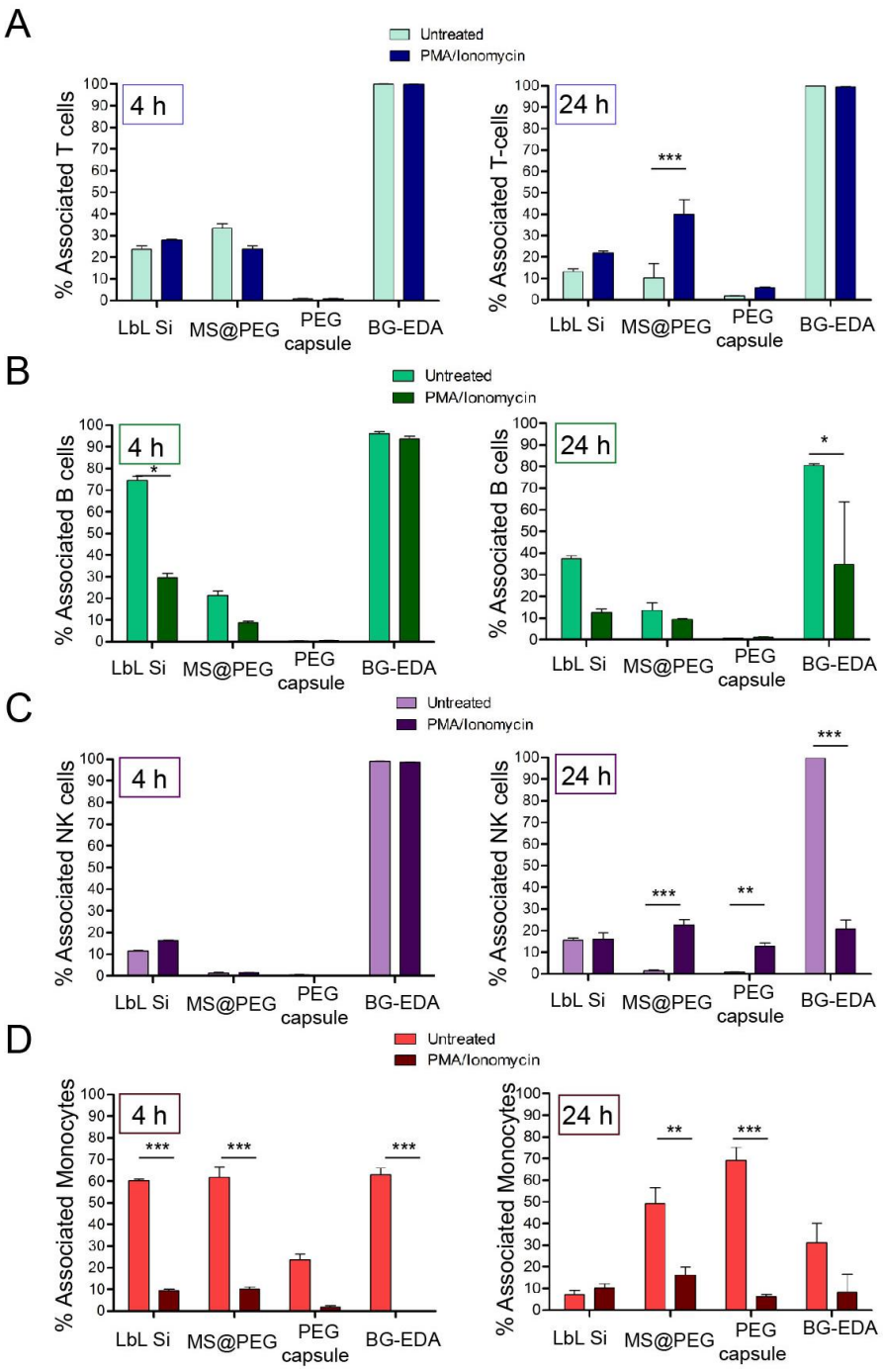

Figure 4.3. Particle association with immune cells subtypes by flow cytometry. Association with T cells (A), B cells (B), NK cells (C) and CD14+ Monocytes (D) as assessed following 4 and 24 h treatment with particles. Data are shown as the average mean ± standard error of the mean (n = 2). Statistical analyses were performed using one way-ANOVA with Tukey's multiple comparison test. ***$p < 0.001$

4.4.2. Pseudovirus-infected HuT 78 T cells

The study of the HIV-1 viral cycle, entry and infection is challenging due to safety concerns, inefficient production of highly concentrated virus titers and restrictions regarding infectivity limited to certain cell types. Therefore, the use of HIV-1 pseudotyped viruses, i.e., HIV-1 vectors incorporating glycoproteins of other viruses, combined with a modification of the HIV viral genome for increased safety, has been proposed as a model to study HIV infection in preclinical drug development.[43]

The HIV-1 pseudotyped virus or pseudovirus used in the current study represents a model of a single round of infection and was generated with a mOrange reporter (as a fluorescence-based indicator of infection) and a VSV-G envelope (enabling high infectivity). The pseudovirus was used to infect a HuT 78 T-cell line for 3 days using two different values of a multiplicity of infection (MOI): 0.2 (medium infection) and 1 (high infection). Control cells, i.e. without pseudovirus treatment (non-infected) were also prepared. To assess how infection affects cell-particle interaction, we studied association and internalization of AF_{647}-labelled particles (LbL Si, MS@PEG, PEG capsuled ad BG-EDA) *via* flow cytometry and confocal microscopy, following 1, 4 and 24 h incubation with infected and non-infected cells.

Analysis of particle association with a whole cell population indicates a higher association of LbL Si particles with infected cells (~ 30% for MOI=1 and 35% for MOI=0.2) compared to non-infected control (25%) (**Figure 4.4A**). However, the difference is small and decreases with time down to 20% particles association for all levels of infection following 24 h incubation. The effectiveness of infection was assessed by flow cytometry, indicating that addition of virus at MOI=1 resulted in ~ 20% of pseudovirus-positive cells (**Figure 4.4B**). Among the infected cells, i.e., positive for pseudovirus, ~ 10% of cells were associated with particles. While in the whole cell population association with particle decreases with time, the population of infected cells show the opposite trend of increased association reaching 20% after 24 h (**Figure 4.4C**).

Using confocal microscopy, particle internalization was assessed in infected cells following 4 and 24 h incubation with particles. Representative confocal microscopy images show cellular uptake of AF_{647}-LbL Si particles, and the presence of pseudovirus or infection is confirmed by the expression of mOrange reporter (**Figure 4.4D**).

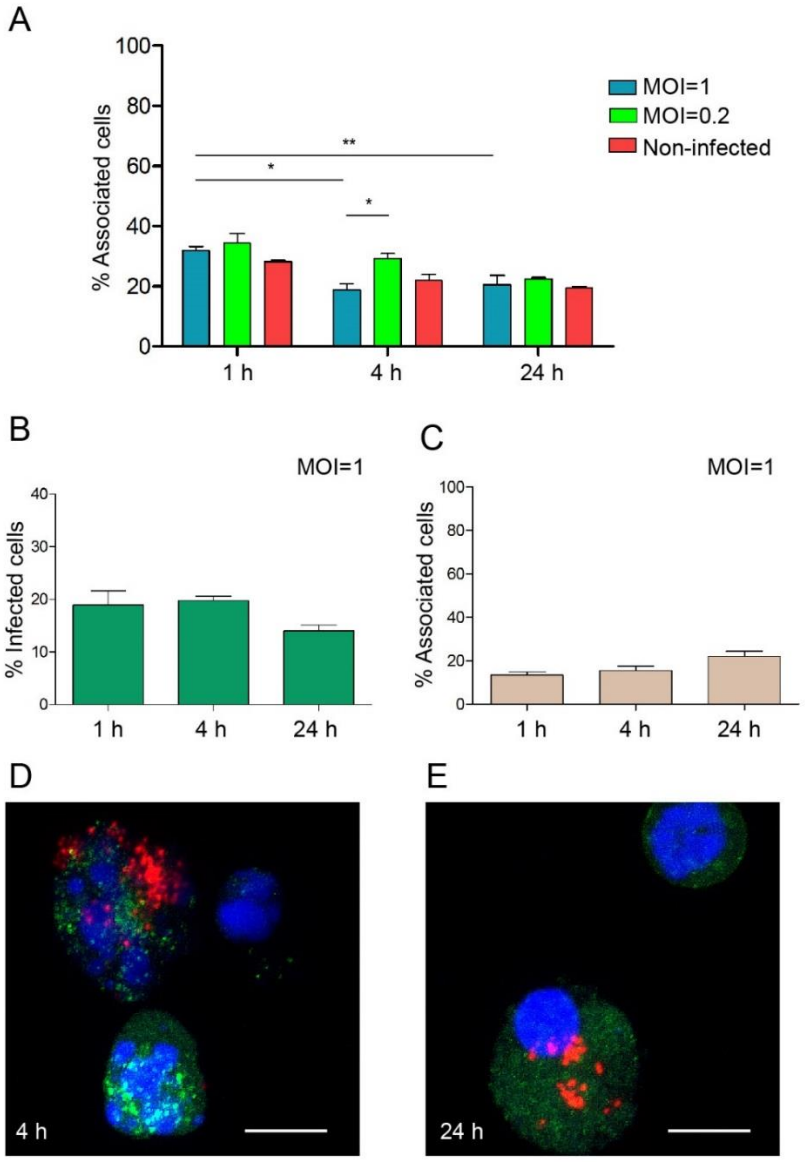

Figure 4.4. Association of LbL Si particles with pseudovirus-infected/non-infected HuT 78 cells. Cell association of 837 nm LbL Si particles, analyzed by flow cytometry and presented as % of particles-associated cells (A). The level of infection following pseudovirus treatment at MOI=1 (B) and the association of AF_{647}-particles with pseudovirus-infected cells (C). Maximum projections of confocal microscopy images showing particle internalization in infected cells after 4 h (D) and 24 h (E) of incubation. Nuclei were stained with Hoechst 10333 (blue), particles are red (AF_{647}-labelled) and the pseudovirus-associated mOrange reporter is presented in green. *Scale bars are 5 μm.* Data are shown as the average mean ± standard error of the mean (n = 3). Statistical analyses were performed using one way-ANOVA with Tukey's multiple comparison test. **$p < 0.01$

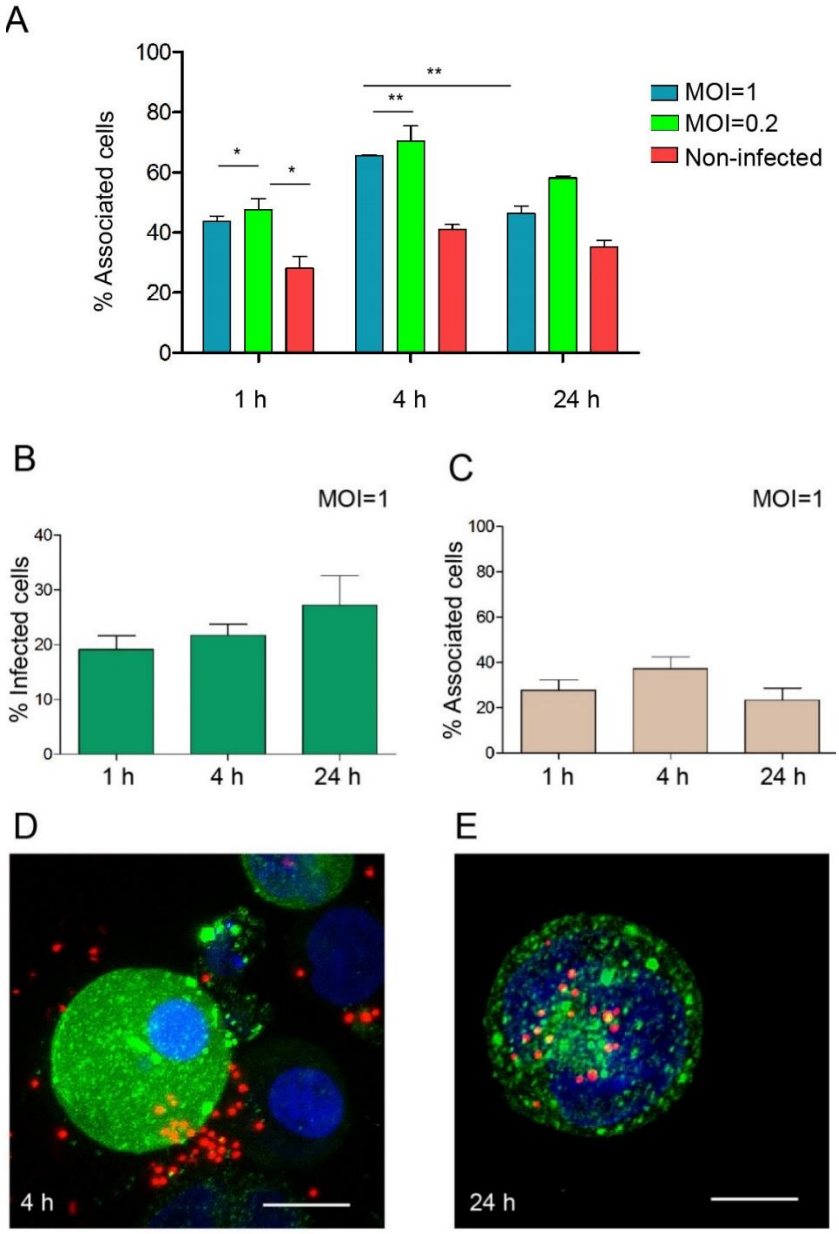

Figure 4.5. MS@PEG particles association with pseudovirus-infected/non-infected HuT 78 cells. Cell association of 400 nm MS@PEG particles analyzed by flow cytometry and presented as % of particles-associated cells (A). The level of infection following pseudovirus treatment at MOI=1 (B) and the association of AF_{647}-particles with pseudovirus-infected cells (C). Maximum projections of confocal microscopy images showing particle internalization in infected cells after 4h (D) and 24 h (E) of incubation. Nuclei were stained in Hoechst 10333 (blue), particles are red (AF_{647}-labelled) and the pseudovirus-associated mOrange reported is presented in green. *Scale bars are 5 μm.* Data are shown as the average mean ± standard error of the mean (n = 3). Statistical analyses were performed using one way-ANOVA with Tukey's multiple comparison test. **$p < 0.01$

A different pattern was observed for MS@PEG. Following 1 h incubation with particles, highly infected cells showed ~45% particle association, which increased up to 70% at the 4 h time point (**Figure 4.5A**). For comparison, particle association with uninfected cells reached ~25% and 40% for 1 and 4 h incubation time, respectively. The infection level was also assessed by flow cytometry to identify the percentage of pseudovirus-positive cells (**Figure 4.5B**). In the infected cell population, particle association oscillated between 20 and 40% (**Figure 4.5C**). High particle association with infected cells was further confirmed by confocal microscopy, showing particles in the proximity of cell membrane 4 h after particles addition (**Figure 4.5D**), and extended incubation resulted in efficient cellular uptake of MS@PEG (**Figure 4.5E**).

As expected, PEG capsules showed low association (1-3%) with cells regardless of the infection state or incubation time (**Figure 4.6A**), and more detailed analysis of pseudovirus-infected cells confirm this result (**Figure 4.6B and C**). Due to the low association and the rare occurrence of particle-positive cells, imaging was not performed.

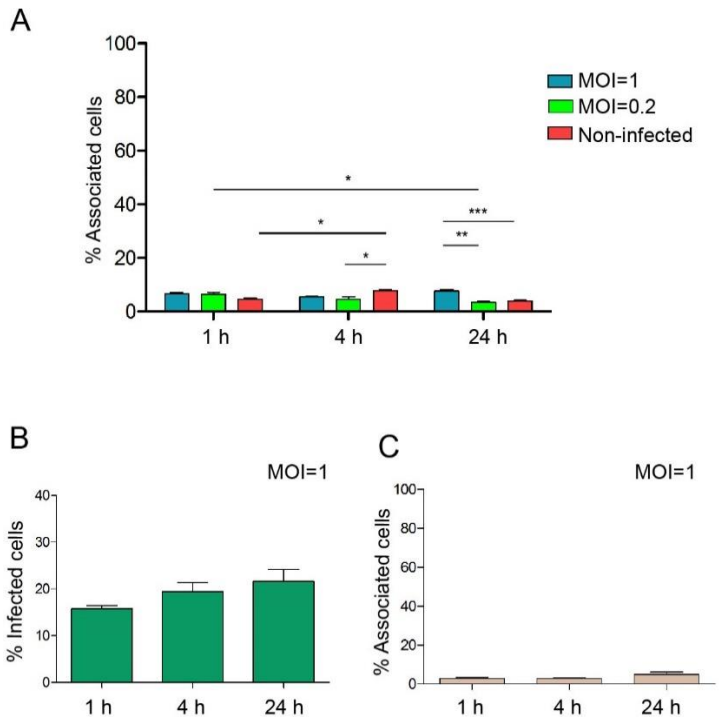

Figure 4.6. PEG capsules association with pseudovirus-infected/non-infected HuT 78 cells. Cell association of 400 nm PEG capsules analyzed by flow cytometry and presented as % of particles-associated cells (A). The level of infection following pseudovirus treatment at MOI=1 (B) and the association of AF_{647}-particles with pseudovirus-infected cells (C). Data are shown as the average mean ± standard error of the mean (n = 3). Statistical analyses were performed using one way-ANOVA with Tukey's multiple comparison test. ***p < 0.001

On the contrary, BG-EDA particles showed high association with cells (>90 %) regardless of the infection state (**Figure 4.7A, B and C**) and internalized particles could be identified *via* confocal microscopy in pseudovirus-infected cells (**Figure 4.7D and E**).

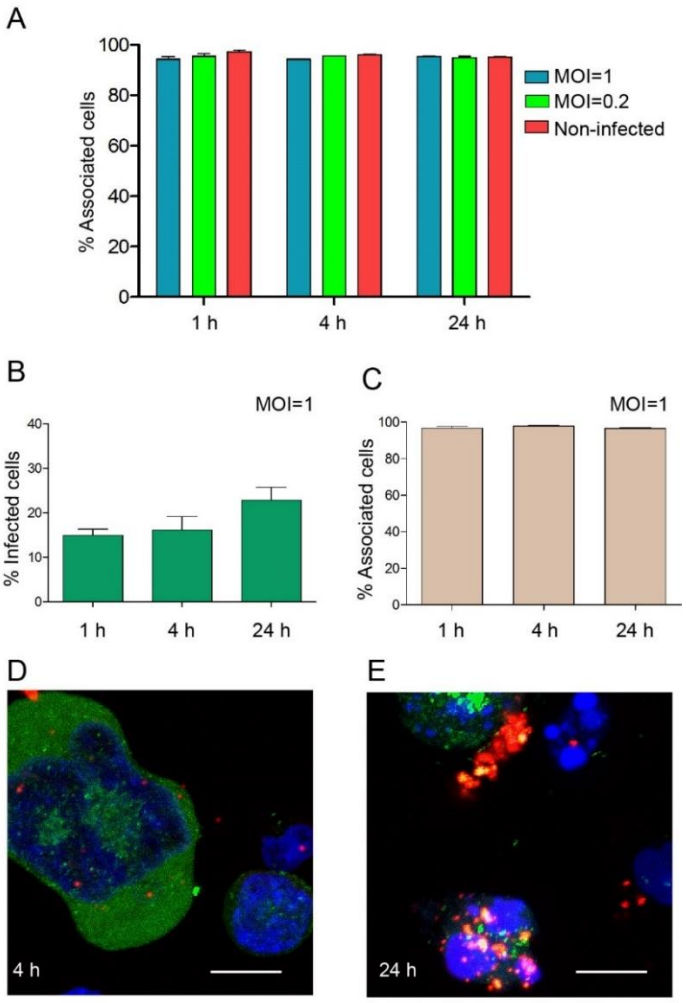

Figure 4.7. BG-EDA association with pseudovirus-infected/non-infected HuT 78 cells. Cell association of BD-EDA particles analyzed by flow cytometry and presented as % of particles-associated cells (A). The level of infection following pseudovirus treatment at MOI=1 (B) and the association of AF_{647}-particles with pseudovirus-infected cells (C). Maximum projections of confocal microscopy images showing particle internalization in infected cells after 4h (D) and 24 h (E) of incubation. Nuclei were stained in Hoechst 10333 (blue), particles are red (AF_{647}-labelled) and the pseudovirus-associated mOrange reported is presented in green. *Scale bars are 5 μm.* Data are shown as the average mean ± standard error of the mean (n = 3).

4.4.3. JLat T cells -a model of HIV latency

One of the important obstacles to finding an HIV cure is the presence of the latent reservoir within resting T cells, that can reactivate rapidly after cessation of antiretroviral therapy, leading to virus rebound.[44] Due to the low abundance and lack of specific markers of cells carrying a quiescent virus, T cell lines-based models have been established to study the HIV latency mechanism. One such model is based on JLat T cells, containing an integrated HIV-1 genome that produces incomplete virions and carrying a GFP fluorescent reporter.[45] JLat cells were used in this study to compare particle uptake in latently-infected (to model cells not producing virus) and reactivated T cells (to model cells actively producing virus). Cells were first reactivated by 24 h treatment with PMA/Ionomycin. When reactivated, JLat cells express GFP. Latently infected cells were considered as the group without PMA/Ionomycin treatment. Latent and reactivated cells were incubated with AF_{647}-labelled LbL Si particles, MS@PEG, PEG capsules and BG-EDA for 4 h. Imaging flow cytometry—a technique combining the advantages of flow cytometry and fluorescence microscopy, was used to enable a high-throughput analysis of particle internalization in a latent and reactivated model of HIV infection.[46] Cell membranes were stained with AF_{549}-wheat germ agglutinin to enable the analysis of particle internalized by cells of internalized. To assess particle internalization in reactivated samples, only GFP-expressing cells were included in the analysis. The internalization of cells was assessed based on the internalization factor: cells with high internalization factor contain particles, while cells with low internalization factor are not associated with particles or particle are bound to the cell surface. For the non-reactivated cells internalization factor was assessed based on the spatial relationship between the fluorescent signal of particle and membrane stain, and for the reactivated cells the internalization factor was based on the spatial relationship between the fluorescent signal of the particles and virus produced in the cytosol. While the measured difference in association for latent and reactivated cells for LbL Si particles and MS@PEG was negligible (**Figure 4.8 and 4.9**), a clear difference was observed for two other tested systems. PEG capsules were internalized in 7% of latently infected cells and up to 47.7% in reactivated cells (**Figure 4.10**). While the previously demonstrated results for PEG capsules interactions with pseudovirus-infected T cells show generally low association of capsules with cells, results presented here suggest unusually high uptake of PEG capsules upon cell-integrated virus reactivation. Further studies, investigating the activity of endocytic pathways following virus reactivation should be performed in an

attempt to gain some insight into why PEG capsules show such high internalization in reactivated JLat cells. Increase in particles uptake upon cell reactivation was also observed for BG-EDA showing 14% internalization in non-activated and 83% in reactivated cells (**Figure 4.11**).

It should be noted that analysis of particle internalization in reactivated cells includes a series of gating steps to identify not only particle- and GFP-positive cells, but also focused population. Efficient binding of the particles to cell membrane is a first step in particle-cell interaction and dictates particle uptake. It varies depending on the particle system and the number of focused cells cannot be control by the user. As a result, the number of of cells included in the analysis varied between samples and was overall lower for non-reactivated samples where the cell image was outlined by membrane stain. Nevertheless, the comparison between latent and reactivated HIV intesction cell model for a given particle system indicates that cell reactivation induces ~4x fold increase in cellular uptake of PEG capsules and BG-EDA.

It may be surprising that despite the low association, we observed particle internalization in pseudovirus-infected cells. T cells are often described as 'difficult to transfect' and are non-phagocytic cells. Limited examples of particle-mediated drug delivery to T cells include formulation with size below 300 nm. In contrast, in this study only BG-EDAis <300 nm, while MS@PEG particles/PEG capsules are 400 nm and LbL Si 837 nm. PMA and ionomycin are generally used to stimulate a non-specific immune response *in vitro*, and such treatment initiates a cascade of cellular processes leading to a production of various secretory molecules, including cytokines, that alter the microenvironment and can potentially affect the cell health.[46] Also, activation of cells is associated with the reorganization of the cytoskeleton, inducing changes in the spatial density of receptors on the cell membrane.[47] Therefore, a thorough understanding of this mechanism and its potential impact on particles association and uptake is crucial for improved engineering of drug delivery systems, especially in the context of using ligand/antibodies to target specific cell population.

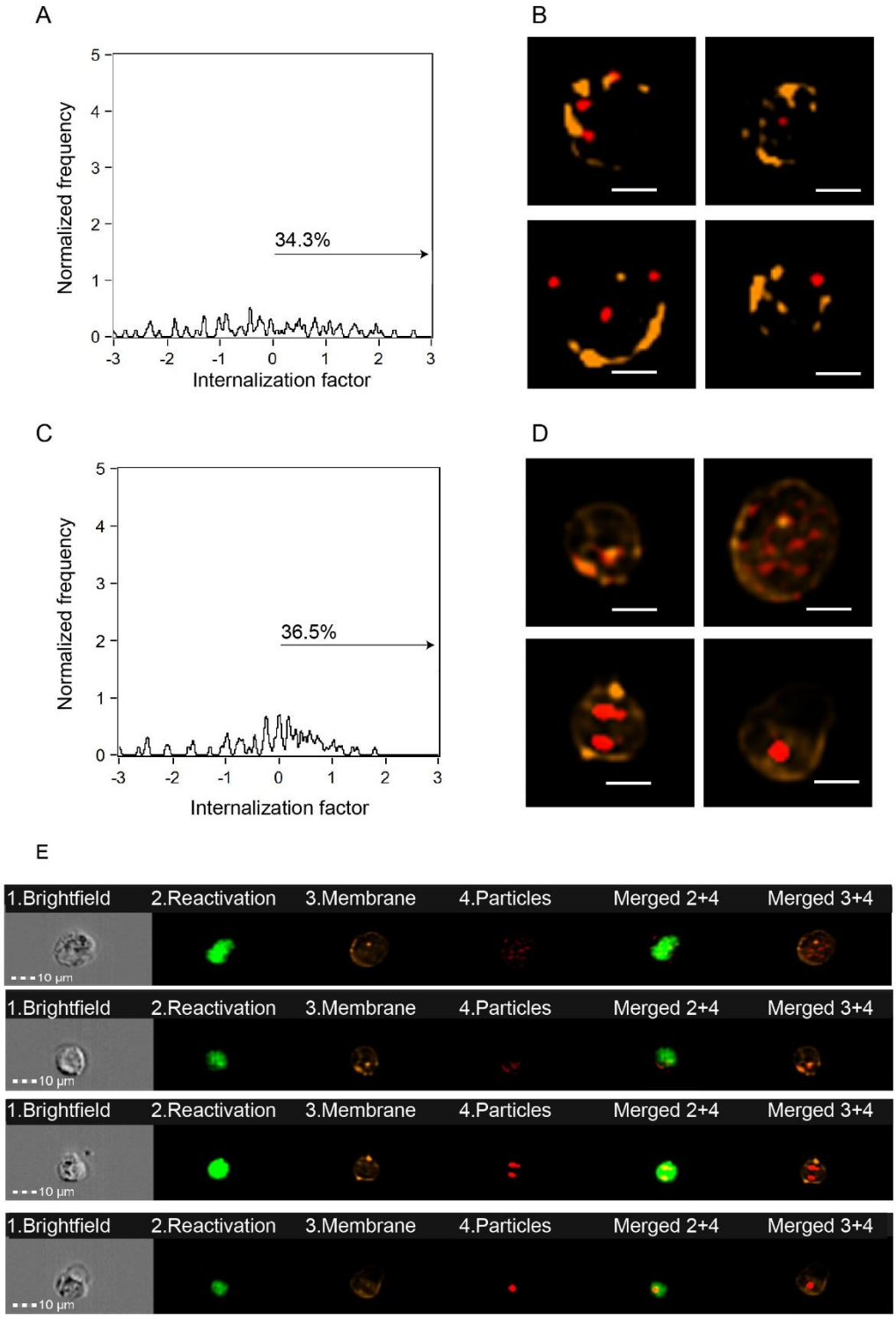

Figure 4.8. LbL Si particle internalization in HIV latency model via imaging flow. Particles internalization analysis in latently infected cells (A) and representative images (B). Internalization in reactivated cells (C) and representative images (D). Additional images of reactivated cells with internalized particles (E). Reactivation corresponds to GFP expression, cell membranes were stained with AF_{594} WGA and particles were labelled with AF_{647}.

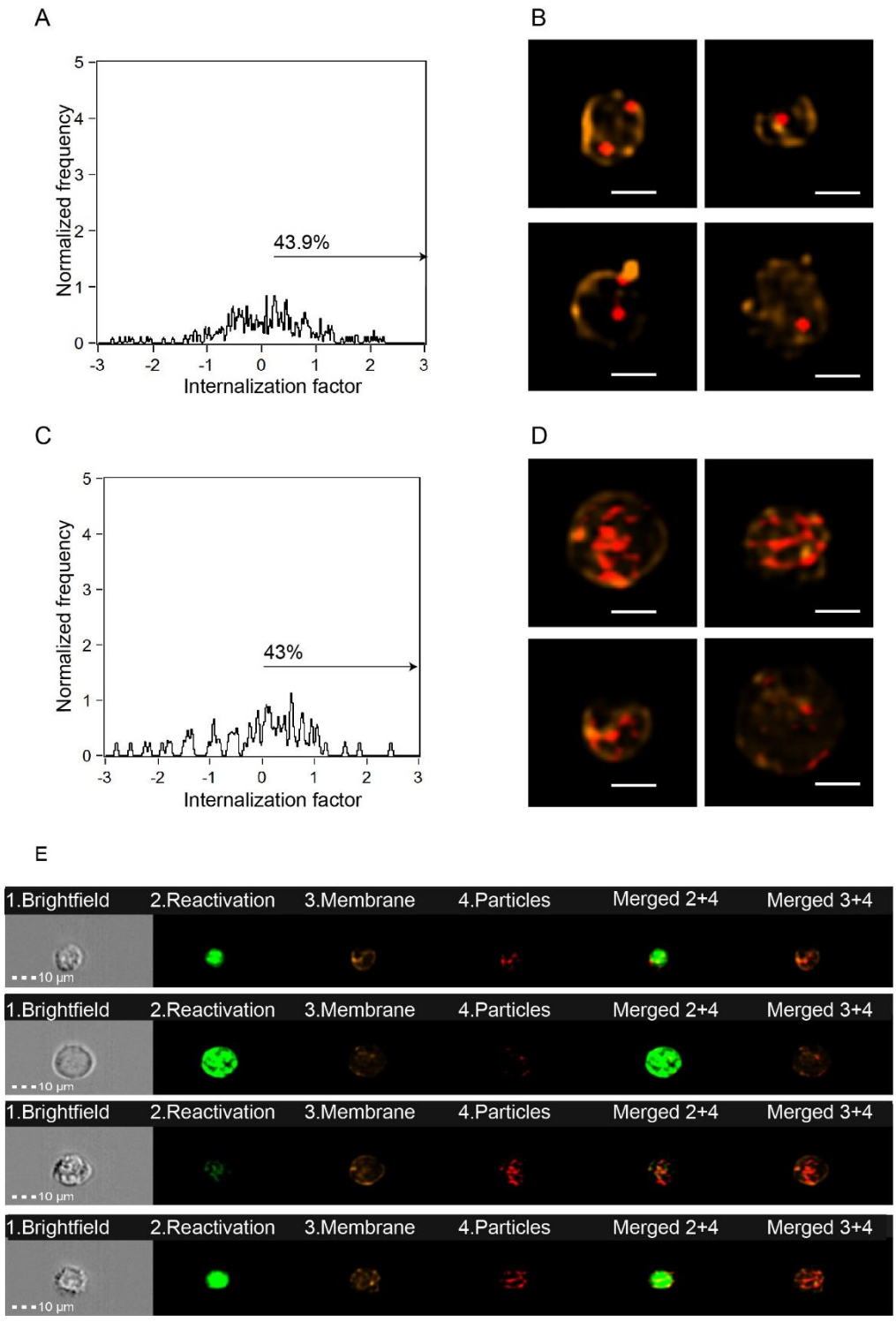

Figure 4.9. MS@PEG internalization in HIV latency model via imaging flow. Particles internalization analysis in latently infected cells (A) and representative images (B). Internalization in reactivated cells (C) and representative images (D). Additional images of reactivated cell with internalized particles (E). Reactivation corresponds to GFP expression, cell membranes were stained with AF_{594} WGA and particles were labelled with AF_{647}.

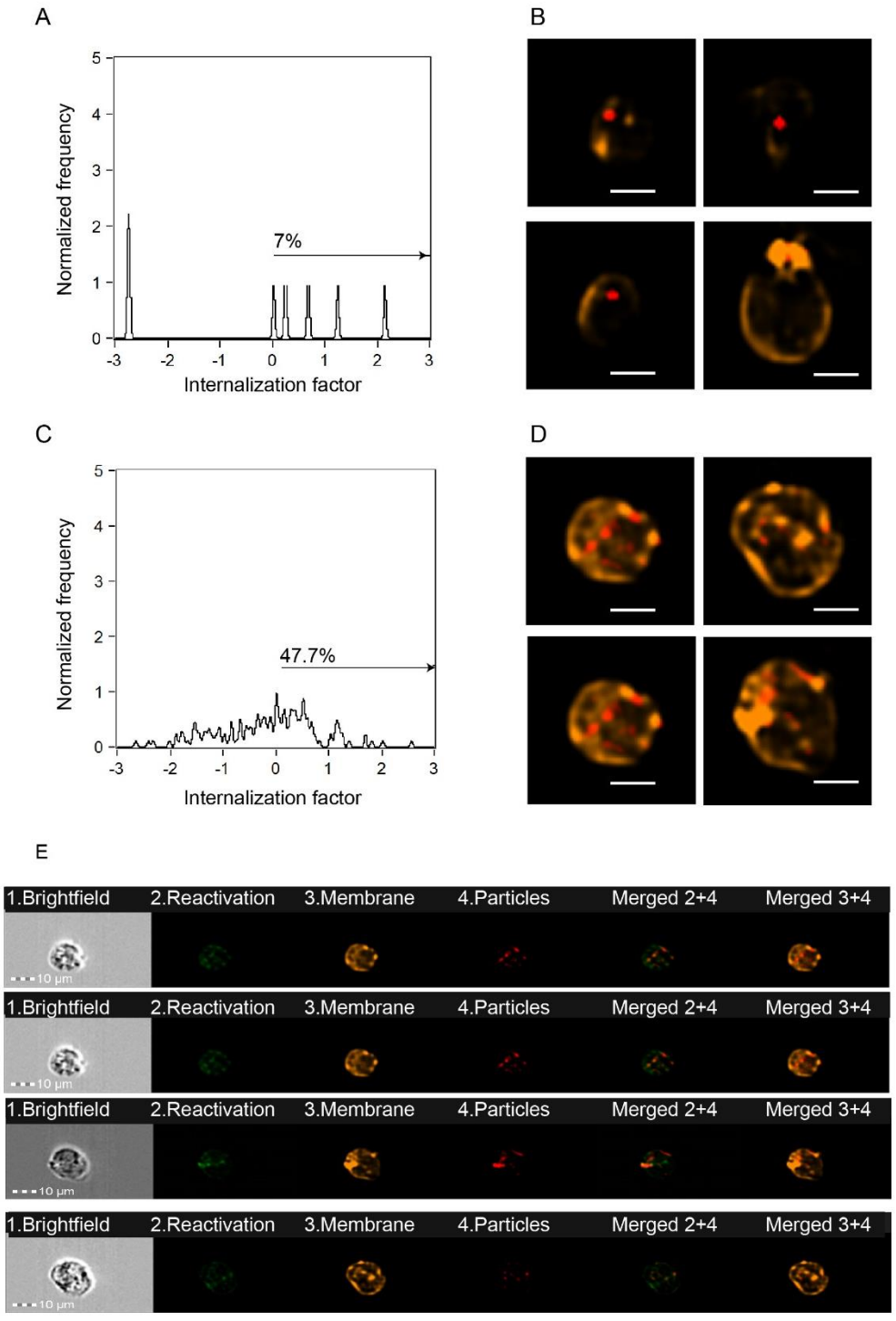

Figure 4.10. PEG capsules internalization in HIV latency model via imaging flow. Particles internalization in latently infected cells (A) and representative images (B). Internalization in reactivated cells (C) and representative image (D). Additional images of reactivated cells with internalized particles (E). Reactivation corresponds to GFP expression, cell membranes were stained with AF_{594} WGA and particles were labelled with AF_{647}.

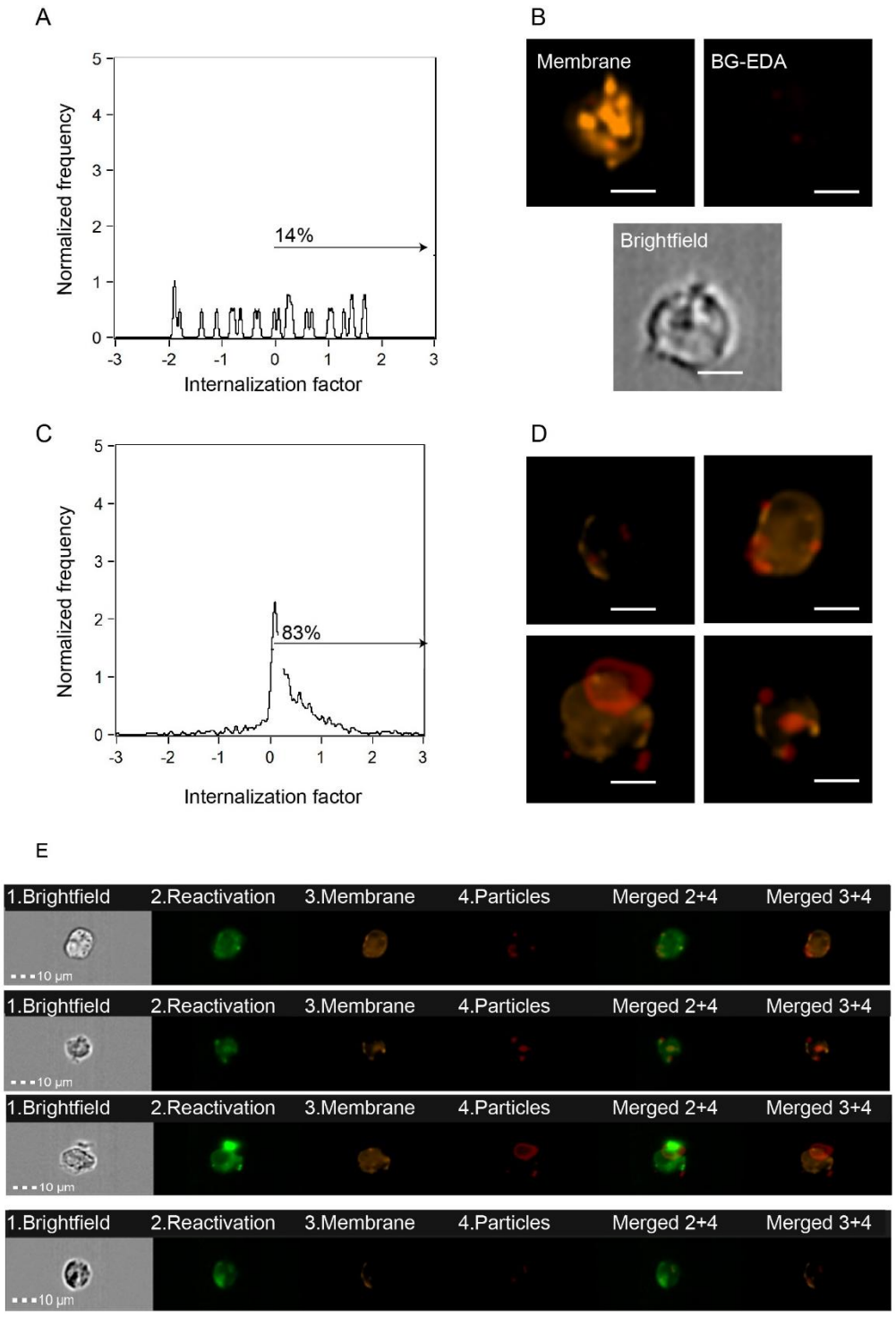

Figure 4.11. BG-EDA internalization in HIV latency model via imaging flow. Particles internalization in latently infected cells (A) and representative images (B). Internalization in reactivated cells (C) and representative images (D). Additional images of reactivated cells with internalized particles (E). Reactivation corresponds to GFP expression, cell membranes were stained with AF_{594} WGA and particles were labelled with AF_{647}.

4.5. Conclusions

In summary, the effect of immune cell activation and presence of infection on the interaction with particles was investigated. Four types of particle systems, namely LbL Si, MS@PEG, PEG capsules and BG-EDA were used. The activation of PBMCs with PMA/Ionomycin have been shown to increase the expression of T cell and NK cell activation marker. Activation of T cells and NK cells resulted in an increased association with 400 nm MS@PEG particles following 24 h incubation, however, had little effect on association with other tested particles. The same set of particles was used to test their interaction with two HIV infection models: pseudovirus-infected HuT 78 T cells and JLat A2 latency model. Pseudovirus-infected cells showed a higher association with LbL Si particles and MS@PEG particles. Soft, more flexible systems including PEG capsules and BG-EDA have shown cell association pattern independent of infection. In the HIV latency model, virus reactivation by PMA/Ionomycin resulted in an enhanced internalization of PEG capsules and BG-EDA (47% and 83%, respectively) compared to non-reactivated cells (7% and 14%, respectively). The observed differences in association patterns for various particles with cells in their activated/infected or and non-activated/non-infected state can be partly due to a decreased cell viability upon activation or HIV infection. Further studies focusing on the activity of endocytosis pathways involved in the uptake of particles with various sizes and physicochemical properties (such as the panel used in this chapter), and possible changes in particles internalization mechanism following cell activation/infection should be conducted. Additionally, MS@PEG is the only particle system used characterized by a negative surface charge, which may have implication in the type of protein corona formed from the medium containing infected or activate cells. Therefore, changes in the protein corona composition (e.g. the presence of cytokines secreted upon cell activation or reactivated virus production) and the persistence of cytoskeleton changes associated with viral entry could be also explored.

4.6. References

1. R. K. Singh, J. C. Knowles and H. W. Kim, J. Tissue. Eng, 2019, 10, 2041731419877528.
2. J. P. Liu, T. T. Wang, D. G. Wang, A. J. Dong, Y. P. Li and H. J. Yu, Acta Pharmacol. Sin, 2017, 38, 1-8.
3. Y. Xin, M. Yin, L. Zhao, F. Meng and L. Luo, Cancer Biol. Med., 2017, 14, 228-241.
4. N. Oh and J. H. Park, Int. J. Nanomedicine, 2014, 9 Suppl 1, 51-63.
5. F. Blank, P. A. Stumbles, E. Seydoux, P. G. Holt, A. Fink, B. Rothen-Rutishauser, D. H. Strickland and C. von Garnier, Am. J. Respir. Cell Mol. Biol., 2013, 49, 67-77.
6. E. Frohlich, Int. J. Nanomedicine, 2012, 7, 5577-5591.
7. E. C. Cho, Q. Zhang and Y. Xia, Nat. Nanotechnol., 2011, 6, 385-391.
8. A. Tchoryk, V. Taresco, R. H. Argent, M. Ashford, P. R. Gellert, S. Stolnik, A. Grabowska and M. C. Garnett, Bioconjug. Chem., 2019, 30, 1371-1384.
9. C. G. England, T. Priest, G. Zhang, X. Sun, D. N. Patel, L. R. McNally, V. van Berkel, A. M. Gobin and H. B. Frieboes, Int J Nanomedicine, 2013, 8, 3603-3617.
10. H. Chikaura, Y. Nakashima, Y. Fujiwara, Y. Komohara, M. Takeya and Y. Nakanishi, Biosurf. Biotribol., 2016, 2, 18-25.
11. S. R. Mulay, M. Herrmann, R, Bilyy, A. Gabibov and H. J. Anders, *Nano- and Microparticle-Induced Cell Death, Inflammation and Immune Responses.* Frontiers Media, Lausanne, 2019.
12. R. J. Errington, M. R. Brown, O. F. Silvestre, K. L. Njoh, S. C. Chappell, I. A. Khan, P. Rees, S. P. Wilks, P. J. Smith and H. D. Summers, Cell Cycle, 2010, 9, 121-130.
13. J. A. Kim, C. Aberg, A. Salvati and K. A. Dawson, Nat. Nanotechnol., 2011, 7, 62-68.
14. G. E. Kaiko, J. C. Horvat, K. W. Beagley and P. M. Hansbro, Immunology, 2008, 123, 326-338.
15. A. T. Phan, A. W. Goldrath and C. K. Glass, Immunity, 2017, 46, 714-729.
16. X. An, V. G. Sendra, I. Liadi, B. Ramesh, G. Romain, C. Haymaker, M. Martinez-Paniagua, Y. Lu, L. G. Radvanyi, B. Roysam and N. Varadarajan, PLoS One, 2017, 12, e0181904.
17. C. D. Tsoukas, B. Landgraf, J. Bentin, M. Valentine, M. Lotz, J. H. Vaughan and D. A. Carson, J. Immunol., 1985, 135, 1719-1723.
18. W. Ai, H. Li, N. Song, L. Li and H. Chen, Int. J. Environ. Res. Public Health, 2013, 10, 3834-3842.

19. Y. Amakata, Y. Fujiyama, A. Andoh, K. Hodohara and T. Bamba, Clin. Exp. Immunol., 2001, 124, 214-222.
20. M. R. Hepworth, L. A. Monticelli, T. C. Fung, C. G. Ziegler, S. Grunberg, R. Sinha, A. R. Mantegazza, H. L. Ma, A. Crawford, J. M. Angelosanto, E. J. Wherry, P. A. Koni, F. D. Bushman, C. O. Elson, G. Eberl, D. Artis and G. F. Sonnenberg, Nature, 2013, 498, 113-117.
21. A. A. Okoye and L. J. Picker, Immunol. Rev., 2013, 254, 54-64.
22. I. V. Grishkan, A. Ntranos, P. A. Calabresi and A. R. Gocke, Cell Immunol., 2013, 284, 68-74.
23. B. Stolp and O. T. Fackler, Viruses, 2011, 3, 293-311.
24. D. A. Fletcher and R. D. Mullins, Nature, 2010, 463, 485-492.
25. L. He, E. J. Sayers, P. Watson and A. T. Jones, Sci. Rep., 2018, 8, 7318.
26. A. Boneh, S. Mandala and H. S. Tenenhouse, Biochim. Biophys. Acta, 1989, 1012, 308-316.
27. C. Liu and T. E. Hermann, J. Biol. Chem., 1978, 253, 5892-5894.
28. J. Cui, R. De Rose, K. Alt, S. Alcantara, B. M. Paterson, K. Liang, M. Hu, J. J. Richardson, Y. Yan, C. M. Jeffery, R. I. Price, K. Peter, C. E. Hagemayer, P. S. Donnelly, S. J. Kent and F. Caruso, ACS Nano, 2015, 9, 1571-1580.
29. H. Sun, J. Cui, Y. Ju, X. Chen, E. H. H. Wong, J. Tran, G. G. Qiao and F. Caruso, Bioconjug. Chem., 2017, 28, 1859-1866.
30. M. Wojnilowicz, Q. A. Besford, Y. L. Wu, X. J. Loh, J. A. Braunger, A. Glab, C. Cortez-Jugo, F. Caruso and F. Cavalieri, Biomaterials, 2018, 176, 34-49.
31. J. Cui, K. Alt, Y. Ju, S. T. Gunawan, J. A. Braunger, T. Y. Wang, Y. Dai, Q. Dai, J. J. Richardson, J. Guo, M. Bjornmalm, C. E. Hagemeyer and F. Caruso, Biomacromolecules, 2019, 20, 3592-3600.
32. M. A. Sullivan, F. Vilaplana, R. A. Cave, D. Stapleton, A. A. Grey-Weale and R. G. Gilbert, Biomacromolecules, 2010, 11, 1094-1100.
33. Immune Monitoring Platform, Centre Physiopathologie de Toulouse-Purpan (CPTP), PBMC Isolation from Buffy Coats or Whole Blood. PBMC Cryopreservation, 2015.
34. R. Chen, J. Curran, F. Pu, Z. Zhuola, Y. Bayon and J. A. Hunt, Polymers (Basel), 2017, 9.
35. R. K. Katial, D. Sachanandani, C. Pinney and M. M. Lieberman, Clin. Diag. Lab. Immunol., 1998, 5, 78-81.

36. K. J. Nicholas, A. R. Greenplate, D. K. Flaherty, B. K. Matlock, J. S. Juan, R. M. Smith, J. M. Irish and S. A. Kalams, Cytometry A, 2016, 89, 271-280.
37. J. Killick, G. Morisse, D. Sieger and A. L. Astier, Semin. Immunopathol., 2018, 40, 37-48.
38. A. Horowitz, K. A. Stegmann and E. M. Riley, Front. Immunol., 2011, 2, 88.
39. M. Guilliams, F. Ginhoux, C. Jakubzick, S. H. Naik, N. Onai, B. U. Schraml, E. Segura, R. Tussiwand and S. Yona, Nat. Rev. Immunol., 2014, 14, 571-578.
40. P. Italiani and D. Boraschi, Front. Immunol., 2014, 5, 514.
41. MACS Mitenyl Biotec website, https://www.miltenyibiotec.com/US-en/resources/macs-handbook/human-cells-and-organs/human-cell-sources/blood-human.html (accessed February 2020).
42. S. F. Ziegler, F. Ramsdell and M. R. Alderson, Stem Cells, 1994, 12, 456-465.
43. A. Schultz, S. Koch, M. Fuss, A. S. Mazzotta, M. Sarzotti-Kelsoe, D. A. Ozaki, D. C. Montefiori, H. von Briesen, H. Zimmermann and A. Meyerhans, PLoS One, 2012, 7, e51715.
44. E. Hamlyn, F. M. Ewings, K. Porter, D. A. Cooper, G. Tambussi, M. Schechter, C. Pedersen, J. F. Okulicz, M. McClure, A. Babiker, J. Weber, S. Fidler, S. Insight and S. Investigators, PLoS One, 2012, 7, e43754.
45. C. A. Spina, J. Anderson, N. M. Archin, A. Bosque, J. Chan, M. Famiglietti, W. C. Greene, A. Kashuba, S. R. Lewin, D. M. Margolis, M. Mau, D. Ruelas, S. Saleh, K. Shirakawa, R. F. Siliciano, A. Singhania, P. C. Soto, V. H. Terry, E. Verdin, C. Woelk, S. Wooden, S. Xing and V. Planelles, PLoS Pathog., 2013, 9, e1003834..
46. D. Walker, J. Jason, K. Wallace, J. Slaughter, V. Whatley, A. Han, O. C. Nwanyanwu, P. N. Kazembe, H. Dobbie, L. Archibald and W. R. Jarvis, Clin. Diagn. Lab. Immunol., 2002, 9, 1049-1056.
47. K. H. Roh, B. F. Lillemeier, F. Wang and M. M. Davis, Proc. Natl. Acad. Sci. USA, 2015, 112, E1604-1613.

Chapter 5

Particle-mediated delivery of frataxin plasmid DNA to a human sensory neuronal model of Friedreich's Ataxia

5.1. Abstract

Friedreich ataxia is a genetic disease associated with cardiomyopathy and neurodegeneration of the cerebellar brain region and sensory neurons of dorsal root ganglia. It is caused by a mutation of frataxin gene, resulting in decreased levels of mitochondrial protein frataxin. With limited treatment options available to date, increasing frataxin protein levels through gene therapy is envisaged to improve therapeutic outcomes for patients with Friedreich's Ataxia. A non-viral strategy using submicrometer-sized multilayered particles to deliver frataxin-encoding plasmid DNA is presented. Particle treatment resulted in a 27000-fold increase in frataxin gene expression within 2 days *in vitro* in a stem cell-derived neuronal model of FRDA. These results highlight the potential use of templated particles in gene therapy targeting neurodegenerative diseases of the peripheral nervous system.

5.2. Introduction

Friedreich ataxia (FRDA) is an autosomal recessive disease characterized by neurodegeneration and cardiomyopathy and is the most common form of all inherited ataxias known to date.[1] Prominent regions of neurodegeneration occur within the cerebellar brain region and sensory neurons of the dorsal root ganglia (DRG).[2] Neurodegeneration in FRDA affects primarily the peripheral sensory neurons systems.[3] Symptoms include limb ataxia, areflexia, sensory loss, and motor dysfunction, accompanied by cardiomyopathy and diabetes as the disease progresses.[4,5] Although symptoms may vary between patients and are related to the severity of the disease, patients usually become wheelchair-bound within 15 years after the onset of disease.[6] Further neurodegeneration significantly reduces their quality of life and arrhythmias and heart failure that develop as a result were identified as the most common cause of death.[7] FRDA is associated with progressive degeneration of large sensory neurons in the DRG and their axonal projection in the posterior columns and degeneration of the spinocerebellar and corticospinal tracts of the spinal cord.[8] FRDA occurs as a result of the presence of a trinucleotide GAA repeat expansion in the first intron of the FRATAXIN (FXN) gene located on chromosome 9, resulting in a reduced level of the small mitochondrial protein frataxin (FXN).[9] The severity and progress of FRDA depend on the number of repeats in the *FXN* gene, which ranges from 70 to over 1000 in most severe cases.[10] The presence of GAA expansion causes epigenetic changes in the chromatin and affects transcription of *FXN*.[11] Reduced levels of FXN lead to cytotoxicity and cell death within the nervous system and cardiac tissue.

Considerable effort has been made toward the development of new treatments for FRDA and several agents showed promising results in animal and cellular models, however, results from clinical trials were often inconclusive.[12,13] As to this date, there is no cure to FRDA and therapies are aimed partly at slowing down the neurodegeneration, but mostly at providing relief in symptoms.

Encouraged by promising results for several other genetic diseases,[14,15] preclinical studies using alternative gene and cell replacement therapies for the treatment of FRDA have been initiated. For example, an attempt to excise the mutated fragment of FXN gene was demonstrated by Yanjie L. et al. in studies utilizing zinc finger nucleases (ZFNs) to remove the GAA expansion in FRDA patient-derived cells.[16] This strategy resulted in increased *FXN* mRNA and protein expression. Moreover, the therapeutic effect and increased ATP levels were

also demonstrated in iPSC derived neuronal cells and the successful correction of iPSCs strongly supports the potential of cell replacement therapies in FRDA.[17] Virus-based, gene therapy approach was used by Piguet et al. to deliver FXN expressing vector to a conditional mouse model with *FXN* deletion to target major neuronal subpopulation affected in FRDA and a reversal of sensory ataxia was observed.[18] Another viral strategy was used by Perdomini et al, where treatment of a mouse model by adenovirus-based FXN expressing vector fully prevented cardiomyopathy associated with FRDA.[19] Although promising, the use of viruses as gene delivery vectors is not without challenges. Safety concerns regarding spontaneous mutations of the vector, immunogenicity and proinflammatory effect have led to research into more versatile and biocompatible drug delivery systems.[20,21] In this approach, therapeutic cargo can be encapsulated by inorganic, lipid or polymer-based nanoparticles and delivered into tissues.[22,23,24] Only a few studies have reported the use of nanoparticles in the treatment of FRDA. Lipid nanoparticles containing *FXN* mRNA was administered intravenously in adult mice in the work of Nabhan et al.[25] The use of RNA therapy resulted in over 50% of *mFXN* being processed to mature protein within 24 h *in vivo* and was the first reported attempt to deliver therapeutic mRNA to the dorsal root ganglia. However, the effect of *FXN* mRNA is short-lasting and would require sustained delivery to ensure continuous protein production.

In the present study, we describe the use of a highly biocompatible layer-by-layer (LbL) particle system to deliver an *FXN* expression plasmid into sensory neurons derived from FRDA-induced pluripotent stem cells (iPSC). We used confocal microscopy to show internalization of particles by patient-derived neurons, supported by functional data showing up to a 27000-fold increase in *FXN* cDNA when compared to untreated cells. This study highlights the potential of particle-mediated DNA delivery in gene therapy for FRDA.

5.3. Experimental section

5.3.1. Materials

Silica particles (0.889 ± 0.003 µm, 5% w/v aqueous solution) were purchased from microParticles GmbH (Berlin, Germany). Poly(ethylenimine) (PEI) low molecular weight 50 wt% solution in water, poly-L-arginine hydrochloride, molecular weight >70000; poly(sodium

4-styrenesulfonate) (PSS) molecular weight ~70000, albumin from bovine serum (BSA), Dulbecco's phosphate buffered saline (DPBS), without calcium chloride or magnesium chloride, agarose, glucose, and 4′,6-diamidino-2-phenylindole (DAPI) were purchased from Sigma-Aldrich (St. Louis, MI, USA). Plasmid DNA (pEGFP, 3 kbp) was obtained from CSIRO (Australia) and pcDNA3-Luc (5.9 kbp) was a gift from Dr. Yunti Zhang. Sodium chloride (NaCl) was purchased from Chem-Supply (Gillman, Australia). Alexa Fluor *N*-hydroxysuccinimide (NHS) dyes (AF_{488} and AF_{555}), Alamar blue cell viability reagent, wheat germ agglutinin (WGA), Alexa Fluor 488 conjugate (WGA-AF_{488}), Hoechst 33342 (10 mg mL^{-1} solution in water), lipofectamine, N2B27 medium, Dulbecco's modified Eagle's medium (DMEM)/F12 medium, insulin, transferrin, and selenium additives, N_2 supplement, retinol-free B27 supplement, penicillin-streptomycin, GlutaMAX, and PureLink RNA mini kit were purchased from Life Technologies (Scoresby, Australia). Dialysis tubing (molecular weight cutoff (MWCO) 3.5 kDa) and Nunc Lab-Tek II Chamber microscopy slides were purchased from Thermo Fisher Scientific (Scoresby, Australia). DNA electrophoresis sample loading dye was purchased from Bio-Rad (Gladesville, Australia). Brain-derived U-87 MG glioblastoma cell line (HTB-14) was purchased from the American Type Culture Collection (ATCC; Manassas, VA, USA). DMEM (with 4.5 g L^{-1} glucose and L-glutamine) and trypsin (10X) were purchased from Lonza (Basel, Switzerland). Fetal bovine serum was purchased from Bovogen Biologicals (Keilor East, Australia). Paraformaldehyde 4% aqueous solution (EM grade, 4% PFA) was purchased from Electron Microscopy Sciences. Vitronectin and Tesr-E8 basal medium were purchased from StemCell Technologies. Y-27632 was purchased from Selleckchem. Brain-derived neurotrophic factor (BDNF), fibroblast growth factor-basic (FGF-basic), beta nerve growth factor (bNGF), and neutrotrophin-3 (NT-3) were purchased from PeproTech. CHIR99021 and SB431542 were purchased from Tocris Bioscience. Bone morphogenetic protein 2 (BMP2), goat anti-human TRKA (AF175), sheep anti-human/mouse/rat PV (AF5058), and goat anti-human SPP1 (AF1433) were purchased from R&D Systems. Mouse anti-human TRKB (NBP1-47898) was purchased from Novus Biologicals. Rabbit anti-human TRKC (701985) was purchased from Thermo Fisher Scientific. Mouse anti-human PRPH (H00005630-M02) was purchased from Abnova. Chicken anti-human/mouse/rat TUBB3 (ab41489) was purchased from Abcam. Secondary antibodies donkey Alexa Fluor 488 and donkey Alex Fluor 568 were purchased from Thermo Fisher Scientific, and donkey anti-chicken AF_{488} was purchased from Jackson ImmunoResearch. Dako fluorescent mounting medium was purchased from Agilent Technologies. Donkey serum

was purchased from Millipore (Millipore Corporation, Billerica, MA, USA) and Milli-Q water was obtained from a Millipore Milli-Q purification system.

5.3.2. Quartz crystal microbalance with dissipation (QCM-D) monitoring

Layer-by-layer (LbL) film buildup of cationic poly-L-arginine (PLArg) and anionic PSS) and subsequent adsorption of DNA was studied using QCM-D. The gold crystal QCM surface was cleaned by exposure to Piranha solution (one part of 30% H_2O_2 in three parts of H_2SO_4) for 2 min, followed by rinsing in pure water and drying with nitrogen. *Caution: Piranha solution is highly corrosive. Extreme care should be taken when handling Piranha solution and only small quantities should be prepared.* PEI solution (2 mg mL^{-1}) was prepared in Milli-Q water with 1 M NaCl. PSS (1 mg ml^{-1}) and PLArg (1 mg ml^{-1}) solutions were prepared in 50 mM sodium acetate buffer pH 5.2, which was also used in washing steps after each layer. PEI was deposited on the electrode as the first (primer) layer. After 15 min of incubation, the excess polymer was removed by rinsing for 5 min with water. Sequential deposition of PSS and PLArg (15 min adsorption followed by three washing cycles in buffer) was repeated until four PSS/PLArg bilayers or $(PSS/PLArg)_4$ were formed. To assess DNA binding to the PLArg-terminated film, DNA (10 µg mL^{-1} in 50 mM sodium acetate buffer pH 5.2) was introduced and adsorbed for 20 min, followed by washing with buffer. The mass of deposited nucleic acid was calculated using Sauerbrey's equation:[26]

$$\Delta F = -\frac{2F_0^2}{A(\mu_q \rho_q)^{1/2}} \Delta m$$

where F_0 is the resonance frequency of the crystal (9×10^6 Hz), μ_q is the shear modulus of the quartz (2.947×10^{13} g m^{-1} s^{-2}), ρ_q is the density of the quartz (2.648×10^6 g m^{-3}), and A is the piezoelectric area of the electrode.

5.3.3. Atomic force microscopy (AFM)

Silicon wafers were ultrasonically cleaned in ethanol for 2 h to remove any unwanted residues on the surface and dried under a nitrogen stream. PEI-$(PSS/PLArg)_2$ and PEI-$(PSS/PLArg)_2$-DNA films were prepared on silicon wafers using the adsorption and washing

conditions as those described for QCM and dried under a gentle stream of nitrogen. AFM experiments were conducted on a JPK NanoWizard II BioAFM instrument. Typical scans were performed in tapping mode with MikroMasch silicon cantilevers (NSC/CSC). The roughness of the air-dried films was analyzed using JPK SPM image processing software (version V.3.3.32).

5.3.4. Preparation of multilayered particles

Multilayered particles were prepared by LbL deposition of PEI-(PSS/PLArg)$_4$ on spherical silica particles. Silica particles (40 µL, 0.05 wt%) were washed by dispersing in 200 µL of Milli-Q water and mixed vigorously by vortexing, followed by centrifugation (500 *g*, 1.5 min). The supernatant was removed, and the dispersion and centrifugation cycles were repeated once with water then twice with buffer (50 mM sodium acetate buffer pH 5.2). Polyelectrolyte solutions were prepared as per the procedure described for QCM-D. To prime the LbL film buildup, PEI was adsorbed as the first layer. Specifically, 200 µL of PEI was added to 200 µL of the silica particle suspension in water. Adsorption was carried out for 15 min, followed by centrifugation (conditions as described above). The supernatant was removed, and the particles were re-dispersed in 500 µL of water, followed by centrifugation. The particles were washed in water three times. For the subsequent formation of PSS/PLArg bilayers, 500 µL of polyelectrolyte was added to 200 µL of particles in sodium acetate buffer. After 15 min adsorption, three washing cycles were performed using buffer as the dispersant. For the AF$_{488}$- or AF$_{555}$-labelled particles, the PLArg labelled with the dye was used as the seventh layer (see below for labelling method). To monitor the assembly process, a small volume of particle sample was removed after each deposition step for ζ-potential measurements. Particles were counted using an Apogee A50-Microflow cytometer.

5.3.5. Particle characterization

The LbL assembly on particles was monitored by measuring the change in ζ-potential after each layer deposition. For the ζ-potential measurements, 2 µL of the sample (~8×10^6 particles µL^{-1}) was dispersed in 798 µL of water. To assess nucleic acid binding, DNA was complexed to the particles for 20 min in 30 µL of sodium acetate buffer pH 5.2 (2×10^6 particles per 0.5 µg of DNA), followed by the addition of 760 µL of Milli-Q water. All measurements were

performed at 25 °C in folded capillary cells (DTS1070, Malvern Instruments) using a Zetasizer Nano-ZS instrument (Malvern Instruments).

For the scanning electron microscopy (SEM) analysis, silicon wafers were cleaned in a bath (100 mL of 80% H_2SO_4, 35 mL H_2O_2 and 20 mL Milli-Q water) at room temperature and dried with compressed nitrogen gas. Particle suspensions (2 µL of stock suspended in 18 µL of 5 mM sodium acetate buffer) were deposited on the silicon wafer and air-dried. Samples were washed with Milli-Q water four times. Images were acquired using an FEI Quanta 200 field-emission scanning electron microscope at an operation voltage of 10 kV.

5.3.6. Labelling PLArg with Alexa Fluor-NHS dyes

For labelling, 10 mg of PLArg (equivalent to 0.057 mmol of arginine monomer) was dissolved in 5 mL of 50 mM sodium acetate buffer, pH 5.2. Either AF_{488} or AF_{555} (2.8×10^{-4} mmol) was added and the resulting solution was incubated for 2 h, protected from light, with mixing. Excess dye was removed by dialysis (MWCO 3.5 kDa) against Milli-Q water for 2 days (5 times water change). The product was freeze-dried and stored at 4 °C until further use.

5.3.7. DNA–Particle complexation

Analysis of DNA–particle complexation was performed using agarose gel electrophoresis. Particle suspensions with varying numbers of particles per sample (1×10^5, 2×10^5, 2×10^6, 8×10^6, 3.6×10^7, and 7.2×10^7) were prepared in 50 mM sodium acetate buffer, pH 5.2. Model plasmid DNA (pEGFP, 3 kbp) was diluted in the same buffer and added to each particle suspension (100 ng of DNA per sample). After 20 min of incubation (room temperature, mixed by vortexing every 5 min), samples were centrifuged (600 *g*, 2 min) and 30 µL of the supernatant that contained unbound DNA was mixed with 6 µL of nucleic acid loading dye and loaded in a 1.6% agarose gel. Electrophoresis was carried out for 50 min at 110 V. Samples containing DNA only or particles only in buffer were also loaded as controls.

5.3.8. Cell culture

U87-MG human brain glioblastoma (ATCC HTB-14) cell line was cultured in DMEM supplemented with 10% fetal bovine serum. Cells were cultured at 37 °C, 5% CO_2 in a humidified atmosphere.

5.3.9. Particle–cell association

In 24-well plates, cells were seeded at 6×10^4 cells per well in 400 µL of medium and left overnight at 37 °C, 5% CO_2 in a humidified atmosphere. Particles labelled with AF_{555} were added at varying particle-to-cell ratios of 10, 50, 200, and 500 for 24 h at 37 °C, 5% CO_2 in a humidified atmosphere. After incubation, the cells were detached by trypsinization (200 µL of 0.05% trypsin) and washed twice by centrifugation–resuspension cycles (300 *g*, 5 min). Cells were suspended in 200 µL of PBS containing 1% BSA and analyzed on a BD Accuri C6 flow cytometer. Data were acquired for at least 1×10^4 cells per sample.

5.3.10. Cellular uptake of fluorescently labelled particles by U87-MG cells

Cells were seeded in 8-well chamber slide at 6×10^4 cells per well in 400 µL of medium and left overnight at 37 °C, 5% CO_2 in a humidified atmosphere. The media was aspirated and replaced with 370 µL of fresh medium, to which 30 µL of AF_{555}-labelled particle suspension was added at a particle-to-cell ratio of 200. After incubation for 24 h (37 °C, 5% CO_2 in a humidified atmosphere), the cells were washed twice with DPBS and incubated for 5 min at room temperature with WGA solution at 10 µg mL^{-1} in DPBS, after which fixation was performed for 10 min at room temperature using 4% PFA. Nuclei were stained using Hoechst 33342 (1 µg mL^{-1}). Cells were imaged with a Nikon A1R confocal microscope equipped with a 60× oil objective.

5.3.11. Cell viability

Cells were plated on a 96-well plate at 1×10^4 cells per well in 100 µL of medium and left overnight at 37 °C, 5% CO_2 in a humidified atmosphere. Particle suspensions were prepared in 50 mM sodium acetate buffer pH 5.2, with varying numbers of particles per sample (1×10^5,

5×10^5, 2×10^6, and 5×10^6) at respective particle-to-cell ratios of 10, 50, 200, and 500. For samples containing model plasmid DNA (pcDNA3-Luc), particle suspensions were prepared in the same way and incubated with 0.5 μg of DNA for 20 min at room temperature in sodium acetate buffer prior to addition to U87-MG cells. Particles, with or without DNA, were added to cells and incubated for 24 h at 37 °C, 5% CO_2 in a humidified atmosphere. After incubation, the media was aspirated and replaced with 100 μL of fresh medium, to which 10 μL of Alamar blue reagent was added. After incubation for 4 h (37 °C, 5% CO_2 in a humidified atmosphere), cell fluorescence (excitation 560 nm/emission 590 nm) was measured on a Tecan Infinite M200 microplate reader.

5.3.12. Friedreich ataxia (FRDA) iPSC cell culture and differentiation to sensory neurons

This project was approved by The University of Melbourne Human Ethics committee (1545394 and 0829937). Culture and differentiation of sensory neurons were done by Dr Serena Viventi. FRDA 'FA10' iPSC lines were maintained as bulk culture in feeder-free conditions on vitronectin-coated dish using Tesr-E8 basal medium. Differentiation of FRDA iPSC to sensory neurons was performed using previously published protocols.[27,28] Briefly, iPSCs were plated per laminin-coated organ culture dish in TeSR-E8 complete medium supplemented with 10 μM Y-27632 for 24 h. Then, TeSR-E8 complete medium was replaced with N2B27 medium containing 1:1 mix of neurobasal medium (NBM) and DMEM/F12 medium, 1% insulin/transferrin/selenium, 1% N_2 supplement, 1% retinol-free B27 supplement, 1% GlutaMAX, 1% penicillin-streptomycin, 0.3% glucose, and supplemented with CHIR99021 (3 μM) and SB431542 (10 μM). After 5 days, cells were harvested, spun at 200 *g* for 3 min and resuspended in NBM containing 1% insulin/transferrin/selenium, 1% N_2 supplement, 1% retinol-free B27 supplement, 1% penicillin-streptomycin, 1% GlutaMAX, and supplemented with 10 ng mL^{-1} of BMP2 and 20 ng mL^{-1} of bFGF. Cells were then cultured in ultralow attachment plates at 37 °C and 5% of CO_2 in a humidified incubator for 4–6 days to promote neurosphere (NSP) formation. The following day, the cells were cultured in NBM complete medium with 10 ng mL^{-1} BDNF, 10 ng mL^{-1} NGF, and 10 ng mL^{-1} NT-3 supplements to support differentiation to sensory neurons. After two weeks, NSPs were mechanically dissociated and plated onto poly-D-lysine and laminin-coated dishes for an additional 7 days in NBM supplemented with 10 ng mL^{-1} BDNF, 10 ng mL^{-1} NGF, and 10 ng mL^{-1} NT-3 to support maturation of neurons, cultured as a monolayer.

5.3.13. Incubation of particles with FRDA iPSC-derived sensory neurons

Confocal microscopy. AF_{488}-labelled particles were used to examine particles uptake in sensory neurons. For samples without plasmid DNA, 30 µL of particle suspension (2×10^6 particles) in 50 mM sodium acetate buffer was prepared immediately before addition to cells. For samples containing particles with bound DNA, a particle suspension (2×10^6) was prepared in sodium acetate buffer and incubated with 0.5 µg of pcDNA3-Luc for 20 min at room temperature, before addition to human sensory neurons cells. Particles were added to 3 weeks differentiated FRDA iPSC-derived sensory neurons for an incubation period of 24 h, after which cells were washed with DPBS, fixed with 4% PFA, and incubated with Cell Mask Deep Red Plasma membrane at 5 µg mL^{-1} in DPBS for 10 min at room temperature. Nuclei were stained using DAPI (1 µg mL^{-1}). Images were acquired on a Nikon A1R confocal microscope equipped with a 60× oil objective.

Quantitative polymerase chain reaction (Q-PCR) analyses. Cells were incubated with particles or particles with bound frataxin *(FXN)-green fluorescent protein (GFP)* expression plasmid for 24 h (particle preparation as described above), after which cells were washed extensively with supplemented NBM and cultured for another 24 h or 13 days before harvesting.

5.3.14. Gene expression analyses

Gene expression analyses were performed by Dr Serena Viventi. For each sample, total RNA was extracted using PureLink RNA mini kit according to the manufacturer's instructions and then processed to generate cDNA. Q-PCR analysis was performed on cDNA samples and experiments were conducted to obtain relative levels of each transcript normalized to the endogenous controls E74-like ETS Transcription Factor 1 (ELF1), glyceraldehyde 3-phosphate dehydrogenase (GAPDH), and hydroxymethylbilane synthetase (HMBS) for each sample. The specific probes (Life Technologies) that were used in the present study were FXN (Hs00175940_m1) and Caspase 3 (CASP3; Hs00234387_m1). Probes used as controls were ELF1 (Hs00152844_m1), GAPDH (Hs02758991_g1), and HMBS (Hs00609297_m1).

5.3.15. Immunostaining analyses of differentiated FRDA iPSC

Immunostaining of differentiated sensory neurons was performed by Dr Serena Viventi. Cells were fixed with 4% PFA on ice for 10 min and permeabilized for 15 min at room temperature using 0.2% triton-X100 solution. Incubation with primary and secondary antibodies was performed in 10% normal donkey serum/DPBS blocking solution overnight at 4 °C and for 1 h at room temperature, respectively. The following antibody dilutions were used: goat anti-human TRKA (1:200); mouse anti-human TRKB (1:200); rabbit anti-human TRKC (1:250); sheep anti-human/mouse/rat PV (1:500); goat anti-human SPP1 (1:500); mouse anti-human PRPH (1:200); and chicken anti-human/mouse/rat TUBB3 (1:2000). All Alexa Fluor secondary antibodies were used at 1:1000 dilution except for donkey anti-chicken secondary antibody, which was used at 1:200. Nuclei were stained using DAPI (1 μg mL^{-1}). Three washes with DPBS solution were performed at each step, allowing 3 min between each wash. Samples were mounted onto slides (Super Frost Plus Slide, Thermo Fisher Scientific) using Dako fluorescent mounting medium, imaged immediately or stored at 4 °C. For long storage, samples were kept at −80 °C.

5.3.16. Statistical analyses

Statistical analyses were performed using GraphPad Prism 5 software. Q-PCR data are presented as the mean average ± standard error of the mean, with $n = 3$ biological replicate experiments and $n > 3$ technical replicate samples for each replicate experiment.

5.4. Results and discussion

Particles were prepared *via* the templated layer-by-layer (LbL) assembly method using interacting PSS and PLArg to form a multilayered film on spherical silica template. The LbL method has been used previously to prepare polymeric capsules and coatings on planar and colloidal substrates, offering versatility in terms of composition and substrates.[27,28] Preparation of nanoparticles *via* LbL methods enables precise engineering of particles physicochemical properties, such as size, shape and surface chemistry; and the preparation is simplified by a variety of templates that are commercially available.[29] The loading of drugs, including small molecular weight drugs, proteins, and nucleic acids within the template itself, embedded within the multilayer film, or adsorbed on the particle surface, has been demonstrated for various applications including cancer therapy, atherosclerosis, and vaccines.[30,31,32] In the present study, a film of alternating layers of anionic PSS and cationic PLArg was formed on 889 nm PEI-coated silica particles (**Scheme 5.1**).

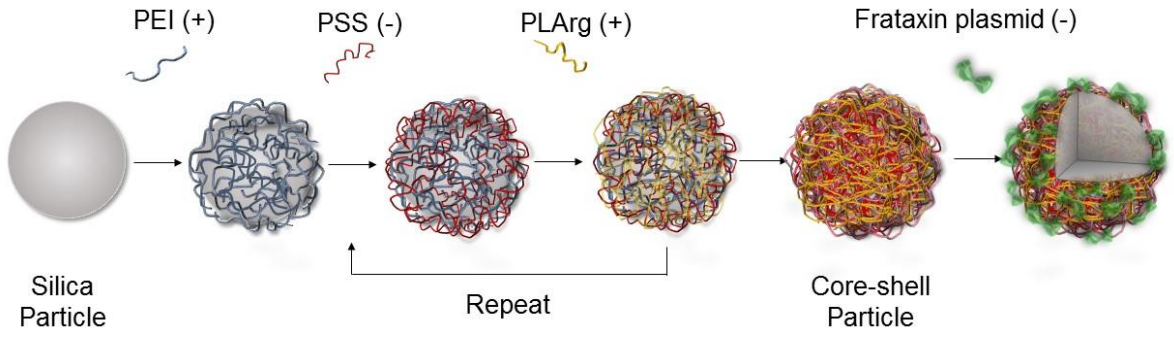

Scheme 5.1. LbL assembly on silica particles. LbL core-shell particles were prepared by deposition of anionic PSS and cationic PLArg on PEI-coated silica template. Plasmid DNA was adsorbed on the particle surface *via* electrostatic interactions.

First, the formation of film was studied using quartz crystal microgravimetry with dissipation (QCM-D, **Figure 5.1A**). Mass of the adsorbed material on a planar surface was measured by a decrease in the resonance frequency of an oscillating piezoelectric crystal and a stepwise pattern observed corresponds to the LbL assembly of the film. The mass of adsorbed DNA was calculated according to Sauerbrey's equation,[26] obtaining an estimated coverage of 0.43 μg DNA per cm^3. This is consistent with reported DNA complexation on polycationic

surfaces, including poly-β-amino esters, where plasmid DNA coverage of up to 0.44 μg of DNA per cm^2 was observed per bilayer.[33] The same sequence of polyelectrolytes was used to form LbL film on spherical silica templates, i.e., PLArg-terminated core-shell particles. The assembly process was monitored by ζ-potential measurements after each deposition step and the pattern of charge reversal confirmed the sequential deposition of PLArg and PSS on a PEI-coated silica template (**Figure 5.1B**). Complexation of plasmid DNA was studied by atomic force microscopy (AFM). The increase of film roughness after DNA adsorption [from RMS=0.6 nm for PEI-$(PSS/PLArg)_2$ to RMS=1.4 nm for PEI-$(PSS/PLArg)_2$-DNA] confirmed electrostatic binding of DNA to the PLArg-terminated surface (**Figure 5.1C**). Particles prepared with AF_{488}-labelled PLArg as a seventh layer were prepared to enable tracking *via* flow cytometry and confocal microscopy. Example of fluorescently labelled LbL particles (889 nm) is presented in **Figure 5.1D**. To complete particles characterization, scanning electron microscopy (SEM) was used to assess changes in particles surface morphology (**Figure 5.1E**).

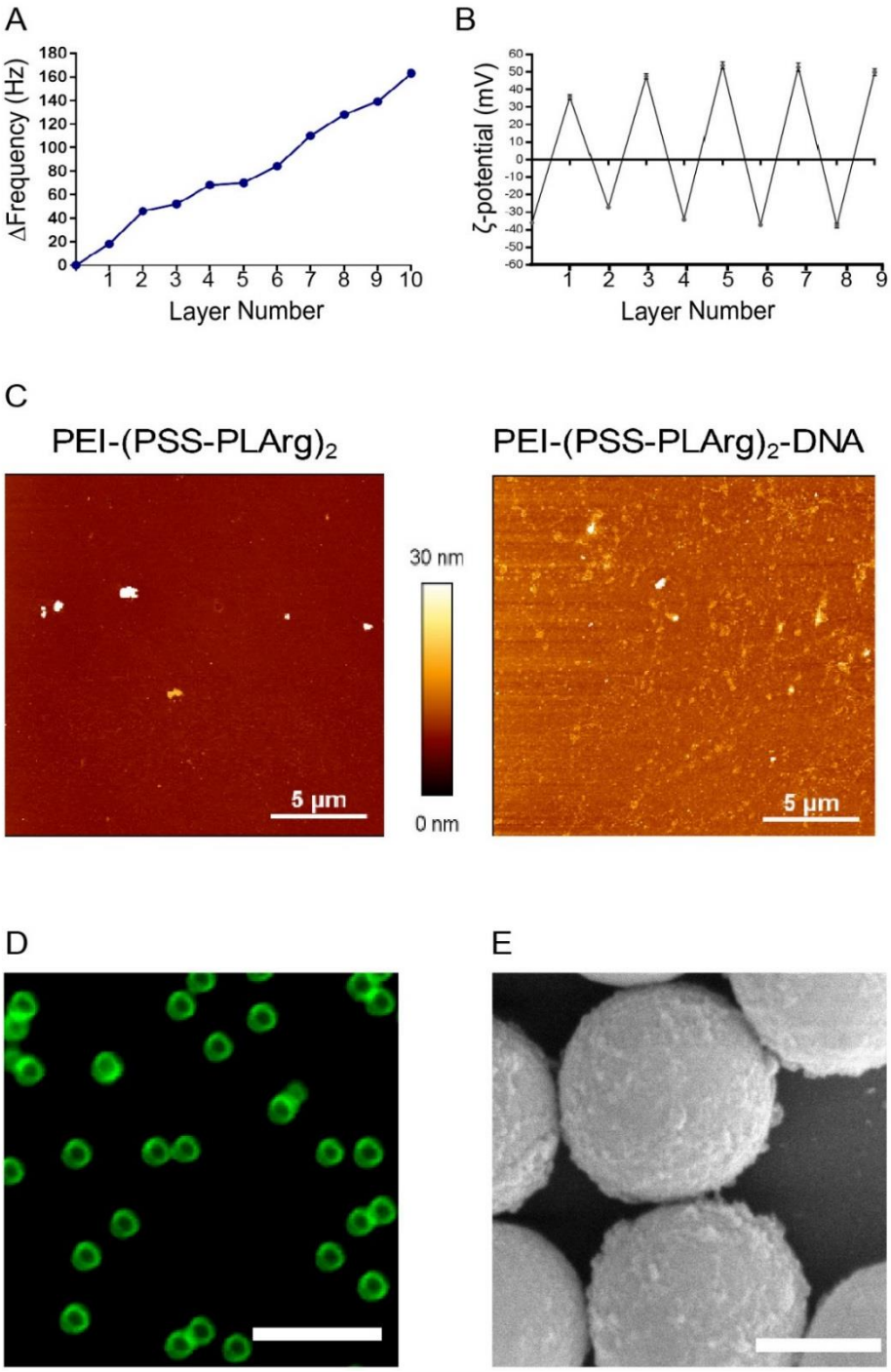

Figure 5.1. LbL film and particles characterization. (A) LbL film assembly was monitored by QCM-D. The odd layer numbers correspond to PLArg (except Layer 1, which is PEI), and the even layer number corresponds to PSS (except Layer 10, which is plasmid DNA). (B) ζ-potentials measurement showing the LbL film deposition on silica particles (Layer 0). (C) AFM images showing the change in roughness after LbL film and plasmid DNA deposition on a flat silica surface. (D) Confocal microscopy image of fluorescently labelled particles (AF_{488}-PLArg used as 7th layer). (E) SEM image of LbL particles. *Scale bars are 5 µm.*

The initial cell association and internalization experiments were performed using brain-derived glioblastoma cell line U-87 MG. Spherical silica templates (889, 500 and 235 nm size) were used to prepare core-shell particles with a film structure PEI-(PSS/PLArg)$_4$. Soft, hollow capsules, obtained after silica core dissolution, were also used. Association of particles at varying sizes and rigidity (core-shell particles and capsules) was first studied *via* flow cytometry. Core-shell particles showed a higher association with U-87 MG after 24 h incubation, with the highest association (>85%) for 889 nm silica particles (**Figure 5.2A**). To examine whether this effect is dose-dependent, we repeated this experiment using 889 nm core-shell particles at varying particle-to-cell ratios (**Figure 5.2B**). From **Figure 5.2B** it can be estimated that a particle-to-cell ratio above 100 suffices to achieve over 80% cell association.

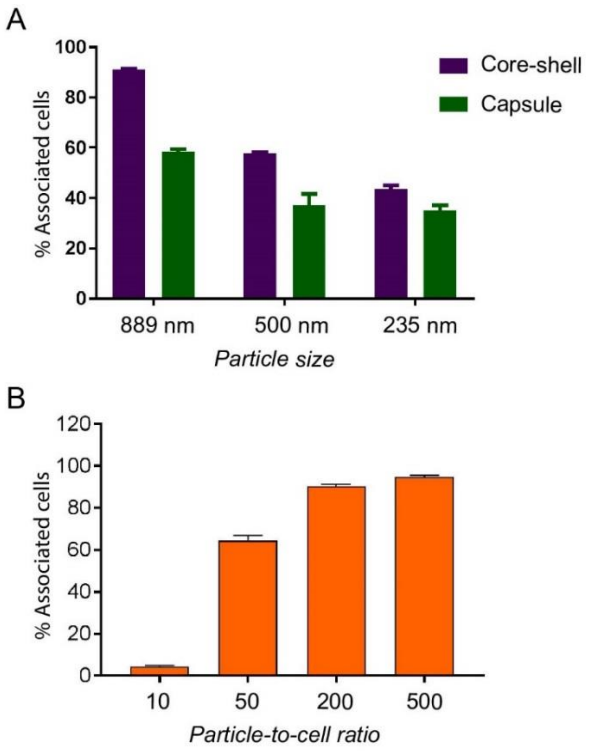

Figure 5.2. LbL particles association with U-87 MG. (A) Cell association of core-shell particles and capsules (AF_{488}-PLArg used as 7th layer) after 24 h incubation at particle-to-cell ratio 200. (B) Cell association of 889 nm LbL silica particles (AF_{555}-PLArg used as 7th layer) at different particle-to-cell ratios after 24 h incubation.

Interactions with cells were further studied *via* confocal microscopy, which revealed that the majority of core-shell particles were internalised, regardless of particles size (**Figure 5.3A to 5.3D**).

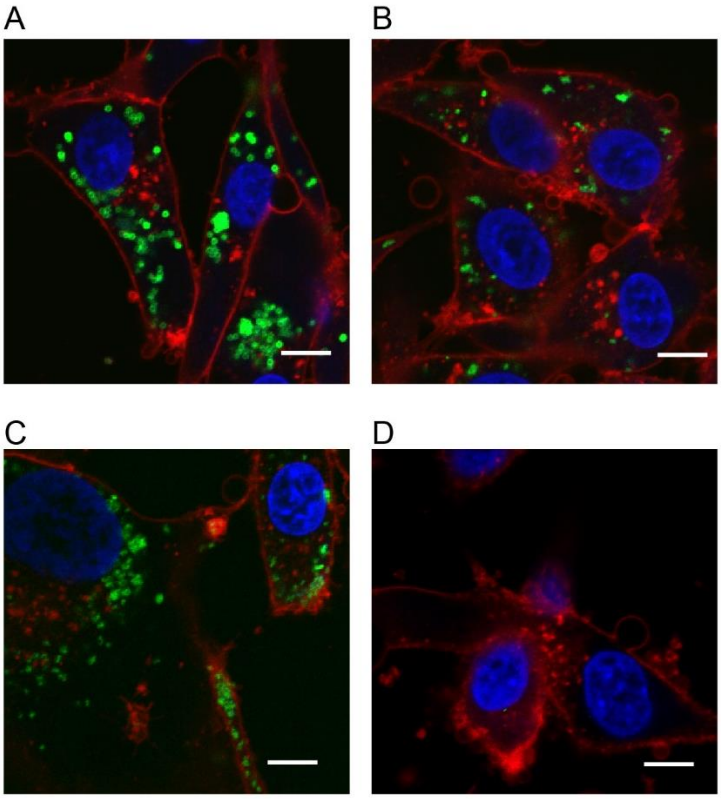

Figure 5.3. Particles internalization in U-87 MG. Cell internalization of LbL core-shell particles after 24 h incubation: (A) 889 nm, (B) 500 nm, (C) 235 nm and (D) untreated cells control. AF_{488}-PLArg was used as 7^{th} layer. Nuclei were stained with Hoechst 33342 (blue) and cell membrane was stained with Cell Mask Deep Red Plasma membrane stain. *Scale bars are 10 μm.*

Based on these results, LbL 889 nm core-shell particles were used to optimize DNA binding. Loading of plasmid DNA was based on electrostatic interactions between cargo (DNA) and particles surface (PLArg). Complexation of DNA was first studied using agarose gel electrophoresis. **Figure 5.4A** shows a gradual binding of plasmid DNA (100ng, pEGFP 3kbp) with an increasing number of particles. The absence of free plasmid DNA band on the gel indicates the particle-to-DNA ratio at which all DNA is bound to the particles. The complete complexation of 100 ng DNA occurs after incubation with $> 2\times10^6$ particles, corresponding to

an estimated surface coverage of 1961–490 ng DNA per cm^2. Upon DNA adsorption, the particle surface charge is expected to shift from positive, owing to the PLArg outer layer, to negative, owing to the phosphate groups on DNA. Measurement of the ζ-potential, which is indicative of the surface charge of the particles, indeed shows a shift from positive to negative ζ-potentials, *i.e.*, from 54 ± 5 mV to −45 ± 4 mV. The overall negative charge on the particles is advantageous—previous reports have shown that regardless of nanoparticle shape and material, negatively charged nanoparticles interact with neuronal membranes and are more efficiently internalized than positive or neutral particles.

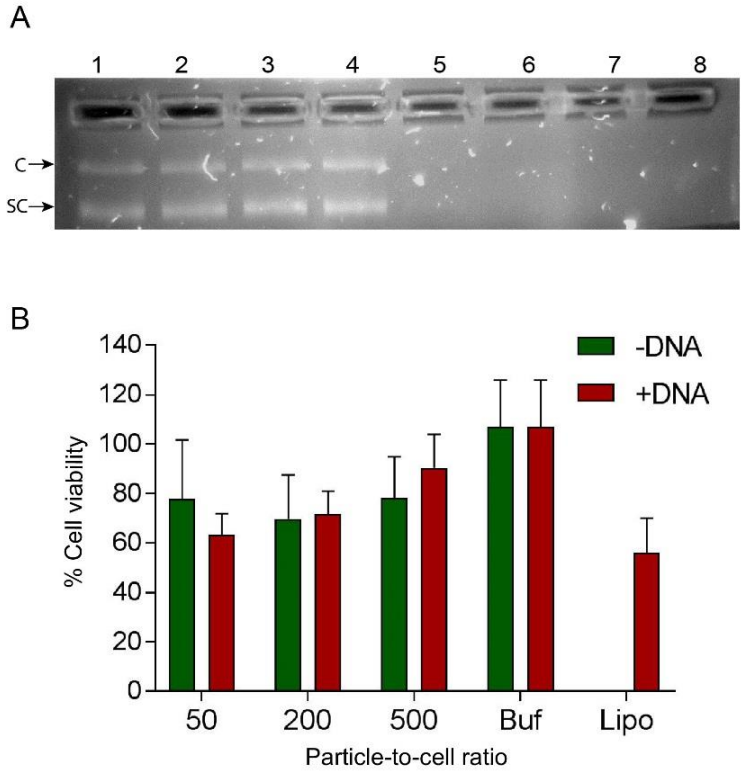

Figure 5.4. DNA complexation and cytotoxicity. (A) Agarose gel electrophoresis analysis of pEGFP plasmid DNA complexation by particles: Lane 1, plasmid DNA; Lanes 2–7, particle/DNA complexes at different ratios (DNA complexed by 1×10^5, 2×10^5, 2×10^6, 8×10^6, 3.6×10^7, and 7.2×10^7 particles, respectively); and Lane 8, particles only control. The two bands in Lanes 1–4 correspond to two conformations of plasmid DNA: circular (C) and supercoiled (SC). (B) Viability of cells after incubation for 24 h with bare core-shell particles (−DNA) (green) and DNA (pcDNA3-Luc)-coated core-shell particles (+DNA) (red) added at varying particle-to-cell ratios as measured by Alamar blue cell viability reagent. Controls: cells incubated with buffer (Buf) and cells incubated with lipofectamine complexed with DNA (Lipo).

The cytotoxicity of proposed system was tested using PLArg-terminated particles (no DNA) and particles with complexed DNA (0.5 μg DNA) at varying particle-to-cell ratios. At least 70% cell viability was observed at particle-to-cell ratios above 50 (**Figure 5.2B**) and attained higher cell viability than the commonly used transfection reagent lipofectamine.

Given the low cytotoxicity, high cell association of the particles and efficient DNA complexation, we tested the uptake of our particle system in patient-derived FRDA iPSCs. This approach allowed us to test the proposed *FXN* plasmid delivery system in a more accurate model of FRDA, i.e. human cells carrying the genetic information of the disease. FRDA iPSC cells were differentiated by the Dottori group (University of Wollongong) using their previously published protocol.[34] Characterization of the differentiated sensory neurons was performed by immunostaining. As presented in **Figure 5.5**, used cell model consists of heterogenous subpopulations of sensory neurons present in DRG, namely i) nociceptors (TRKA), ii) mechanoreceptors (TRKB), and iii) proprioceptors (TRKC, osteopontin and parvalbumin).

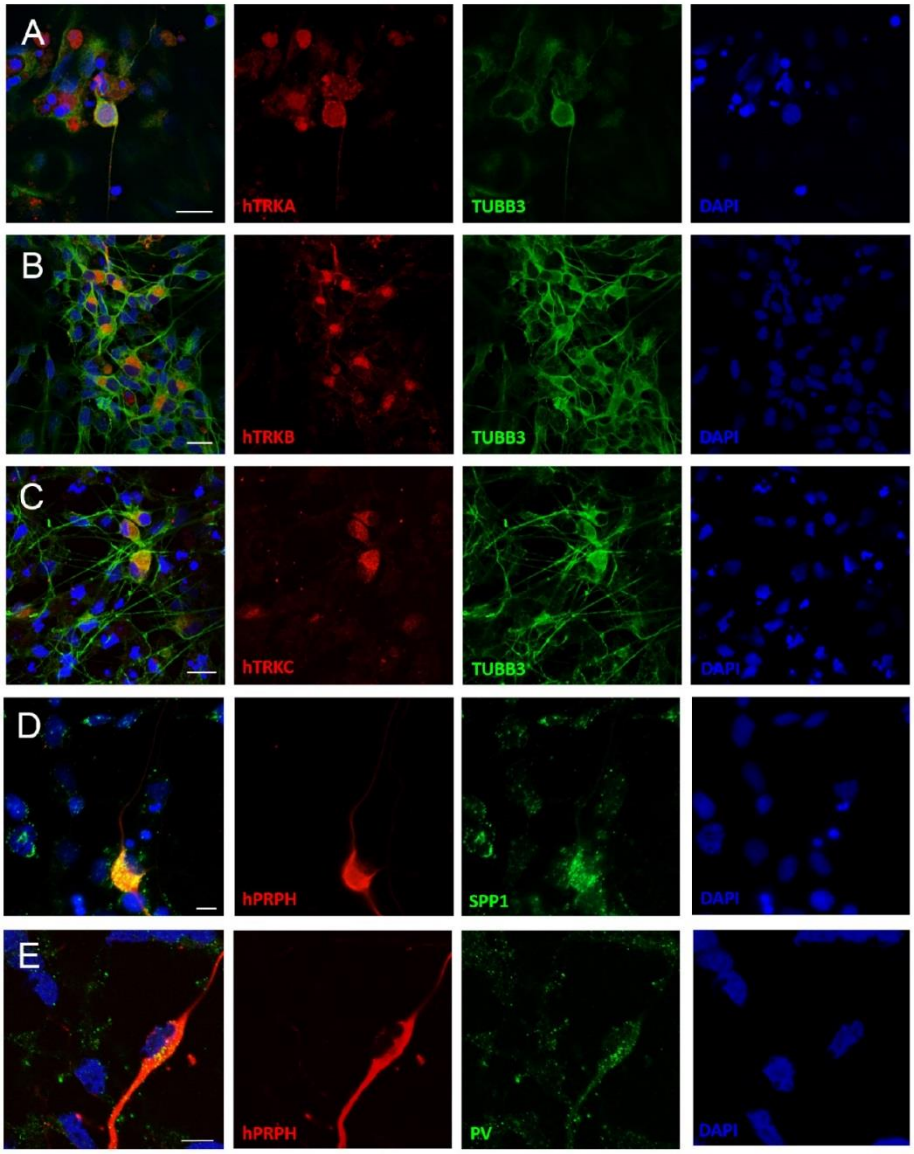

Figure 5.5. Characterization of FRDA-derived human sensory neurons. Neurons show expression of sensory neuronal markers (A) TRKA (red) and β III tubulin (green), (B) TRKB (red) and β III tubulin (green), (C) TRKC (red) and β III tubulin (green), (D) peripherin (PRPH, red) and osteopontin (SSP1, green), and (E) peripherin (red) and parvalbumin (PV, green). DAPI-stained nuclei are shown in blue. *Scale bars are 20 μm (A-D) and 10 μm (E).*

The uptake of fluorescently-labelled particles with complexed plasmid DNA (pcDNA-Luc) was confirmed by confocal microscopy following 24 h incubation. Representative image of sensory neurons treated with AF_{488}-labelled particles coated with DNA is shown in **Figure 5.6**.

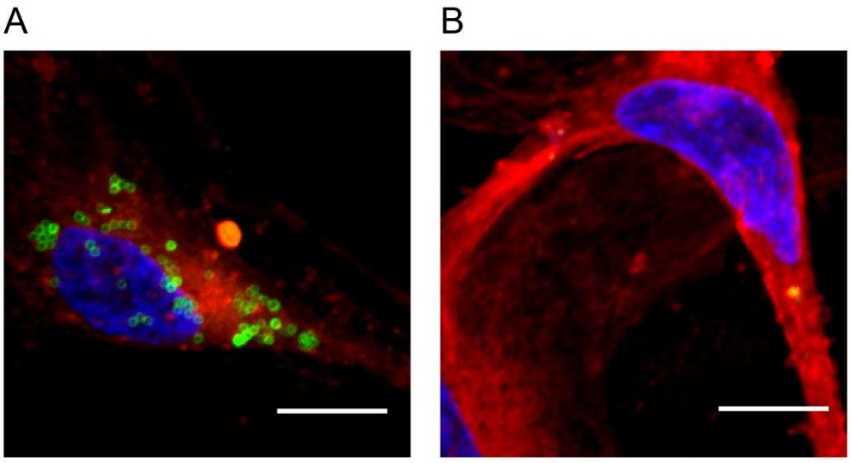

Figure 5.6. Particles internalization in iPSC-derived sensory neurons. Confocal microscopy images showing maximum intensity projection of (A) cells treated with LbL particles coated with plasmid DNA (pcDNA3-Luc); and (B) untreated cells control. AF_{488}-PLArg was used as 7th layer. Nuclei were stained with Hoechst 33342 and cell membrane was stained with Cell Mask Deep Red Plasma membrane stain. *Scale bars are 10 μm.*

In the last stage, we used the same experimental condition to deliver FXN-GFP expression plasmid. Cells were treated with LbL 889 nm core-shell particles (no DNA) or LbL particles with bound FXN plasmid for 24 h. After incubation, cells were washed and incubated for additional 24 h (2 days post-transfection) or 13 days (14 days post-transfection). We used quantitative polymerase chain reaction (Q-PCR) to assess the functional effect of delivered DNA (i.e., levels of FXN cDNA compared to endogenous levels in untreated cells). Results indicate that particle-mediated FXN-DNA delivery resulted in a 27000-fold and 1300-fold increase in FXN cDNA levels as measured 2 and 14 days pos-transfection, respectively (**Figure 5.7A**). Analysis of the expression of cell death marker (CASP 3) was also performed to assess potential cytotoxicity of our particles system in neurons, however, no significant differences among all treatment groups were observed.

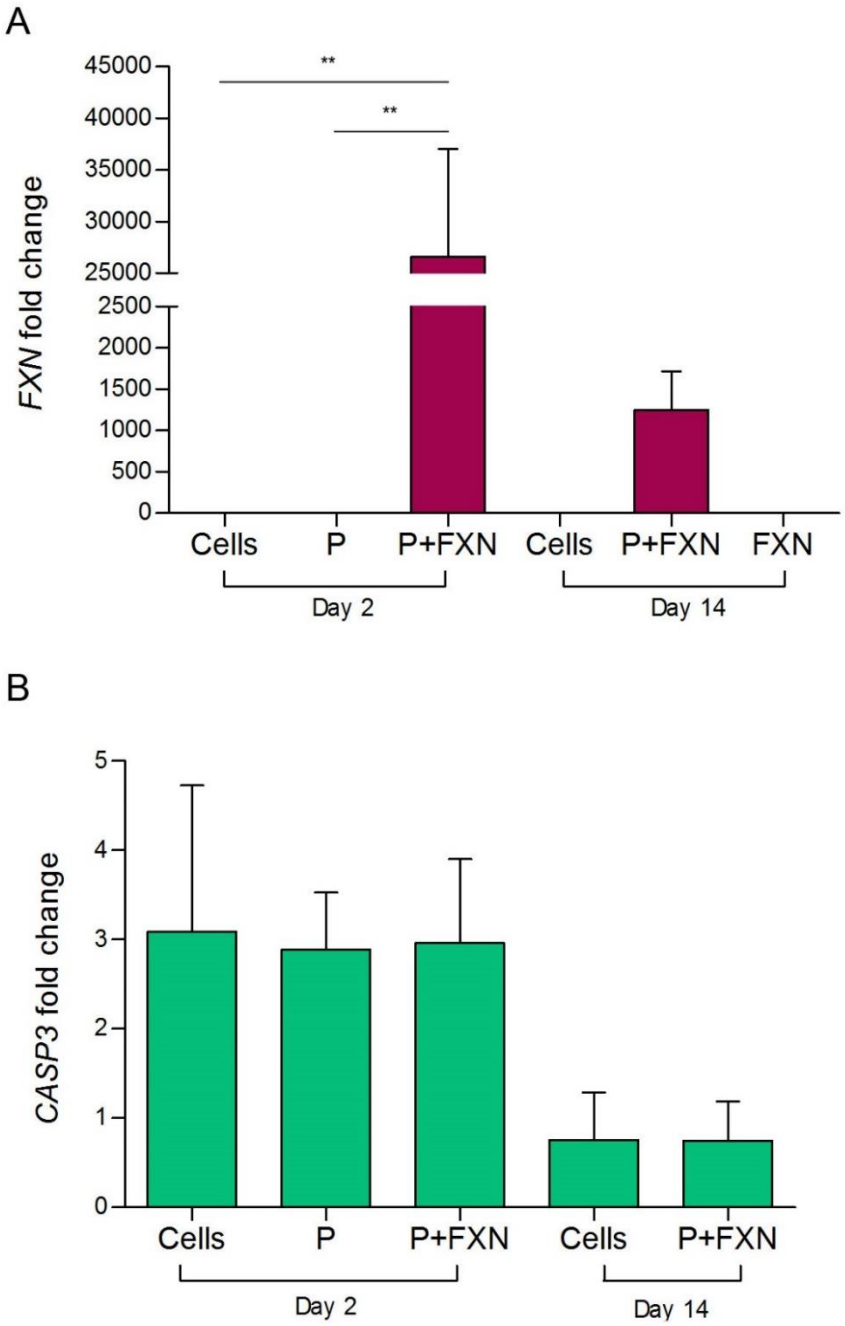

Figure 5.7. Frataxin plasmid (FXN) delivery in FRDA-derived human sensory neurons. (A) qPCR analysis showing fold change of *FXN* cDNA level normalized to untreated cell control (Cells) 2 and 14 days post-transfection. (B) Analysis of apoptosis as shown by qPCR analysis of fold change in *CASP3* expression. Cells were treated with bare LbL silica particles (P) or LbL particles coated with *FXN* plasmid (P+FXN). Control sample containing cells treated with *FXN* plasmid DNA (FXN) was also analysed. Data are shown as the average mean ± standard error of the mean, with n = 3 biological replicate experiments and n > 3 technical replicate samples for each replicate experiment. Statistical analyses were performed using one way-ANOVA with Tukey's multiple comparison test. **$p < 0.01$

In previous reports, it has been shown that exceedingly high expression of FXN can be toxic to cells.[35] Interestingly, despite a significant increase in *FXN* cDNA following treatment with DNA-coated particles, no changes suggesting increased expression of cell death protein was observed. A possible explanation is that although our results show a significant increase in *FXN* at a genetic level, it may not directly translate to the amount of a functionally active protein. It has been established that major *FXN* mRNA encodes the human FXN with MW ~23 kDa. After translocation to the cytosol, the full-length human FXN requires further processing involving at least two intermediate forms to become an active, mitochondrial protein.[36] Therapeutic approach inducing increased expression of mitochondrial FXN is a multistep process, which in the context of gene therapy greatly relies on the design and compatibility of plasmid itself. Delivered plasmid DNA needs to be optimized to modulate *FXN* transcription, e.g. by changing the promoter.

5.5. Conclusions

In summary, this chapter describes the use of PLArg-containing LbL particles to deliver *FXN* expression plasmid to a stem-cells derived model of FRDA. Upon treatment for 2 days, a 27000-fold increase in *FXN* cDNA (indicative of *FXN* transcript) was detected, compared to untreated control. Importantly, no toxic effect was observed in human sensory neurons following treatment with newly engineered FXN DNA delivery system, suggesting its high biocompatibility. The main finding of this study is to highlight the potential of LbL particles in gene therapy for FRDA to increase FXN levels and improve mitochondrial function. Further particles engineering, e.g. functionalization *via* antibodies to target specific neuronal subpopulations, and optimization of the delivered DNA construct, could significantly improve its therapeutic outcome, bringing us closer to finding a more effective treatment for FRDA.

5.6. References

1. M. V. Evans-Galea, A. Pebay, M. Dottori, L. A. Corben, S. H. Ong, P. J. Lockhart and M. B. Delatycki, *Hum. Gene. Ther.*, 2014, **25**, 684-693.
2. D. Simon, H. Seznec, A. Gansmuller, N. Carelle, P. Weber, D. Metzger, P. Rustin, M. Koenig and H. Puccio, *J. Neurosci.*, 2004, **24**, 1987-1995.
3. J. V. Llorens, S. Soriano, P. Calap-Quintana, P. Gonzalez-Cabo and M. D. Molto, *Front. Neurosci.*, 2019, **13**, 75.
4. A. Cook and P. Giunti, *Br. Med. Bull.*, 2017, **124**, 19-30.
5. S. Noval, I. Contreras, I. Sanz-Gallego, R. K. Manrique and J. Arpa, *Eye (Lond)*, 2012, **26**, 315-320.
6. Quantum Rehab website, https://www.quantumrehab.com/meeting-your-needs/living-with-friedreichs-ataxia.asp (accessed February 2020).
7. A. Hanley, R. Corrigan, S. Mohammad and B. MacMahon, *Ir. Med. J.*, 2010, **103**, 117-118.
8. A. H. Koeppen, A. B. Becker, J. Qian and P. J. Feustel, *J. Neuropathol. Exp. Neurol.*, 2017, 76, 101-108.
9. D. Kumari, B. Hayward, A. J. Nakamura, W. M. Bonner and K. Usdin, *Mutat. Res.*, 2015, **781**, 14-21.
10. A. M. Silva, J. M. Brown, V. J. Buckle, R. Wade-Martins and M. M. Lufino, *Hum. Mol. Genet.*, 2015, **24**, 3457-3471.
11. S. Al-Mahdawi, R. M. Pinto, O. Ismail, D. Varshney, S. Lymperi, C. Sandi, D. Trabzuni and M. Pook, *Hum. Mol. Genet.*, 2008, **17**, 735-746.
12. C. Rummey, E. Kichula and D. R. Lynch, *Expert Opin. Orphan D.*, 2018, **6**, 219-230.
13. S. L. Perlman, *J. Child Neurol.*, 2012, **27**, 1217-1222.
14. R. J. Brentjens, I. Riviere, J. H. Park, M. L. Davila, X. Wang, J. Stefanski, C. Taylor, R. Yeh, S. Bartido, O. Borquez-Ojeda, M. Olszewska, Y. Bernal, H. Pegram, M. Przybylowski, D. Hollyman, Y. Usachenko, D. Pirraglia, J. Hosey, E. Santos, E. Halton, P. Maslak, D. Scheinberg, J. Jurcic, M. Heaney, G. Heller, M. Frattini and M. Sadelain, *Blood*, 2011, **118**, 4817-4828.
15. S. R. Kumar, D. M. Markusic, M. Biswas, K. A. High and R. W. Herzog, *Mol. Ther. Methods Clin. Dev.*, 2016, **3**, 16034.
16. J. Li, N. Rozwadowska, A. Clark, D. Fil, J. S. Napierala and M. Napierala, *Stem Cell Res.*, 2019, **40**, 101529.

17. Y. Li, U. Polak, A. D. Bhalla, N. Rozwadowska, J. S. Butler, D. R. Lynch, S. Y. R. Dent and M. Napierala, *Mol. Ther.*, 2015, **23**, 1055-1065.
18. F. Piguet, C. de Montigny, N. Vaucamps, L. Reutenauer, A. Eisenmann and H. Puccio, *Mol. Ther.*, 2018, **26**, 1940-1952.
19. M. Perdomini, B. Belbellaa, L. Monassier, L. Reutenauer, N. Messaddeq, N. Cartier, R. G. Crystal, P. Aubourg and H. Puccio, *Nat. Med.*, 2014, **20**, 542-547.
20. S. Nayak and R. W. Herzog, *Gene Ther.*, 2010, **17**, 295-304.
21. C. E. Thomas, A. Ehrhardt and M. A. Kay, *Nat. Rev. Genet.*, 2003, **4**, 346-358.
22. M. F. Osborn and A. Khvorova, *Nucleic Acid Ther.*, 2018, **28**, 128-136.
23. J. M. Lee, T. J. Yoon and Y. S. Cho, *Biomed. Res. Int.*, 2013, **2013**, 782041.
24. M. Lee and S. W. Kim, *Pharm. Res.*, 2005, **22**, 1-10.
25. J. F. Nabhan, K. M. Wood, V. P. Rao, J. Morin, S. Bhamidipaty, T. P. LaBranche, R. L. Gooch, F. Bozal, C. E. Bulawa and B. C. Guild, *Sci. Rep.*, 2016, **6**, 20019.
26. G. Sauerbrey, *Z. Phys.*, 1959, **155**, 206.
27. J. J. Richardson, M. Bjornmalm and F. Caruso, *Science*, 2015, **348**, aaa2491.
28. Y. Yan, M. Björnmalm and F. Caruso, Chemistry of Materials, 2013, 26, 452-460.
29. M. Keeney, X. Y. Jiang, M. Yamane, M. Lee, S. Goodman and F. Yang, *J. Mater. Chem. B*, 2015, **3**, 8757-8770.
30. Z. Poon, D. Chang, X. Zhao and P. T. Hammond, *ACS Nano*, 2011, **5**, 4284-4292.
31. M. S. Suh, J. Shen, L. T. Kuhn and D. J. Burgess, *Int. J. Pharm.*, 2017, **517**, 58-66.
32. P. A. Jorquera, K. E. Oakley, T. J. Powell, N. Palath, J. G. Boyd and R. A. Tripp, *Vaccines (Basel)*, 2015, **3**, 829-849.
33. R. J. Fields, C. J. Cheng, E. Quijano, C. Weller, N. Kristofik, N. Duong, C. Hoimes, M. E. Egan and W. M. Saltzman, *J. Control. Release*, 2012, **164**, 41-48.
34. A. J. Alshawaf, S. Viventi, W. Qiu, G. D'Abaco, B. Nayagam, M. Erlichster, G. Chana, I. Everall, J. Ivanusic, E. Skafidas and M. Dottori, *Sci. Rep.*, 2018, **8**, 603.
35. T. Vannocci, R. Notario Manzano, O. Beccalli, B. Bettegazzi, F. Grohovaz, G. Cinque, A. de Riso, L. Quaroni, F. Codazzi and A. Pastore, *Dis. Model Mech.*, 2018, **11**, dmm.032706.
36. K. Z. Bencze, K. C. Kondapalli, J. D. Cook, S. McMahon, C. Millan-Pacheco, N. Pastor and T. L. Stemmler, *Crit. Rev. Biochem. Mol. Biol.*, 2006, **41**, 269-291.

Chapter 6

Distribution of particles in stem cell-derived 3D neuronal cell models: effect of particle size, charge and density

6.1. Abstract

Neurodegenerative diseases are characterized by a progressive loss of neuronal subpopulations with no cure available to this day. One of the reasons for a poor clinical outcome of newly developed drug formulations is the lack of appropriate *in vitro* human cell models for research and validation. Stem cell technologies provide an opportunity to address this challenge, by using patient-derived cells as a platform to test various drug formulations, including particle-based drug carriers. The therapeutic efficacy of drug delivery systems relies on an efficient cellular uptake of the carrier and can be dependent on its size, shape and surface chemistry. While a considerable effort has been made to understand that effect in 2D cell culture models, little is known on how nanoparticles physicochemical properties affect their interactions with 3D cell models of neurodegenerative diseases. In the present study, we systematically investigated the role of particles size, charge and density in their interactions with iPSC-derived 3D human neuronal cell cultures. Specifically, templated layer-by-layer particle with silica or polystyrene cores; and self-assembled, glycogen/DNA polyplexes were used. Results show that particles with size <300 nm effectively penetrate neurospheres. We have also shown a functional effect of delivered plasmid DNA up to 6 days post-transfection with glycogen/DNA polyplexes. The results provide guidance in nanoparticles design for therapies aimed at neurodegenerative disease. They also demonstrate the application of 3D models of transplantable human sensory neurons in pre-clinical drug formulation development.

6.2. Introduction

Current advances in nanotechnology present an opportunity to develop therapeutic strategies for targeting diseases that are not curable with conventional methods.[1] Drug delivery systems based on chemically engineered micro- and nanoparticles can encapsulate therapeutic cargo, such as proteins, nucleic acid and/or small molecular weight drugs,[2,3]and improve their therapeutic efficacy.[4] The use of nanoparticle-based formulations is advantageous as it can increase drug stability in the biological fluid, protect from enzymatic degradation in the bloodstream, improve transportation through biological membranes and minimize off-target immune response activation.[5] The use of targeting ligands potentially allows for cell-specific drug delivery with minimal side effects[6] and the composition and type of particles used determine the mechanism of drug loading. Recent evidence suggests that physicochemical properties of the carrier itself, including size, shape, and charge; play an important role in determining particle interaction with cells.[7,8,9] However, available reports on how these properties affect cell association, internalization, and toxicity, largely focus on 2D cell culture models, particularly with neuronal cell models.[10] Although this is often of value to provide information about *in vitro* behaviour of the newly engineered delivery system, there are diseases in which 2D cell models are too simplistic and lack important characteristics of physiologically relevant *in vivo* structures.[11] This has become visible during the development of cancer therapeutics. Previously available 2D models used for pre-clinical drug screening lacked features such as extracellular matrix (ECM), enhanced cell to cell contact, hypoxia and necrosis present in the *in vivo* tumours.[12,13,14] Therefore, insufficient *in vitro* models often led to a poor clinical outcome of initially promising nanoformulations.[15]

More advanced *in vitro* cell models are also much needed for the development of therapies aimed at neurodegenerative diseases.[16] Development of stem cell technologies in recent years introduced new opportunities for nanomedicine, by providing more accurate disease models.[17] Cells obtained from patients carry a unique genetic profile of the disease and can be differentiated to any type of cells, including neurons, and the possibility to culture them in a three-dimensional (3D) structure allows to establish *in vitro* model mimicking structural complexity of the human nervous system.[18,19] More advance, stem cell-derived 3D cell models mimicking brain architecture have been shown superior to 2D models while studying electrophysiological interaction of cells,[20] cell differentiation[21,22,23] and cell-ECM interactions.[24] Additionally, when used in a combination with a cell replacement therapy,

differentiated cells could be used for an *ex vivo* drug delivery followed by *in vivo* transplantation of patient-derived cells, thus minimizing the risk of donor cells rejection.[25] One of the diseases that lack an accurate study model is Friedreich's ataxia (FRDA) primarily affecting the peripheral nervous system.[26] It is a genetic disease caused by a mutation in a frataxin gene (*FXN*), resulting in a decreased level of mitochondrial protein frataxin (FXN) involved in iron metabolism.[27] FRDA manifests in progressive degeneration of sensory neurons in dorsal root ganglia (DRG).[28] Recently, Dottori and co-workers have established a protocol to obtain the FRDA model using stem cell technology.[28,29] The resulting iPSC-derived 3D neurospheres (NSPs) were created by reprogramming fibroblasts from FRDA patients into stem cells, which were then differentiated into neurons. The resulting 3D structures consist of a heterogeneous population of sensory neurons subtypes and constitute a valuable model to study the complexity of DRG region at a physiological level. More generally, they can be used as a platform to study various drug formulation for therapies against diseases affecting the nervous system.

In this study, we report how physicochemical properties of nanoparticles influence their association, penetration and distribution in iPSC-derived NSPs, a model of FRDA. Previous studies have reported on the toxicity of particles in neuronal cell lines,[30,31,32] and Leite et al have recently tested the interactions of modified gold and polylactic acid nanoparticles with 3D iPSC-derived brain organoids.[32] In the present study, we use a versatile layer-by-layer (LbL) particle systems with various sizes (235 nm - 1μm), charges (positive and negative), and densities (silica and polystyrene core). We systematically investigated how these properties influence particle interaction with 3D NSPs. We also tested a soft, self-assembled nanoparticle system based on chemically modified bovine glycogen (BG-EDA), which was previously used to deliver siRNA into tumour spheroids[33] and apply it to deliver *FXN*-expressing plasmid DNA as a therapeutic strategy for FRDA. Our results provide useful guidance for designing nanoparticles for drug delivery into 3D neurodegenerative disease cell models and for applying such models for testing therapeutic agents for the treatment of FRDA.

6.3. Experimental section

6.3.1. Materials

Silica particles (0.235 µm, 0.387 µm and 0.889 µm, 5% w/v aqueous solution) and polystyrene particles (0.288 µm, 0.45 µm and 1.01 µm, 5% w/v aqueous solution) were purchased from microParticles GmbH (Berlin, Germany). Poly(ethylenimine) (PEI) low molecular weight 50 wt% solution in water, poly-L-arginine hydrochloride, molecular weight >70000; poly(sodium 4-styrenesulfonate) (PSS) molecular weight ~70000, bovine liver glycogen (BG), ethylenediamine (EDA), sodium meta-periodate, sodium cyanoborohydride, albumin from bovine serum (BSA), sodium acetate, sodium bicarbonate, Dulbecco's phosphate buffered saline (DPBS), without calcium chloride or magnesium chloride, Accutase and agarose were purchased from Sigma-Aldrich (St. Louis, MI, USA). Plasmid DNA (pEGFP, 3 kbp) was obtained from CSIRO (Australia) and FXN-23 plasmid was a gift from Professor Mirella Dottori's group. Optimal cutting temperature (O.C.T.) medium was purchased from ProSciTech (Kirwan, Australia). Sodium chloride (NaCl) was purchased from Chem-Supply (Gillman, Australia). Alexa Fluor 647 N-hydroxysuccinimide (NHS) dye, wheat germ agglutinin (WGA), Alexa Fluor 488 conjugate (WGA-AF_{488}), Hoechst 33342 (10 mg mL^{-1} solution in water), N2B27 medium, Dulbecco's modified Eagle's medium (DMEM)/F12 medium, insulin, transferrin, and selenium additives, N2 supplement, retinol-free B27 supplement, penicillin-streptomycin and GlutaMAX were purchased from Life Technologies (Scoresby, Australia). Dialysis tubing (molecular weight cutoff (MWCO) 3.5 kDa) and Nunc Lab-Tek II Chamber microscopy slides were purchased from Thermo Fisher Scientific (Scoresby, Australia). DNA electrophoresis sample loading dye was purchased from Bio-Rad (Gladesville, Australia). DMEM (with 4.5 g L^{-1} glucose and L-glutamine) and trypsin (10X) were purchased from Lonza (Basel, Switzerland). Fetal bovine serum was purchased from Bovogen Biologicals (Keilor East, Australia). Paraformaldehyde 4% aqueous solution (EM grade, 4% PFA) was purchased from Electron Microscopy Sciences. Vitronectin and Tesr-E8 basal medium were purchased from StemCell Technologies. Brain derived neurotrophic factor (BDNF), and neutrotrophin-3 (NT-3) were purchased from PeproTech. Illustra NAP-5 columns were purchased from GE Healthcare and Life Sciences (Silverwater, Australia). CHIR99021 and SB431542 were purchased from Tocris Bioscience. Bone morphogenetic protein 2 (BMP2) was purchased from R&D Systems. Milli-Q water was obtained from a Millipore Milli-Q purification system (Millipore Corporation, Billerica, MA, USA).

6.3.2. Particles preparation

Particles with silica core. Silica particles (Si) with sizes 235 nm, 387 nm and 837 nm were used to deposit film composed of polyethyleneimine (PEI, prepared as 2 mg mL^{-1} solution in Milli-Q water with 1 M NaCl), polystyrene sulfonate (PSS, prepared as 1 mg $^{-1}$solution in 50 mM sodium acetate buffer pH 5.2 with 0.5 M Na Cl) and poly-L-arginine (PLArg, prepared as 1 mg mL^{-1} solution in 50 mM sodium acetate buffer pH 5.2). Silica particles (40 µL, 0.05 wt %) were first washed with water three times by centrifugation/resuspension cycles. Centrifugation speed varied depending on particle size: 1500 *g* for 3 min for 235 nm and 387 nm particles and 500 *g*, 1.5 min for 837 nm silica particles. After each centrifugation step, the supernatant was removed, and the particle pellet was resuspended in 200 µL of Milli-Q water. After the 3rd wash, the pellet was resuspended in 200 µL Milli-Q water and 200 µL of PEI was added to the particle suspension. After 15 minutes of mixing at room temperature, excess PEI was removed by 4 centrifugation/resuspension cycles as described above, using 50 mM sodium acetate buffer, pH 5.2 in the last two washes. The same buffer was used in all subsequent steps during washing and adsorption. After PEI, further formation of the film included deposition of additional (PSS-PLArg) bilayer for positively-charged particles (terminated with PLArg), and (PSS-PLArg-PSS) for negatively-charged particles (terminated with PSS). Final particles were resuspended in 100 µL of sodium acetate buffer and stored at 4^{o}C until further use. A small portion of particles was removed after the final deposition step for ζ-potential measurements and particles counting.

Particles with polystyrene core. Polystyrene particles (40 µL, 5% w/v) with sizes 288 nm, 450 nm and 1000 nm were washed three times with 200 µl of MilliQ-water by centrifugation/resuspension cycles. Centrifugation speed varied depending on particle size: 10000 *g*, 10 min for 288 nm and 450 nm particles and 1000 *g*, 3 min for 1000 nm particles. Positively-charged particles were fabricated by deposition of PEI. Briefly, after the last washing step, the pellet was resuspended in 200 µL of MilliQ-water and 200 µL of PEI solution (2 mg mL^{-1} in MilliQ-water solution with 1 M NaCl) was added, followed by 15 min mixing at room temperature and 3 washes by centrifugation/resuspension as described above. Uncoated PS particles, i.e. without PEI layer, were used as negatively-charged particles. Uncoated or PEI-coated PS particles were resuspended in 100 µL of MilliQ-water and stored

at 4°C until further use. A small portion of particles was removed after the final deposition step for ζ-potential measurements and particles counting.

Synthesis of BG-EDA. Bovine glycogen (BG) nanoparticles functionalized with ethylenediamine (EDA) were synthesized according to a previously described method. Briefly, 100 mg of commercially available bovine glycogen was dissolved in 6 mL of 0.6 M acetic buffer (pH 5.0) followed by the addition of 0.12 mmol sodium periodate and incubated for 2 h with stirring protected from light. Then, 0.6 mmol of EDA was added followed by the immediate addition of sodium cyanoborohydride (1.2 mmol). The reaction was incubated overnight and the product was purified by dialysis against Milli-Q water and freeze-dried.

6.3.3. Preparation of fluorescently-labelled particles

Fluorescently-labelled particles with silica cores were prepared by using Alexa Fluor 647-labelled PLArg (AF647-PLArg) as the 3rd layer in the LbL film assembly. To prepare AF647-PLArg, 5 mg of PLArg (MW > 70000) was dissolved in 2.5 mL of 50 mM sodium acetate buffer, pH 5.2. AF 647-NHS dye (2.4× 10−4 mmol) was added to the solution and incubated for 4 h, protected from light, with mixing. Unbound dye was removed by dialysis (MWCO 3.5 kDa) in Milli-Q water for 2 days (5 times water change). The final product was freeze-dried and stored at 4°C until further use.

Particles with polystyrene core (PS) were obtained as FITC-labelled and no further modification was required.

Fluorescently labelled BG-EDA nanoparticles were prepared by addition of 20 µL of 1 mg mL^{-1} Alexa Fluor 647-NHS dye to 4 mg mL^{-1} BG-EDA (2 mg of BG-EDA in 0.5 mL of 0.1 M sodium bicarbonate buffer at pH 8). The reaction was carried out for 4 h in the dark at room temperature (21°C). Unreacted dye was removed using Illustra NAP-5 filter columns (GE Healthcare) as per manufacturer protocol and freeze-dried.

6.3.4. Particles characterization

The ζ-potential measurement was performed by microelectrophoresis using a Zetasizer Nano-ZS instrument (Malvern Instruments). A small volume of particles suspension (2 µL)

was dispersed in 998 µL of Milli-Q water. All measurements were performed in folded capillary cells (DTS1070, Malvern Instruments) at 25°C. LbL particles were also counted using an Apogee A50-Microflow cytometer to determine particle concentration. For flow cytometry, 2 µL of particles was added to 398 µL of MilliQ-water and counted by flow cytometry based on FSH vs SSH plots. Imaging of particles in solution was performed using Nikon A1R confocal microscope.

6.3.5. Complexation of plasmid DNA

Analysis of BG-EDA/DNA complex formation was performed using agarose gel electrophoresis. Model pEGFP plasmid (3 kbp) expressing green fluorescent protein was prepared as a solution at 0.4 µg mL^{-1} in DPBS. BG-EDA solution was prepared at 2 mg mL^{-1} in DPBS. Complex formation was studied using varying BG-EDA-to-plasmid DNA weight/weight ratio (0.5, 1, 10, 15, 20 and 30) in 30 µL final volume and incubated at room temperature for 30 min. Next, 5 µL of nucleic acid loading dye was added and mixed for 10 s by vortexing. 30µL of solution containing BG-EDA/DNA complexes was loaded onto 1.6% agarose gel and electrophoresis was carried out for 30 min at 150 V. Control samples containing only DNA or BG-EDA were prepared in 30 µL of DPBS.

6.3.6. Neurospheres preparation

iPSCs were plated on a laminin-coated organ culture dish in TeSR-E8 medium supplement with 10 µM Y-27632. After 24 h, the medium was removed and replaced with N2B27 medium containing NBM-DMEM/F12 medium (1:1 mixture) supplemented with 1% N2 and 1% B-27 supplements, 1% IST-A, 1% L-Glutamine, 1% Penicillin/Streptomycin, 0.3 % glucose. This medium was also supplemented with CHIR99021 and SB431542 (3 and 10 µM, respectively). After 5 days of incubation, cells were harvested and moved to the second (differentiation) medium, i.e. NBM supplemented with 1 N2 and 1% B-27 supplements, 1% IST-A, 1 % L-Glutamine, 1% Penicillin/Streptomycin. This medium was also supplemented with BMP2 and bEGF (10 and 20 ng mL^{-1}, respectively). After 6 days of incubation, the medium was removed and replaced with fresh NBM medium supplemented with BDNF, NGF NT-3 supplements (10 ng mL−1 each). Cells were incubated for 2 weeks, with medium changed every 3-4 days. After

an additional 14 days of culture, differentiated NSPs were sent to the University of Melbourne for further experiments.

6.3.7. Particle-NSP association

LbL silica core particles and PS particles. NSPs,in 96-well round-bottom plates were placed in 200 μL of fresh NBM culture medium.. Particle suspensions (Si 837 nm, 387 nm and 235 nm; and PS 1000 nm, 450 nm and 288 nm) were prepared at 3.0 x 10^7 particles in 30 μL. With a rough estimate of cell number in one NSP to be between 1x10^5 to 3x10^5, that number of particles corresponds to particles-to-cell ratio between 100 to 300, respectively. For static cell culture conditions, NSPs were incubated with particles for 72 h at 37 °C, 5% CO_2 in a humidified atmosphere. For dynamic cell culture incubation, plates were mounted onto the orbital shaking platform set at 120 rpm and incubated for 72 h at 37 °C, 5% CO_2 in a humidified atmosphere.

BG-EDA was prepared in DPBS and added to cells at a final concentration of 10 μg mL^{-1}.

6.3.8. Transfection of NSPs

BG-EDA/DNA complexes (using pEGFP, FXN-M17, FXN-23 or FXN-24 plasmids) for transfection were prepared in DPBS at a w/w ratio of 20, as described for gel electrophoresis. For pEGFP plasmid, two amounts of plasmid DNA were delivered, i.e. 0.5 or 1 μg per well. After 30 min incubation at room temperature, 30 μL of solution containing BG-EDA/DNA complexes was added to NSPs. After 48 h, the supernatant was removed and 200 μL of fresh medium was added. NSPs were cultured for another 48 h (4 days post-transfection) or 96 h (6 days post-transfection).

DNA transfection was assessed by the intensity of GFP expression (for model pEGFP, FXN_M17 and FXN_M23 plasmids) or tomato-red (FXN_M24 plasmid). NSPs were washed and processed for flow cytometry analysis as described below/above. Transfection efficiency was expressed as mean fluorescent intensity (MFI) in the treated cell sample normalized to the MFI of the untreated cell control.

6.3.9. Dissociation of NSPs for Flow cytometry

Washing and dissociation of NSPs were performed in a 96-well round-bottom plate. Cell culture medium was removed and NSPs were washed twice with 200 µL of DPBS. Additional washing was done by transferring each NSP to a new well containing 200 µL of DPBS. This washing process by placing the NSP in well containing 200 µL of DPBS was repeated twice. After the final wash, each NSP was transferred to an empty well and 150 µL of Accutase solution was added. NSPs were left to dissociated for 30 min at room temperature with occasional mixing by pipetting. Next, 100 µL of 1% BSA-PBS solution was added to each well. The dissociated cells were centrifuged at 250 *g* for 7 min in the plate and the supernatant was discarded. The cell pellet was resuspended in 200 µL of 1% BSA-PBS solution and centrifuged again (250 *g* for 7 min). Pelleted cells were resuspended in 200 µL of DPBS and pipetted through a cell strainer for analysis. Cell association of particles was analyzed on a BD Accuri C6 flow cytometer and is expressed as % of cells that are AF_{647}-positive (for LbL silica core particles) or FITC-positive (for polystyrene core particles).

6.3.10. Cryostat sectioning of NSPs for confocal imaging

Cell culture medium was removed and NSPs were washed twice with 200 µL of DPBS. Additional washing was done by transferring each NSP to a new well containing 200 µL of DPBS. This washing process by placing the NSP in well containing 200 µL of DPBS was repeated twice. Next, NSPs were fixed with 4% paraformaldehyde for 15 min at room temperature. Paraformaldehyde was then removed, and cells were washed once with 200 µL of DPBS. NSPs were kept in a 20% sucrose solution in DPBS until further processing. Before cutting into sections, NSPs were placed in optimal cutting temperature (O.C.T.) medium in a square cryostat mold and frozen at -20^{o}C. At least 20 sections (20 µm thick) were collected for each NSP.

Slides were then washed by rinsing in DPBS until traces of the O.C.T. medium were removed. Slides were placed in Hoechst solution (1:10000 in DPBS) and incubated for 5 min at room temperature, followed by 3 rinses with DPBS. For membrane staining, slides were placed in AF_{488}-WGA solution (5 µg mL^{-1}) and incubated for 5 min at room temperature, followed by 3 rinses with DPBS. Slides were then air-dried in the fume hood. Thin glass slides were placed on top of the samples mounted with few drops of Pro Gold anti-fade mounting

media. Cells were imaged with a Nikon A1R confocal microscope equipped with a 20x air objective or 40x water objective.

6.4. Results and discussion

6.4.1. Particles preparation

Neurospheres are 3D cell models mimicking the structural complexity of interconnecting neurons in the nervous system.[24] We selected templated particles as a well-characterized particle system with tunable physicochemical properties such as size and surface chemistry to test particle association with neurospheres. Layer-by-layer (LbL) assembly was chosen as a method of particles preparation to deposit a multilayered film on a spherical template. Templates of various types, differing in size, material and density, are commercially available and can be further engineered to modify particles properties. In this study, we used two types of templates, i.e. silica (Si) and polystyrene (PS), which were successfully used in the past to prepare particles with the application in cancer therapies and vaccines. By using particles of the same size and surface charge, but of different materials, we can compare the impact of particle density on interactions with the biological system. The density of silica is 1.8 g cm^3 and the density of PS is 1.05 g cm^3. Therefore, the presence of Si core could be expected to show a higher sedimentation rate compared to a lighter PS core. In addition, we used three different sizes for each type of template, i.e., 837, 387 and 235 nm for Si particles; and 1000 nm, 450 and 288 nm for PS particles. To prepare LbL Si particles, the template was primed with PEI to introduce a positive charge on the surface and facilitate the growth of the film through the electrostatic interaction of negatively charged PSS and positively charged PLArg. The film was formed with AF_{647}-PLArg to fluorescently label the particles and allow the tracking of particles by flow cytometry and confocal microscopy. To investigate how particle surface charge influence on cell association, we prepared negatively-charged particles, i.e. terminated with PSS (giving the final shell structure [PEI-PSS-(AF_{647}-PLArg)-PSS]; and positively-charged particles, i.e. terminated with PLArg (final shell structure [PEI-PSS-(AF_{647}-PLArg]. PS particles were obtained as FITC-labelled, eliminating the need to use additional fluorescent material in the film. We also compared negatively- and positively-charged PS particles (bare PS and PEI-coated particles, respectively). The ζ-potential of particles, indicative of surface charge, was measured on DLS. Information on the physicochemical

properties of the particles, including size, charge and composition are summarized in **Table 6.1** and examples of particle images are in **Figure S6.1**.

Table 6.1. Particles characterization

Name	Template	Density[a] (g/cm^3)	Size[b] (nm)	Charge[c] (mV)	Outer layer	Fluorophore
Si 837 (+)	Silica	1.8	832	21.9 ± 3	PLArg	AF647 (shell)
Si 837 (-)	Silica	1.8	832	-40.1 ± 6	PSS	AF647 (shell)
Si 387 (+)	Silica	1.8	387	30.1 ± 7	PLArg	AF647 (shell)
Si 387 (-)	Silica	1.8	387	-41.6 ± 4	PSS	AF647 (shell)
Si 235 (+)	Silica	1.8	235	28.7 ± 8	PLArg	AF647 (shell)
Si 235 (-)	Silica	1.8	235	-42.9 ± 7	PSS	AF647 (shell)
PS 1000 (+)	Polystyrene	1.05	1000	37.7 ±4	PEI	FITC (core)
PS 1000 (-)	Polystyrene	1.05	1000	-38.5 ± 4	-	FITC (core)
PS 450 (+)	Polystyrene	1.05	450	34.7 ± 5	PEI	FITC (core)
PS 450 (-)	Polystyrene	1.05	450	-37.2 ± 6	-	FITC (core)
PS 288 (+)	Polystyrene	1.05	288	19.0 ± 8	PEI	FITC (core)
PS 288 (-)	Polystyrene	1.05	288	-43.6 ± 8	-	FITC (core)
BG-EDA (free)	Soft particle (glycogen)	Not available	27	33 ± 4	-	AF647
BG-EDA (complex)	Soft particle (complexed with DNA)	Not available	178	4.53 ± 2	-	AF647 (BG-EDA)

6.4.2. Particles association with NSPs by flow cytometry

We first compared how particle size influences binding and penetration into the NSPs using flow cytometry. The association of positively-charged particles with cells within the NSPs increase with decreasing size of Si core, from 20% association for 837 nm Si particles to 65% for 235 nm Si particles (**Figure 6.1A**). Next, we compared how surface charge influences the association with cells within the NSPs. Particle surface charge was modulated by varying the outer layer of the particles. To confer a negative charge, PSS was deposited as the outer layer and confer a positive charge, the particles were terminated with a PLArg outer layer. The overall trend points to a higher association for positively-charged particles (PLArg-terminated), with the most pronounced difference for the smallest particles of 235 nm Si (**Figure 6.2A**). In the next step, we looked at the effect of particle density on the association of cells from NSPs. The particles used had comparable size and charge, but different core density, i.e., Si (1.8 g/cm^3) and PS (density 1.05 g/cm^3). **Figures 6.1C** and **6.1D** indicate a higher association with cells from NSPs for particles with Si core. To investigate whether the potential effect of particle sedimentation can be eliminated by cell culture condition, we compared static and dynamic (orbital mixing) conditions. As can be seen in **Figure S6.2**, no significant difference was observed when particles were incubated with NSPs with or without mixing. **Figure 6.1C** and **6.1D** shows a generally low association of particles prepared with a PS template, with cell association at10% for 1000 nm particles and 25% for 288 nm particles.

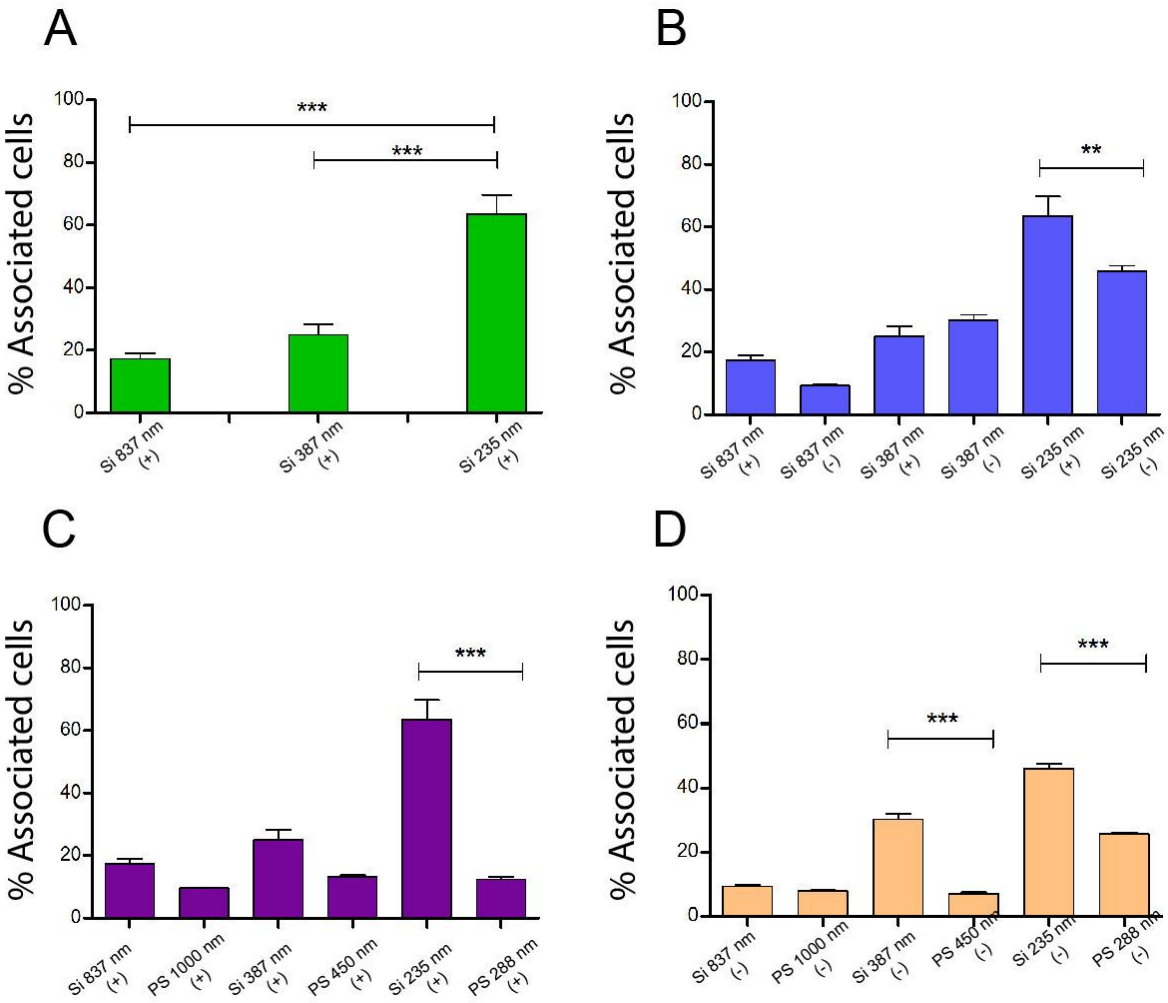

Figure 6.1. Association of particles with iPSC-derived neurospheres. The effect of silica particles size (A) and charge (B) on particle association with NSPs by flow cytometry. The effect of core density (PS or Si particles) on association with NSPs of positively-charged (C) and negatively-charged (D) particles. Data are shown as the average mean ± standard error of the mean (n = 4). Statistical analyses were performed using one way-ANOVA with Tukey's multiple comparison test. ***$p < 0.001$

6.4.3. Particles distribution in NSPs by confocal microscopy

In the next step, we used confocal microscopy to analyse the distribution of the particles in NSPs. Frozen NSPs were cut into 20 μm-thick sections. Representative cross-sections from the surface and centre of the sphere are shown in **Figure 6.2** (for 235 nm, 387 nm, 837 nm Si particles) and **Figure 6.3** (for 288 nm, 450 nm, 1000 nm PS particles). Higher resolution images of NSP cross-sections are presented in **Figure S6.3-S6.8**. Imaging of sections derived from

NSPs treated with LbL Si particles confirmed results obtained by flow cytometry. It also indicated that the smallest particles (235 nm) are able to penetrate deep into the sphere, regardless of their surface charge. Contrary to what could be expected from cell association studies, PS particles could be observed inside sections to up to ~ 200 μm of depth. Interestingly, with positively charged particles, i.e. PLArg-terminated LbL Si particles and PEI-coated PS particles, the high binding observed from flow cytometry was localized on the surface of the spheres. This may indicate that particles are unable to penetrate the NSP, which may be due to particle size and/or electrostatic interactions between positively-charged particles and negatively-charged extracellular matrix (ECM) components.

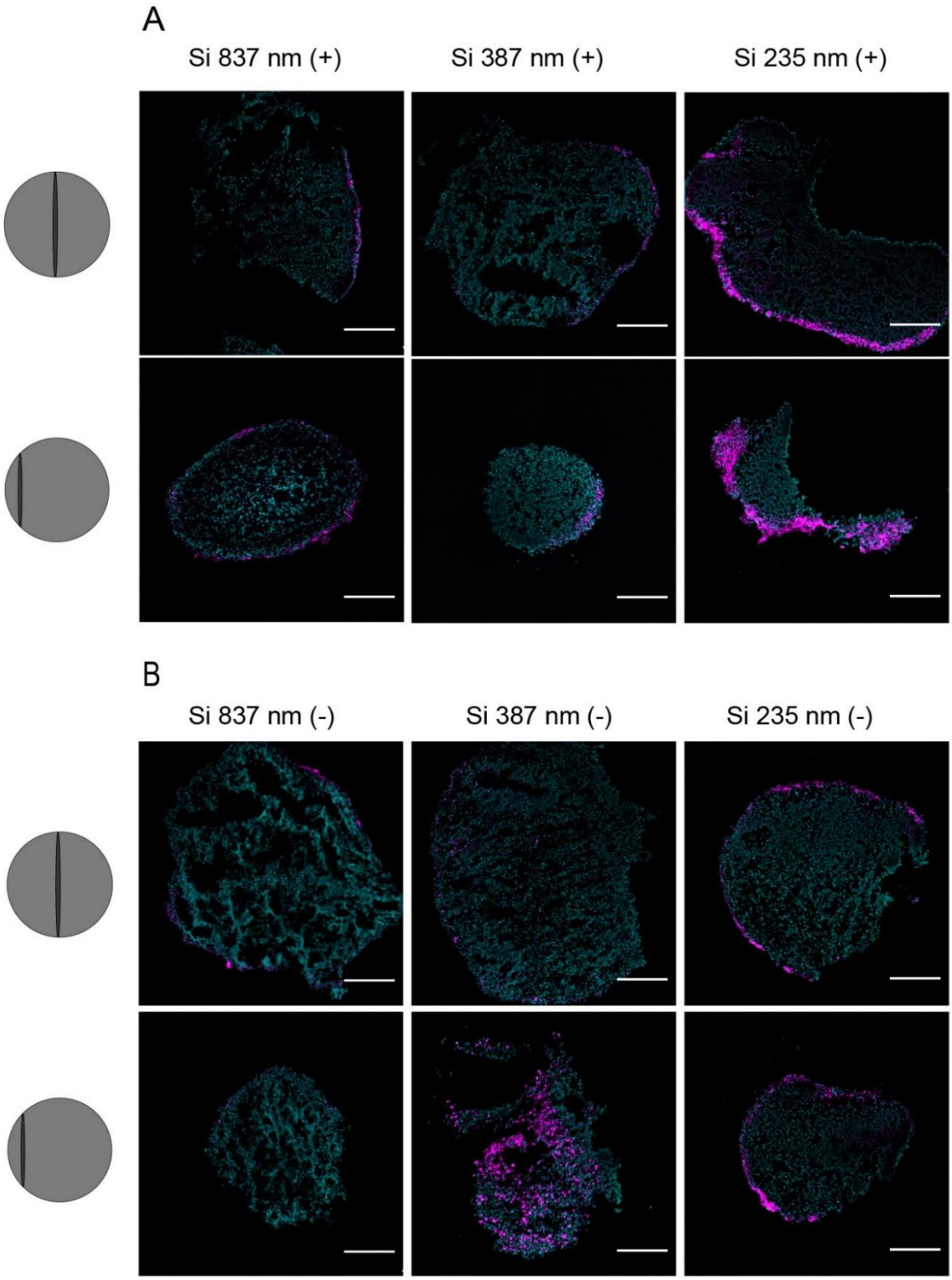

Figure 6.2. Distribution of LbL Si particles in iPSC-derived neurospheres. Images show two representative cross-sections taken from the middle and the surface of the neurospheres after treatment with positively charged (A) and negatively charged (B) particles. Particles were prepared with silica cores 837 nm, 387 nm and 235 nm. Nuclei were stained with Hoechst and pseudo coloured as cyan, and FITC-labelled particles are in magenta. *Scale bars are 100 μm.*

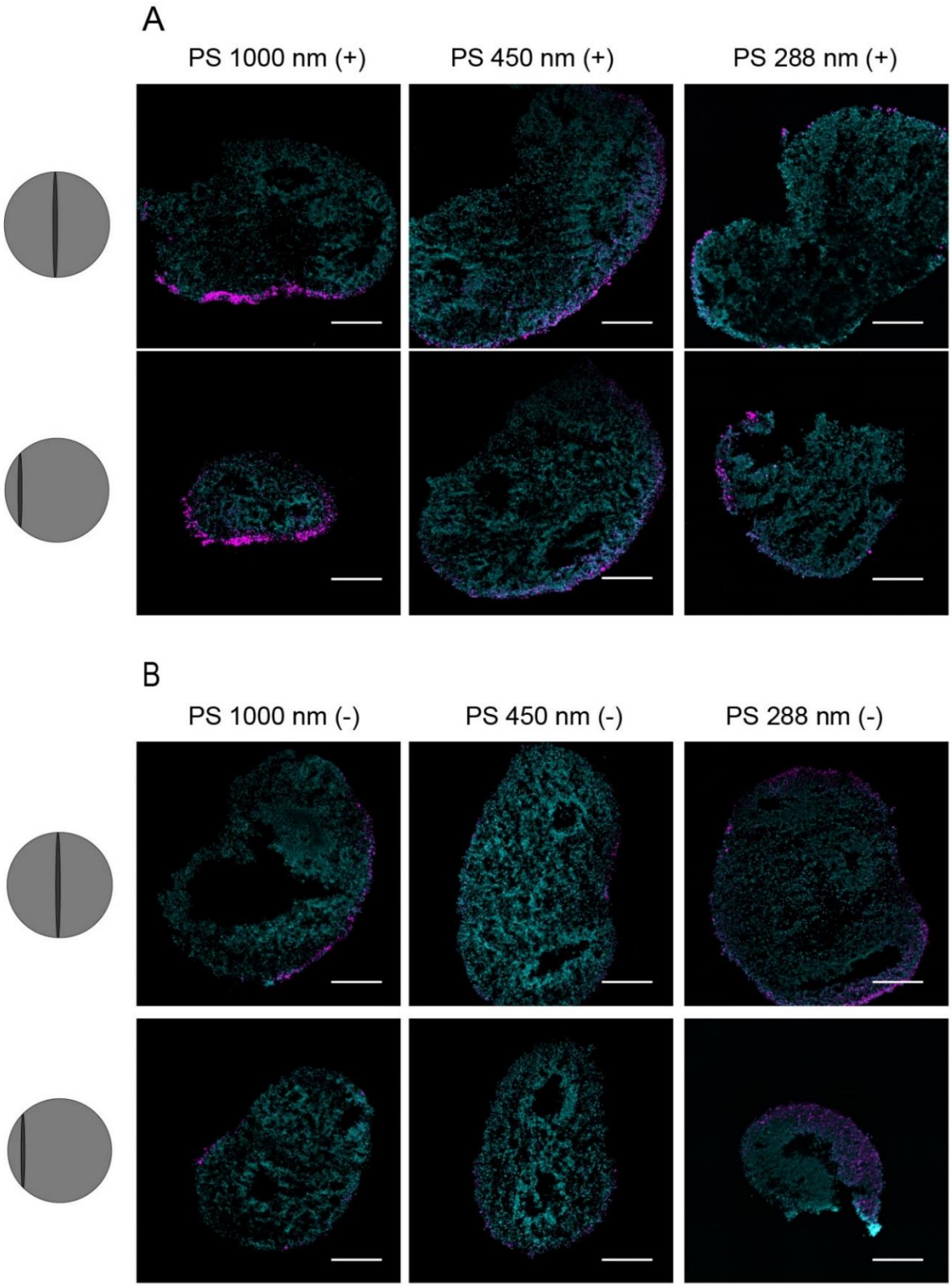

Figure 6.3. Distribution of PS particles in iPSC-derived neurospheres. Images show two representative cross-sections taken from the middle and the surface of the neurospheres after treatment with positively charged (A) and negatively charged (B) particles. Particles were prepared with polystyrene cores 1000 nm, 450 nm and 288 nm. Nuclei were stained with Hoechst and pseudo coloured as cyan, and FITC-labelled particles are in magenta. *Scale bars are 100 μm.*

Having established that particles with Si core are able to penetrate NSPs, we investigated how deep in the sphere they penetrate by imaging the middle section of the sphere at different depths, i.e. at the surface (<50 μm), 100-150 μm and 200-250 μm (**Figure 6.4**). All types of tested LbL Si particles can be seen close to the surface of the NSP and 387 nm particles penetrate the NSP up to 150 μm deep. The smallest (235 nm) particles terminated with PLArg could reach cell at depths of 250 μm. Results presented so far focused on particles with a solid template. Nanoparticles design for targeting human nervous system is most often discussed in the context of drug delivery to the brain. As such, it has been generally accepted that crossing the blood-brain barrier (BBB) requires nanoparticles with the size <100 nm.[34] However, this can be often challenging and not applicable to all types of therapeutic formulations/cargo. The size restriction may not be accurate for alternative therapies with a different route of administration, aimed at neurodegenerative diseases affecting areas other than brain.

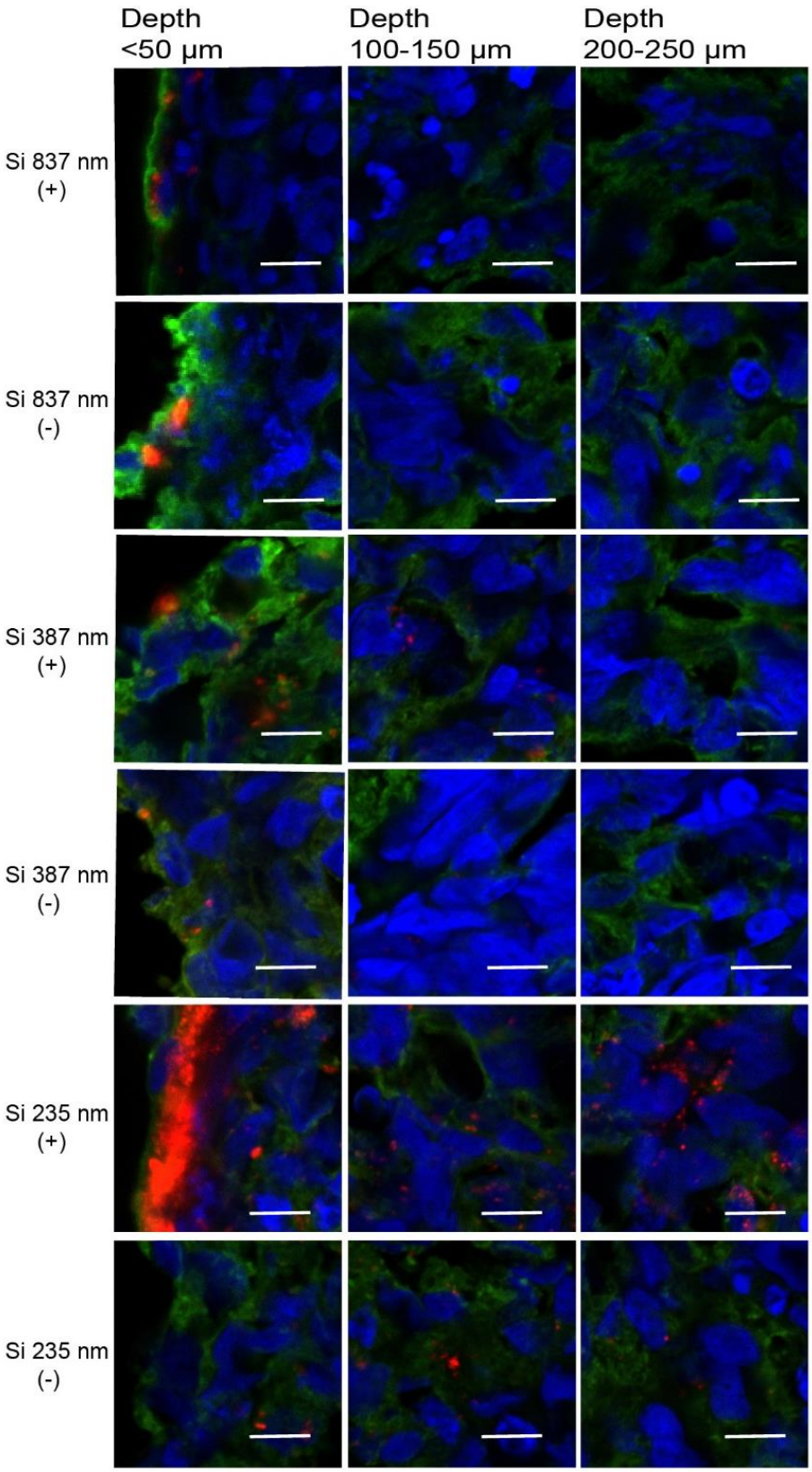

Figure 6.4. Penetration of LbL Si particles into iPSC-derived neurospheres. Images show the middle section of the sphere at different depths. Nucleus stain (Hoechst) is blue, cell membrane (AF_{488}-wheat germ agglutinin) is green and AF_{647}-labelled particles are red. *Scale bars are 20 µm.*

6.4.4. Amine-modified bovine glycogen as a delivery system of DNA to NSPs

In the next step, flexible, "soft" particle system based on bovine-derived glycogen (**Figure S6.1C**) was tested. Glycogen is a naturally occurring biomolecule, structured as a nanoparticle with a diameter of ~ 30 nm and an inherent negative charge. BG was previously chemically modified to introduce amine groups (ethylenediamine-modified) enabling the loading of negatively charged nucleic acid to form spherical complexes as demonstrated by TEM and Stochastic Optical Reconstruction Microscopy (STORM) imaging.[33] BG-EDA complexed with siRNA was found to penetrate into a 3D model of prostate cancer and confer gene silencing. Other glycogen derivatives obtained by modification with 3-(dimethylamino)-1-propylamine (DMAPA-Glyp) and 1-(2-aminoethyl) piperazine (AEPZGlyp) were used to form 100-250 nm complexes with DNA and were effective in transfection of brain tissue of Sprague rats.[35]

In our studies, we first looked at the NSPs penetration by free BG-EDA nanoparticles. The presence of evenly distributed nanoparticles in cross-sectional images taken from the surface and the middle of the NSP indicate deep penetration into the NSPs. Representative confocal images are presented in **Figure 6.5**.

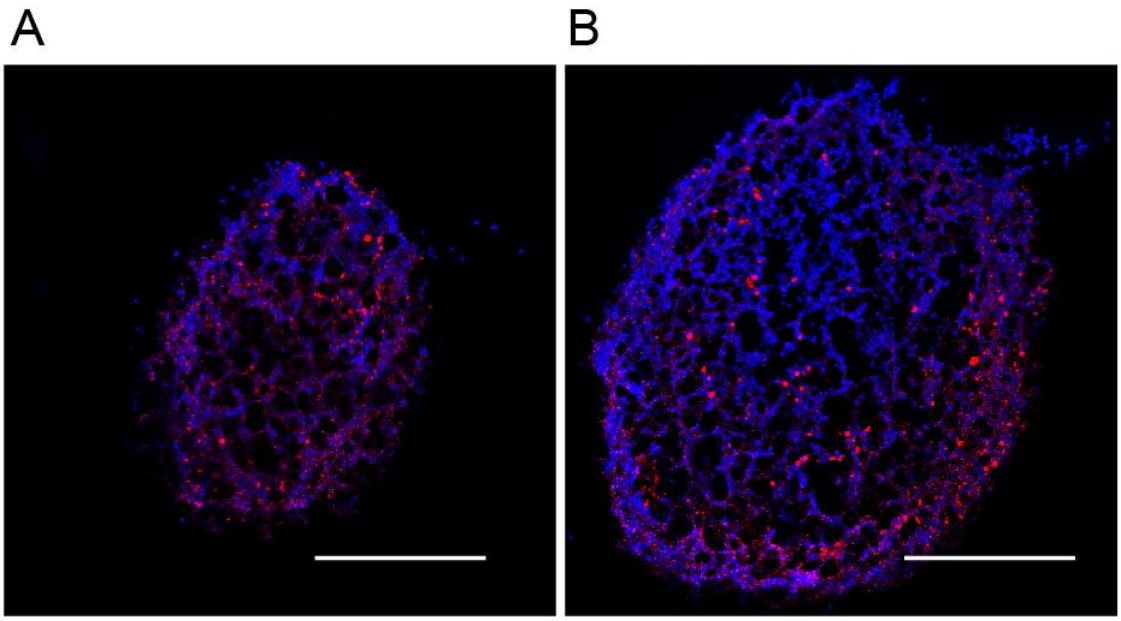

Figure 6.5. Distribution of BG-EDA in iPSC-derived neurospheres. Images show two representative sections from the surface (A) and middle (B) of the neurospheres. Nucleus stain (Hoechst) is blue and AF_{647}-labelled BG-EDA is red. *Scale bars are 100 μm.*

The ability of BG-EDA to complex plasmid DNA and transfect cells within the NSPs was examined. Polyplex formation between BG-EDA and a model plasmid expressing green fluorescent protein (pEGFP) was studied by agarose gel electrophoresis (**Figure 6.6A**). A constant amount of DNA (0.5 μg) was incubated with varying amounts of glycogen to obtain polyplexes with various glycogen:DNA w/w ratio. The absence of a DNA band indicates polyplex formation, while the presence of a DNA band indicates the presence of excess or free DNA in the mixture. From **Figure 6.6A**, it appears that effective complex formation occurs between glycogen:DNA w/w ratios of 20 and 30. For transfection experiments, the glycogen-to-DNA ratio of 20 was chosen, at which the polyplex had a diameter of 180 nm and a slightly positive charge. The association of BG-EDA/DNA polyplexes with cells from within NSPs was compared with that of free glycogen (**Figure 6.6B**). Both complexed and free BG-EDA showed high cell association with 60% of cells within the NSPs associating with free BG-EDA and over 80% of cells for BG-EDA/DNA.

Finally, the functional effect of pEGFP plasmid DNA transfected in NSPs (**Figure 6.6C**) was assessed. BG-EDA/pEGFP polyplexes (w/w ratio 20) were incubated with NSPs for 4 or 6 days. A two-fold increase in the GFP expression was observed 4 days post-transfection in cell treated with BG-EDA/pEGFP polyplexes (w/w ratio 20), compared to untreated cells. The expression of GFP was confirmed by confocal microscopy (**Figure 6.6D**). This effect was enhanced by delivering a higher amount of plasmid (from 0.5 μg to 1 μg) and by increasing the time of incubation from 4 days to 6 days, i.e., GFP expression was measured 6 days post-transfection. Since the NSPs were derived from FRDA iPSC with a genetic profile representing the disease, the delivery of a therapeutically-relevant plasmid DNA encoding *GFP-FXN* was tested as a gene therapy approach to treat FRDA (**Figure S6.9**). The results are consistent with those obtained for the model plasmid, showing a two-fold increase in GFP protein expression in FRDA patient-derived cells that can potentially be further modulated by engineering the promoter region of the plasmid. Taken together, these results show potential in the use of BG-EDA in gene therapy aimed at FRDA.

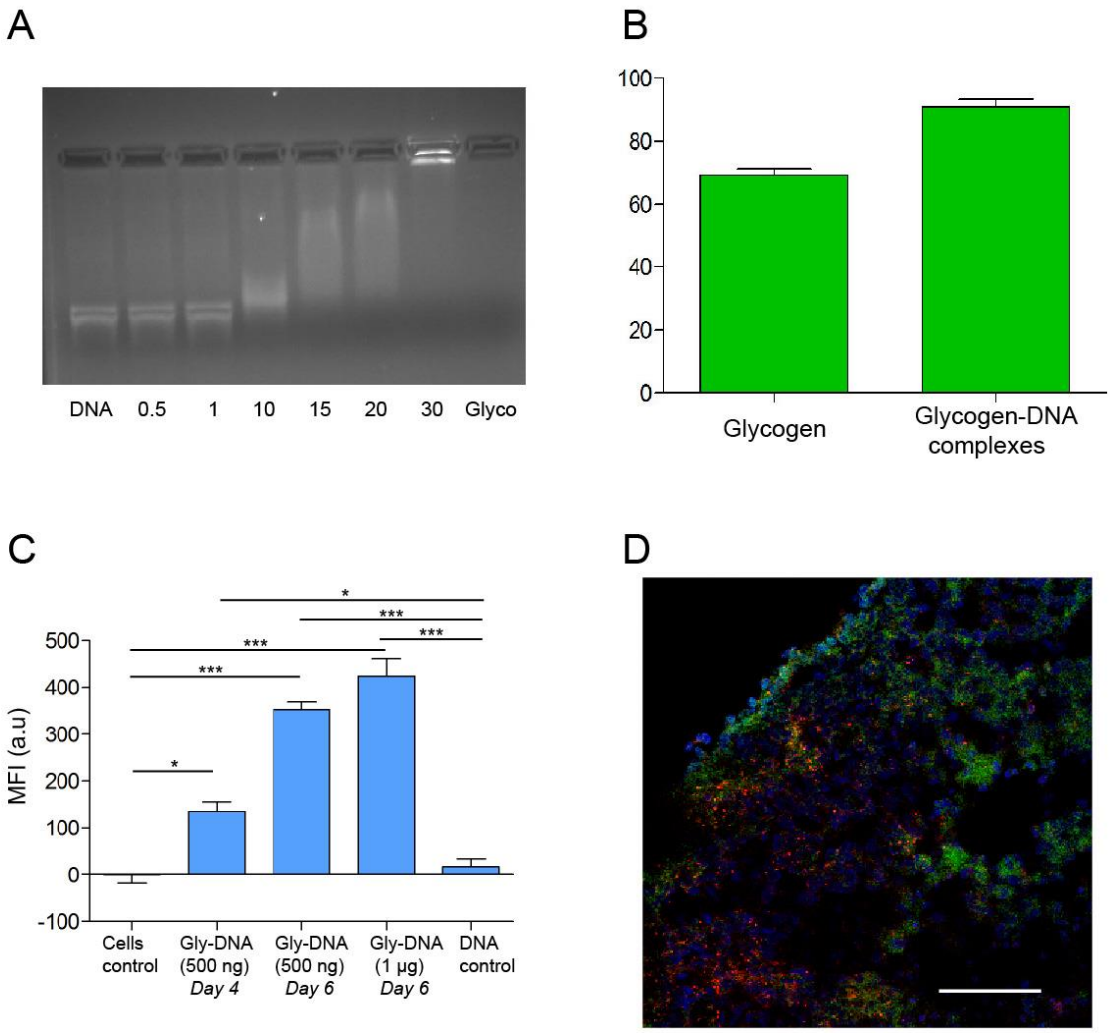

Figure 6.6. Characterization of glycogen-DNA complexes. Agarose gel electrophoresis analysis (A) of plasmid DNA complexation with BG-EDA: Lane 1, plasmid DNA; Lanes 2-7, BG-EDA/DNA complexes at different w/w ratios; and Lane 8, BG-EDA control. Glycogen cell association by flow cytometry (B) showing association of AF_{647}-labelled BG-EDA and BG-EDA/DNA complexes at w/w ratio 20 with neurospheres. Glycogen-mediated DNA transfection (C) as shown by an increase in GFP fluorescence after treatment with BG-EDA/pEGFP formed at w/w ratio 20. Confocal microscopy image (D) showing a section of neurosphere transfected with AF_{647}-labelled BG-EDA complexed with GFP-expression plasmid. *Scale bar is 100 µm.* Data are shown as the average mean ± standard error of the mean (n = 3). Statistical analyses were performed using one way-ANOVA with Tukey's multiple comparison test. ***$p < 0.001$

6.5. Conclusions

In these studies, the effects of particle size, surface charge and density on their distribution and penetration in 3D iPSC-derived human neuronal models was investigated. Particles with a 'hard' silica/polystyrene core were prepared *via* LbL assembly on spherical templates. The results indicate that a positive surface charge and a size within 230-280 nm facilitates penetration of the particles to the interior of the NSP. Particles that were more dense, due to the presence of a silica core, showed enhanced penetration, (up to 300 μm deep in the sphere), while lighter particles (PS core) with a similar size and charge were also able to enter the NSP, but less efficiently. "Soft" glycogen nanoparticles (30 nm) showed an even distribution within the NSPs. When assembled with plasmid DNA to form a polyplex (180 nm), the polyplexes also efficiently penetrated NSPs and importantly, the delivered pEGFP plasmid DNA was functional as demonstrated by the expression of GFP in neurons up to 6 days post-transfection. This work provides guidance on particle design for delivery to 3D neuronal culture. While nanoparticle design for crossing the blood-brain-barrier has been a major focus in brain delivery research, other routes for brain delivery and in combination with cell replacement therapy can be exploited to tackle some of the currently incurable neurodegenerative diseases. The stem cell-derived 3D neuronal cell model used in this work was a useful platform to screen various particle formulations and could be used in future studies to identify the most effective nanomedicines for drug delivery to neurons.

6.6. References

1. L. Naldini, *Nature*, 2015, **526**, 351-360.
2. J. M. Morachis, E. A. Mahmoud and A. Almutairi, *Pharmacol. Rev.*, 2012, **64**, 505-519.
3. A. Chowdhury, S Kunjiappan, T. Panneerselvam, B. Somasundaram and C. Bhattacharjee, *Int. Nano Lett.*, 2017, **7**, 91-122.
4. S. Senapati, A. K. Mahanta, S. Kumar and P. Maiti, *Signal Transduct. Target. Ther.*, 2018, **3**, 7.
5. E. Blanco, H. Shen and M. Ferrari, *Nat, Biotechnol.*, 2015, **33**, 941-951.
6. B. Yu, H. C. Tai, W. Xue, L. J. Lee and R. J. Lee, *Mol. Membr. Biol.*, 2010, **27**, 286-298.
7. A. E. Nel, L. Madler, D. Velegol, T. Xia, E. M. Hoek, P. Somasundaran, F. Klaessig, V. Castranova and M. Thompson, *Nat. Mater.*, 2009, **8**, 543-557.
8. J. Zhang, H. Tang, Z. Liu and B. Chen, *Int. J. Nanomedicine*, 2017, **12**, 8483-8493.
9. R. A. Petros and J. M. DeSimone, *Nat. Rev. Drug Discov.*, 2010, **9**, 615-627.
10. R. Edmondson, J. J. Broglie, A. F. Adcock and L. Yang, *Assay Drug Dev. Technol.*, 2014, **12**, 207-218.
11. M. Jorfi, C. D'Avanzo, D. Y. Kim and D. Irimia, *Adv. Healthc. Mater.*, 2018, **7**, 1700723.
12. M. Zanoni, F. Piccinini, C. Arienti, A. Zamagni, S. Santi, R. Polico, A. Bevilacqua and A. Tesei, *Sci. Rep.*, 2016, **6**, 19103.
13. S. A. Langhans, *Front. Pharmacol.*, 2018, **9**, 6.
14. W. Shi, D. Weng and W. Niu, *Cancer Transl. Med.*, 2016, **2**, 154-161.
15. H. L. Jang, Y. S. Zhang and A. Khademhosseini, *Nanomedicne (Lond.)*, 2016, **11**, 1495-1497.
16. E. G. Z. Centeno, H. Cimarosti and A. Bithell, *Mol. Neurodegener.*, 2018, **13**, 27.
17. J. Penney, W. T. Ralvenius and L. H. Tsai, *Mol. Psychiatry*, 2020, **25**, 148-167.
18. I. Y. Chen, E. Matsa and J. C. Wu, *Nat. Rev. Cardiol.*, 2016, **13**, 333-349.
19. A. Cota-Coronado, P. B. Ramirez-Rodriguez, E. Padilla-Camberos, E. F. Diaz, J. M. Flores-Fernandez, D. Avila-Gonzalez and N. E. Diaz-Martinez, *Drug Discov. Today*, 2019, **24**, 334-341.

20. M. D. Tang-Schomer, J. D. White, L. W. Tien, L. I. Schmitt, T. M. Valentin, D. J. Graziano, A. M. Hopkins, F. G. Omenetto, P. G. Haydon and D. L. Kaplan, *Proc. Natl. Acad. Sci. USA*, 2014, **111**, 13811-13816.
21. S. M. Chambers, Y. Qi, Y. Mica, G. Lee, X. J. Zhang, L. Niu, J. Bilsland, L. Cao, E. Stevens, P. Whiting, S. H. Shi and L. Studer, *Nat. Biotechnol.*, 2012, **30**, 715-720.
22. M. D. Neely, M. J. Litt, A. M. Tidball, G. G. Li, A. A. Aboud, C. R. Hopkins, R. Chamberlin, C. C. Hong, K. C. Ess and A. B. Bowman, *ACS Chem. Neurosci*., 2012, **3**, 482-491.
23. W. Li, W. Sun, Y. Zhang, W. Wei, R. Ambasudhan, P. Xia, M. Talantova, T. Lin, J. Kim, X. Wang, W. R. Kim, S. A. Lipton, K. Zhang and S. Ding, *Proc. Natl. Acad. Sci. USA*, 2011, **108**, 8299-8304.
24. A. M. Hopkins, E. DeSimone, K. Chwalek and D. L. Kaplan, *Prog. Neurobiol.*, 2015, **125**, 1-25.
25. S. Talib and K. A. Shepard, *Stem Cells Transl. Med.*, 2020, DOI: 10.1002/sctm.19-0375.
26. F. Piguet, C. de Montigny, N. Vaucamps, L. Reutenauer, A. Eisenmann and H. Puccio, *Mol. Ther.*, 2018, **26**, 1940-1952.
27. D. E. Crombie, C. L. Curl, A. J. A. Raaijmakers, P. Sivakumaran, T. Kulkarni, R. C. B. Wong, I. Minami, M. V. Evans-Galea, S. Y. Lim, L. Delbridge, L. A. Corben, M. Dottori, N. Nakatsuji, I. A. Trounce, A. W. Hewitt, M. B. Delatycki, M. F. Pera and A. Pebay, *Aging*, 2011, **9**, 1440-1449.
28. J. Liu, P. J. Verma, M. V. Evans-Galea, M. B. Delatycki, A. Michalska, J. Leung, D. Crombie, J. P. Sarsero, R. Williamson, M. Dottori and A. Pebay, *Stem Cell Rev. Rep.*, 2011, **7**, 703-713.
29. A. J. Alshawaf, S. Viventi, W. Qiu, G. D'Abaco, B. Nayagam, M. Erlichster, G. Chana, I. Everall, J. Ivanusic, E. Skafidas and M. Dottori, *Sci. Rep.*, 2018, **8**, 603.
30. Y. Zeng, Y. Kurokawa, Q. Zeng, T. T. Win-Shwe, H. Nansai, Z. Zhang and H. Sone, *Toxicol. Sci.*, 2016, **152**, 128-144.
31. L. Hoelting, B. Scheinhardt, O. Bondarenko, S. Schildknecht, M. Kapitza, V. Tanavde, B. Tan, Q. Y. Lee, S. Mecking, M. Leist and S. Kadereit, *Arch. Toxicol.*, 2013, **87**, 721-733.
32. P. E. C. Leite, M. R. Pereira, G. Harris, D. Pamies, L. M. G. Dos Santos, J. M. Granjeiro, H. T. Hogberg, T. Hartung and L. Smirnova, *Part. Fibre Toxicol.*, 2019, **16**, 22.

33. M. Wojnilowicz, Q. A. Besford, Y. L. Wu, X. J. Loh, J. A. Braunger, A. Glab, C. Cortez-Jugo, F. Caruso and F. Cavalieri, *Biomaterials*, 2018, **176**, 34-49.
34. D. Furtado, M. Bjornmalm, S. Ayton, A. I. Bush, K. Kempe and F. Caruso, *Adv. Mater*., 2018, **30**, 1801362.
35. X. Liang, X. Ren, Z. Liu, Y. Liu, J. Wang, J. Wang, L. M. Zhang, D. Y. Deng, D. Quan and L. Yang, *Int. J. Nanomedicine*, 2014, **9**, 419-435.

6.7. Supporting Information

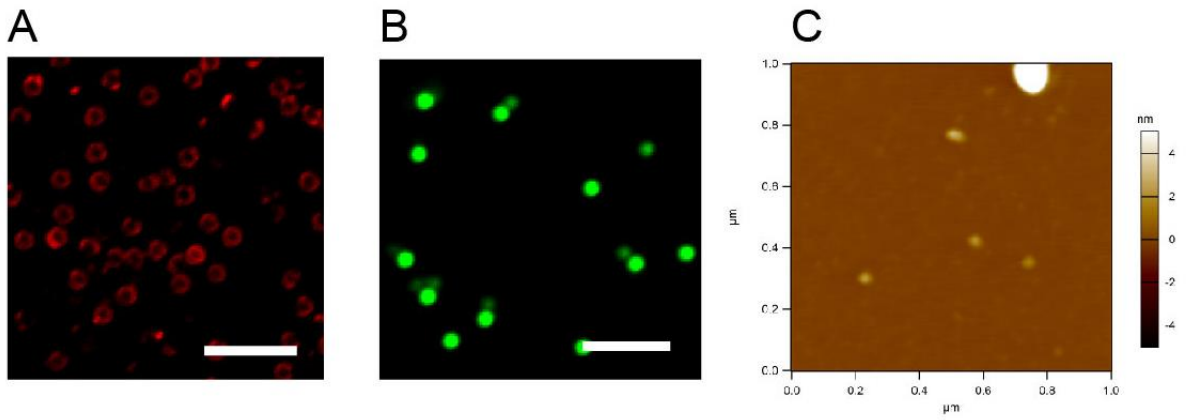

Figure S6.1. Particles imaging. Confocal microscopy images of templated core-shell particles with silica cores (837 nm) and a layer of AF_{647}-labelled PLArg (A); and PEI-coated FITC-labelled polystyrene particles (1µm) (B). AFM image of BG-EDA nanoparticles (C). *Scale bars are 5 µm.*

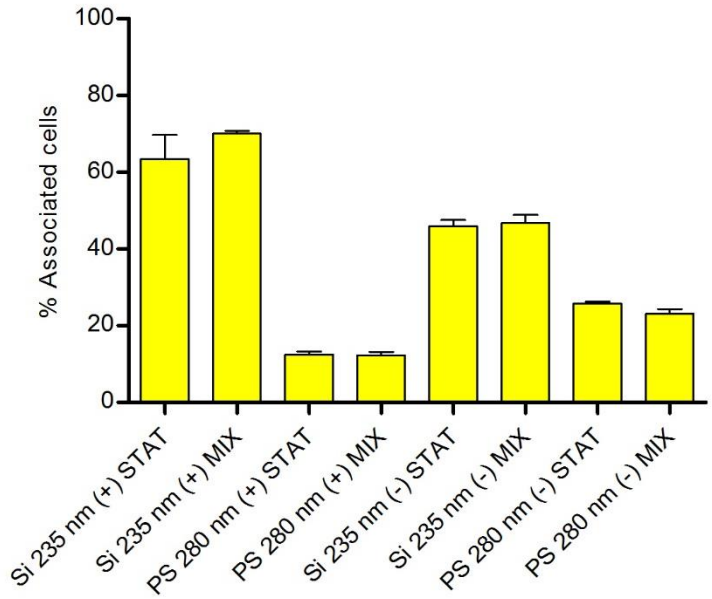

Figure S6.2. Comparison of static (STAT) and dynamic (MIX) cell culture conditions. The association of particles with cells in the NSPs after incubation at 37 °C for 72 h under static or dynamic conditions and disassembly of the NSPs for flow cytometry analysis. The particles tested include PLArg- (+) or PSS-terminated (-) silica particles (235 nm) and PEI-coated (+) or uncoated (-) polystyrene particles (280 nm). Data are shown as the average mean ± standard error of the mean (n = 3).

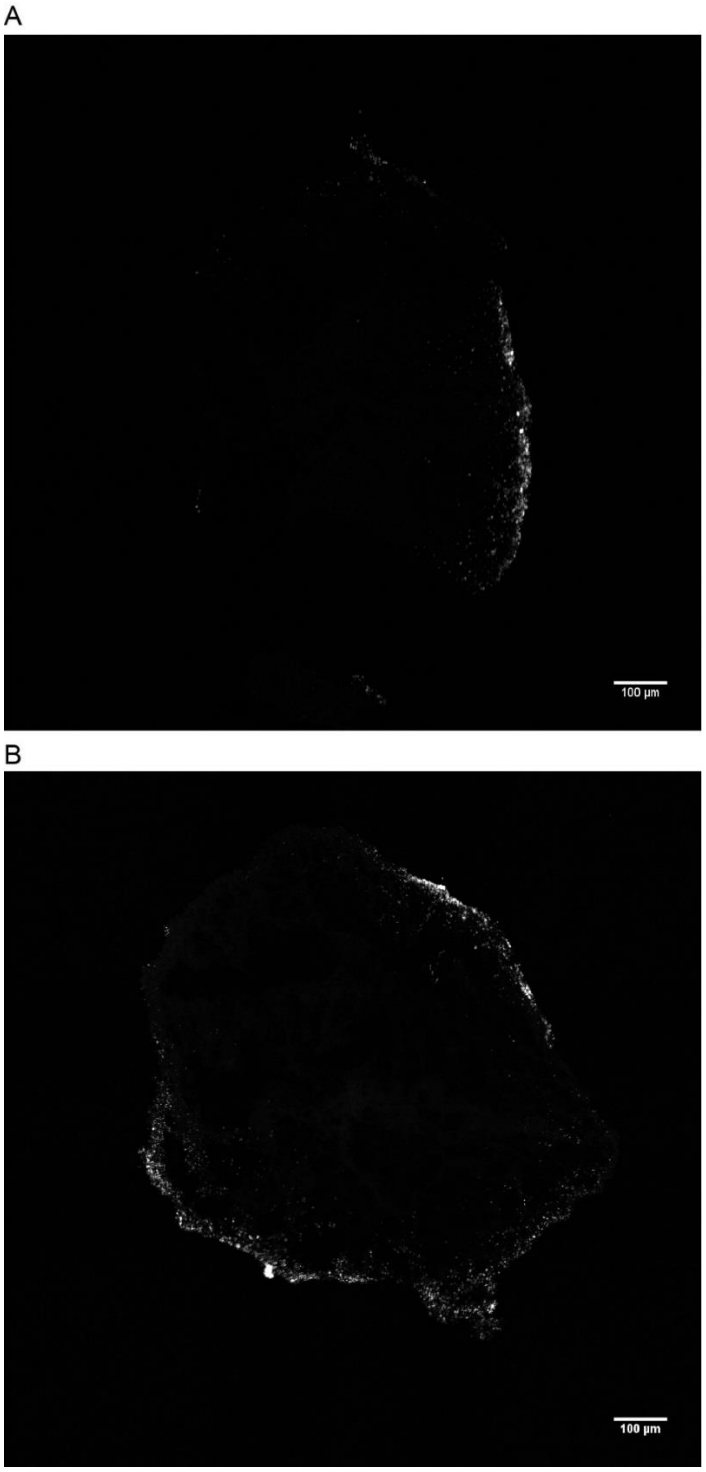

Figure S6.3. Particle distribution in neurospheres. Confocal microscopy images showing a cross-section of NSPs incubated with positively-charged (A) and negatively-charged (B) silica (837 nm) particles, coated with PLArg and PSS, respectively. Images show the fluorescence of AF_{647}-labelled particles in greyscale.

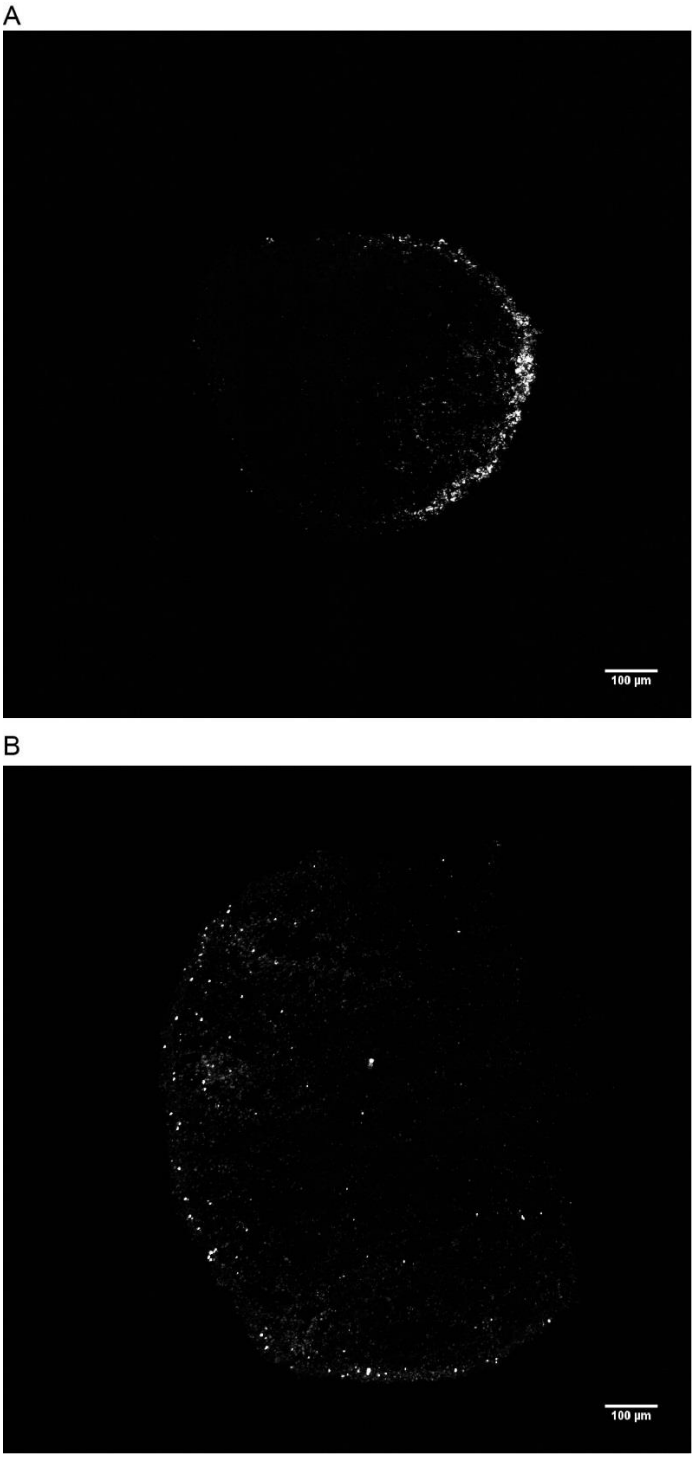

Figure S6.4. Particles distribution in neurospheres. Confocal microscopy images showing a cross-section of NSPs incubated with positively-charged (A) and negatively-charged (B) silica (387 nm) particles, coated with PLArg and PSS, respectively. Images show the fluorescence of AF_{647}-labelled particles in greyscale.

.

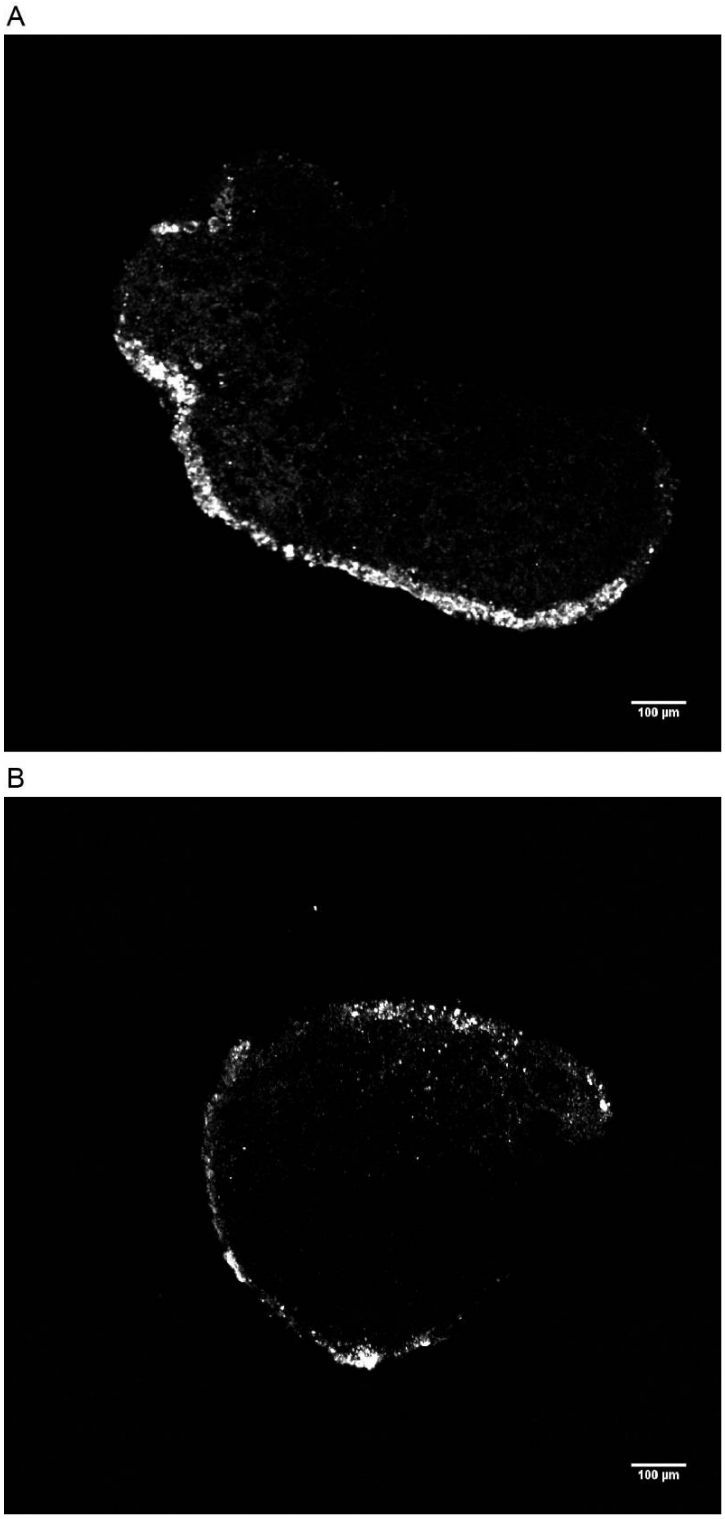

Figure S6.5. Particles distribution in neurospheres. Confocal microscopy images showing a cross-section of NSPs incubated with positively-charged (A) and negatively-charged (B) silica (235 nm) particles, coated with PLArg and PSS, respectively. Images show the fluorescence of AF_{647}-labelled particles in greyscale.

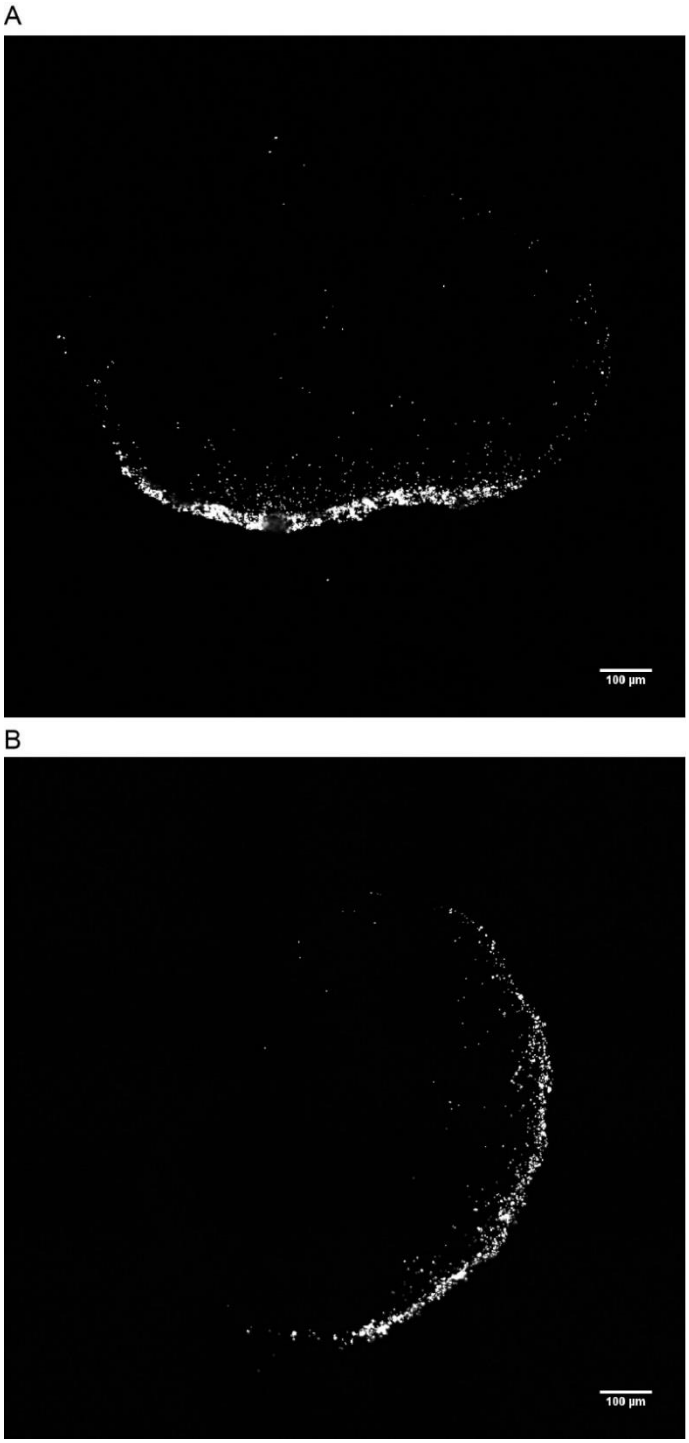

Figure S6.6. Particles distribution in neurospheres. Confocal microscopy images showing a cross-section of NSPs incubated with positively-charged (A) and negatively-charged (B) polystyrene (1000 nm) particles, coated with PEI and uncoated, respectively. Images show the fluorescence of AF_{647}-labelled particles in greyscale.

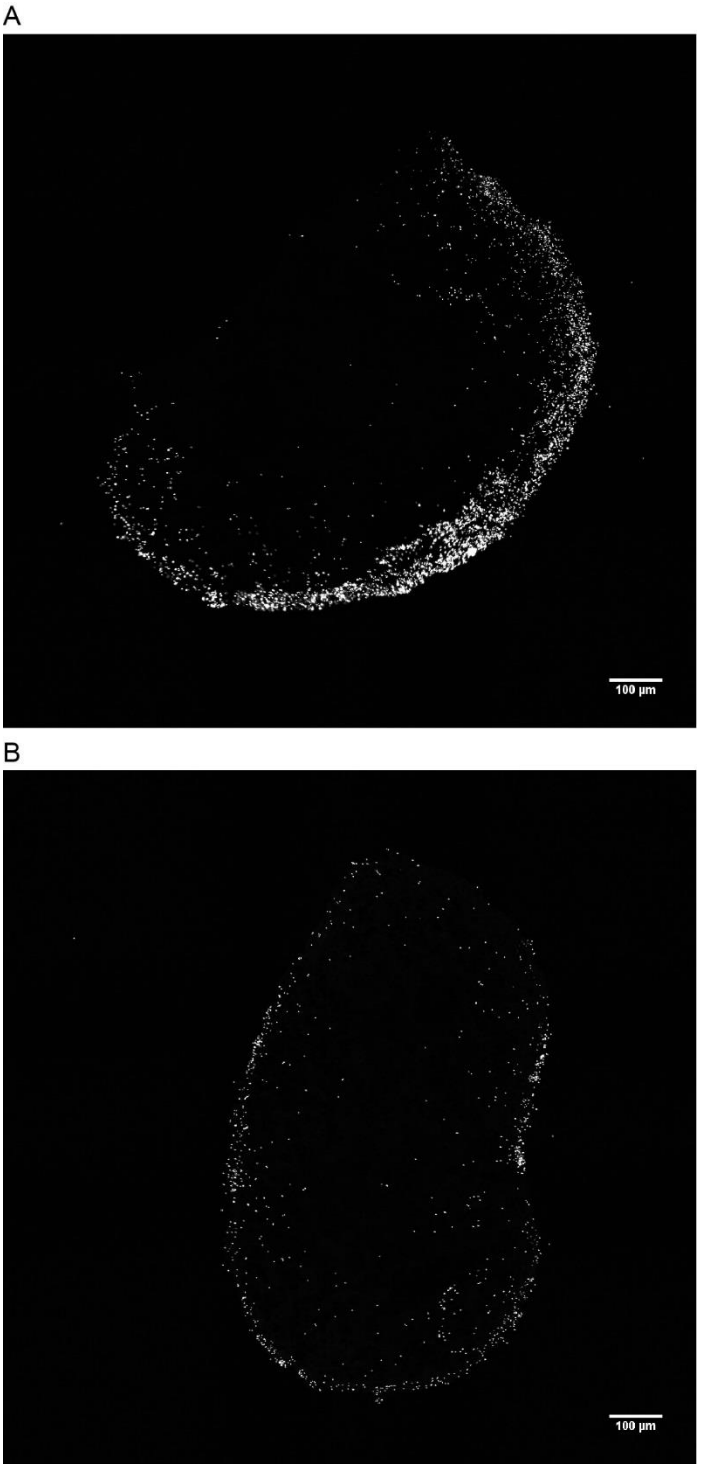

Figure S6.7. Particles distribution in neurospheres. Confocal microscopy images showing a cross-section of NSPs incubated with positively-charged (A) and negatively-charged (B) polystyrene (450 nm) particles, coated with PEI and uncoated, respectively. Images show the fluorescence of AF_{647}-labelled particles in greyscale.

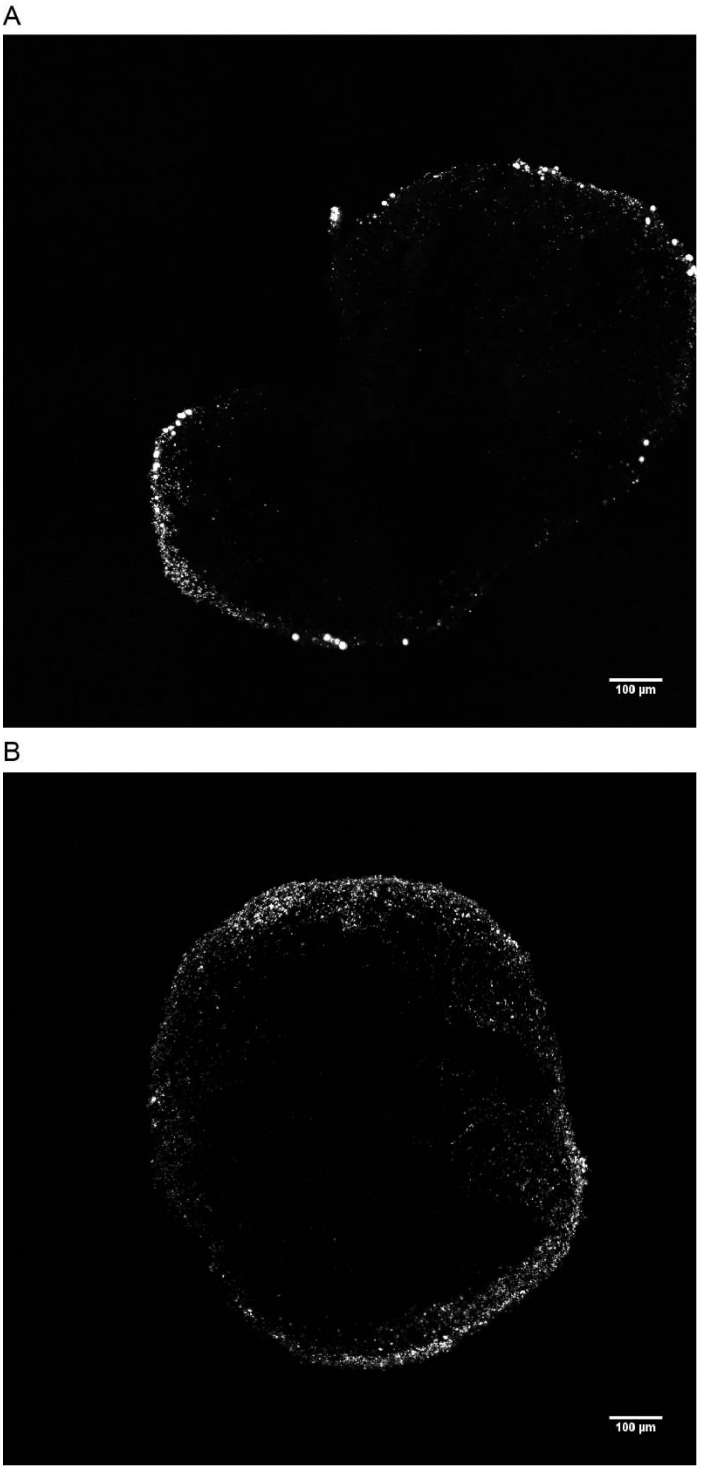

Figure S6.8. Particles distribution in neurospheres. Confocal microscopy images showing a cross-section of NSPs incubated with positively-charged (A) and negatively-charged (B) polystyrene (288 nm) particles, coated with PEI and uncoated, respectively. Images show the fluorescence of AF_{647}-labelled particles in greyscale.

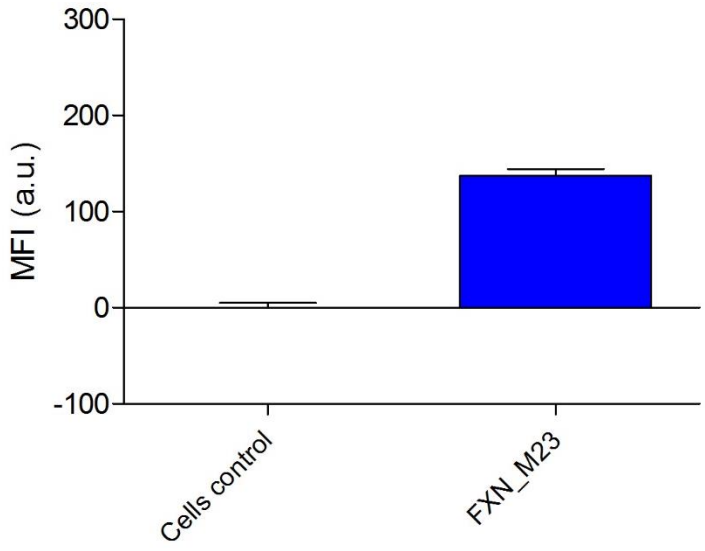

Figure S6.9. Glycogen-mediated plasmid delivery 4 days post-transfection. Flow cytometry results showing mean fluorescent intensity (MFI) after transfection with frataxin-expressing plasmid complexed with BG-EDA. Data are shown as the average mean ± standard error of the mean (n = 2). *FXN-M23 is pPB-ef1a-FXN-IRES-eEGFP-neo.*

Chapter 7

Conclusions and Perspectives

Drug therapies have been typically aimed at reversing or reducing disease symptoms through pharmacological intervention. In recent years, a better understanding of the mechanism of many diseases, often on a genetic level, and the development of new diagnostic and therapeutic tools, enabled the development of gene therapies aimed at prevention and/or treatment by manipulation of the natural gene expression process. The introduction of exogenous RNA allows for the silencing of malfunctioning genes, and DNA therapeutics aims to introduce new products of defective genes. Therapeutic approaches combining gene therapy with cell replacement therapy are emerging as a promising course of treatment, enabling autologous transplantation of genetically modified cells, thus minimizing the risk of transplant rejection. The effectiveness of therapeutics based on nucleic acids may be strongly limited, however, as their physicochemical properties make them susceptible to degradation by nucleases and inefficient in crossing biological barriers. Advances in nanotechnology enable the formulation of material-based gene carriers to encapsulate and/or complex DNA and RNA therapeutics to improve nucleic acids stability, protect from degradation, minimize off-target immune activation and prevent premature clearance by blood. Engineered gene delivery carriers have the potential to combine the benefits of gene therapeutics with efficient and targeted drug delivery, therefore offering a new pathway to develop treatments to the diseases that are not curable with currently available methods. The objective of the research project presented in this thesis was to develop material-based gene delivery system in therapy against HIV infection affecting the immune system and in Friedreich's ataxia – a rare genetic disease associated with neurodegeneration of the peripheral nervous system.

Chapter 3 described the use of polyarginine-containing particles in HIV therapy. The preparation of particles *via* layer-by-layer assembly, characterization and optimization of siRNA loading, followed by a functional gene suppression by targeting cytosolic mRNA in non-infected cell lines was demonstrated. Luciferase gene downregulation *via* post-transcriptional gene silencing (PTGS) was achieved by delivering luciferase-targeting siRNA bound to LbL core-shell particles and capsules, resulting in 50 and 40 % of gene knockdown, respectively. The optimized system was also used to target viral DNA integrated into the genome of HIV-infected cell lines and primary T cell and monocyte-derived macrophages. The viral suppression *via* transcriptional/epigenetic gene silencing (TGS) was demonstrated by delivering a siRNA sequence specific to the HIV 5’ long terminal repeat (LTR) promoter, resulting in a decreased level of viral reverse transcriptase enzyme, indicating inhibition of infection progression. Nowadays HIV infection is mostly manageable by early intervention

with antiretroviral therapy (ART), however, it does not affect the quiescent infection established in CD4 T cells and macrophages. The establishment of HIV latent reservoir in cellular and anatomical sites of the immune system remains the major obstacle to finding a sterilizing cure, that would allow for ART cessation without the risk of viral rebound. The particle-mediated anti-HIV siRNA delivery system presented in this chapter is the first reported example of using nanotechnologies to induce transcriptional gene silencing (TGS) as a means to control the viral genome by permanently locking it in a quiescent state. Particles surface engineering by adding targeting moieties could result in a more efficient siRNA delivery. Such an attempt was presented in this chapter by modifying the particle surface with an HIV-derived protein coating (i.e., viral envelope) utilizing the fusogenic properties of the viral capsid for enhanced binding and internalization in CD4/CCR5 expressing cells. Nevertheless, nanoparticle targeting to latently infected cells (mainly resting CD4 T cell carrying a fragment of integrated viral genome) remains a challenge due to the physiology of the resting cells (non-dividing and non-phagocytic), low abundance and difficulty to identify biomarkers specific for latent infection. The recent discovery of a new CD32a marker identified in infected CD4 T cells and present in cells residing in anatomical sites of latent reservoir opens the possibility to engineer nanoparticles to target CD32a receptors by attaching CD32a-specific antibodies to the particle surface. An alternative to targeting by an antibody is the modification of the particle surface with CD4-specific Designed Ankyrin Repeat Protein (DARPin), that has been shown to prevent viral infection without impairment of T cells functions by competitive inhibition and high affinity to the CD4 receptor used by HIV during cell entry. The preliminary *in vitro* results of the delivery of the nucleic acid by particles targeting CD4 T cells should be validated *in vivo*. While locking the latent reservoir in a permanently quiescent state is the ultimate therapeutic goal, a careful evaluation of the toxicity of the newly engineered carriers in immunocompromised *in vivo* models of HIV infection is required. Secondly, biodistribution studies of the proposed particle system are needed to accurately assess the potential of reaching various cellular and anatomical sites potentially harbouring HIV infected cells (e.g., lymph nodes, brain, gut).

Chapter 4 investigated the effect of cell properties on cell-particle interactions in activated primary peripheral blood mononuclear cells (PBMCs), pseudovirus-infected T cells and an HIV-latency model. In addition to LbL particles used in Chapter 3, polyethylene glycol mesoporous/hydrogel particles (MS@PEG/PEG capsule) and amine-functionalized bovine glycogen particles, an emerging nucleic acid delivery system, were used to assess cell

association and internalization depending on the physiological state of cells. In the PBMCs, cell activation resulted in an increased association of MS@PEG particles in T cells and NK cells. Studies of infected T cells indicate that the level of infection may affect the interaction with particle, particularly for MS@PEG. Contrary, in HIV latency model the cell reactivation had little effect on the internalization of LbL core-shell and MS @ PEG particles, however, less dense and more flexible formulations including PEG capsules and glycogen were internalized more efficiently in a model of active cells. While in literature, most of the reported nanoparticles used for drug delivery into T cells had diameters below 300 nm, the MS@PEG/PEG capsules and LbL particles used in this study exceed this size. These results suggest that the activation and progress of infection in T cells may influence cell-particle interaction and should not be neglected in the assessment of newly engineered particles for HIV therapy. This effect may be due to progressing apoptotic changes associated with infection and ultimately nucleus fragmentation. Noteworthy, virus infection in the early stages is associated with rearrangements of the cell cytoskeleton. Particle internalization mechanism and changes in the activity of different endocytosis pathways, as well as the persistence of actin changes associated with the viral entry and its implication in the particle-cell interactions, should be further explored. In addition, the second observation from the presented results is that the susceptibility of the particles to cell activation/infection-dependent association may depend on the type of particle. One of the suggested directions for future research could be the analysis of the protein corona formed on the particle surface from media containing activated and infected cells. Expected secretion of cytokines, signalling molecules and HIV virions in more advanced infection models can influence the surface identity of the particles and have implications on cell association.

Chapter 5 described the use of LbL polyarginine-containing particles in Friedreich's ataxia (FRDA) therapy. Characterization of the PEI-(PSS/PLArg)$_4$ film on planar and spherical surfaces and optimization of DNA loading was presented. Size-dependent particle uptake was demonstrated by flow cytometry and particles internalization was confirmed by confocal microscopy. Particles were used to deliver frataxin-encoding plasmid DNA to patient-derived iPSC neurons as a proposed therapy aimed at increasing the levels of frataxin, which is insufficient in FRDA. Particle-mediated FXN plasmid delivery resulted in a 27000-fold increase in frataxin transcript (mRNA) following 2 days treatment and uptake of DNA-coated particle was confirmed by confocal microscopy. These studies demonstrate the use of nanotechnology to deliver therapeutic plasmid to transplantable neurons and provide the basis

for further research towards combined gene and cell therapies, e.g. particle-mediated *ex vivo* transfection followed by transplantation of frataxin-expressing cells. The ongoing research on sensory neurons characteristics, namely identification of new markers, offers the opportunity for particle targeting to cells most susceptible to FRDA-associated neurodegeneration. One potential direction of future studies is to modify the particle surface using antibodies/ligands to Tropomyosin Receptor Kinase C or parvalbumin, which are expressed by sensory neurons implicated in FRDA.

Chapter 6 investigated the influence of particle physicochemical properties on their interaction with three dimensional (3D) neuronal cell models. The association, distribution and penetration of particles were assessed in iPSC-derived neurospheres. Templated layer-by-layer particles with various sizes (235 nm - 1μm), charges (positive and negative), densities (silica and polystyrene core), and soft, self-assembled system comprising amine-modified bovine glycogen complexed with plasmid DNA were used. From these studies, it was determined that a net positive charge and a size <300 nm enhances NSP penetration properties, as 235 nm LbL silica core particles were observed at ~250 μm depth of the sphere (600-800 μm in size). Glycogen particles, which are <30 nm in size, showed an even distribution across the neurosphere sections, displaying penetration properties superior to the templated LbL particles and was therefore optimized for DNA binding. The functional effect of glycogen-mediated EGFP plasmid delivery in neurospheres was assessed by flow cytometry and confocal microscopy, which showed an increase in GFP fluorescence in a time- and dose-dependent manner. Neurodegenerative diseases are usually discussed in the context of the central nervous system and therefore focus on the design of nanoparticles capable of crossing the blood-brain barrier. Instead, the results presented in this chapter highlight the possibility of using nanomaterials in gene therapy aimed at neurodegenerative diseases affecting the peripheral nervous system that may require different administration route, e.g. injection or cell transplantation, that should be considered in the gene carrier design. The 3D neuronal cell model employed in this chapter mimics the complexity of nervous tissue and have been presented as a valuable platform for screening various therapeutic formulations. Significant progress has been made towards a better understanding of the process of protein corona formation on particles, its effect on particles physicochemical properties and consequently, particle-cell interactions. While the majority of reports describes the protein corona derived from blood, the research into particle surface changes upon contact with the cerebrospinal fluid (CSF) is yet to be demonstrated. Compared to blood plasma, CSF contains fewer proteins,

glucose and potassium/calcium ions, however, more sodium/chloride ions in addition to various growth factors. A better understanding of the interaction of nanoparticles with CSF could contribute to the field of drug development to the human nervous system.

This thesis presented research toward the development of material-based gene delivery system to address challenges in HIV and Friedreich's ataxia therapies. This research was also aimed to gain a better understanding of the bio-nano interaction by studying particle-cell interactions depending on particles and cell properties. A novel therapeutic strategy to control the HIV genome by particle-mediated gene delivery for transcriptional gene silencing was presented. The use of an advanced patient-derived 3D cell model of a neurodegenerative disease presented an approach of drug testing in cells reflecting the genotype of the disease, demonstrating an alternative to costly and often premature use of animal models. The results presented in this thesis allowed the identification of potential new research directions, highlighting the need for further studies to gain a comprehensive understanding of particle interactions with T cells and neurons. Demonstrated therapeutic strategy of particle-mediated gene silencing to target viral DNA can pave the way for future studies on double-targeted gene therapies aimed at genetic control of various diseases and infections at the level of transcription (TGS) and translation (PTGS). Fundamental studies on bio-nano interactions in the presence of secreted cytokines, signalling molecules and viral particles in more advanced infection models could contribute to a better understanding of changes in particles surface identity and their implication on cellular uptake. The development and validation of new drug delivery systems to neurons could be facilitated by studies of interactions between particles and cerebrospinal fluid as a part of system characterization for a more accurate prediction of its clinical efficacy.